ADAPTIVE MODEL PREDICTIVE CONTROL AND DYNAMIC ANALYSIS FOR MAGLEV SYSTEMS

LU YANG

PhD

The Hong Kong Polytechnic University

2025

The Hong Kong Polytechnic University

Department of Civil and Environmental Engineering

Adaptive Model Predictive Control and Dynamic Analysis for Maglev Systems

LU Yang

A thesis submitted in partial fulfillment of the requirements for the degree of
Doctor of Philosophy

February 2025

CERTIFICATE OF ORIGINALITY

I hereby declare that this thesis is my own work and that, to the best of my knowledge and belief, it reproduces no material previously published or written, nor material that has been accepted for the award of any other degree or diploma, except where due acknowledgement has been made in the text.

_____ (Signed)

LU Yang (Name of student)

Abstract

Maglev technology has emerged as a revolutionary solution for modern transportation, offering high-speed, low-friction, and energy-efficient alternatives to conventional rail systems. Countries like Japan, Germany, and China have led the way in deploying operational maglev trains, showcasing advancements in dynamic modeling, levitation control, and system integration. Despite these achievements, several critical challenges persist in maglev suspension control. From a performance perspective, maintaining precise control of the levitation gap to ensure passenger comfort and operational safety remains difficult, particularly under poor track conditions. Nonlinear electromagnetic force characteristics inherently complicate controller design, leading to challenges in ensuring stability and accuracy. Additionally, variations in system parameters, such as mass changes due to passenger load variations and external environmental disturbances, pose significant difficulties for conventional controllers. These issues, combined with measurement noise and disturbances caused by track irregularities, further degrade control performance and system robustness. Addressing these multifaceted challenges comprehensively constitutes the primary objective of this research.

A detailed dynamic model of the electromagnetic suspension (EMS) system was developed to analyze its nonlinear characteristics and constraints. Conventional Proportional-integral-derivative (PID) control methods were initially implemented, revealing significant limitations in scenarios involving high-frequency disturbances, such as rapid levitation gap variations and

measurement noise. To overcome these issues, Model Predictive Control (MPC) was designed and validated, demonstrating superior performance in trajectory tracking, stability, and constraint handling compared to PID control. The integration of Kalman filters further enhanced the robustness of MPC under noisy measurements.

To address model inaccuracies and dynamic parameter variations, an Adaptive Model Predictive Control (AMPC) strategy was proposed. The AMPC framework, utilizing ARX-based adaptive models, showed remarkable improvements in handling real-time system changes. Simulation and experimental results validated its capability to minimize tracking errors, maintain stability, and outperform traditional MPC under dynamic conditions, such as mass variations and external disturbances.

The thesis further extended the analysis to a two-point suspension system and three-dimensional dynamic models that incorporate train-track-bridge interactions. Simulations demonstrated the AMPC controller's effectiveness in maintaining levitation stability and reducing oscillations under track irregularities and high-speed operations, highlighting its robustness and practical applicability.

The findings of this research contribute to the advancement of maglev suspension control systems by offering improved performance, adaptability, and stability. Future work will focus on integrating detailed control circuit simulations, exploring machine learning-based adaptive control algorithms to further enhance real-time adaptability, mitigate reliance on accurate modeling, and address residual limitations observed in AMPC strategies, as well as optimizing energy efficiency for multi-bogie suspension systems.

LIST OF PUBLICATIONS

1. Wang, S. M., Ni, Y. Q., Sun, Y. G., **Lu, Y.**, & Duan, Y. F. (2022). Modelling dynamic interaction of maglev train–controller–rail–bridge system by vector mechanics. *Journal of Sound and Vibration*, *533*, 117023.
2. Ni, Y. Q., Wang, S. M., Jiang, G. F., **Lu, Y.**, Lin, G. B., Pan, H. L., Xu, J. Q., & Hao, S. (2022). Multiple damage detection of maglev rail joints using time-frequency spectrogram and convolutional neural network. *Smart Structures and Systems*, *29*(4), 625-640.
3. Sun, Y. G., Wang, S. M., **Lu, Y.**, Xu, J. Q., & Xie, S. (2021). Control of Time Delay in Magnetic Levitation Systems. *IEEE Magnetics Letters*, *13*, 1-5.
4. Sun, Y. G., Wang, S. M., **Lu, Y.**, & Xu, J. Q. (2022). Gaussian process dynamic modeling and backstepping sliding mode control for magnetic levitation system of maglev train. *Journal of Theoretical and Applied Mechanics*, *60*(1), 49-62.
5. Chen, C., Xu, J. Q., **Lu, Y.**, Lin, G. B., & Ji, W. (2023). Experimental study on vertical vehicle-rail-bridge coupling of medium and low speed maglev train based on track beam with different stiffness. *Journal of Vibration and Control*, *29*(17-18), 4129-4142.
6. Li, H. W., Zhang, D., **Lu, Y.**, Ni, Y. Q., Xu, Z. D., Zhu, Q., & Wang, S. M. (2024). Self-Tuning Dual-Layer Sliding Mode Control of Electromagnetic Suspension System. *IEEE Transactions on Intelligent Transportation Systems*, *26*(2), 2366-2380
7. **Lu, Y.**, Wang, S. M., Zhu, Q., Liu, S. Y, & Ni, Y. Q. (2023). Online Monitoring System for Short Stator Maglev Train. *Proceedings of the 14th International Workshop on Structural Health Monitoring*, Stanford, United States, 373-380

Acknowledgements

I would like to express my heartfelt gratitude to all those who have supported me throughout my academic journey. First and foremost, I would like to thank my supervisor, Prof. Ni Yiqing, for his invaluable guidance, constant support, and insightful suggestions. I would also like to extend my sincere thanks to my co-supervisor, Dr. Wang Sumei, whose expertise, advice, and thoughtful feedback have greatly enriched my work.

I am deeply grateful to my family for their unwavering love, patience, and encouragement throughout my studies.

Finally, I would like to thank my friends and colleagues for their companionship and assistance during this journey

Table of Contents

LIST OF FIGURES

LIST OF TABLES

Chapter 1. Introduction

The rapid urbanization and globalization of society have created an ever-increasing demand for efficient, sustainable, and high-capacity transportation systems [1-3]. Traditional transportation networks are often strained under the pressures of growing populations, environmental concerns, and the need for faster connectivity. As a result, the development of advanced technologies that can meet these demands has become a critical focus for researchers and policymakers. Among these technologies, magnetic levitation (maglev) transportation systems stand out as a transformative solution for the future of mobility [4, 5].

1.1. Research Background and Motivations

The development of maglev (magnetic levitation) transportation systems represents a significant advancement in modern rail technology. Since their inception, maglev systems have demonstrated unique advantages over conventional wheel-based rail systems (WRS), such as higher operational speeds, reduced maintenance, and enhanced energy efficiency [4, 6-8]. These attributes make maglev systems an attractive alternative for meeting the growing demands of high-speed and sustainable transportation.

Maglev systems operate by utilizing electromagnetic forces to achieve levitation and propulsion, eliminating the need for mechanical components like wheels and axles. This fundamental difference introduces a range of benefits, such as reduced wear and tear, lower noise, and smoother rides.

Given the aforementioned advantages, the maglev train system has emerged as one of the most favored modes of transportation. The global landscape of maglev development varies, with

countries like China, Japan, Korea, Germany, British and the USA each contributing uniquely to its advancement [4, 9-14].

Despite considerable advancements, maglev suspension systems still encounter significant control challenges that hinder broader adoption and optimal performance. Specifically, these challenges include [4, 14-17]:

- Nonlinear Dynamics: The electromagnetic levitation forces depend nonlinearly on both the air gap and coil current, causing difficulties in achieving precise and stable control, particularly under varying operating conditions.
- External Disturbances and Parameter Variations: Maglev systems frequently experience disturbances from irregular track conditions and varying operational environments, requiring control systems to robustly handle unpredictable changes. Additionally, mass variations due to passenger load fluctuations significantly impact system dynamics, posing further control challenges.
- Measurement Noise and High-frequency Disturbances: Sensor noise and rapid fluctuations in levitation gap caused by track irregularities degrade measurement accuracy, complicating the control task and potentially compromising stability and safety.

Traditional control methods, such as Proportional-Integral-Derivative (PID) controllers, have been widely used but often fall short in handling nonlinearities, disturbances, and parameter variations. These limitations have highlighted the need for more sophisticated control strategies that can address the inherent complexities of maglev systems.Although various advanced control methods, including nonlinear control strategies (e.g., Sliding Mode Control and

backstepping), optimal methods (e.g., LQR), adaptive control, and intelligent control techniques (such as fuzzy logic and neural networks), have significantly improved the performance of maglev suspension systems, they still present inherent limitations. Nonlinear control approaches often introduce practical issues such as chattering, adversely affecting passenger comfort and system longevity. Optimal strategies, critically depend on accurate predictive modeling, and their performance rapidly deteriorates with model inaccuracies or unforeseen dynamic changes. Adaptive control methods can dynamically compensate for uncertainties, yet they typically exhibit slower adaptation to abrupt disturbances or parameter shifts. Similarly, intelligent control methods, despite their potential adaptability, often require extensive training data and complex design processes, limiting their immediate practicality and robustness in unpredictable real-world scenarios. Additionally, the experimental validation of these advanced methods remains limited, particularly under realistic or full-scale conditions.

The importance of robust control systems for maglev technology cannot be overstated. Effective control ensures stable levitation, precise positioning, and safe operation under varying conditions, including load changes and external disturbances [18, 19]. MPC has emerged as a promising solution to address these challenges [20, 21]. By predicting system behavior over a finite horizon and optimizing control inputs accordingly, MPC offers superior handling of nonlinearities and constraints. Its ability to incorporate multivariable interactions and anticipate future states makes it particularly suited for maglev applications, where precise control and stability are paramount.

This research focuses on the design, implementation, and evaluation of MPC strategies for

short-stator maglev suspension systems.

1.2. Research Objectives

The objectives of this research are as follows:

(1). To analyze the dynamic and nonlinear characteristics of short-stator maglev suspension systems, with a particular focus on the challenges arising from electromagnetic forces and system constraints.

(2). To develop a MPC framework capable of addressing the nonlinearities and constraints inherent in maglev systems, ensuring enhanced stability and performance.

(3). To conduct simulations and experiments that compare the control performance of MPC with traditional methods such as PID controllers, evaluating their effectiveness in various scenarios.

(4). To investigate the integration of adaptive techniques into MPC (adaptive MPC) to enhance the control system's ability to cope with parameter variations, external disturbances, and uncertainties.

(5). To verify the effectiveness of Adaptive MPC (AMPC) through full-scale three-dimensional simulation models, demonstrating its potential for real-world application.

1.3. Thesis Outline

Chapter 1 Introduction

- Overview of the evolution and significance of maglev technology.
- Identification of challenges in levitation and suspension systems.
- Motivations for employing advanced control strategies and the objectives of the research.

Chapter 2 Literature Review

- Comprehensive review of maglev technology development, classification, and modeling approaches.
- Analysis of control strategies, highlighting limitations of traditional methods.
- Identification of research gaps and formulation of research directions, emphasizing the need for robust control methods like MPC and AMPC.

Chapter 3 Numerical Dynamic Model of EMS Unit and PID Controller Design

- Development of a numerical dynamic model for EMS systems.
- Design and performance evaluation of PID controllers through simulations.
- Highlighting limitations of PID in high-frequency and noisy conditions, setting the stage for advanced control methods.

Chapter 4 Model Predictive Control for Maglev Suspension System

- Design and implementation of an MPC controller with Kalman filter integration.
- Stability analysis and simulation studies showcasing MPC's superior performance over PID.
- Identification of MPC's sensitivity to prediction model accuracy, emphasizing the need for adaptive methods.

Chapter 5 Adaptive Model Predictive Control for Maglev Suspension System

- Introduction of AMPC with ARX-based adaptive modeling.
- Simulation and experimental validation of AMPC's ability to handle model inaccuracies and improve trajectory tracking.
- Demonstrating AMPC's robustness in adapting to real-time system changes and noise.

Chapter 6 Two-Point Suspension Control System Based on ARX-AMPC

- Dynamic modeling and control design for a two-point suspension system.
- Comparative analysis of PID, MPC, and AMPC performance in simulations and experiments.
- Highlighting AMPC's advantages in managing dynamic interactions and maintaining stability.

Chapter 7 Dynamic Performance Analysis of the Maglev Train Using AMPC Under Track Irregularities and High-Speed Operation

- Development of a 3D dynamic model integrating train, track, and bridge systems.
- Analysis of AMPC's performance under varying track conditions and speeds.
- Validation of AMPC's robustness and passenger comfort enhancement in practical applications.

Chapter 8 Conclusions and Recommendations

- Summarize the key conclusions of this thesis and provide recommendations for future research.

Chapter 2. Literature Review

The core aim of this study, as previously mentioned, is to perform an in-depth dynamic analysis of the maglev train-track-bridge system and propose effective levitation control strategies informed by the analysis results. Accordingly, this chapter focuses on four key areas: the characteristics of maglev technology, current advancements in dynamic simulation research, and the study of levitation control algorithms.

2.1. Development of Maglev Technology

2.1.1. Characteristics and Classification of Maglev Train

Maglev trains are broadly classified based on the levitation technology they utilize. These technologies differ in their mechanisms for achieving levitation and propulsion, each offering unique benefits and facing specific challenges. The two primary maglev technologies are electromagnetic suspension (EMS) and electrodynamic suspension (EDS) [22-26].

(1). Electromagnetic suspension

The EMS system relies on electromagnetic forces to lift the train. In this configuration, electromagnets are installed on the train's bogies, which interact with ferromagnetic guideways to generate the levitation force. By continuously fine-tuning the magnetic field through an advanced control mechanism, the train is lifted above the track, effectively eliminating mechanical friction and allowing for smoother, faster travel. The key challenge for EMS systems lies in maintaining a precise levitation gap—typically between 8 and 10 millimeters—between the train and the guideway. This is achieved through a real-time feedback system that

adjusts the current supplied to the electromagnets, ensuring stability and safety throughout operation.

EMS-based maglev systems can be further divided into two categories depending on their propulsion system configuration, as shown in Figure 2.1 [22]. The first type features long stators, where the linear motor is integrated into the entire length of the track. The second type incorporates short stators, where the motor components are installed on the train itself. The Shanghai Maglev Train, which connects Shanghai Pudong International Airport to the city's downtown area, serves as a prominent example of EMS technology utilizing long stators. This implementation highlights the efficiency of EMS for high-speed urban transportation.

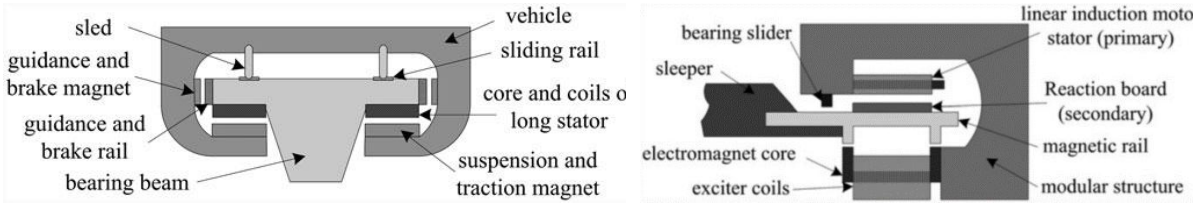

a) EMS used long stators b) EMS used short stators

Figure 2.1 Principle of two types EMS maglev train (Liu et al. 2015)

This study specifically focuses on the short stator EMS system, which has been increasingly applied in low- to medium-speed maglev transportation. By examining the control challenges and performance characteristics of short stator EMS technology, this research aims to optimize levitation control strategies for improved dynamic performance.

(2). Electrodynamic Suspension

EDS maglev systems utilize superconducting magnets to produce strong magnetic fields. These

magnetic fields interact with conductive coils embedded in the guideway, inducing electric currents that generate opposing magnetic fields, thus lifting the train. A distinctive feature of the EDS system is that the levitation force increases as the train's speed rises. Consequently, the train must achieve a minimum velocity before sufficient levitation occurs, differentiating EDS from EMS systems.

The working principle of EDS maglev systems is illustrated in Figure 2.2 [22]. Unlike EMS systems, EDS relies on superconducting magnets, which require cryogenic cooling systems to operate effectively. While this technology enables exceptional levitation performance and stability, it results in higher infrastructure costs and energy requirements due to the need for superconducting materials and cooling systems.

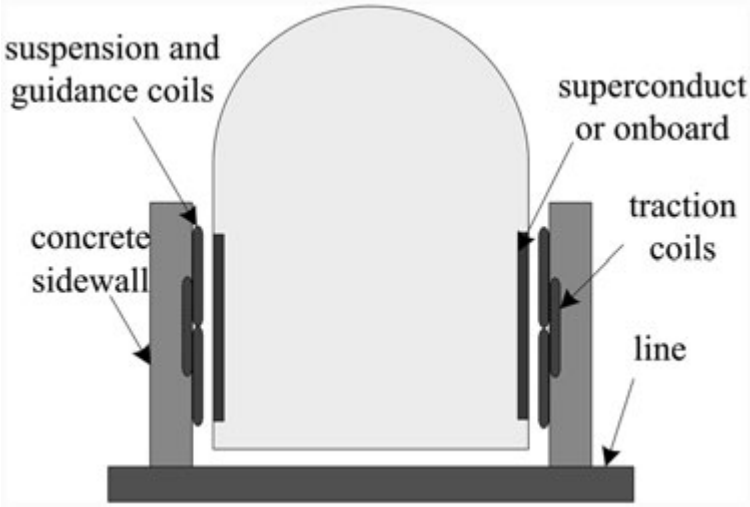

Figure 2.2 Principle of EDS maglev train (Liu et al. 2015)

2.1.2. Major Achievements in the World

Maglev technology has garnered global attention for its potential to revolutionize transportation systems. Various countries have made significant strides in the development and application of

maglev systems, showcasing their technological capabilities and addressing the demand for faster, more efficient, and sustainable transportation. The following section highlights the key achievements and progress made by leading nations in the field of maglev technology.

China has been a frontrunner in operationalizing maglev technology. The Shanghai Maglev Train, which connects Shanghai Pudong International Airport with the city center, is the world's first commercially operated high-speed maglev. It was inaugurated in 2004 and can reach speeds of up to 431 km/h, showcasing China's commitment to embracing and advancing maglev technology. Beyond Shanghai, cities such as Changsha, Beijing, Fenghuang, and Qingyuan have successively launched commercial maglev transportation lines. China is actively exploring further applications of maglev technology, with plans to expand its network and develop trains capable of reaching speeds up to 600 km/h.

Japan, known for its pioneering Shinkansen (bullet train) network, has also been a key player in maglev development. The country has invested heavily in the Chuo Shinkansen project, a maglev line designed to connect Tokyo and Osaka. Utilizing the superconducting maglev system, this train is expected to reach speeds of up to 505 km/h, potentially cutting the travel time between the two cities in half. Although facing various challenges, including high costs and environmental concerns, the project underscores Japan's ambition to lead in high-speed rail technology.

South Korea has contributed to the maglev field with a more urban focus. The Incheon Airport Maglev, which began operations in 2016, is South Korea's first commercial maglev line, albeit with more modest speeds of 110 km/h. Primarily serving as a demonstration and research

project, it reflects Korea's interest in integrating maglev technology into its urban transportation infrastructure.

Germany has a storied history with maglev technology, dating back to early research and development in the 20th century. The Transrapid system, developed by Siemens and ThyssenKrupp, achieved significant milestones, including the construction of a test line in Emsland. Despite the technology's promise, widespread commercial application in Germany has been limited, largely due to high costs and logistical challenges. However, Germany's contributions to maglev technology, particularly in engineering and safety systems, remain influential.

The British maglev train operated in Birmingham between 1984 and 1995, represents a notable chapter in the development of magnetic levitation transportation systems. This system was the world’s first commercial maglev system and was developed as a shuttle between Birmingham airport and a nearby rail station. The system operated over a distance of approximately 600 meters. Despite the pioneering efforts and technical achievements, the Birmingham maglev faced challenges, including high costs and limited utility due to its short route. The system was eventually closed in 1995 due to reliability and design problems.

In the United States, maglev development has been more tentative, with several proposed projects but limited implementation. The country has explored the potential for maglev systems in various corridors, such as the proposed route between Washington, D.C., and Baltimore. Despite the enthusiasm, progress has been slow, hindered by high costs, regulatory hurdles, and competition from other forms of transportation. However, ongoing research and feasibility

studies suggest a continued interest in maglev's potential to transform American transportation.

a) Shanghai Maglev Line

b) Changsha Maglev Express Line

c) Beijing Maglev Line S1

d) Fenghuang Maglev Sightseeing Express Line

e) Qingyuan Maglev Tourism Line

f) Korea Incheon Airport Maglev Line

g) Japan Yamanashi Maglev Line

Figure 2.3 Commercial Maglev Lines in the World

2.2. Modelling of Maglev System

The dynamic characteristics of Maglev train systems have been extensively studied through simulation models, evolving from simple two-dimensional frameworks to advanced three-dimensional analyses. These models are instrumental in capturing the complex interactions between the vehicle, guideway, and surrounding infrastructure, thereby enhancing our understanding of system behavior and improving design optimization. Early studies focused on fundamental 2D models that revealed essential vehicle-guideway dynamics, including vibration modes, control stability, and guideway irregularities. However, with advancements in computational power and the increasing need for higher accuracy, the focus has shifted to 3D simulations. These sophisticated models incorporate additional degrees of freedom, electromagnetic forces, and component flexibilities, enabling a more comprehensive representation of real-world operations. Moreover, factors such as soil-structure interaction, bridge dynamics, and the influence of eddy currents have been integrated into these simulations to address the challenges of operational stability, ride comfort, and infrastructure design,

ultimately driving the development of more efficient and robust Maglev systems.

2.2.1. Two-dimensional Simulation Models

Early research on Maglev dynamics primarily relied on two-dimensional models to capture the essential interactions between the vehicle and the guideway. Wang, Li et al. [27] introduced a double-deck model consisting of Bernoulli-Euler beams and evenly distributed springs to simulate the dynamic response of guideways subjected to moving vehicles. Their work provided valuable insights into natural frequencies and modes, which are essential for mitigating vehicle-guideway interactions and improving system stability.

Building on this foundation, Zheng, Wu et al. [28] developed a comprehensive numerical analysis of a Maglev vehicle system that incorporates a control framework, revealing the complex dynamics of vehicle behavior when accounting for flexible guideways. They introduced a five-degree-of-freedom model that considers heave, sway, pitch, roll, and yaw motions, marking a significant advancement in simulation capabilities. By integrating control parameters and disturbances, their study offered a nuanced understanding of system stability under varying conditions.

Zhao and Zhai [29] d extended this approach by proposing a 10-degree-of-freedom model to analyze the vertical random response and ride quality of Maglev vehicles. Their research emphasized the impact of guideway irregularities on ride comfort, advocating for careful guideway design to optimize the passenger experience. The use of direct time integration and discrete fast Fourier transform methods provided a robust foundation for understanding vehicle dynamics.

Yang and Yau [30] further expanded the scope by considering the soil-structure interaction in the dynamic analysis of Maglev systems. They introduced an iterative interacting method to study the Maglev train-guideway/foundation-soil system, highlighting the importance of soil dynamics in infrastructure design and system performance.

Zhang and Huang [31] introduced a practical vehicle/guideway model that incorporated real-world data through field measurements and model updating methodologies. Their case studies on operational Maglev lines demonstrated the accuracy and applicability of their approach, addressing real-world complexities in Maglev dynamics.

2.2.2. Three-dimensional Simulation Models

With advancements in computational capabilities, researchers have expanded the scope of dynamic analysis to three-dimensional simulations, offering a more detailed representation of system behavior by incorporating additional degrees of freedom and component flexibilities to address the complexities inherent in real-world operations.

Wen et al. [32] initiated this shift by establishing a 3D numerical model that emphasized the magnet-track interaction. Their study revealed the profound influence of vehicle dynamics on suspension electromagnetic forces, underscoring the interdependence between vehicle behavior and magnetic forces. Building on this, Z. Wang et al. [33] b developed a Maglev train-viaduct interaction model that incorporated the flexibilities of system components. By validating their results against measured dynamic responses, they demonstrated the critical role of support flexibility in accurately simulating Maglev dynamics.

Liu & Guo [34] introduced a state-space framework for analyzing linear random vibrations in

coupled vehicle-bridge systems. This approach provided a deeper understanding of how fluctuating currents and vehicle motion interact dynamically within a 3D environment. Taking into account real-world forces, H. Wang et al. [35] integrated experimental levitation force data into their 3D model of high-temperature superconducting (HTS) Maglev vehicles and bridges. Their study offered practical insights into dynamic interactions under operational conditions.

Li et al. [36] advanced this research further by conducting field tests to validate a finite element-based 3D simulation model for medium- low-speed Maglev systems. A key outcome of their study was the demonstration of a novel levitation bogie design that significantly enhanced dynamic performance. The optimization of suspension systems became a focal point in the work of Feng et al. [37], who combined field experiments with simulation platforms. Their results emphasized the importance of secondary suspension optimization for improving ride quality, especially at higher speeds.

To address large-scale infrastructure dynamics, Liu & Guo [38] developed a detailed 3D model to analyze spatial vibration characteristics of EMS-type Maglev vehicles over long-span bridges. Their iterative approach for solving coupled equations provided new insights into vertical and lateral interactions within the system. D. Wang et al. [39] extended this understanding to the bridge design domain by exploring vertical dynamics between low-to-medium-speed Maglev trains and bridges. Validated through field tests, their work highlighted the impact of bridge girder height on overall system performance.

Wang et al. [40] tackled the challenge of high-speed operations by analyzing vibrations caused by EMS Maglev trains passing through tunnels. By integrating train-guideway-tunnel-soil

interactions, they provided a holistic perspective on the system's dynamic behavior in confined environments. Li et al. [41] addressed specific infrastructure challenges with a rigid-flexible coupled dynamics model for train-turnout systems. Their analysis, validated through field data, highlighted the critical influence of turnout support stiffness and parameter optimization on dynamic performance.

Finally, L. Wang et al. [42] i investigated the dynamic responses of HTS Maglev systems under track random irregularities. Their study, conducted using Universal Mechanism (UM) software, examined vertical-lateral coupling effects across various speeds and bridge spans. The results affirmed the system's operational stability and smoothness.

2.3. Levitation Control Methods

With the rapid advancements in maglev technology, ensuring stable and efficient levitation control has become a critical research focus. The development of control methods spans multiple approaches, including linear, nonlinear, optimal, adaptive, and intelligent strategies. Each control methodology addresses specific challenges in maglev systems, such as nonlinearity, system uncertainties, dynamic load variations, and energy efficiency. This section provides a comprehensive review of levitation control methods, highlighting their theoretical foundations, practical implementations, and contributions to improving system stability, responsiveness, and robustness. By exploring both classical and advanced control techniques, this review offers insights into the evolution of control strategies and identifies future directions for achieving enhanced performance under dynamic and uncertain operating conditions.

2.3.1. Linear and Nonlinear Control Methods

Levitation control in maglev systems often begins with linear control strategies due to their simplicity and ease of implementation. Among these, Proportional-Derivative (PD) and Proportional-Integral-Derivative (PID) controllers have been widely explored. Rojas-Moreno and Cuevas-Condor [43] highlight the superiority of PID control over PD, demonstrating its ability to minimize steady-state error and reduce settling time. While PID controllers remain a cornerstone in maglev applications, Yaseen [44] compares PID with the Linear Quadratic Regulator (LQR) and shows that LQR achieves improved stability, especially under dynamic load variations, making it a robust choice for real-world systems.

The evolution of PID control further extends its application scope. Traditional single-degree-of-freedom PID designs have been enhanced with two-degree-of-freedom configurations, as described by Ghosh, Krishnan et al. [45]. In addition, Swain, Sain et al. [46] introduce fractional-order PID controllers, which provide more flexibility in tuning and demonstrate superior performance in achieving smoother responses and greater stability.

However, linear control methods often struggle when dealing with system nonlinearities and uncertainties inherent to maglev systems. To address these challenges, nonlinear control techniques have gained prominence. Sliding Mode Control (SMC) has emerged as a popular strategy due to its robustness in handling nonlinear dynamics and disturbances. Kong et al. [47], Yang et al. [48], and Xu et al [49] emphasize that SMC effectively mitigates uncertainties and ensures stable levitation. Despite its advantages, SMC suffers from the “chattering” phenomenon, which limits its practical application. Goel and Swarup [50] introduce High-

Order Sliding Mode Control (HOSMC) as a solution to reduce chattering while maintaining precision, marking a significant advancement in this domain.

Beyond SMC, researchers have explored alternative nonlinear strategies to improve control performance. Adaptive robust control methods, such as those presented by Sun et al. [51], combine robustness with adaptability to dynamic conditions, ensuring enhanced control accuracy. Similarly, backstepping control, as investigated by Wai and Lee [52], Malik et al. [53], and He et al. [54], integrates adaptive mechanisms with systematic mathematical frameworks. These approaches emphasize the importance of accurate system modeling and address complex nonlinear behaviors in maglev systems.

To further enhance energy efficiency and system robustness, researchers have proposed innovative control strategies. Tzeng and Wang [55] introduce a zero-power control method leveraging controlled permanent-magnet electromagnets to minimize power consumption without compromising stability. Park et al. [56] extend this line of research, focusing on energy-efficient designs that balance performance and resource utilization. Nonlinear PID controllers, as explored by Liu et al. [57], represent a hybrid approach, combining the simplicity of PID with the ability to address nonlinearities. Ni et al. [58], complement this by developing robust control designs based on improved suspension force models, providing tailored solutions for complex system dynamics and operational uncertainties.

Overall, while linear control methods such as PID and LQR provide a solid foundation for maglev levitation, nonlinear strategies—particularly SMC, HOSMC, and adaptive robust control—offer significant advancements in addressing the challenges posed by system

nonlinearity and uncertainties. The integration of energy-efficient designs and hybrid approaches highlights the ongoing efforts to optimize maglev control systems for stability, precision, and efficiency.

2.3.2. Optimal Control Methods

Optimal control techniques have emerged as powerful tools to refine control strategies in maglev systems, offering enhanced stability, performance, and energy efficiency. These methods leverage advanced mathematical frameworks and optimization algorithms to address both linear and nonlinear system dynamics effectively.

Linear optimal control methods, such as the Linear Quadratic Regulator (LQR), remain foundational in the design of maglev controllers. Raj, Swain, and Mishra [59] employ the Hamilton-Jacobi-Bellman (HJB) equation to develop LQR controllers for both infinite and finite-time horizons, achieving optimal system performance in linearized scenarios. Building on this foundation, Abbas et al. [60], and Dey et al. [61] integrate Particle Swarm Optimization (PSO) with LQR and PID controllers, respectively. The inclusion of PSO significantly enhances control precision and robustness, demonstrating improved responses under varying operational conditions.

As system nonlinearities and instabilities pose significant challenges, researchers have turned to advanced optimal control strategies. Gandhi and Adhyaru [62] utilize feedback linearization to design an optimal controller that effectively stabilizes electromagnetic levitation systems by addressing nonlinear behaviors. Tran et al. [63] extend this concept further by incorporating system constraints into a nonlinear optimal control framework. Using stable manifold theory

and Lagrange multipliers, they develop controllers that maintain system performance while adhering to practical constraints.

The rise of fractional-order controllers has introduced additional flexibility in optimizing maglev system performance. Ataşlar et al. [64] optimize fractional PID controllers using a hybrid algorithm, enhancing system robustness and stability. This innovative approach is further advanced by Sain et al. [65], and Wai et al. [66], who employ optimization techniques such as the Jaya algorithm and PSO to fine-tune I-PD and PID controllers. These efforts highlight the potential of fractional and hybrid approaches in achieving optimal performance with minimal tuning complexity.

To address the challenge of computational and hardware limitations, researchers have explored suboptimal control strategies. Pati et al. [67] propose a model reduction technique that simplifies control efforts while maintaining satisfactory performance, offering a cost-effective alternative to traditional optimal control approaches. This strategy is particularly beneficial for real-world applications where system complexity and resource constraints are critical concerns.

In addition to traditional optimal methods, MPC has emerged as a robust solution for maglev systems operating under dynamic and uncertain conditions. Zhang et al.[68] introduce a two-level state feedback MPC framework that effectively addresses system nonlinearities and instabilities. By incorporating predictive optimization and disturbance resistance, the proposed MPC design achieves superior precision and robustness, making it well-suited for complex maglev systems.

In conclusion, optimal control methods play a pivotal role in improving the performance and

robustness of maglev systems. From classical LQR designs and fractional-order controllers to advanced nonlinear strategies and MPC frameworks, these techniques provide a systematic approach to achieving stability and precision. The continued exploration of computationally efficient and adaptable optimization techniques highlights their importance in addressing real-world challenges such as system constraints, hardware limitations, and operational uncertainties.

2.3.3. Adaptive Control Methods

Building on the limitations of linear, nonlinear, and optimal control strategies in managing uncertainties and dynamic conditions, adaptive control emerges as a promising solution for maglev systems. Unlike fixed-gain controllers, adaptive control strategies can dynamically adjust system parameters to accommodate changes in operating conditions, offering superior stability, robustness, and efficiency. This section reviews key advancements in adaptive control methods, focusing on their ability to address nonlinearities, real-time disturbances, and system uncertainties while ensuring operational stability and ride comfort.

Adaptive control strategies often begin with methods that ensure system stability under uncertain conditions. Dalwadi et al. [69] introduce a reference model-assisted adaptive control structure that adapts to variations in the operating environment, maintaining optimal performance. Similarly, Zhou et al. [70] propose an adaptive vibration control method, emphasizing its role in enhancing ride comfort and mitigating disturbances. These works lay the foundation for adaptive approaches by demonstrating their ability to maintain system stability in dynamic and uncertain scenarios.

The challenge of nonlinear dynamics and uncertainties has spurred the development of advanced adaptive controllers. Yaseen et al. [71] and Huang et al. [72] address this by introducing innovative solutions such as Adaptive Terminal Sliding Mode Control (AT-SMC) and adaptive backstepping control, both of which effectively compensate for uncertainties while ensuring desired performance. In parallel, Bidikli and Bayrak [73] present a self-tuning robust RISE controller, while Xu et al. [74] develop an adaptive robust constrained state controller tailored for nonlinear maglev vehicles. These approaches illustrate the growing sophistication of adaptive techniques in managing highly nonlinear systems and uncertain parameters.

Real-time adaptability is critical for maglev systems operating under load disturbances and time delays. Zhang and Li [75] propose a real-time adaptive control method to handle significant variations in load conditions, ensuring smooth system operation. Addressing the challenge of time delays, Milani et al. [76] develop an adaptive robust controller that dynamically compensates for delay effects. These studies highlight the importance of real-time adaptive strategies in achieving robust control under rapidly changing operating environments.

To address specific challenges such as flexible track conditions and magnetic nonlinearities, researchers integrate robust and sliding mode control strategies with adaptive mechanisms. Chen et al. [77] introduce a sliding mode robust adaptive control method that leverages Radial Basis Function (RBF) network approximation to compensate for nonlinear dynamics. Similarly, Ren et al. [78] focus on the levitation control of medium and low-speed maglev vehicles, considering magnetic saturation and eddy current effects. The incorporation of neural networks

within adaptive frameworks underscores their potential to handle complex dynamics and enhance system robustness.

Optimization and disturbance rejection also play a pivotal role in adaptive control strategies. Shafiq and Akhtar [79] present an adaptive control strategy that combines an Adaptive Finite Impulse Response (FIR) filter with a PID controller to stabilize maglev systems under disturbances. Humaidi et al. [80] explore Active Disturbance Rejection Control (ADRC) optimized by Particle Swarm Optimization (PSO), demonstrating the superior performance of Linear ADRC (LADRC) in rejecting external disturbances and maintaining robust system stability.

To summarize, adaptive control methods provide dynamic and robust solutions to address the challenges of uncertainties, nonlinearities, and operational disturbances in maglev systems. By incorporating real-time adaptability, advanced robust techniques, and optimization methods, these strategies ensure enhanced system stability, responsiveness, and efficiency. The continued integration of neural networks and optimization algorithms within adaptive frameworks highlights future directions for improving maglev control under complex and dynamic conditions.

2.3.4. Intelligent Control Methods

While linear and optimal control methods provide foundational stability and precision, and adaptive control offers real-time parameter adjustment, they often fall short when managing intricate nonlinear behaviors and external disturbances. Intelligent control methods, incorporating tools like fuzzy logic, neural networks, and hybrid strategies, introduce

adaptability, learning capabilities, and enhanced robustness, making them particularly suitable for modern maglev systems under dynamic operating conditions.

Fuzzy Logic Control (FLC) is one of the pioneering techniques in intelligent control for maglev systems. Ahmad et al. [81] demonstrate the advantages of FLC over traditional PID controllers, highlighting its superior efficiency in reducing power consumption and minimizing maintenance requirements. Zhang et al. [82] extend the application of fuzzy logic by developing a Takagi-Sugeno fuzzy controller for magnetic levitation ball systems, improving performance and disturbance rejection. Sun et al. [83] further integrate fuzzy sliding-mode control to enhance robustness for low-speed maglev trains, effectively addressing system nonlinearities and external disturbances.

The fusion of fuzzy logic with other control techniques has led to significant advancements in maglev stability and performance. Wai and Lee [84] propose an adaptive fuzzy-neural-network control strategy that combines sliding-mode control with fuzzy neural networks, effectively compensating for nonlinearities and instabilities. Building on this, Wai et al. [85] introduce an observer-based adaptive fuzzy-neural-network control system, where adaptive observation enhances stability and efficiency in hybrid maglev systems. Sun et al. [86] further contribute by integrating fuzzy logic with the Analytic Hierarchy Process (AHP) to create a three-grade fuzzy evaluation framework for optimal controller selection, providing a systematic approach to decision-making in maglev train control.

Neural networks have also shown substantial potential in intelligent control by enabling systems to learn and adapt in real-time. Lairi and Bloch [87] develop a minimal neural network

structure for maglev system modeling and control, demonstrating its ability to avoid overfitting and improve generalization. Yau [88] explores a neuro-PI controller to manage maglev vehicles' dynamic responses, showcasing the adaptability of neural networks in vibration control. Qin et al. [89] adopt a data-driven approach using state-dependent ARX models and Gaussian radial basis function neural networks to optimize system parameters, emphasizing the role of predictive and adaptive control strategies.

Hybrid intelligent control methods further enhance system robustness by combining multiple techniques to overcome specific challenges. Zhang et al. [90] propose a hybrid control strategy that integrates particle swarm sliding-mode control with fuzzy PID control to address chattering issues in sliding mode control (SMC). Similarly, Ataşlar-Ayyıldız and Karahan [91] optimize PID-type fuzzy controllers using the Cuckoo Search algorithm, illustrating the impact of optimization algorithms on control precision and stability. Shiakolas et al. [92] utilize a real-time digital control environment, providing an effective platform for neural network-based controllers, while Xu et al. [93] introduce an adaptive neuron-PID controller, enhancing dynamic performance through intelligent learning mechanisms.

Additional contributions highlight the use of intelligent control to address time delays and dynamic instabilities. Sun et al. [94] investigate the Hopf bifurcation phenomenon in maglev systems, proposing a fuzzy adaptive tuning PID controller that provides real-time adjustment and vibration suppression. Sun et al. [95] address time delay issues using a Takagi-Sugeno fuzzy model, ensuring system robustness against disturbances. Chen et al. [96] pioneer an adaptive inversion control method for maglev trains, incorporating neural network state

observation to improve precision and stability.

In summary, intelligent control methods integrate fuzzy logic, neural networks, and optimization algorithms to address the challenges of nonlinearity, uncertainties, and dynamic disturbances in maglev systems. By combining adaptive learning, hybrid strategies, and real-time tuning, these approaches significantly enhance control precision, robustness, and energy efficiency. The continued evolution of intelligent control techniques highlights their potential to drive future advancements in maglev system performance and stability.

2.4. Model Predictive Control

2.4.1. Overview of MPC

In the context of maglev system control strategies discussed earlier, MPC represents an advanced and versatile approach that bridges the gap between traditional linear control, nonlinear control, optimal control, and adaptive control. While each of these methods has its strengths, MPC combines their key advantages—such as predictive optimization, robustness, and adaptability—into a unified framework capable of addressing system complexities, nonlinearities, and operational constraints [97, 98].

The foundation of MPC lies in its predictive nature [20, 21, 99, 100]. In each control step, MPC utilizes a dynamic system model to predict future states over a predefined prediction horizon. The controller then solves a constrained optimization problem, minimizing a cost function that accounts for tracking error, control effort, and energy efficiency. Typical formulations of the cost function may include quadratic terms to penalize deviations from the reference trajectory and excessive actuator usage. The optimization process incorporates constraints such as input

and state bounds, ensuring the feasibility and safety of the control actions.

MPC relies on solving a dynamic optimization problem at each control step using a system model to predict future behavior over a defined prediction horizon. By minimizing a cost function that typically balances tracking accuracy, control effort, and energy efficiency, MPC determines an optimal control sequence that adheres to system constraints such as input saturation, state bounds, and disturbance limits. Only the first control input of the sequence is applied, and the process is repeated at the next time step with updated system states. This receding horizon strategy ensures that MPC can adapt to changing operating conditions and disturbances in real time.

2.4.2. Predictive Models

The performance of an MPC controller is significantly influenced by the choice of the predictive model and optimization algorithm, particularly in systems with nonlinearities, disturbances, and constraints. Here, we discuss common predictive model types, each offering distinct trade-offs in terms of accuracy and computational demand.

Linear Predictive Models

The choice of the predictive model and optimization algorithm significantly influences the controller's performance, particularly in systems with nonlinearities, disturbances, and constraints. Linear models are commonly used due to their simplicity and computational efficiency. State-space representations, transfer functions, and autoregressive models (ARX) are typical linear approaches in MPC applications [101]. However, their accuracy is limited when applied to systems with pronounced nonlinearities. Efforts to mitigate this include gain

scheduling and piecewise linearization, where linear models are updated based on operating conditions [102].

Nonlinear Predictive Models

Nonlinear models are crucial for capturing complex system dynamics. Nonlinear autoregressive models (NARX), neural networks, and physics-informed models are often employed. While these models provide higher fidelity, they impose significant computational burdens, especially in real-time implementations [103]. Koopman operator theory, which transforms nonlinear dynamics into linear spaces, has recently emerged as an alternative to reduce computational complexity [104].

Adaptive and Data-Driven Predictive Models

Adaptive predictive models dynamically update their parameters to reflect real-time changes in system behavior. For example, ARX-based adaptive models have shown promising results in improving tracking accuracy under varying operating conditions [105]. Data-driven models, leveraging machine learning techniques, such as Gaussian processes and deep learning, are gaining traction for their ability to learn complex dynamics from historical data [106]. However, challenges remain in ensuring stability and interpretability [107].

2.4.3. Optimization Techniques in MPC

MPC employs a variety of optimization techniques to solve the underlying control problem efficiently. These methods ensure that the constraints are respected while minimizing the cost function, which typically balances tracking accuracy and energy efficiency.

Quadratic Programming (QP)

Quadratic programming is widely used in linear MPC, where the cost function and constraints are quadratic and linear, respectively. Efficient solvers like CVXGEN and OSQP allow real-time implementation in systems with fast dynamics [108]. Interior-point and active-set methods are popular QP techniques, with the former offering robust solutions and the latter excelling in small-scale problems [109].

Nonlinear Programming (NLP)

or systems with nonlinear models or constraints, nonlinear programming methods are necessary. Sequential quadratic programming (SQP) and interior-point methods dominate this domain [110]. SQP iteratively solves QP approximations of the nonlinear problem, while interior-point methods maintain feasibility during iterations. However, the computational demands of NLP often necessitate hardware acceleration using GPUs or FPGAs [111].

Mixed-Integer Programming (MIP)

Mixed-integer programming extends MPC to hybrid systems with discrete and continuous variables. Applications include switching systems and hybrid vehicles, where binary decision variables represent switching states [112]. Solvers like Gurobi and CPLEX facilitate MIP implementation, though their high computational cost often requires heuristics or approximations [113].

Real-Time Optimization Techniques

Real-time feasibility remains a critical challenge in MPC. Recent advancements include online optimization methods like fast gradient descent, alternating direction method of multipliers (ADMM), and model predictive static programming (MPSP) [114]. These methods balance

computational efficiency with optimality, enabling MPC deployment in embedded systems and high-frequency applications [115].

2.4.4. Constraint Handling in MPC

Handling constraints effectively is a crucial aspect of MPC. Various techniques are employed to ensure that system constraints are respected while minimizing the cost function.

Explicit Constraint Enforcement

In traditional MPC, constraints are explicitly handled by incorporating them directly into the optimization problem. This typically involves the use of inequality constraints in the optimization problem formulation. The MPC optimization problem can be written as:

$$\min_{u_0, u_1, \ldots, u_{N-1}} J(u_0, u_1, \ldots, u_{N-1}) \tag{2.1}$$

subject to: $x_{min} \leq x(t) \leq x_{max}, u_{min} \leq u(t) \leq u_{max}$, and dynamics constraints where J is the cost function that typically balances tracking error and control effort. The inclusion of state and input constraints in this manner guarantees that the resulting optimal trajectory satisfies the specified bounds, but it can lead to computational difficulties when the constraints are active over a large portion of the prediction horizon [102].

Explicit handling is commonly used in systems where constraints are not frequently violated and can be integrated into standard optimization solvers such as QP [116]. However, the explicit enforcement of constraints often results in increased computational complexity, particularly for large-scale systems with multiple constraints.

Soft Constraints

Soft constraints provide more flexibility by allowing certain violations of the constraints, but

with penalties. This is typically achieved by introducing slack variables or penalty terms in the cost function. The cost function for a system with soft constraints might look like:

$$\min_{u_0,u_1,\ldots,u_{N-1}} J(u_0,u_1,\ldots,u_{N-1}) + \lambda \cdot \sum_{k=0}^{N-1} \text{penalty}\big(x(t_k),u(t_k)\big) \tag{2.2}$$

where λ is a penalty factor that penalizes violations of the constraints. These penalties allow the optimization process to "softly" violate constraints when necessary, thus enabling the controller to handle unforeseen disturbances or system uncertainties without failing entirely [117]. The use of soft constraints is particularly beneficial when exact adherence to constraints is not critical, but deviations must be minimized.

Adaptive Constraint Handing

Adaptive constraint handling techniques are particularly useful in dynamic environments where constraints may change over time. These methods adjust the constraints based on real-time information about system performance or external disturbances. For instance, in systems where the physical boundaries change (e.g., track geometry variations in maglev systems), adaptive MPC frameworks can modify constraint bounds dynamically to reflect these changes and maintain safe operations [112].

Adaptive methods often use a model of the system or historical data to predict potential violations of constraints and adjust the optimization strategy accordingly. This can be achieved through adaptive penalty functions, dynamic constraint scaling, or real-time constraint updates in the optimization problem formulation [118].

Robust MPC

Robust MPC is designed to handle uncertainties in both the system model and constraints. In

this approach, uncertainty is explicitly considered in the optimization problem, often by using worst-case scenarios or stochastic models. The goal is to find a control policy that guarantees system performance despite disturbances or modeling errors. This is particularly important in real-world applications where disturbances (such as measurement noise, unmodeled dynamics, or external perturbations) can cause constraint violations if not properly addressed.

One common method for robust MPC is using scenarios or probabilistic constraints, where the optimization problem is solved for multiple possible future scenarios, ensuring that the system remains feasible with high probability [119]. In some cases, robust MPC also incorporates the concept of invariant sets to guarantee that the system will not violate constraints for any possible initial condition or disturbance.

Constraint Relaxation Techniques

In some cases, it may be necessary to relax certain constraints temporarily to avoid infeasibility. Constraint relaxation is achieved by slightly modifying the constraint limits to allow the optimization problem to remain solvable. This approach is typically used in scenarios where the system is near the boundary of feasibility, and relaxing some constraints can prevent the system from becoming stuck in a suboptimal solution.

A common method for constraint relaxation involves introducing a "relaxation parameter" that gradually adjusts the constraint bounds in real-time. This approach is typically used in systems that experience rapidly changing dynamics or large disturbances [120]. The challenge with constraint relaxation lies in balancing the need for feasibility with the system's performance goals.

2.4.5. Computational Efficiency and Real-Time Implementation

Accelerated Optimization Solvers

The computational efficiency of constraint handling in MPC is a critical factor for real-time applications. To handle large numbers of constraints or high-dimensional state spaces, many recent advancements focus on optimizing the solvers used to solve the underlying optimization problem. Techniques such as model predictive static programming (MPSP), fast gradient methods, and the use of hardware acceleration (e.g., GPUs or FPGAs) have shown promise in reducing the time required to solve large-scale MPC problems with constraints [114].

Recent studies also focus on algorithmic improvements to reduce the complexity of constraint handling, such as using efficient warm-start techniques to initialize optimization problems or utilizing dual decomposition methods to split the problem into more manageable subproblems [115].

2.4.6. Application of MPC

MPC has found widespread application across various industrial and engineering domains due to its ability to handle multi-variable systems, enforce constraints, and adapt to dynamic conditions in real time. Its versatility and predictive optimization capabilities make it a valuable tool for improving performance, efficiency, and robustness in complex systems.

In the process control industry, MPC remains one of the most prominent and mature control strategies. It is widely employed in chemical, petrochemical, and manufacturing processes, where maintaining operational constraints and optimizing system performance are critical. Qin and Badgwell [121] conducted a comprehensive review of MPC applications in process

industries, demonstrating its success in optimizing production efficiency, reducing energy consumption, and maintaining product quality under varying conditions. MPC's capability to predict future states allows it to respond proactively to disturbances, ensuring smooth operation and minimizing downtime.

In energy systems, MPC plays a critical role in renewable energy integration, smart grid management, and energy storage optimization. Parisio et al. [122] applied MPC for energy dispatch in microgrids, ensuring cost-efficient and reliable operation under fluctuating demand and renewable generation. In battery management systems, MPC has been shown to enhance performance and extend battery life by optimizing charging and discharging processes [123].

The automotive industry has extensively utilized MPC for advanced driver assistance systems (ADAS), powertrain control, and autonomous vehicles. Kapania et al. [124] implemented MPC for real-time lane-keeping and adaptive cruise control, achieving robust performance under varying road and traffic conditions. Similarly, He et al. [125] demonstrated the benefits of MPC in hybrid electric vehicles, where it optimizes energy management to reduce fuel consumption and emissions.

Robotics has also seen significant advancements with MPC, particularly in trajectory planning, collision avoidance, and multi-robot coordination. Nascimento et al. [126] provide a comprehensive review of MPC techniques for trajectory tracking in nonholonomic mobile robots. They emphasize that both linear MPC (LMPC) and nonlinear MPC (NMPC) can address path-following and motion constraints effectively, with NMPC providing superior accuracy for highly dynamic systems. Teatro et al. [127] extend NMPC for omnidirectional

mobile robots, incorporating obstacle avoidance directly into the optimization problem. This approach allows for collision-free navigation and smooth path tracking in real time.

For maglev systems, MPC has also been explored to address various control challenges. In hybrid levitation systems, MPC effectively stabilizes systems incorporating both superconducting and normal conducting coils, while efficiently handling state constraints such as air gap limits and input voltage saturation [97]. For multi-point levitation systems, cooperative MPC strategies explicitly consider the coupling dynamics between multiple levitation points, ensuring synchronized control and enhanced robustness against track irregularities [128]. In permanent magnet-based maglev systems, MPC integrated with fuzzy PID control improves speed tracking accuracy and reduces energy consumption by combining predictive optimization with real-time control adjustments [129].

2.5. Summary and Research Remarks

Summary

This section provides a brief summary of the key areas covered in this chapter. The literature review focuses on maglev technology, its modeling, and various levitation control methods, including traditional, optimal, adaptive, and intelligent strategies.

Maglev technology has been extensively developed with two main levitation types: EMS and EDS. EMS, particularly short-stator systems, has gained prominence due to its practical application in low-medium-speed maglev transportation. Short-stator EMS systems present significant control challenges, particularly in maintaining a stable levitation gap and addressing dynamic operating conditions.

The modeling of maglev systems has progressed from early two-dimensional (2D) approaches to advanced three-dimensional (3D) simulations. While 2D models capture basic vehicle-guideway dynamics, 3D models incorporate bridge flexibilities, soil-structure interactions, and external disturbances to provide a more realistic representation of system behavior. These developments have greatly improved our understanding of maglev dynamics and performance. Levitation control strategies have evolved to address the complexities of maglev systems. Traditional linear control methods such as PID and LQR offer simplicity but face limitations when managing nonlinearities and uncertainties. To address these challenges, nonlinear methods like Sliding Mode Control (SMC) and backstepping control have been developed, providing improved robustness at the cost of practical issues like chattering. Optimal control methods, including MPC, have emerged as powerful tools due to their predictive optimization and ability to manage system constraints. Meanwhile, adaptive control methods dynamically adjust control parameters to accommodate system uncertainties, ensuring better stability under varying conditions. Finally, intelligent control methods integrate fuzzy logic, neural networks, and hybrid strategies to further enhance adaptability and performance. Table 2.1 summarizes the key advantages and disadvantages of commonly used advanced control approaches in maglev systems, providing a comparative overview of their suitability for different control challenges.

Table 2.1 Advantages and Disadvantages of Advanced Control Approaches for Maglev Systems

Control Approach	Advantages	Disadvantages

Linear Control (PID, LQR)	Simple structure, easy implementation, good for linear systems	Limited robustness, inadequate handling of nonlinearities and uncertainties
Nonlinear Control (SMC, Back stepping)	Robust to uncertainties, effective against nonlinearities and disturbances	SMC suffers from chattering; backstepping complexity increases rapidly with system order
Optimal Control (LQR, MPC)	Good performance through optimization, handles constraints effectively	High dependence on accurate models, computationally intensive for complex or nonlinear models
Adaptive Control	Real-time parameter adjustment, effective in handling uncertainties and system variations	Slower response to abrupt disturbances, complexity in real-time parameter estimation
Intelligent Control (Fuzzy Logic, Neural Networks)	Adaptive and robust, suitable for nonlinear systems, ability to learn and handle uncertainties	Requires extensive training data, computationally intensive, difficulty in interpretability

MPC has gained particular attention as it combines the strengths of these control strategies. By predicting system behavior and solving an optimization problem at each time step, MPC ensures precise and robust performance even under complex and uncertain operating conditions. Table 2.2 presents a comparison of various MPC-based strategies, highlighting their modeling approaches, benefits, and limitations to clarify their respective roles in improving maglev levitation control.

Table 2.2 Comparison Among Different MPC Approaches

MPC Approach	Key Features	Advantages
Linear MPC	Uses linear predictive models, QP	Computationally efficient, easy to implement
Nonlinear MPC	Employs nonlinear models and NLP	High accuracy for complex and nonlinear dynamics
Robust MPC	Accounts for model uncertainties using worst-case scenarios or stochastic approaches	Enhanced robustness to uncertainties and disturbances
Adaptive MPC	Predictive models updated dynamically based on real-time data	Handles system variations effectively, improved accuracy under changing conditions
Data-driven MPC	Predictive models derived from historical data using machine	Learns complex dynamics from data, flexible and adaptive

Research Gap

Despite these advancements of MPC, significant challenges remain. The control accuracy of existing strategies deteriorates under dynamic conditions such as external disturbances or parameter variations. A mismatch between the predictive model and the actual system dynamics, such as changes in mass, further limits performance. Additionally, while numerous control strategies have been proposed, experimental validation is often limited, particularly in realistic or large-scale systems.

Research Direction

To address these research gaps, this study focuses on designing MPC and Adaptive MPC to improve levitation control accuracy and robustness under dynamic and uncertain conditions. The performance of the proposed controllers will be thoroughly evaluated through simulation and experimental validation. Furthermore, a three-dimensional simulation model will be employed to verify the effectiveness of Adaptive MPC in more complex maglev systems, including dynamic vehicle-track-bridge interactions. By bridging these gaps, this research aims to advance levitation control strategies for maglev systems, ensuring precision, robustness, and practical applicability.

Chapter 3. Numerical Dynamic Model of EMS Maglev System and Traditional Controllers Design

3.1. Introduction

The EMS maglev system, characterized by its reliance on electromagnetic attraction forces, is simplified for analysis into a single electromagnet suspension model. The model includes detailed considerations of dynamic responses, electromagnetic forces, and suspension gaps. The PID controller is utilized to manage the suspension gap by adjusting the current applied to the electromagnets, ensuring stable levitation despite disturbances. Key parameters such as proportional, integral, and derivative gains are fine-tuned to optimize performance. Simulation results under various conditions, including the presence of noise measurement, demonstrate the controller's capabilities and limitations. The findings highlight the need for advanced control algorithms to address high-frequency noise and improve overall system stability and accuracy.

3.2. Simplification of EMS Maglev System

The short stators EMS maglev train utilizes the electromagnetic attraction force between the train and the track to achieve suspension. The structure of the maglev system like Figure 3.1 shows. One carriage is supported by five maglev bogies by the connection of air springs. One bogie has four air springs located at the four ends of the bogie. The air spring can filter the high frequency vibration which passes through the bogie to the carriage. It means the vibration of the carriage has lower frequency than the bogie. One bogie is decoupled into two parts, left part and right part, by the special structural design. The left and right part are connected by the anti-rolling thin beams. The connection between the anti-rolling beam and the bogie main part

is rotatable in gravity direction and fixed in the other two directions. The connections between two anti-rolling beams are two joints with allowed translational displacement in the speed direction and the two joints can resist the rolling movement of the two main parts of one bogie. The rail is between the top beam and the bottom beam of the bogie. The electromagnets are fixed on the bottom beam of the bogie. There are four electromagnets for the left part and right part of the bogie respectively. The electromagnetic attraction force between the bottom beam of bogie and rail will be generated when the current is applied to the electromagnets. Then the bogies will be levitated, and the bogies will jack the carriage. The air gap between the bottom beam of bogie and bottom side of the rail is the control object and the ideal air gap is 8mm to 10mm. To achieve the ideal air gap, the controller needs to calculate the appropriate current applied to electromagnets in real time and send it to the electromagnets. When the maglev train is running, the irregularity of the rail and the dynamic response between the train system and the track system will lead the unstable of the air gap, so to calculate an appropriate current to make the air gap stable is the key point of the suspension control system.

The linear induction motors are fixed under the bogie top beams. When current goes through the linear induction motors, the air gap magnetic field will be generated and then the induced current will be generated on the inductor plate of the rail. The induced current interacts with the air gap magnetic field to generate traction force.

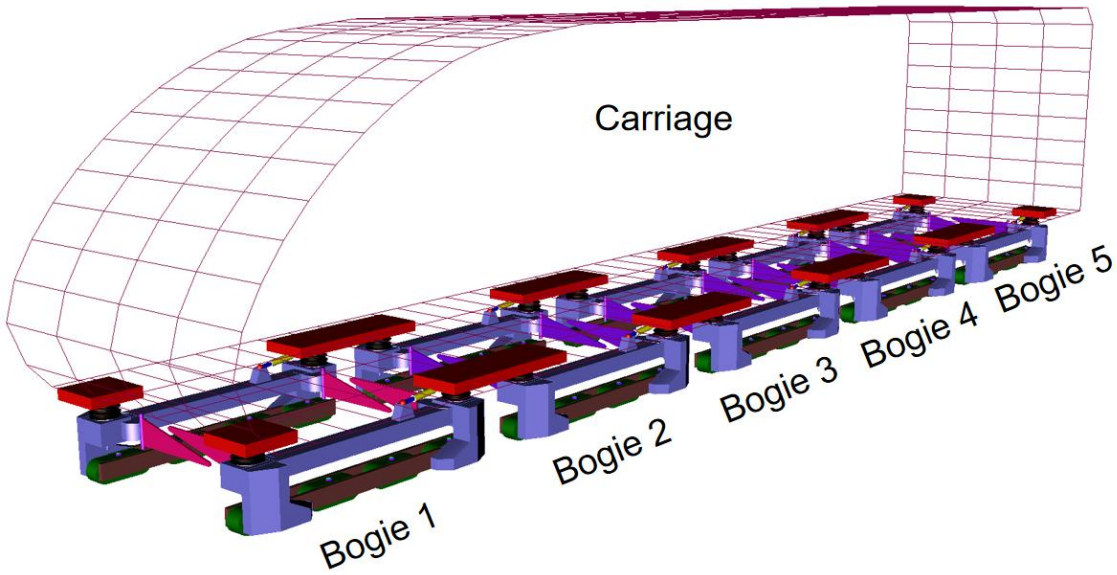

Figure 3.1 Structure of maglev system

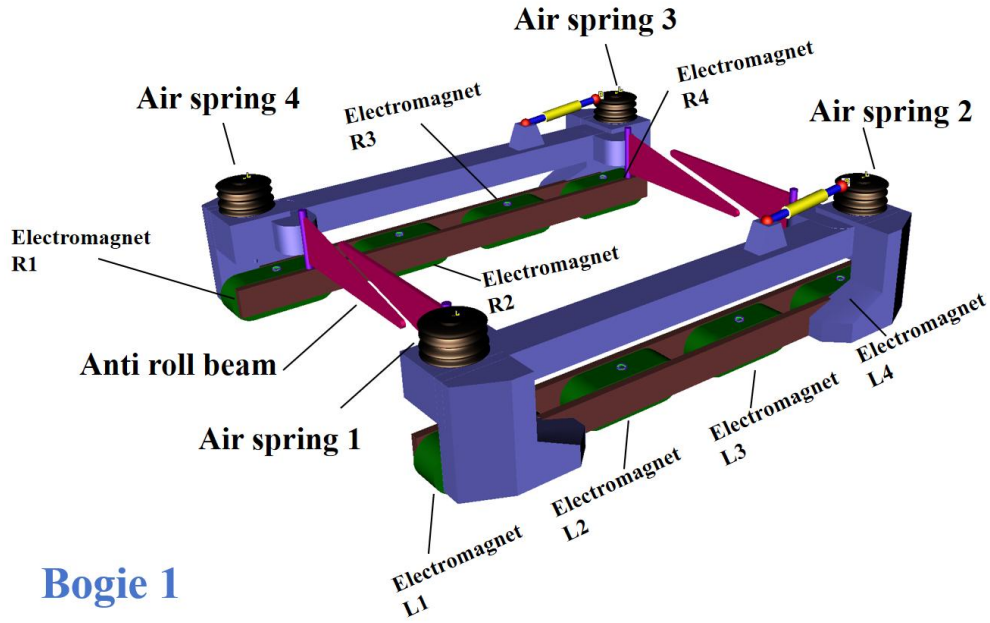

Figure 3.2 Schematic diagram of suspension bogie

According to the specifications of the structure of the short stator maglev system, to simplify the simulation and the analysis of the dynamic response and controller performance, the system

can be simplified to a simple point model, like Figure 3.3 shows. In the model, the time-varying current input to the single magnet suspension system is $i(t)$, and the input voltage is $u(t)$. Φ_l represents the instantaneous magnetic flux, Φ_m represents the leakage flux, and Φ_t represents the main magnetic flux generated in the electromagnet.

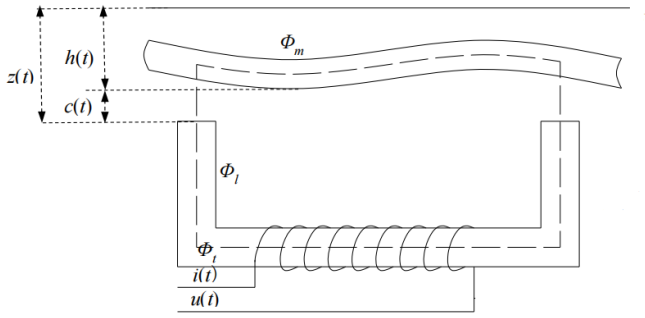

Figure 3.3 Model of a single electromagnet suspension

In practice, under the action of the maglev train load and errors such as track installation during construction, the maglev track will deform, causing additional imbalance in the electromagnet suspension system. To consider the change in spatial position of the track position under the above factors, the concept of absolute space position is introduced in the dynamic equation of the single electromagnet suspension system, the reference plane shown in Figure 3.3. Thus, the positional relationship among the absolute reference plane, the track surface, and the electromagnet is as shown in Equation (3.1):

$$z(t) = h(t) + c(t) \tag{3.1}$$

where: $h(t)$ is the position of the track surface under external comprehensive factors; $c(t)$ is the vertical distance between the magnet surface and the track surface, the suspension gap; $z(t)$ is the total distance between the magnet surface from the reference plane.

3.2.1. Suspension Principle

According to the principles of electromagnetism, the effective magnetic resistance in the magnet is:

$$R(t) = \frac{2c(t)}{\mu_0 A} \tag{3.2}$$

where: $R(t)$ is the effective magnetic resistance, related to the dynamic suspension gap, A is the magnetic pole area, μ_0 is the magnetic permeability. According to Kirchhoff's law, the relationship between current and main magnetic flux and magnetic resistance is expressed as:

$$ni(t) = \Phi(t) \cdot R(c) \tag{3.3}$$

where: n is the number of coils wound around the magnet. The main magnetic flux $\Phi(t)$ is related to the current and suspension gap and can be written as:

$$\Phi(t) = \frac{\mu_0 Ani(t)}{2c(t)} \tag{3.4}$$

The electromagnetic suspension force can be expressed by the relationship between the magnetic linkage and the magnetic field energy, where the magnetic field energy is the integral of the magnetic linkage over time, expressed as:

$$W(t) = \int_0^t \psi(t)dt = \frac{\mu_0 An^2 i^2(t)}{4c(t)} \tag{3.5}$$

where, $\psi(t)$ is the magnetic linkage in the electromagnet, related to the main magnetic flux $\Phi(t)$, and can be organized as:

$$\psi(c, i(t)) = n\Phi(t) = \frac{\mu_0 An^2 i(t)}{2c(t)} \tag{3.6}$$

The electromagnetic force $F(t)$ is the derivative of the magnetic field energy with respect to the suspension gap, expressed as:

$$F(t) = \frac{\partial W_c(t)}{\partial c(t)} = \frac{\partial\left(\frac{\mu_0 A n^2 i(t)^2}{4c(t)}\right)}{\partial c(t)} = \frac{\mu_0 A n^2}{4}\left[\frac{i(t)}{c(t)}\right]^2 \tag{3.7}$$

Through the above derivation, Equation (3.7) provides the expression formula for the electromagnetic suspension force, which is related to the current and suspension gap, and is inversely proportional to the suspension gap and directly proportional to the current in a nonlinear relationship.

According to the law of electromagnetic induction, the relationship between voltage and current in the electromagnet system is as shown in Equation (3.8):

$$u(t) = Ri(t) + \frac{d\psi}{dt} = Ri(t) + \frac{d}{dt}[L(t) \cdot i(t)] \tag{3.8}$$

where $L(t)$ is the inductance of the electromagnet, which changes over time and is expressed as:

$$L(t) = \frac{n}{i(t)}\phi_T = \frac{n}{i(t)} \cdot \frac{ni(t)}{R(c)} = \frac{n^2}{R(c)} = \frac{\mu_0 A n^2}{2c(t)} \tag{3.9}$$

Combining Equations (3.8) and Equations (3.9), the expression for the voltage in the electromagnet system can be derived as:

$$u(t) = Ri(t) + \frac{\mu_0 A n^2}{2c(t)} \cdot \frac{di(t)}{dt} - \frac{\mu_0 A n^2 i(t)}{2[c(t)]^2} \cdot \frac{dc(t)}{dt} \tag{3.10}$$

If the suspension control system adopts voltage control, rapid changes in feedback signals may not be promptly tracked due to the delay caused by inductance, thus limiting the effectiveness of control. There exists a basic proportional relationship between the voltage across the magnet and the current in the winding. Therefore, adjusting the voltage is essentially equivalent to controlling the current in the electromagnetic coil. Within the frequency range of the

suspension system, direct control of the linearized current can be achieved. In this scenario, the system can avoid the influence of inductance and nonlinear characteristics, leading to a simpler design of the controller.

Figure 3.3 shows the vertical force diagram of the suspended electromagnet, with a downward direction as positive. The suspended electromagnet is subjected to downward gravity mg and other external loads $f_0(t)$ (such as seismic loads, impact loads, loads caused by uneven tracks, etc.), and is levitated by the electromagnetic suspension force $F(t)$. These three forces balance vertically. Since the electromagnetic suspension force acts directly on the track, the track experiences a reaction force $F(t)$ in the opposite direction of the electromagnetic suspension force, as shown in Figure 3.4.

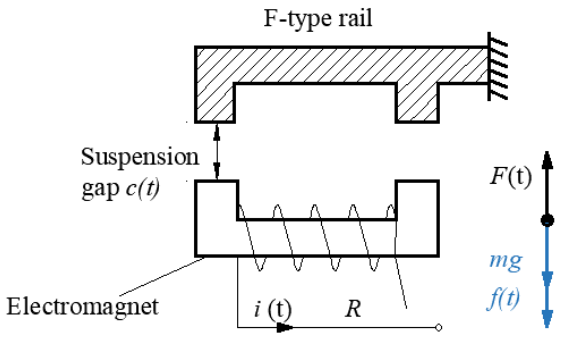

Figure 3.4 Direction of magnetic force

Based on D'Alembert's principle, the vertical motion equation of the suspended electromagnet can be established as:

$$m\ddot{z}(t) = mg - F(t) + f(t) \tag{3.11}$$

When the external load $f(t) = 0$ and the vibration acceleration of the electromagnet is 0, the electromagnet is in a static equilibrium state, that is, in the stable state:

$$mg = F_0 = \frac{\mu_0 A n^2}{4}\left[\frac{i_0}{c_0}\right]^2 \tag{3.12}$$

where i_0 and c_0 are the rated current and suspension gap designed for the suspension system, that is, the current and suspension gap to overcome the suspended mass. Therefore, the total suspension current and suspension gap can be expressed as:

$$i(t) = \Delta i(t) + i_0 \tag{3.13}$$

$$c(t) = \Delta c(t) + c_0 \tag{3.14}$$

where $\Delta i(t)$, $\Delta c(t)$ are the fluctuation values of the suspension system's current and suspension gap caused by the external load $f(t)$.

3.2.2. Guidance Principle

In the short stator maglev transportation system, the lateral motion lacks active control mechanisms. Instead, the system relies on the lateral component of its levitation force to provide the necessary lateral restoring force. Figure 3.5 illustrates the mechanism by which the vertical levitation force contributes a lateral component, thereby serving as the guidance force.

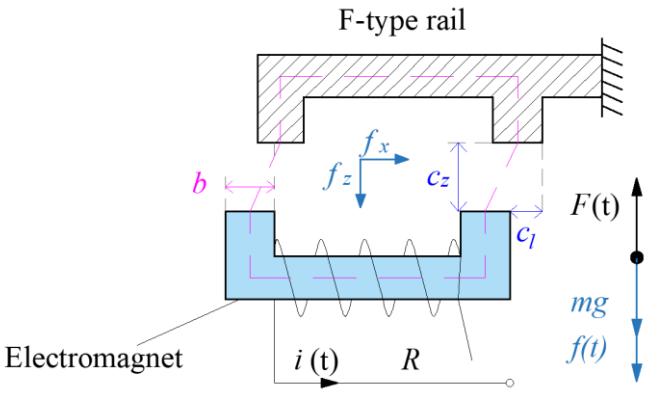

Figure 3.5 Electromagnetic force between electromagnet and F-type rail

According to the force analysis between F-type rial and electromagnet [130, 131], the

relationship between vertical levitation force and guidance force can be describe by

$$\begin{cases} f_z = F(t)\left[1 + \dfrac{2c_z}{\pi b} - \dfrac{|c_l|}{b} + \dfrac{c_l}{\pi b}\tan^{-1}\left(\dfrac{c_z}{c_l}\right)\right] \\ f_y = F(t)\dfrac{2c_z}{\pi b}\tan^{-1}\left(\dfrac{c_l}{c_z}\right) \end{cases} \tag{3.15}$$

Where f_z is the vertical component of the electromagnetic force $F(t)$, f_y is the lateral component of $F(t)$, c_z is the vertical air gap, c_l is the relative displacement between electromagnet and F-type rail, b is the thickness of U-shaped iron core.

When the lateral relative displacement c_l is relatively small, the relationship between the lateral force f_y and the vertical force f_z can be approximated as a linear function of the lateral displacement c_l, expressed as:

$$f_y = k_0 c_l f_z + O({c_l}^2) \tag{3.16}$$

where $k_0 = \frac{2}{2c_z + \pi b}$.

This approximation indicates that the system can passively maintain lateral stability without the need for active control mechanisms.

Table 3.1 gives the parameters of the suspension unit.

Table 3.1 Parameters of suspension unit

$m\ (kg)$	$\mu_0\ (H \cdot m^{-1})$	$A(m^2)$	n
750	$4\pi \times 10^{-7}$	0.0196	340

3.3. Traditional Controllers Design

3.3.1. PID Controller Design

The suspension unit model, as detailed in section 3.2, was developed using the commercial software SIMULINK. A PID controller was employed to regulate and maintain a consistent

suspension gap. This controller adjusts the electric current flowing through the coils, which generates the electromagnetic force required for levitation. The PID controller manages the entire process, from levitating the suspension unit off the ground to achieving and maintaining the desired suspension gap. By precisely controlling the current, the system compensates for external disturbances or system variations, ensuring stable and reliable levitation performance. In addition to constructing the dynamic suspension model, another crucial aspect of this part is the design and tuning of the three parameters of the PID controller. This involves carefully selecting the proportional, integral, and derivative gains to ensure optimal performance. Incorrect parameter settings can lead to instability, causing the suspension system to diverge and fail to maintain the desired suspension gap. The Ziegler-Nichols method is a heuristic tuning method that provides a systematic way to set initial PID parameters. It involves two main approaches: the reaction curve method and the ultimate gain method. The ultimate gain method was utilized to determine the PID parameters. The process involved the following steps:

Step 1. Initial parameter settings:

Set $k_i = 0$ and $k_d = 0$.

Step 2. Finding the critical gain:

Gradually increase k_p until the system begins to oscillate with a constant amplitude. Note the critical gain k_{pc} and the oscillation period T_u.

Step 3. Apply the Ziegler-Nichols tuning rules:

Use the critical gain and oscillation period to set the initial PID parameters as: $k_p = 0.6k_{pc}$, $k_i = \frac{2k_p}{T_u}$, $k_d = k_p T_u/8$.

By following these steps, the initial parameters of the PID controller can be determined. Numerous simulation tests were conducted to fine-tune these parameters and verify the performance of the controller, ensuring optimal operation.

3.3.2. Root Locus Controller Design

As discussed in previous sections, PID control is widely used in EMS maglev systems due to its simplicity and acceptable performance in practical applications. However, in order to provide a broader evaluation of classical control strategies, this section introduces the design and analysis of a root locus-based controller. The root locus method is a foundational tool in classical control theory that offers graphical insight into the movement of closed-loop poles as a function of controller gain. While limited to linear time-invariant systems, it allows designers to adjust performance criteria such as damping ratio, natural frequency, and transient response characteristics.

The design begins with a simplified second-order transfer function of the plant, denoted as:

$$G(s) = \frac{K}{Ms^2 + D} \tag{3.17}$$

Where K is the equivalent stiffness coefficient derived from magnetic force linearization, M is the equivalent mass of the levitated object, D is the lumped damping and gravitational equivalent.

The proportional control law is given as:

$$u(t) = -K_L e(t) \tag{3.18}$$

Combining this with the plant yields the open-loop transfer function:

$$G_{OL}(s) = \frac{K_L K}{Ms^2 + D} \tag{3.19}$$

To analyze the closed-loop dynamics, the root locus of the open-loop transfer function is plotted as K_L varies. The design goal is to position the closed-loop poles such that the damping ratio ζ and ω_n natural frequency satisfy predefined transient performance specifications:

$$\begin{aligned} \zeta &\geq \zeta_{min} \\ \omega_n &\geq \omega_{min} \end{aligned} \tag{3.20}$$

Through graphical analysis and iterative gain selection, the dominant poles can be positioned to meet the desired settling time T_s, overshoot, and stability margins. Pole locations are verified using the standard second-order system relation:

$$s_{1,2} = -\zeta\omega_n \pm j\omega_n\sqrt{1-\zeta^2} \tag{3.21}$$

3.3.3. State Feedback Controller Design

In addition to the root locus-based approach, this section explores a classical state feedback control strategy. State feedback control enables direct pole placement through full state measurements or estimations, offering greater flexibility in shaping system dynamics compared to output-based feedback. It serves as another benchmark to evaluate the limitations of classical linear control in the context of electromagnetic suspension.

Assume the system dynamics can be written in a controllable state-space form:

$$\dot{x}(t) = Ax(t) + Bu(t) y(t) = Cx(t) \tag{3.22}$$

Where $x(t) \in \mathbb{R}^n$ is the state vector, typically including position and velocity, $u(t) \in \mathbb{R}$ is the control input (current), $y(t) \in \mathbb{R}$ is the system output (levitation gap), A, B, C are constant system matrices.

The state feedback control law is:

$$u(t) = -Kx(t) \tag{3.23}$$

The closed-loop dynamics become:

$$\dot{x}(t) = (A - BK)x(t) \tag{3.24}$$

The feedback gain matrix K is selected such that the eigenvalues of $A - BK$ match desired closed-loop pole locations, ensuring adequate damping and responsiveness. Desired pole locations are generally chosen based on performance indices such as settling time, rise time, and overshoot constraints.

The feedback gain is computed using pole placement techniques (e.g., Ackermann's formula). The desired poles are placed in the left-half complex plane to ensure system stability and suitable transient dynamics. The degree of aggressiveness in control depends on how far the poles are placed from the imaginary axis. In practical implementation, the state vector includes levitation gap and vertical velocity. Full-state feedback is assumed to be available from sensors or estimated through observers (e.g., Kalman filters).

3.4. Simulation with PID Control

After determining the initial parameters, numerous simulation tests were conducted to refine the PID settings. The simulations were designed to replicate various operating conditions and disturbances to ensure the robustness of the control system. A key focus was on achieving a stable and rapid levitation process, where the suspension unit transitions smoothly from the initial condition to the desired levitation height. By observing the initial lift-off and ensuring smooth and rapid levitation without oscillations or instability, the PID parameters for the suspension unit were finalized as $k_p = 12000$, $k_i = 10000$, $k_d = 1000$.

The system under control is the suspension unit described in section 3.2, utilizing the controller detailed in section 3.3. Both the dynamic system and the controller were modeled in SIMULINK. The sample time step and control time step were set to 0.001s to ensure precise and responsive control.

3.4.1. Levitation Process Simulation

The objective was to achieve precise control of the levitation gap from 18mm to 8mm. Five sets of PID parameters were selected based on extensive preliminary simulations that helped narrow down the optimal range. The chosen PID parameter sets for the final simulations were as Table 3.2 shows:

Table 3.2 Parameters of PID controller

No.	P	I	D
1	12000	10000	1000
2	12000	5000	1000
3	8000	5000	1000
4	8000	5000	400
5	4000	2500	400

These parameters were selected to explore the impact of different proportional, integral, and derivative gains on the system's performance, focusing on critical performance metrics such as steady-state error, overshoot, settling time, rise time, maximum velocity, maximum acceleration, and current consumption. The simulations were carried out using SIMULINK, and data for displacement, velocity, acceleration, and current were recorded over time.

Figure 3.6 illustrates the suspension gap during the levitation process and the steady-state error

at the third second using PID controllers with the different parameters listed in Table 3.2. PID Set 1 achieves the fastest settling time of 0.458 seconds, demonstrating its efficiency in reaching stability. PID Set 3 also performs relatively well with a settling time of 1.249 seconds. On the other hand, PID Sets 2, 4, and 5 have longer settling times of 2.747 seconds, 2.634 seconds, and 2.731 seconds respectively, indicating a slower stabilization process. At the third second, PID Set 1 has the lowest steady-state error of 0.003 mm, indicating exceptional precision in reaching the target displacement. In comparison, PID Set 3 has a slightly higher error of 0.034 mm, and PID Sets 4 and 5 have errors of 0.120 mm and 0.118 mm respectively. PID Set 2 has the highest steady-state error of 0.141 mm among the five sets, though still within an acceptable range for precise control applications.

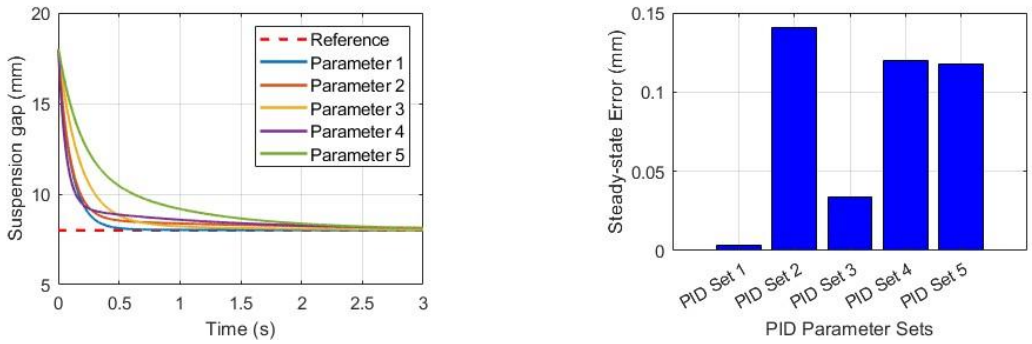

(a) Suspension gap (b) Steady-state error

Figure 3.6 Suspension unit levitation process using PID controller

Figure 3.7 depicts the current variation during the levitation process. Figure 3.8 presents the maximum current values for each PID set. The steady-state currents are relatively similar across all PID sets, with values around 10.8A to 11.0A at the third second. PID Sets 1 and 2 have the highest maximum currents of 120A, while PID Sets 3 and 4 have maximum currents of 80A.

PID Set 5 stands out with the lowest maximum current of 40A.

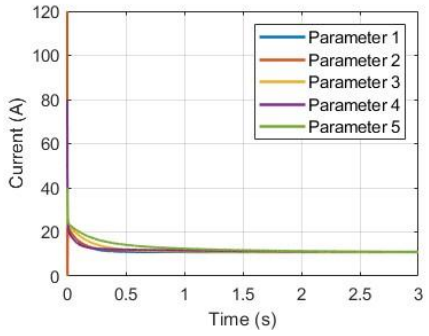

Figure 3.7 Current of the suspension unit

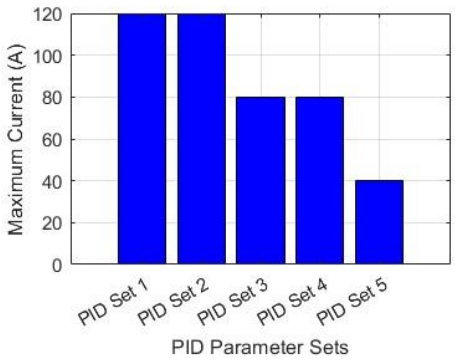

Figure 3.8 Maximum current of the suspension unit

Without a current limitation, PID Set 1 provides the fastest stabilization and highest precision, achieving the lowest steady-state error (0.003 mm) and shortest settling time (0.458 seconds). Therefore, the parameters of PID Set 1 were selected for further simulation and analysis.

3.4.2. Trajectory Tracking Simulation

In this section, the focus is on performing trajectory tracking simulations using the parameters from PID Set 1 (P=12000, I=10000, D=1000). The suspension unit is initially stabilized at a levitation gap of 8mm. The target trajectory to be followed is defined by the function $y = 1.7\sin(\text{frequency} \cdot t) + 8$, which simulates a sinusoidal path with different frequencies. The primary objective of these simulations is to assess the performance of PID Set 1 in trajectory tracking under varying frequency conditions. Three frequencies are used for the simulations: 2.79 rad/s, 3.49 rad/s, 4.19 rad/s. For each frequency, the simulation calculates the response of the suspension unit.

Figure 3.9 illustrates the performance of the PID controller in enabling the suspension unit to

track the specified trajectories. The time-series plot shows that the PID displacement closely follows the reference trajectory with minimal lag and amplitude discrepancy. At a frequency of 2.79 rad/s, the PID controller demonstrates robust performance with a Mean Absolute Error (MAE) of approximately 0.25 mm and a Maximum Absolute Error (Max Error) of around 0.45 mm, indicating effective control with minimal deviations. As the frequency increases to 3.49 rad/s, the controller's tracking accuracy declines, with the MAE rising to approximately 0.32 mm and the Max Error to about 0.55 mm. At the highest frequency of 4.19 rad/s, the PID controller faces significant challenges, with the MAE reaching approximately 0.38 mm and the Max Error peaking at around 0.62 mm. The corresponding time-series plot highlights substantial phase lag and amplitude reduction, demonstrating the controller's struggle to track the high-frequency trajectory accurately.

Overall, the results indicate that while the PID controller performs well at lower frequencies, its effectiveness diminishes as the frequency increases, leading to larger errors and reduced tracking precision. This suggests the necessity for exploring alternative control strategies to maintain effective control at higher frequencies.

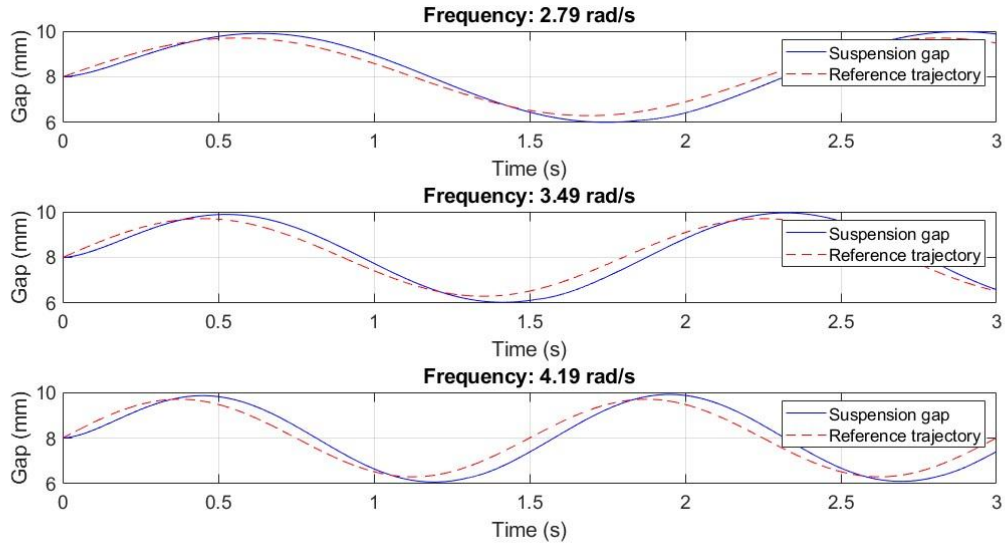

Figure 3.9 Suspension unit trajectory tracking process using PID controller

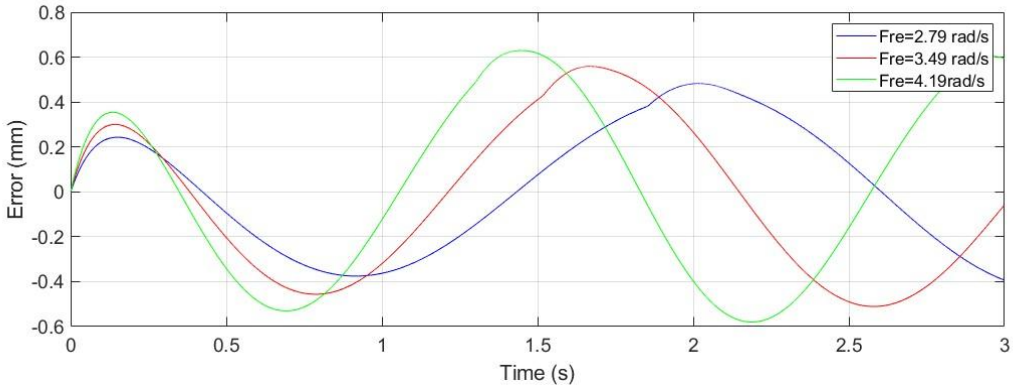

Figure 3.10 Error of suspension unit trajectory tracking process using PID controller

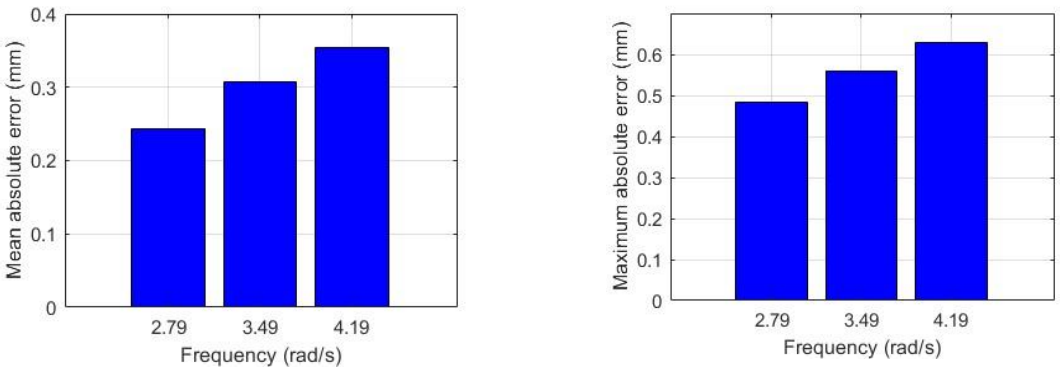

Figure 3.11 Mean absolute error of trajectory tracking process using PID controller

Figure 3.12 Maximum absolute error of trajectory tracking process using PID controller

3.4.3. Trajectory Tracking Simulation with Measurement Noise

Measurement noise, stemming from sensor inaccuracies and environmental factors, is an unavoidable aspect of practical systems. Incorporating noise measurement into the simulated system and evaluating the PID controller's performance under these conditions is essential for ensuring the controller's effectiveness in real-world applications. In this section, the adopted simulation method involves adding white noise to the system's output signals to simulate the noise encountered in sensor measurements.

Figure 3.13 illustrates the low measurement noise added to the simulation model, with a maximum amplitude of 0.001 mm. Figure 3.14 depicts the high measurement noise introduced into the simulation model, with a maximum amplitude of 0.003 mm. The reference gap is set at 8 mm, and the initial state of the suspension unit is stable at this value.

In the presence of low measurement noise (maximum amplitude of 0.001 mm) at a frequency of 1000 Hz, which matches the sensor sampling frequency. Figure 3.15 presents the simulation results of the suspension gap under high measurement noise. The PID controller demonstrates a Mean Absolute Error (MAE) of approximately 0.0002768 m, a Maximum Absolute Error (Max Error) of around 0.0005547mm, and a Standard Deviation of Error of about 0.0002768mm. The analysis reveals that the suspension unit's movement includes high-frequency components due to the added noise. These metrics indicate that the controller can

maintain relatively accurate tracking despite the low noise level.

However, when higher measurement noise (maximum amplitude of 0.003 mm) is introduced at the same frequency of 1000 Hz, the system becomes unstable and diverges. The increased noise significantly disrupts the control process, leading to an inability of the PID controller to maintain the desired suspension gap. The high-frequency noise components, matching the sensor sampling rate, overwhelm the controller's corrective actions, causing the system to lose stability and fail to track the reference trajectory.

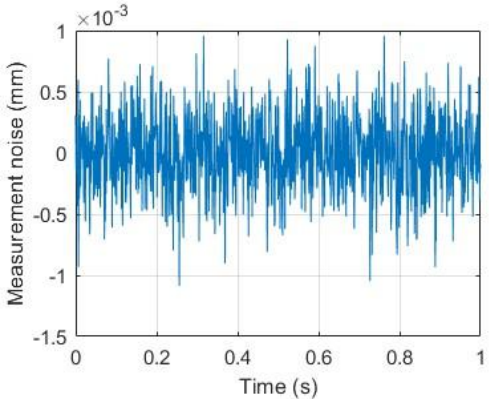

Figure 3.13 Low measurement noise

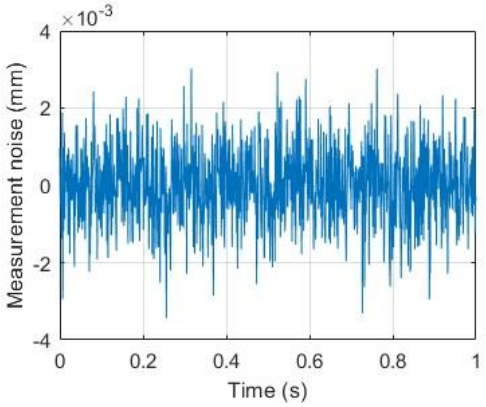

Figure 3.14 High measurement noise

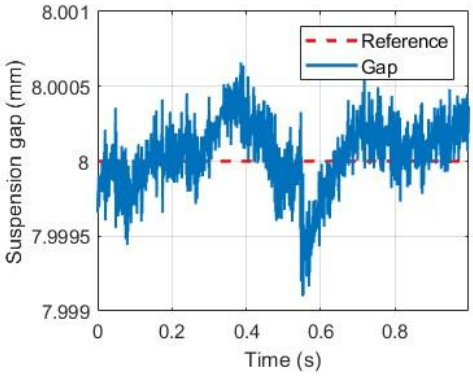

Figure 3.15 Suspension gap with low

measurement noise

3.5. Conclusions

The analysis of the PID controller's performance in the suspension system, considering both simulation data and the impact of measurement noise, reveals significant limitations. The PID controller demonstrates reasonable performance under low-frequency and low-noise conditions. For instance, with a low measurement noise of 0.001 mm and a frequency of 2.79 rad/s, the controller achieves a Mean Absolute Error (MAE) of approximately 0.25 mm and a Maximum Absolute Error (Max Error) of around 0.45 mm. However, as the frequency increases to 4.19 rad/s, these errors escalate to an MAE of 0.38 mm and a Max Error of 0.62 mm, indicating reduced tracking accuracy.

When Gaussian noise with a maximum amplitude of 0.003 mm is introduced, matching the sensor sampling frequency of 1000 Hz, the system becomes unstable and diverges. The MAE under noisy conditions increases to approximately 0.0002768 mm, with the Max Error reaching 0.0005547 mm. This significant disruption demonstrates the PID controller's inability to handle high-frequency noise effectively, leading to a failure in maintaining the desired suspension gap. These findings suggest that while PID controllers can provide adequate control in low-noise and low-frequency scenarios, their performance degrades significantly under more challenging conditions. The high-frequency noise components and the corresponding control inaccuracies underscore the need for more advanced control algorithms. Future work should focus on developing and implementing robust control strategies, to enhance system stability and performance under varying operational conditions and noise levels. This improvement is

crucial for achieving precise and reliable control in practical applications where noise and high-frequency dynamics are inevitable.

Chapter 4. Model Predictive Control for Maglev Suspension System

4.1. Introduction to MPC

MPC originated in the late seventies and has developed considerably since then [21, 132-134]. The term Model Predictive Control does not designate a specific control strategy but rather an ample range of control methods which make explicit use of a model of the process to obtain the control signal by minimizing an objective function. The methodology MPC is characterized by the following strategy, represented in Figure 4.1:

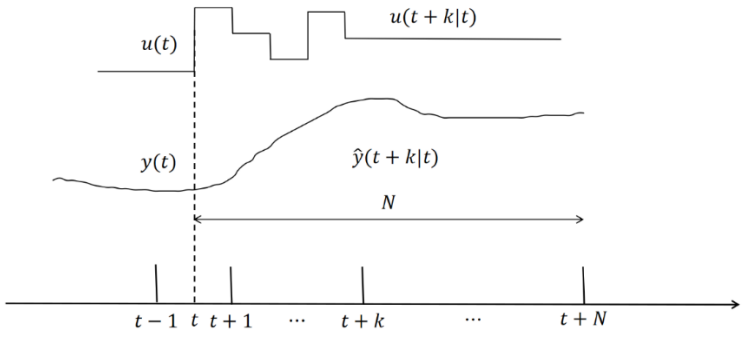

Figure 4.1 MPC strategy

① The future outputs for a determined horizon N, called the prediction horizon, are predicted at each instant t using the process model. These predicted outputs $y(t+k \mid t)$ for $k = 1 \ldots N$ depend on the known values up to instant t (past inputs and outputs) and on the future control signals $u(t+k \mid t), k = 0 \ldots N-1$, which are those to be sent to the system and calculated.

② The set of future control signals is calculated by optimizing a determined criterion to keep the process as close as possible to the reference trajectory $w(t+k)$ (which can be the setpoint

itself or a close approximation of it). This criterion usually takes the form of a quadratic function of the errors between the predicted output signal and the predicted reference trajectory. The control effort is included in the objective function in most cases. An explicit solution can be obtained if the criterion is quadratic, the model is linear, and there are no constraints; otherwise, an iterative optimization method must be used. Some assumptions about the structure of the future control law are also made in some cases, such as that it will be constant from a given instant.③ The control signal $u(t \mid t)$ is sent to the process whilst the next control signals calculated are rejected, because at the next sampling instant $y(t+1)$ is already known and step 1 is repeated with this new value and all the sequences are brought up to date. Thus the $u(t+1 \mid t+1)$ is calculated (which in principle will be different from the $u(t+1 \mid t)$ because of the new information available) using the receding horizon concept.

In order to implement this strategy, the basic structure shown in Figure 4.2 is used. A model is used to predict the future plant outputs, based on past and current values and on the proposed optimal future control actions. These actions are calculated by the optimizer considering the cost function (where the future tracking error is considered) as well as the constraints.

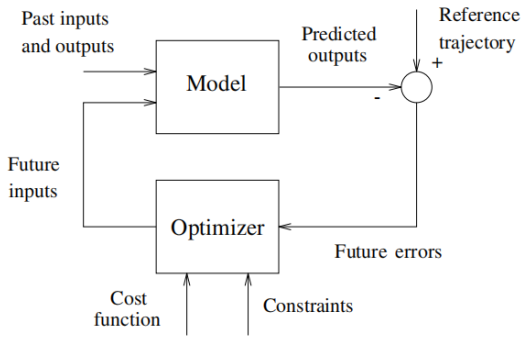

Figure 4.2 Basic structure of MPC

The process model plays, in consequence, a decisive role in the controller. The chosen model must be able to capture the dynamic process to precisely predict the future outputs and be simple to implement and understand. The State Space Model is widespread in the academic research community as the derivation of the controller is very simple even for multivariable cases. The state space description allows for an easier expression of stability and robustness criteria.

The optimizer is another fundamental part of the strategy as it provides the control actions. If the cost function is quadratic, its minimum can be obtained as an explicit function (linear) of past inputs and outputs and the future reference trajectory.

4.2. MPC Controller Design for Maglev Suspension System

In this section, the design and implementation of MPC controller for the maglev suspension unit, as described in Section 3.2, are presented. The efficacy and performance of the MPC controller are rigorously assessed through an extensive evaluation encompassing both simulation outcomes and experimental data, thereby providing a comprehensive analysis of its operational capabilities within the specified application context.

4.2.1. Predictive Model

The simplified maglev suspension unit dynamic model in Section 3.2 can be described by Equation (4.1) and Equation (4.2)

$$m\ddot{z}(t) = mg - F(t) \tag{4.1}$$

$$F(t) = \frac{\mu_0 A N^2}{4}\left[\frac{i(t)}{z(t)}\right]^2 \tag{4.2}$$

where $z(t)$ is the time-varying suspension gap, m is the mass of the whole vehicle divided

equally to every magnet, $F(t)$ is the real-time levitation force, $i(t)$ is the electromagnet winding current, μ_0 is the vacuum permeability of air, A is the magnetic pole are of the electromagnet and N is the number of coil turns.

For concise expression, the Equation (4.2) is written as:

$$F(t) = K\left[\frac{i(t)}{z(t)}\right]^2 \tag{4.3}$$

$$s.t. \qquad 0 \le i(t) \le i_{max}$$

$$0 \le z(t) \le z_{max}$$

where $K = \frac{\mu_0 A N^2}{4}$, i_{max} is the maximum current which the controller can supply, z_{max} is the allowed maximum gap between electromagnets and F-type rail.

Equation (4.3) exhibits pronounced nonlinearity due to the quadratic relationship between the control current $i(t)$ and the levitation gap $z(t)$. This nonlinearity is characterized by the force's inverse square dependence on the levitation gap, resulting in highly sensitive system behavior, particularly at small gap values. Additionally, the coupling between the current and gap introduces complex dynamics, where changes in one variable can lead to non-intuitive responses in the system.

Nonlinear systems typically result in non-convex optimization problems, which are challenging to solve in real-time due to the potential for multiple local minima and the computational complexity involved. By linearizing the system around a specific operating point, the resulting optimization problem becomes convex, significantly simplifying the solution process. This convexity ensures that the optimization algorithms used in MPC can efficiently find a global optimum within the prediction horizon, thereby enhancing the

controller's real-time performance and reliability.

When the system is near the steady-state point (z_0, i_0), the magnetic suspension force Equation (4.3) can be linearized using Taylor expansion method. Assume that the system operates near the steady-state point (z_0, i_0). Let the small deviations from the steady-state point be:

$$\begin{aligned} i(t) &= i_0 + \Delta i(t) \\ z(t) &= z_0 + \Delta z(t) \end{aligned} \tag{4.4}$$

Perform a Taylor series expansion around the steady-state point and retain only the first-order linear terms:

$$F(t) = F_0 + \left.\frac{\partial F(z_0, i_0)}{\partial i(t)}\right|_{(z_0, i_0)} \Delta i(t) + \left.\frac{\partial F(z_0, i_0)}{\partial z(t)}\right|_{(z_0, i_0)} \Delta z(t) \tag{4.5}$$

$$s.t. \qquad 0 \le i(t) \le i_{max}$$

$$0 \le z(t) \le z_{max}$$

where F_0 is the force at the steady-state point. The partial derivatives are calculated as follows:

$$\frac{\partial F}{\partial i} = \frac{\partial}{\partial i}\left(K\frac{i^2}{z^2}\right) = \frac{2Ki}{z^2} \tag{4.6}$$

$$\frac{\partial F}{\partial z} = \frac{\partial}{\partial z}\left(K\frac{i^2}{z^2}\right) = -\frac{2Ki^2}{z^3} \tag{4.7}$$

Therefore, the linearized form of the magnetic levitation force equation around the operating point (z_0, i_0) is:

$$F(t) \approx F_0 + \frac{2Ki_0}{z_0^2}\Delta i(t) - \frac{2Ki_0^2}{z_0^3}\Delta z(t) \tag{4.8}$$

Substitute Equation (4.8) to Equation (4.1) and rewrite the equation in state-space expression:

$$\boldsymbol{z}_{(t)} = \begin{bmatrix} z(t) \\ \dot{z}(t) \end{bmatrix} \tag{4.9}$$

$$\dot{\boldsymbol{z}}_{(t)} = \begin{bmatrix} \dot{z}(t) \\ \ddot{z}(t) \end{bmatrix} = \begin{bmatrix} \dot{z}(t) \\ \frac{2Ki_0^2}{mz_0^3}\Delta z(t) - \frac{2Ki_0}{mz_0^2}\Delta i(t) \end{bmatrix} \tag{4.10}$$

To convert this continuous-time system to a discrete-time system, assume a sampling time T_s and the Euler method was used:

$$z(t+1) = z(t) + T_s \cdot \dot{z}(t) \tag{4.11}$$

$$\boldsymbol{z}_{(t+1)} = \begin{bmatrix} z(t+1) \\ \dot{z}(t+1) \end{bmatrix} = \begin{bmatrix} z(t) \\ \dot{z}(t) \end{bmatrix} + T_s \cdot \begin{bmatrix} \dot{z}(t) \\ \frac{2Ki_0^2}{mz_0^3}z(t) - \frac{2Ki_0}{mz_0^2}i(t) \end{bmatrix} \tag{4.12}$$

This yields the discrete-time state-space equations:

$$\boldsymbol{z}_{(t+1)} = \boldsymbol{A}\boldsymbol{z}_{(t)} + \boldsymbol{B}\boldsymbol{u}_{(t)} \tag{4.13}$$

$$\boldsymbol{y}_{(t)} = \boldsymbol{C}\boldsymbol{z}_{(t)} \tag{4.14}$$

where $\boldsymbol{z}_{(t)} \in \mathbb{R}^3$ is the system states and $\boldsymbol{u}_{(t)} \in \mathbb{R}$ is the control current at time t,

$\mathbf{A} = \begin{bmatrix} 1 & T_s \\ \frac{2Ki_0^2}{mz_0^2}T_s & 1 \end{bmatrix}$ is the system's state transition matrix,

$\mathbf{B} = \begin{bmatrix} 0 \\ -\frac{2Ki_0}{mz_0^2}T_s \end{bmatrix}$ is the control input matrix, $\boldsymbol{y}(t)$ is the output of the system at time t, $\boldsymbol{C} = [1\ 0]$ is the measurement matrix of the system.

Equation (4.13), Equation (4.14) and Equation (4.8) constitute the basic prediction model of the MPC controller.

4.2.2. MPC Controller with Constrains

The discrete-time model Equation (4.13) serves as the foundation for predicting the system's future behavior based on the current state and control input. Equation (4.15) defines the cost function guiding the control input to optimize system behavior, considering the constraints delineated in Equation (4.16) and (4.17).

$$J = \frac{1}{2}\sum_{k=1}^{N_p}\left[\boldsymbol{e}_{(t+k/t)}^{T}\boldsymbol{Q}\boldsymbol{e}_{(t+k/t)} + \boldsymbol{u}_{(t+k/t)}^{T}\boldsymbol{R}\boldsymbol{u}_{(t+k/t)}\right] \tag{4.15}$$

$$\boldsymbol{e}_{min} \leq \boldsymbol{e}_t \leq \boldsymbol{e}_{max} \tag{4.16}$$

$$\boldsymbol{u}_{min} \leq \boldsymbol{u}_t \leq \boldsymbol{u}_{max} \tag{4.17}$$

$$\boldsymbol{e}_{(t)} = \boldsymbol{z}_{ref} - \boldsymbol{z}_{(t)} \tag{4.18}$$

$$\boldsymbol{Q} = \begin{bmatrix} q_1 & \cdots & 0 \\ \vdots & \ddots & \vdots \\ 0 & \cdots & q_n \end{bmatrix}, q_1, q_2, \cdots q_n \geqslant 0$$

$$\boldsymbol{R} = \begin{bmatrix} r_1 & \cdots & 0 \\ \vdots & \ddots & \vdots \\ 0 & \cdots & r_p \end{bmatrix}, r_1, r_2, \ldots, r_p > 0$$

Where N_p is the prediction horizon, which means at time t the controller will predict the states of the system in next N_p time steps, from t to $t + N_p$, $\boldsymbol{z}_{ref}$ is the reference of the system state, $\boldsymbol{e}_{(t)}$ is the error between the system reference and the practice value.

The predictive state at $t + 2$ step is Equation (4.19):

$$\boldsymbol{z}_{(t+2)} = \boldsymbol{A}\boldsymbol{z}_{(t+1)} + \boldsymbol{B}\boldsymbol{u}_{(t+1)} \tag{4.19}$$

Substitute Equation (4.19) into Equation (4.13), the state of the system at time $t + 2$ can be expressed by the state at time t:

$$\boldsymbol{z}_{(t+2/t)} = \boldsymbol{A}^2\boldsymbol{z}_{(t/t)} + \boldsymbol{A}\boldsymbol{B}\boldsymbol{u}_{(t/t)} + \boldsymbol{B}\boldsymbol{u}_{(t+1/t)} \tag{4.20}$$

Repeat the substitution, we can obtain the state of the system at time $t + N_p$:

$$\boldsymbol{z}_{(t+N_p/t)} = \boldsymbol{A}^{N_p}\boldsymbol{z}_{(t/t)} + \boldsymbol{A}^{N_p-1}\boldsymbol{B}\boldsymbol{u}_{(t/t)} + \cdots + \boldsymbol{A}\boldsymbol{B}\boldsymbol{u}_{(t+N_p-2/t)} + \boldsymbol{B}\boldsymbol{u}_{(t+N_p-1/t)} \tag{4.21}$$

To transfer the Equation (4.21) into matrix expression:

$$\boldsymbol{Z}_{(t)} = \begin{bmatrix} \boldsymbol{z}_{(t+1/t)} \\ \boldsymbol{z}_{(t+2/t)} \\ \vdots \\ \boldsymbol{z}_{(t+N_p/t)} \end{bmatrix} \tag{4.22}$$

$$\boldsymbol{U}_{(t)} = \begin{bmatrix} \boldsymbol{u}_{(t/t)} \\ \boldsymbol{u}_{(t+1/t)} \\ \vdots \\ \boldsymbol{u}_{(t+N_p-1/t)} \end{bmatrix}$$

According to Equation (4.21) and Equation (4.22), the matrix expression can be obtained:

$$\boldsymbol{Z}_{(t)} = \boldsymbol{\Phi z}_{(t/t)} + \boldsymbol{\Psi U}_{(t)} \tag{4.23}$$

Where $\boldsymbol{\Phi} = \begin{bmatrix} \boldsymbol{A} \\ \boldsymbol{A}^2 \\ \vdots \\ \boldsymbol{A}^{N_p} \end{bmatrix}$, $\boldsymbol{\Psi} = \begin{bmatrix} \boldsymbol{B} & \boldsymbol{0} & \cdots & \boldsymbol{0} \\ \boldsymbol{AB} & \boldsymbol{B} & \cdots & \boldsymbol{0} \\ \vdots & \vdots & \ddots & \vdots \\ \boldsymbol{A}^{N_p-1}\boldsymbol{B} & \boldsymbol{A}^{N_p-2}\boldsymbol{B} & \cdots & \boldsymbol{B} \end{bmatrix}$.

Equation (4.15) can be written as:

$$J = \frac{1}{2}\boldsymbol{e}_{(t/t)}^T(\boldsymbol{Q} + \boldsymbol{\Phi}^T\boldsymbol{\Theta\Phi})\boldsymbol{e}_{(\mathrm{t/t})} + \boldsymbol{U}_{(t+\mathrm{k/t})}^T\boldsymbol{\Psi}^T\boldsymbol{\Theta\Phi e}_{(t/t)} + \frac{1}{2}\boldsymbol{U}_{(t/t)}^T(\boldsymbol{\Psi}^T\boldsymbol{\Theta\Psi} + \boldsymbol{\Delta})\,\boldsymbol{U}_{(t)} \tag{4.24}$$

$$\boldsymbol{\Theta} = \begin{bmatrix} \boldsymbol{Q} & \cdots & \boldsymbol{0} \\ \vdots & \ddots & \vdots \\ \boldsymbol{0} & \cdots & \boldsymbol{Q} \end{bmatrix}_{(nN_p)\times(nN_p)}$$

$$\boldsymbol{\Delta} = \begin{bmatrix} \boldsymbol{R} & \cdots & \boldsymbol{0} \\ \vdots & \ddots & \vdots \\ \boldsymbol{0} & \cdots & \boldsymbol{R} \end{bmatrix}_{(pN_p)\times(pN_p)}$$

Where n is the number of states of the system, p is the number of the input of the system.

The first element of Equation (4.24) is constant value at each predictive period, so it can be ignored. Equation (4.24) can be simplified continuously as:

$$J = \boldsymbol{U}_{(t)}^T\boldsymbol{K}\boldsymbol{e}_{(t/t)} + \frac{1}{2}\boldsymbol{U}_{(t)}^T\boldsymbol{L}\boldsymbol{U}_{(t)} \tag{4.25}$$

$$\boldsymbol{K} = \boldsymbol{\Psi}^T\boldsymbol{\Theta\Phi}$$

$$\boldsymbol{L} = \boldsymbol{\Psi}^T\boldsymbol{\Theta\Psi} + \boldsymbol{\Delta}$$

Matrix $\boldsymbol{\Gamma}_{(t+k)}$, $\boldsymbol{\Lambda}_{(t+k)}$ and $\boldsymbol{\Gamma}_{N_p}$ are introduced. The Equation (4.16) and Equation (4.17) can be transferred to Equation (4.26) and Equation (4.27).

$$\boldsymbol{\Gamma}_{(t+k)}\boldsymbol{z}_{(t+k)} + \boldsymbol{\Lambda}_{(t+k)}\boldsymbol{u}_{(t+k)} \leq \boldsymbol{\alpha}_{(t+k)} \tag{4.26}$$

$$k = 0, 1, 2, \cdots, N_{\mathrm{p}} - 1$$

$$\boldsymbol{\Gamma}_{N_p} \boldsymbol{z}_{(t+N_p)} \leq \boldsymbol{\alpha}_{N_p} \tag{4.27}$$

where $\boldsymbol{\Gamma}_{(t+k)} = \begin{bmatrix} \mathbf{0}_{p\times n} \\ \mathbf{0}_{p\times n} \\ -\boldsymbol{I}_{n\times n} \\ \boldsymbol{I}_{n\times n} \end{bmatrix}_{(2n+2p)\times n}$, $\boldsymbol{z}_{(t+k)}$ is the state vector of the system with $n \times 1$ dimension, $\boldsymbol{\Lambda}_{(t+i)} = \begin{bmatrix} -\boldsymbol{I}_{p\times p} \\ \boldsymbol{I}_{p\times p} \\ \mathbf{0}_{n\times \mathrm{p}} \\ \mathbf{0}_{n\times p} \end{bmatrix}_{(2n+2p)\times p}$, $\boldsymbol{\alpha}_{(t+k)} = \begin{bmatrix} -\boldsymbol{u}_{\mathrm{low}} \\ \boldsymbol{u}_{\mathrm{high}} \\ -\boldsymbol{z}_{\mathrm{low}} \\ \boldsymbol{z}_{\mathrm{high}} \end{bmatrix}_{(2n+2p)\times p}$ is the limitation of $\boldsymbol{z}_{(t)}$ and $\boldsymbol{u}_{(t)}$, $\boldsymbol{\Gamma}_{N_p} = \begin{bmatrix} -\boldsymbol{I}_{n\times n} \\ \boldsymbol{I}_{n\times n} \end{bmatrix}_{2n\times n}$, $\boldsymbol{\alpha}_{N_p} = \begin{bmatrix} -\boldsymbol{z}_{\mathrm{low}} \\ \boldsymbol{z}_{\mathrm{high}} \end{bmatrix}_{2n\times 1}$

The Equation (4.26) and Equation (4.27) can be expressed together by Equation (4.28):

$$\begin{bmatrix} \boldsymbol{\Gamma}_{(t)} \\ \mathbf{0} \\ \vdots \\ \mathbf{0} \end{bmatrix} \boldsymbol{z}_{(t/t)} + \begin{bmatrix} \mathbf{0} & \cdots & \cdots & \mathbf{0} \\ \boldsymbol{\Gamma}_{(t+1)} & \mathbf{0} & \cdots & \vdots \\ \mathbf{0} & \boldsymbol{\Gamma}_{(t+2)} & \mathbf{0} & \vdots \\ \vdots & \mathbf{0} & \ddots & \mathbf{0} \\ \mathbf{0} & \cdots & \mathbf{0} & \boldsymbol{\Gamma}_{N_p} \end{bmatrix} \begin{bmatrix} \boldsymbol{z}_{(t+1/t)} \\ \boldsymbol{z}_{(t+2/t)} \\ \vdots \\ \boldsymbol{z}_{(\mathrm{t}+N_p/t)} \end{bmatrix} + \begin{bmatrix} \boldsymbol{\Lambda}_{(t)} & \mathbf{0} & \cdots & \mathbf{0} \\ \mathbf{0} & \boldsymbol{\Lambda}_{(t+1)} & \cdots & \vdots \\ \vdots & \mathbf{0} & \ddots & \mathbf{0} \\ \vdots & \cdots & \mathbf{0} & \boldsymbol{\Lambda}_{(t+N_p-1)} \\ \mathbf{0} & \cdots & \cdots & \mathbf{0} \end{bmatrix} \begin{bmatrix} \boldsymbol{u}_{(t/t)} \\ \boldsymbol{u}_{(t+1/t)} \\ \vdots \\ \boldsymbol{u}_{(t+\mathrm{N_p}-1/t)} \end{bmatrix} \leqslant \begin{bmatrix} \boldsymbol{\alpha}_{(t)} \\ \boldsymbol{\alpha}_{(t+1)} \\ \vdots \\ \boldsymbol{\alpha}_{(N_p)} \end{bmatrix} \tag{4.28}$$

For simplicity, we define:

$$\widehat{\boldsymbol{\Gamma}} = \begin{bmatrix} \boldsymbol{\Gamma}_{(2n+2p)\times n} \\ \mathbf{0}_{(2n+2p)\times n} \\ \vdots \\ \mathbf{0}_{(2n+2p)\times n} \end{bmatrix}_{((2n+2p)N_p+2n)\times n} \tag{4.29}$$

$$\check{\boldsymbol{\Gamma}} = \begin{bmatrix} \mathbf{0}_{(2n+2p)\times n} & \cdots & \cdots & \mathbf{0} \\ \boldsymbol{\Gamma}_{(2n+2p)\times n} & \mathbf{0} & \cdots & \vdots \\ \mathbf{0}_{m\times n} & \boldsymbol{\Gamma}_{(2n+2p)\times n} & \mathbf{0} & \vdots \\ \vdots & \mathbf{0} & \ddots & \mathbf{0} \\ \mathbf{0}_{l\times n} & \cdots & \mathbf{0} & \boldsymbol{\Gamma}_{(N_p)_{2n\times n}} \end{bmatrix}_{((2n+2p)N_p+2n)\times(n\times N_p)} \tag{4.30}$$

$$\breve{\boldsymbol{\Lambda}} = \begin{bmatrix} \boldsymbol{\Lambda}_{(2n+2p)\times p} & \mathbf{0} & \cdots & \mathbf{0} \\ \mathbf{0}_{(2n+2p)\times p} & \boldsymbol{\Lambda}_{(2n+2p)\times p} & \cdots & \vdots \\ \vdots & \mathbf{0} & \ddots & \mathbf{0} \\ \vdots & \cdots & \mathbf{0} & \boldsymbol{\Lambda}_{(2n+2p)\times p} \\ \mathbf{0}_{l\times p} & \cdots & \cdots & \mathbf{0}_{2n\times p} \end{bmatrix}_{((2n+2p)N_{\mathrm{p}}+2n)\times(pN_{\mathrm{p}})} \tag{4.31}$$

$$\widehat{\boldsymbol{\alpha}} = \begin{bmatrix} \boldsymbol{\alpha}_{(2n+2p)\times 1} \\ \boldsymbol{\alpha}_{(2n+2p)\times 1} \\ \vdots \\ \boldsymbol{\alpha}_{(N_{\mathrm{p}})2n\times 1} \end{bmatrix}_{((2n+2p)N_{\mathrm{p}}+2n)\times 1} \tag{4.32}$$

Substituting (4.22) into Equation (4.26), it can be written as:

$$\widehat{\boldsymbol{\Gamma}}\boldsymbol{z}_{(t/t)} + \breve{\boldsymbol{\Gamma}}\boldsymbol{Z}_{(t)} + \breve{\boldsymbol{\Lambda}}\boldsymbol{U}_{(t)} \leq \widehat{\boldsymbol{\alpha}} \tag{4.33}$$

Substituting (4.23) into (4.33), Equation (4.34) can be obtained:

$$\left(\breve{\boldsymbol{\Gamma}}\boldsymbol{\Psi} + \breve{\boldsymbol{\Lambda}}\right)\boldsymbol{U}_{(t)} \leq \widehat{\boldsymbol{\alpha}} - \left(\widehat{\boldsymbol{\Gamma}} + \breve{\boldsymbol{\Gamma}}\boldsymbol{\Phi}\right)\boldsymbol{z}_{(t/t)} \tag{4.34}$$

We define Equation (4.35) and Equation (4.36) and substitute them into Equation (4.34) to obtain Equation (4.37)

$$\boldsymbol{K} = \left(\breve{\boldsymbol{\Gamma}}\boldsymbol{\Psi} + \breve{\boldsymbol{\Lambda}}\right) \tag{4.35}$$

$$\boldsymbol{a} = -\left(\widehat{\boldsymbol{\Gamma}} + \breve{\boldsymbol{\Gamma}}\boldsymbol{\Phi}\right) \tag{4.36}$$

$$\boldsymbol{K}\boldsymbol{U}_{(t)} \leq \widehat{\boldsymbol{\alpha}} + \boldsymbol{a}\boldsymbol{z}_{(t/t)} \tag{4.37}$$

Equation (4.25) and Equation (4.37) constitute the cost function final form of MPC controller. The equations constitute a quadratic programming problem with constraints. Finding the optimal control sequence involves solving Equation (4.25) while simultaneously satisfying the constraints in Equation (4.37).

The prediction model above relies heavily on having accurate state information as its starting point. While the prediction model is designed to predict future states, it cannot correct errors in the current state estimate or account for the fact that not all states are able to be directly

measured or observable. Therefore, a state observer, such as a Kalman filter, is essential to estimate the true state of the system, ensuring that the prediction model operates on the most reliable and complete state information.

4.3. Kalman Filter State Observer

Real-world measurements are often contaminated with noise, which can distort the state information provided to the MPC. The prediction model in MPC assumes that the current state is accurately known, but if the input state is noisy, the predictions will also be inaccurate. The Kalman filter addresses this by filtering out noise from the sensor data, providing a cleaner and more accurate estimate of the current state, which the MPC can then use as a reliable starting point for its predictions [135-137].

Moreover, not all states of the system might be directly measurable. For instance, in a magnetic levitation system, the velocity may not be directly measured due to sensor limitations. The prediction model in MPC requires knowledge of all relevant states to predict future behavior accurately. The Kalman filter estimates these unmeasured states by combining the available measurements with the system dynamics, thereby filling in the gaps and ensuring that the MPC has a complete set of state information to work with.

4.3.1. Introduction of the Kalman Filter

The Kalman filter is employed to estimate or predict the future states of a system based on a moving average of measurements affected by white noise, which is inherently unpredictable [138-141]. To provide accurate feedback signals, the Kalman filter requires a model that describes the relationship between the system's inputs and outputs. One of its key strengths is

its ability to adapt to changes in noise statistics effectively. As an optimal estimator, the Kalman filter estimates the state of a dynamically evolving linear system over time. An optimal estimator can be defined as an algorithm that processes all available data to generate an estimate of the system's state while simultaneously optimizing a predefined criterion. In this section, we will first introduce the research model of the Kalman filter. Normally, the discrete state space function with noise can be given by:

$$\boldsymbol{x}_t = \boldsymbol{A}\boldsymbol{x}_{t-1} + \boldsymbol{B}\boldsymbol{u}_{t-1} + \boldsymbol{w}_{t-1} \tag{4.38}$$

where $\boldsymbol{x}_t \in \mathbb{R}^{1\times n}$ is a state vector, $\boldsymbol{A} \in \mathbb{R}^{n\times n}$ is a state matrix, $\boldsymbol{u}_{t-1} \in \mathbb{R}^{p\times 1}$ is an input vector, $\boldsymbol{B} \in \mathbb{R}^{n\times p}$ is an input matrix, and $\boldsymbol{w}_{t-1} \in \mathbb{R}^{n\times 1}$ is named process noise. Specifically, process noise is generated when state vector changes from $\boldsymbol{x}_{t-1}$ to $\boldsymbol{x}_t$, and cannot be accurately established using mathematical models. However, the process noise can be estimated based on the probability distribution of the error. Here, we assume that the process noise obeys a normal distribution with expectation value as 0, and covariance matrix as $\boldsymbol{Q}_c$, which is $\boldsymbol{w}\sim N(\boldsymbol{0}, \boldsymbol{Q}_c)$. The covariance matrix $\boldsymbol{Q}_c$ can be written as

$$\boldsymbol{Q}_c = E(\boldsymbol{w}\boldsymbol{w}^T) = E\left(\begin{bmatrix} w_1 \\ \vdots \\ w_n \end{bmatrix}\begin{bmatrix} w_1 & \cdots & w_n \end{bmatrix}\right) = \begin{bmatrix} \sigma_{w_1}^2 & \cdots & \sigma_{w_1 w_n} \\ \vdots & \ddots & \vdots \\ \sigma_{w_n w_1} & \cdots & \sigma_{w_n}^2 \end{bmatrix} \tag{4.39}$$

If the process noise is independent from each other, then the covariance value of different member comes to be 0, thus the covariance matrix $\boldsymbol{Q}_c$ can be simplified to be a diagonal matrix. Then we define an observation vector $\boldsymbol{z}_t \in \mathbb{R}^{n\times 1}$ as

$$\boldsymbol{z}_t = \boldsymbol{C}_m\boldsymbol{x}_t + \boldsymbol{v}_t \tag{4.40}$$

where $\boldsymbol{C}_m \in \mathbb{R}^{n\times n}$ is an observation matrix, representing linear relationship between the

observation values and state vector, and $\boldsymbol{v}_t \in \mathbb{R}^{n\times 1}$ is measurement noise obeying normal distribution with expectation value as 0, and covariance matrix as $\boldsymbol{R}_c$ ($\boldsymbol{v}\sim N(\boldsymbol{0}, \boldsymbol{R}_c)$). If the process noise is assumed to be independent with each other, the matrix $\boldsymbol{R}_c$ can also be simplified to be a diagonal matrix like $\boldsymbol{Q}_c$.

It can be observed from Equation (4.38) and Equation (4.40) that due to the existence of process noise $\boldsymbol{w}_{t-1}$ and measurement noise $\boldsymbol{v}_t$, accurate state vector $\boldsymbol{x}_t$ and observation vector $\boldsymbol{z}_t$ can not be obtained. The Kalman filter can be designed to fuse the data of the system stated above, so as to obtain a relatively accurate estimation result.

To design the Kalman filter, we firstly define a prior state estimation as

$$\hat{\boldsymbol{x}}_t^- = \boldsymbol{A}\hat{\boldsymbol{x}}_{t-1} + \boldsymbol{B}\boldsymbol{u}_{t-1} \tag{4.41}$$

It can be observed that we use state estimation $\hat{\boldsymbol{x}}_{t-1}$ to replace the real $\boldsymbol{x}_{t-1}$, which is named as posteriori state estimation at time $(t-1)$. Then we rewrite the observation vector as

$$\boldsymbol{z}_t = \boldsymbol{C}_m\hat{\boldsymbol{x}}_{mea\_t} \tag{4.42}$$

where $\hat{\boldsymbol{x}}_{mea\_t}$ is the state estimation from measurement. From measurement data, we can also obtain a state at time (t) as

$$\hat{\boldsymbol{x}}_{mea\_t} = \boldsymbol{C}_m^{-1}\boldsymbol{z}_t \tag{4.43}$$

Now we obtain two state estimation vectors from Equation (4.41) and Equation (4.43), where $\hat{\boldsymbol{x}}_t^-$ is obtained based on the state space function, while $\hat{\boldsymbol{x}}_{mea\_t}$ is obtained from measurement data. Then we fuse these two state vectors using matrix $\boldsymbol{G}_t$ and define a posteriori state estimation at time (t) as

$$\hat{\boldsymbol{x}}_t = \hat{\boldsymbol{x}}_t^- + \boldsymbol{G}_t\left(\hat{\boldsymbol{x}}_{mea\_t} - \hat{\boldsymbol{x}}_t^-\right) = \hat{\boldsymbol{x}}_t^- + \boldsymbol{G}_t\boldsymbol{C}_m^{-1}(\boldsymbol{z}_t - \boldsymbol{C}_m\hat{\boldsymbol{x}}_t^-) \tag{4.44}$$

Let $\boldsymbol{K}_t = \boldsymbol{G}_t \boldsymbol{C}_m^{-1}$, the Equation (4.44) can be simplified as

$$\hat{\boldsymbol{x}}_t = \hat{\boldsymbol{x}}_t^- + \boldsymbol{K}_t(\boldsymbol{z}_t - \boldsymbol{C}_m \hat{\boldsymbol{x}}_t^-) \tag{4.45}$$

where $\boldsymbol{K}_t \in [0, \boldsymbol{C}_m^{-1}]$ is named Kalman gain, and $(\boldsymbol{z}_t - \boldsymbol{C}_m \hat{\boldsymbol{x}}_t^-)$ is named measurement residual.

4.3.2. Kalman Gain Solution

The objective of the Kalman filter now comes to obtain an adequate Kalman gain $\boldsymbol{K}_t$ to make the posteriori state estimation $\hat{\boldsymbol{x}}_t$ approach the real state vector $\boldsymbol{x}_t$. To solve the problem, we introduce estimate error as

$$\begin{aligned} \boldsymbol{e}_t^- &= \boldsymbol{x}_t - \hat{\boldsymbol{x}}_t^- \\ \boldsymbol{e}_t &= \boldsymbol{x}_t - \hat{\boldsymbol{x}}_t \end{aligned} \tag{4.46}$$

where e_t^- is an error of prior state estimation, and $\boldsymbol{e}_t$ is an error of posteriori state estimation vector. Then we replace $\boldsymbol{x}_t$ and $\hat{\boldsymbol{x}}_t^-$ using Equation (4.38) and Equation (4.41) as:

$$\boldsymbol{e}_t^- = \boldsymbol{x}_t - \hat{\boldsymbol{x}}_t^- = \boldsymbol{A}\boldsymbol{x}_{t-1} + \boldsymbol{B}\boldsymbol{u}_{t-1} + \boldsymbol{w}_{t-1} - (\boldsymbol{A}\hat{\boldsymbol{x}}_{t-1} + \boldsymbol{B}\boldsymbol{u}_{t-1}) = \boldsymbol{A}\boldsymbol{e}_{t-1} + \boldsymbol{w}_{t-1} \tag{4.47}$$

The $\boldsymbol{e}_t$ can be represented as

$$\boldsymbol{e}_t = \boldsymbol{x}_t - \hat{\boldsymbol{x}}_t = \boldsymbol{x}_t - (\hat{\boldsymbol{x}}_t^- + \boldsymbol{K}_t(\boldsymbol{z}_t - \boldsymbol{C}_m \hat{\boldsymbol{x}}_t^-)) = (\boldsymbol{I} - \boldsymbol{K}_t \boldsymbol{C}_m)(\boldsymbol{x}_t - \hat{\boldsymbol{x}}_t^-) - \boldsymbol{K}_t \boldsymbol{v}_k \tag{4.48}$$

The covariance matrix of $\boldsymbol{e}_t$ can be obtained as

$$\boldsymbol{P}_t = E[\boldsymbol{e}_t \boldsymbol{e}_t^T] \tag{4.49}$$

The trace of the $\boldsymbol{P}_t$ comes to be

$$\mathrm{Tr}(\boldsymbol{P}_t) = \sigma_{e_{1t}}^2 + \sigma_{e_{2t}}^2 + \cdots + \sigma_{e_{nt}}^2 \tag{4.50}$$

Then the design objective of the Kalman gain comes to be find the minimum $\mathrm{Tr}(\boldsymbol{P}_t)$

$$\boldsymbol{K}_t^* = \mathrm{argmin}\mathrm{Tr}(\boldsymbol{P}_t) \tag{4.51}$$

The optimal Kalman gain can then be derived as

$$K_t^* = \frac{P_t^- C_m^T}{C_m P_t^- C_m^T + R_c} \tag{4.52}$$

The covariance matrix P_t can be represented as

$$P_t = (I - K_t C_m) P_t^- \tag{4.53}$$

4.3.3. Kalman Filter Algorithm Application

With the concepts of the Kalman filter and optimal Kalman gain discussed above, the process of the Kalman filter algorithm application is now concluded in this section. Typically, the entire algorithm is divided into two parts: time update and measurement update, as shown in Figure 4.3.

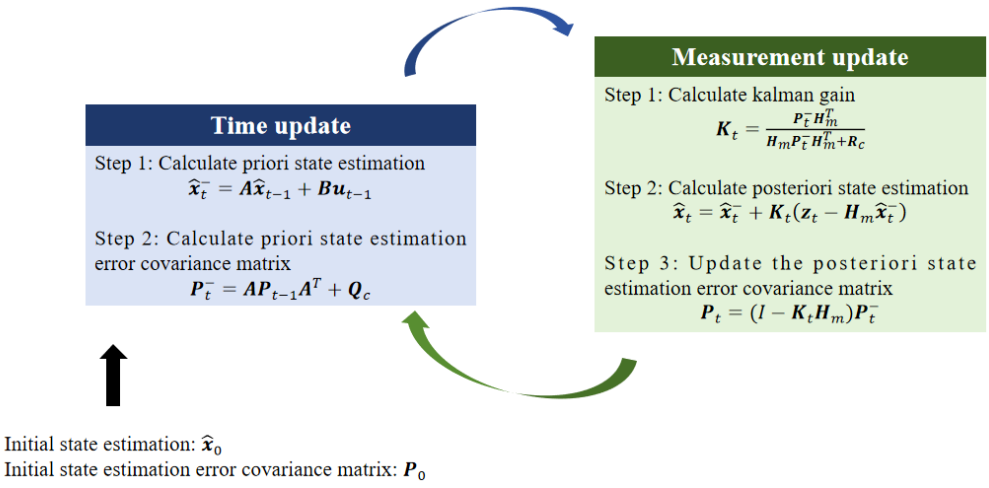

Figure 4.3 Procedure of Kalman filter algorithm

At time $t = 1$, the initial state estimation $\hat{x}_0$ and the covariance matrix of the initial state estimation error P_0. are set. The initial estimated state $\hat{x}_0$ is chosen to be close to the real state, and P_0 is initialized using a matrix with relatively large elements. The $\hat{x}_0$ serves as the initial state for the MPC optimization. At each subsequent step k, the time update part first calculates the prior state estimation $\hat{x}_t^-$ and the prior covariance matrix P_t^-. Then, the measurement

update uses $\boldsymbol{P}_t^-$ and $\boldsymbol{R}_c$ to obtain the Kalman gain $\boldsymbol{K}_t$, allowing for the fused posteriori state estimation $\hat{\boldsymbol{x}}_t$ to be obtained. The posteriori state estimation error covariance matrix $\boldsymbol{P}_t$ is then determined for the next time step.

4.3.4. MPC-Based Control Architecture with Kalman Filter

Figure 4.4 illustrates the execution process of a single-point magnetic levitation system controlled using MPC, integrated with a Kalman filter for state estimation. The workflow begins with the reference input z_{ref} which represents the desired suspension gap of the system. This reference is compared with the actual output z from the suspension unit to generate an error signal. This error signal is fed into the MPC controller.

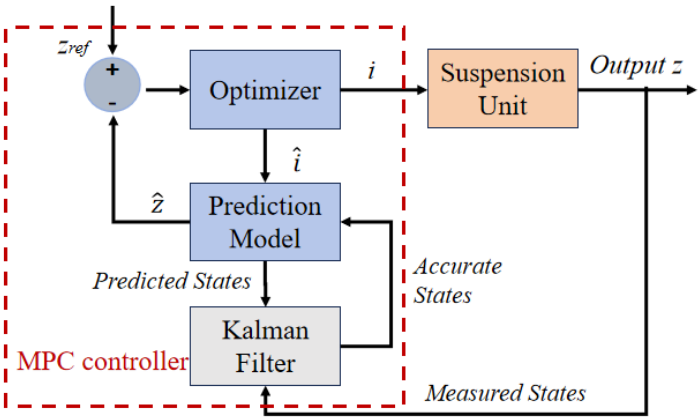

Figure 4.4 Block diagram of MPC controller for suspension unit with Kalman Filter

Within the MPC controller, the optimizer takes the error signal, and based on the predicted future states provided by the Prediction Model, calculates the optimal control input i (the current to be applied to the electromagnet). This control input is then sent to the suspension unit, which adjusts the magnetic field to achieve the desired suspension gap.

The Prediction Model is a critical part of the MPC controller, predicting the future states of the

suspension unit over a given horizon. These predictions are made using the current state estimates $\hat{z}$ provided by the Kalman Filter and the control input $\hat{\imath}$ from the Optimizer. The accuracy of these predictions is essential for the MPC to generate effective control actions.

The Kalman Filter in this setup by providing accurate state estimates $\hat{z}$ from the noisy measured states. It combines the noisy measurements from the suspension unit with the Prediction Model's output to filter out noise and estimate the true state of the system. These accurate state estimates are then fed back into the Prediction Model and Optimizer, ensuring that the MPC controller has reliable information for decision-making.

Finally, the control input iii generated by the MPC is applied to the Suspension Unit, which adjusts the magnetic force to achieve the desired suspension gap, and the system outputs the actual suspension gap z.

This integrated approach, combining MPC with Kalman filter, ensures that the control system can effectively manage the non-linearities and uncertainties inherent in magnetic levitation systems, providing precise control of the levitation height while maintaining stability and robustness against disturbances.

4.4. Simulation Results

With the dynamic model of the suspension unit established and the design and stability proof of the MPC completed, the focus now shifts to simulation studies. This section explores the performance of the MPC under various operating conditions, analyzing how different parameters within the MPC framework influence control effectiveness. The goal is to characterize the behavior of each parameter, identify the strengths and limitations of the MPC

approach, and uncover areas where the control strategy may require further refinement.

In the simulation, the plant model used is the same suspension unit described in Section 3.2, which is also the one employed in the PID control simulations for consistency. The simulations are also performed using SIMULINK. The SIMULINK model diagram is presented in Figure 4.5, illustrating the data flow of the simulation. This model serves as the foundation for both the analysis of MPC characteristics and the comparison of the effectiveness between MPC and PID control approaches. By using a consistent system representation, the results are directly comparable, providing a clear and objective evaluation of each control strategy's performance. The control horizon of MPC controller is consistently set to one.

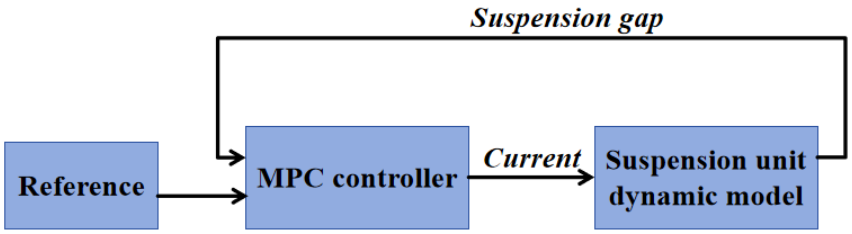

Figure 4.5 SIMULINK diagram of MPC controller simulation

4.4.1. Levitation Process Simulation

The system was tasked with adjusting the suspension gap from an initial value of 18mm to a target value of 8mm. The simulation was performed using a SIMULINK model, with a control interval fixed at 0.001 second. The primary parameter interested of MPC was the prediction horizon, which was varied across eight different values: 5, 10, 15, 20, 25, 30, 35, and 40. For each prediction horizon, the corresponding suspension gap and control current were recorded over time. The output current constraint in the MPC algorithm is set between 0 A and 60 A.

The MPC performance compared against a PID controller used in Section 3.3.3 with parameters P=12000, I=10000, and D=1000. The focus is on understanding how the prediction horizon impacts the controller's ability to stabilize the suspension gap efficiently and accurately. Figure 4.6 displays the time evolution of the suspension gap for each of the 8 prediction horizons. The system's performance improves as the prediction horizon increases, with noticeable differences in overshot and stabilization time. The overshot is the amount by which the suspension gap exceeds the target value of 8 mm before stabilizing. For shorter prediction horizons, such as 5 and 10, the system exhibits a more significant overshot and even falls to the lower system limit (0 mm) before it begins to stabilize towards the target. As the prediction horizon increases, the overshoot progressively decreases, with the gap reaching a minimum of 0.556 mm (overshoot of 7.44 mm) for a horizon of 15, 5.93 mm (overshoot of 2.07 mm) for a horizon of 20, and 7.30 mm (overshoot of 0.70 mm) for a horizon of 25. This trend continues with even smaller overshoots of 0.37 mm at a minimum gap of 7.63 mm for a horizon of 30, 0.18 mm at 7.82 mm for a horizon of 35. At the prediction horizon of 40, the overshot is eliminated.

Stabilization time refers to the time it takes for the suspension gap to settle within a certain threshold of the target value and remain there. At a prediction horizon of 20, the system stabilizes quickly at approximately 0.096 seconds, with noticeable but decreasing overshoot as it approaches the target gap. The horizon of 25 stabilizes slightly later at 0.107 seconds, continuing the trend of reduced overshoot, indicating that the system is achieving finer control. As the horizon increases to 30, the stabilization time extends to 0.129 seconds, with overshoot

becoming smaller, though the system takes longer to fully settle within the narrow bounds. At a horizon of 35, the stabilization time further increases to 0.146 seconds, reflecting an even more conservative approach with minimal overshoot, as the control becomes more precise. Finally, with a horizon of 40, the system stabilizes at 0.122 seconds, where the overshoot is the smallest, balancing accuracy and speed effectively.

Figure 4.7 visually represents the distribution of errors between the actual suspension gap and the target gap of 8 mm across different prediction horizons. For shorter horizons, such as 5 and 10, the error distribution is wide and scattered, with significant deviations from the target gap of 8 mm, including large overshoots reaching up to -7.99 mm. As the prediction horizon increases to 15, the error cloud begins to tighten, indicating better control but still with notable deviations. By horizon 20, the errors are significantly reduced, with the maximum negative error decreasing to around -2.07 mm, showing that the system is becoming more precise. Horizons 25 and 30 further refine this control, with errors clustering closer to zero and maximum negative errors reducing to around -0.70 mm and -0.37 mm, respectively. The longest horizons, 35 and 40, demonstrate the narrowest error distributions, with maximum negative errors of only -0.18 mm and 0 mm.

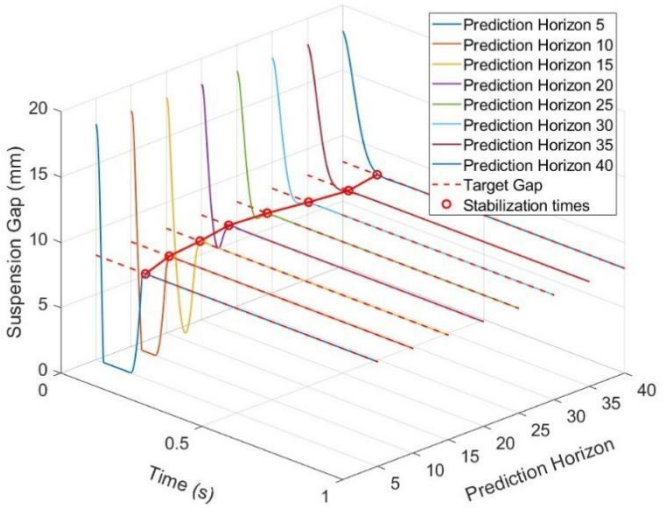

Figure 4.6 Levitation process by MPC with different prediction horizon

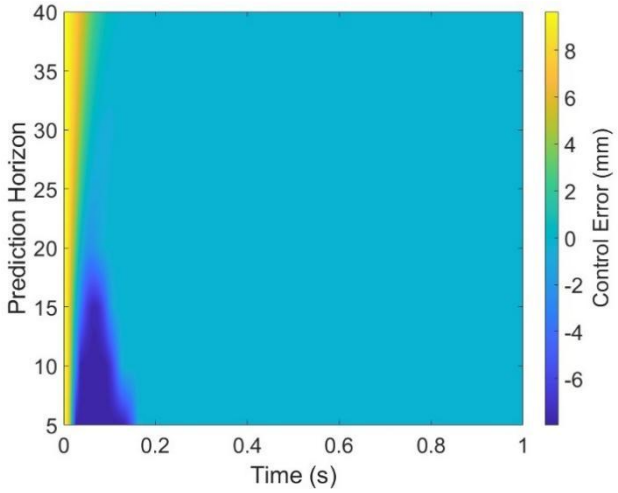

Figure 4.7 Control error of MPC controller with different prediction horizon

Figure 4.8 and Figure 4.9 reveals a clear trend toward stabilization as the prediction horizon increases. At shorter horizons, such as 5 and 10, the system exhibits significant current fluctuations, frequently reaching the upper limit of 60 A. The mean currents during this period are approximately 10.06 A and 10.42 A, with high standard deviations of 7.47 A and 6.42 A,

reflecting aggressive and variable control actions. As the prediction horizon extends to 15 and 20, these fluctuations reduce, with mean currents increasing to 10.59 A and 10.92 A, and standard deviations decreasing to 5.59 A and 4.56 A, indicating more consistent and stable control behavior. In longer prediction horizons, such as 25 and 30, the system further stabilizes, with mean currents rising to 11.17 A and 11.30 A, and the standard deviations dropping to 3.75 A and 3.43 A, showing that the control actions become smoother and more refined. Ultimately, at the longest horizons, 35 and 40, the system's current stabilizes around 10.84 A, with minimal fluctuations (standard deviations of 3.29 A and 3.24 A). This steady current value of 10.84 A corresponds to the required current for stable suspension, indicating that the system achieves optimal control, minimizing variability and maintaining the desired suspension gap with high precision and efficiency. This consistent current across prediction horizons reflects the MPC system's ability to converge on an optimal control strategy, ensuring stability and efficiency in maintaining the suspension gap.

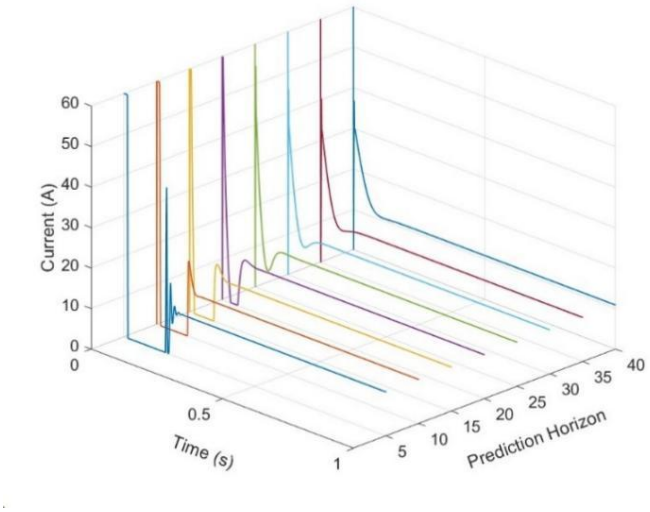

Figure 4.8 Control current across different prediction horizons

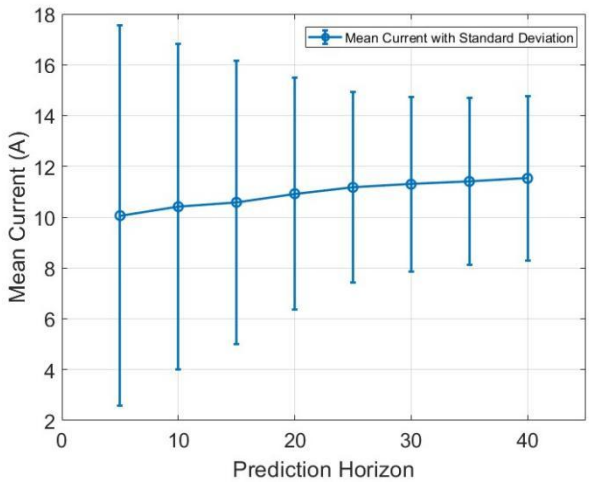

Figure 4.9 Mean and standard deviation of control current for varying prediction horizons

The analysis as illustrated in Figure 4.10, reveals differences between the MPC controller with a prediction horizon (PH) of 40 and the traditional PID controller. The MPC controller rapidly reduces the gap from 18 mm to the target of 8 mm in just 0.122 seconds. This quick and precise response showcases the MPC's ability to efficiently predict and adjust control inputs. The PID controller takes longer, 0.612 seconds, to reach the target gap, indicating a slower controlled

response. Figure 4.11 further highlights the differences in current demand between the two controllers. The MPC controller peaks at 60 A during the initial rapid gap reduction and stabilizes at a steady-state current of 10.84 A, reflecting efficient energy usage. On the other hand, the PID controller requires a much higher peak current of 120 A, suggesting less efficient control.

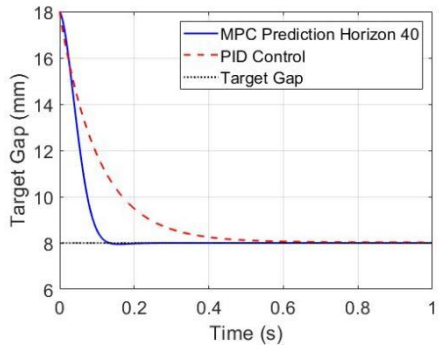

Figure 4.10 Comparison of levitation gap response between MPC (PH=40) and PID controllers

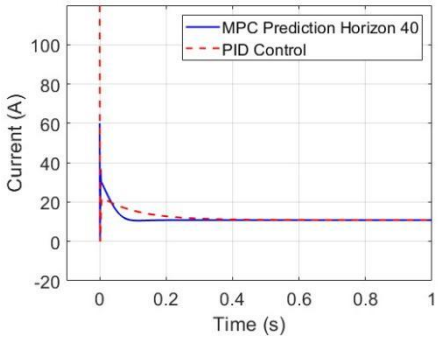

Figure 4.11 Comparison of control current demand between MPC (PH=40) and PID controllers

The comprehensive analysis of the MPC system across various prediction horizons, in comparison with PID control, highlights key characteristics and performance differences. As the prediction horizon in the MPC system increases, the control actions become progressively more refined and stable. Shorter prediction horizons (such as 5 and 10) lead to aggressive control efforts with significant current fluctuations and less precise gap control, often resulting in overshoots and higher energy consumption. However, as the prediction horizon extends to 20, 30, and particularly 40, the system demonstrates superior performance, with minimal overshot, stable current usage around 10.84 A, and precise maintenance of the target gap.

Figure 4.12 and Figure 4.13 illustrate the simulated suspension gap and control current responses under different control strategies, including PID control, MPC with varying prediction horizons (PH = 5 and PH = 40), root locus control, and state feedback control. Two types of target reference scenarios are considered. For the MPC controller with PH = 5, the reference gap decreases gradually from 18 mm to 8 mm at a rate of 0.5 mm per 0.001 seconds, which is designed to evaluate the controller's ability to track a dynamically changing setpoint. In contrast, the MPC controller with PH = 40, as well as the PID controller, root locus controller, and state feedback controller, are tested under a constant reference of 8 mm from the beginning of the simulation. These configurations allow for a comparative analysis of each controller's capability in managing both transient response and steady-state accuracy under different reference dynamics.

The simulation results reveal that the MPC controller with PH = 5 exhibits the best tracking performance in the slowly-varying reference scenario. The suspension gap remains within ±0.1 mm of the reference throughout the transition, with no significant overshoot or oscillation. This is achieved through the predictive nature of MPC, which allows smooth adaptation to gradual changes without invoking abrupt control actions. Although its convergence is slightly slower than MPC with PH = 40, the PH = 5 configuration is specifically designed to handle dynamic references, and its performance remains superior to the PID controller. Notably, the PID controller fails to maintain stability under the same changing reference (not shown in the figure), further highlighting its limited adaptability to reference dynamics. The current response of MPC with PH = 5 also demonstrates more aggressive adjustment in the early phase and at

the stabilization point, reflecting its effort to compensate for continuous reference variation.

In comparison, the root locus-based controller demonstrates relatively slow convergence and poor transient performance. Although it eventually stabilizes near the target gap, the initial response is significantly delayed and less responsive. This behavior is consistent with the limitations of classical proportional control based on root locus design, which lacks integral action and cannot adapt to nonlinear system behavior or varying references. Additionally, as shown in Figure 4.13, the control current generated by this method is smoother but remains relatively high for an extended period, indicating inefficient control effort distribution.

The state feedback controller, on the other hand, exhibits faster convergence and better transient behavior compared to the root locus controller. It achieves a settling time close to that of the MPC controller with PH = 5 and demonstrates improved damping characteristics. However, the lack of predictive optimization results in slightly higher overshoot and suboptimal current utilization. In Figure 4.13, the current response under state feedback control remains within the physical limits without saturation but exhibits sharper transitions than MPC, suggesting less efficient management of control energy.

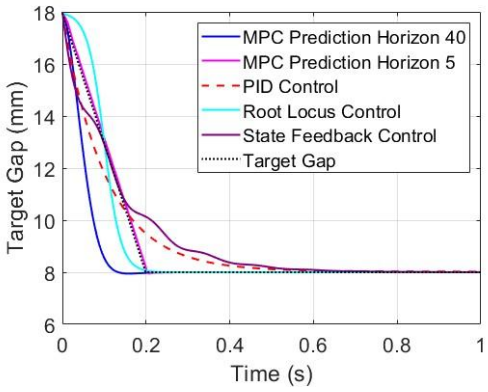

Figure 4.12 Suspension gap response comparison for MPC PH=5, MPC PH=40, PID, Root Locus and State Feedback under different target references

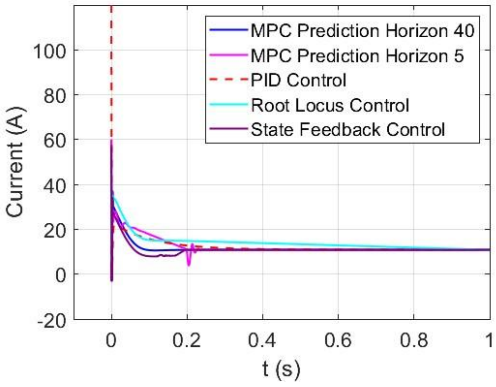

Figure 4.13 Current response comparison for MPC PH=5, MPC PH=40, PID, Root Locus and State Feedback under different target references

According to the simulation results in this section, several conclusions can be drawn. Different control conditions require different prediction horizons to achieve optimal performance. When the current suspension gap is significantly different from the target gap, using a longer prediction horizon results in smoother adjustments, meaning that the control current at each step changes less aggressively from the previous step. However, a longer prediction horizon demands more computational power, as the MPC controller must predict the system states over more future steps. If the prediction model is complex, the required computation time might exceed the control interval, making real-time control challenging.

When the target suspension gap shifts from a landing condition to a suspension condition, a shorter prediction horizon can be used, as it provides better responsiveness to changes in the target gap. For instance, setting a prediction horizon of 5 when changing the suspension gap from 18 mm to 8 mm ensures a smooth and sufficiently fast levitation process while minimizing

computational demands.

When the target suspension gap follows a dynamic change similar to the trend followed by the MPC controller, the system controlled by the PID controller tends to diverge. This highlights that during the levitation process, the PID controller cannot accommodate rapid changes in the target suspension gap as effectively as the MPC.

4.4.2. Analysis of MPC Controller Output Constraints

The simulation in Section 4.4.1 uses MPC controllers with output constraints set between a lower limit of 0 A and an upper limit of 60 A, which aligns with the practical system. In this section, we adjust the output constraints while keeping all other settings consistent with those in Section 4.4.1, to analyze how these constraints impact the performance of the MPC controller during the levitation process. The target suspension gap changes from the initial landing condition to the final desired value, with a rate of 0.05 mm per 0.001 seconds. The constraints are set in four conditions: 0 A to 45 A, 0 A to 50 A, 0 A to 55 A, 0 A to 60 A.

Figure 4.14 shows the suspension gap during the levitation process under different upper constraint currents. Despite the varying constraints, the levitation performance remains consistent. Figure 4.15 shows the corresponding currents. The currents have the same tent in the levitation process, but some difference at the process beginning just the value. At the beginning of the levitation process, all MPC controllers' output reach the upper limit. Then the currents become the same. presents the corresponding current profiles. While the currents exhibit a similar trend throughout the levitation process, there are slight differences in their values at the beginning. At the start of the levitation process, all MPC controllers output

currents that reach the upper limit. Afterward, the currents converge to the same value.

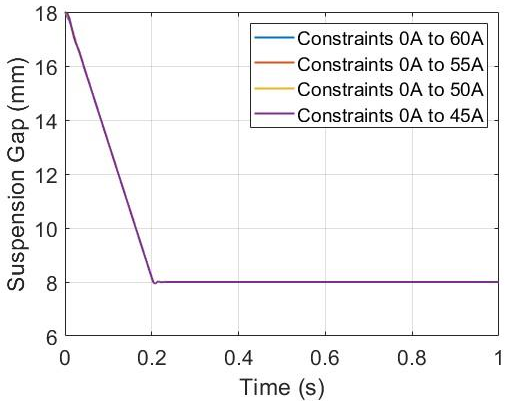

Figure 4.14 Suspension gap with different current constraints

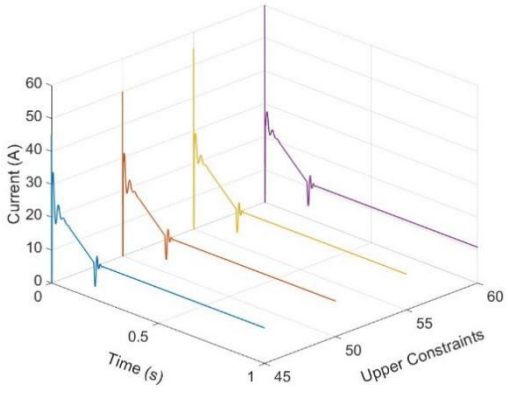

Figure 4.15 Current under different current constraints

4.4.3. Trajectory Tracking

When a maglev train travels over viaducts, the structure undergoes vertical displacement due to dynamic loads. To ensure the suspension system remains stable and the suspension gap is consistently maintained at 8 mm, the train's control system must accurately track these vertical displacements. Typically, a single span of a viaduct measures 25 meters in length, and the corresponding vertical displacement is approximately 1.7 mm.

To simulate the suspension unit's ability to track these displacements while maintaining a stable 8 mm suspension gap, the target trajectory for the controller is modeled by the function $y = 1.7\sin(\text{frequency} \cdot t) + 8$. This function represents a sinusoidal displacement path with varying frequencies, which mimics the vertical movement of the viaduct as the train passes over it. For this study, four specific frequencies were selected: 1.4 rad/s, 2.79 rad/s, 4.19 rad/s, and 5.59 rad/s. These frequencies correspond to the maglev train traveling at speeds of 40 km/h,

80 km/h, 120 km/h, and 160 km/h, respectively, as it crosses a single viaduct span.

Figure 4.16 illustrates the time series of the suspension gap for both the MPC and PID controllers across the different speeds. The results show that the MPC controller consistently outperforms the PID controller in maintaining the suspension gap close to the desired 8 mm across all speeds. Figure 4.17 presents the error time series, representing the deviation of the controlled gap from the reference gap for both controllers. The analysis of these error time series reveals that the MPC controller maintains significantly lower error magnitudes compared to the PID controller, particularly as the train speed increases. Figure 4.18 shows the error distribution for both controllers across the different speeds, providing a statistical overview of the frequency and magnitude of the errors encountered during the simulation.

At lower speeds, the errors for both controllers are relatively small, with the MPC controller demonstrating slightly better performance. However, as the speed increases, the PID controller's errors become more pronounced, with larger amplitude oscillations and slower recovery times. This is especially evident at 120 km/h and 160 km/h, where the PID controller struggles to keep the error within acceptable bounds, leading to frequent and significant deviations from the desired gap. In contrast, the MPC controller exhibits smaller errors and faster convergence back to the desired 8 mm gap, highlighting its superior ability to manage the rapid changes in viaduct displacement at higher speeds.

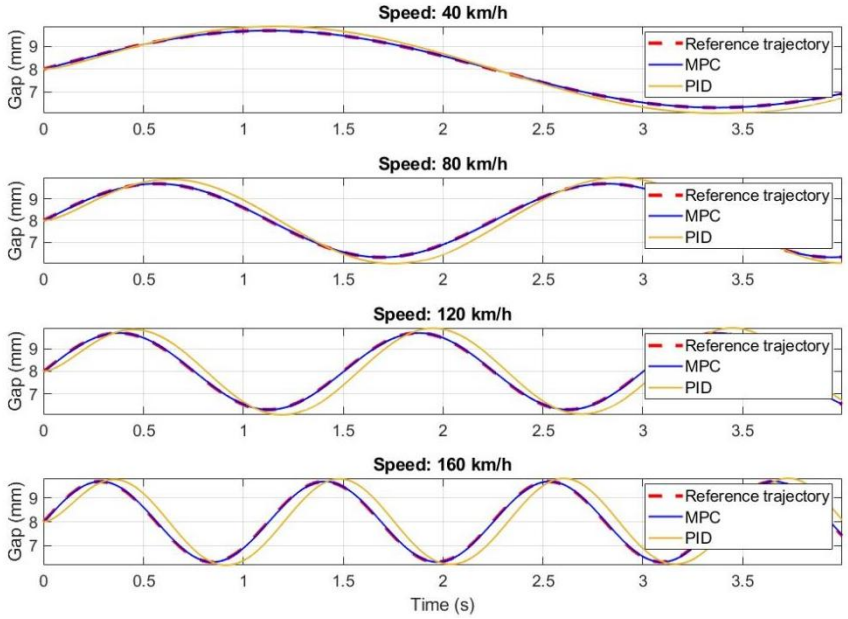

Figure 4.16 Comparison of suspension gap tracking between MPC and PID control at different train speeds

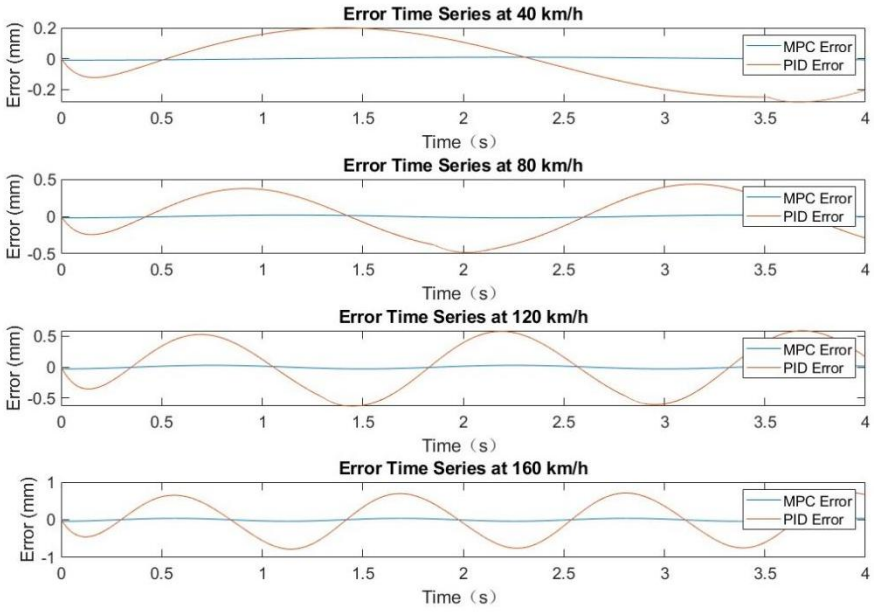

Figure 4.17 MPC and PID error time series from simulation at different speeds

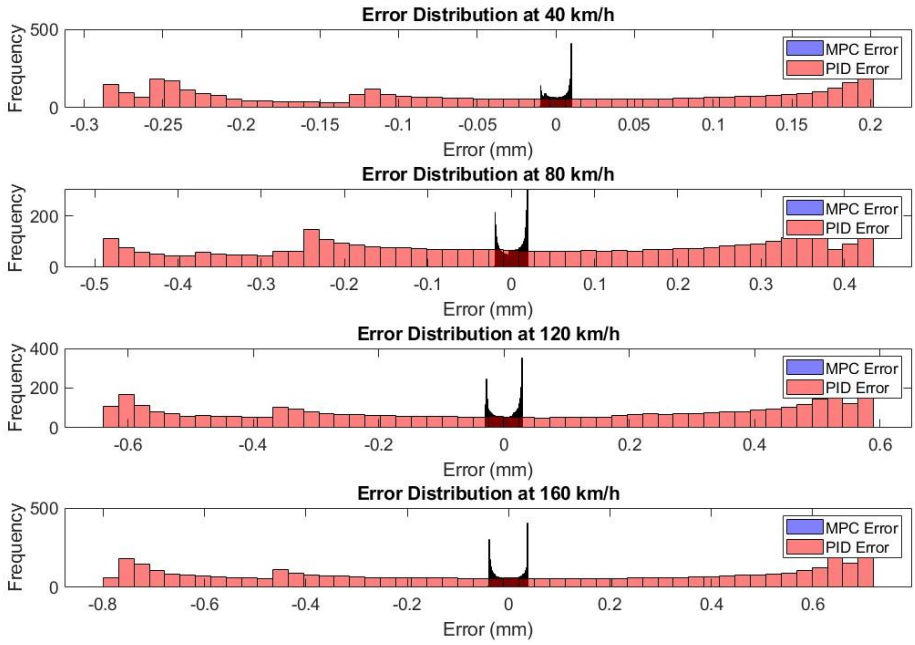

Figure 4.18 MPC and PID error distribution from simulation at different speeds

4.4.4. Impact of Measurement Noise

In magnetic levitation systems, maintaining an accurate suspension gap is crucial for stable operation. However, measurement noise, often present in the sensors monitoring this gap, can significantly affect the system's control performance. Analyzing the impact of such noise on MPC system helps to assess its robustness and reliability in real-world applications.

This section focuses on the analysis of measurement noise effects in a single-point magnetic suspension system. The system is modeled similarly to the one described in Section 3.2, simulating the dynamics of a maglev train. To replicate practical conditions, Gaussian noise is introduced in real-time to the suspension gap output using Simulink's Band-Limited White Noise block. This block generates noise with a zero mean and a specified variance, constrained within a given bandwidth, ensuring that the noise is appropriate for the system's sampling rate.

The block's configuration includes parameters for noise power and sample time, allowing fine control over the intensity and characteristics of the noise added to the sensor measurements. This noise emulates the imperfections in real-world sensor readings, enabling a detailed evaluation of the MPC's performance in handling noisy data.

Figure 4.19 to Figure 4.21 present the results of the first simulation, where both MPC and PID controllers are tested under low measurement noise introduced after the 1-second mark. The measurement noise, which fluctuates between -0.005 mm and +0.005 mm, introduces a minor disturbance to the sensor readings. During the initial second, with no noise present, both controllers successfully maintain the suspension gap at the reference value of 8 mm. After the introduction of noise, MPC demonstrates strong robustness by effectively tracking the reference trajectory. Although some minor oscillations appear due to the noise, they are quickly dampened, and the system remains stable. The current output from both controllers also reflects this behavior. MPC maintains a smoother control current response, while PID exhibits more significant fluctuations in current after the noise introduction, further highlighting MPC's superior noise-handling capability in this minimal noise scenario.

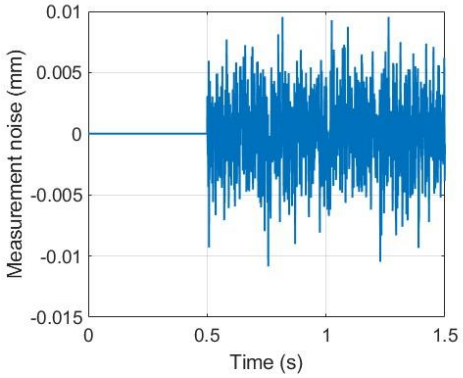

Figure 4.19 Measurement noise in the first set with small noise

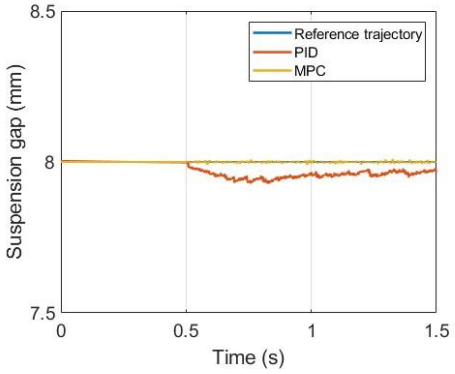

Figure 4.20 Suspension gap for MPC and PID under small noise

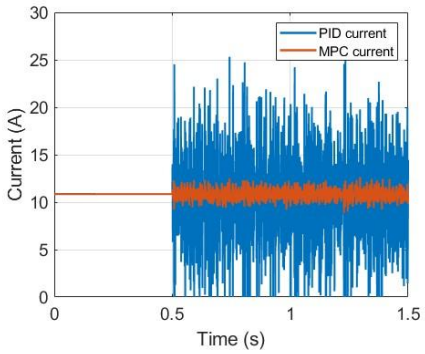

Figure 4.21 Control current for MPC and PID under small noise

Figure 4.22 to Figure 4.24 show the simulation results where a larger level of measurement noise is introduced after the 1-second mark. After the noise is applied, PID control becomes unstable and diverges. Due to this divergence, the results for PID beyond the 1-second mark are no longer meaningful and are excluded from further analysis. In contrast, MPC continues to maintain stability under the influence of the larger noise. The measurement noise, which ranges from -0.02 mm to +0.02 mm, introduces a more significant disturbance than in the first

set. Despite this, MPC adapts and stabilizes the system, with only moderate oscillations in the suspension gap after the noise is applied and the mean suspension gap under MPC control is 7.998 mm, with a minimum of 7.968 mm and a maximum of 8.027 mm. The system's response to this larger noise highlights MPC's robustness in comparison to PID, which could not handle the disturbance. The control current also reflects the system's response to the increased noise. The mean current output by the MPC is 10.71 A, ranging from 4.60 A to 16.38 A.

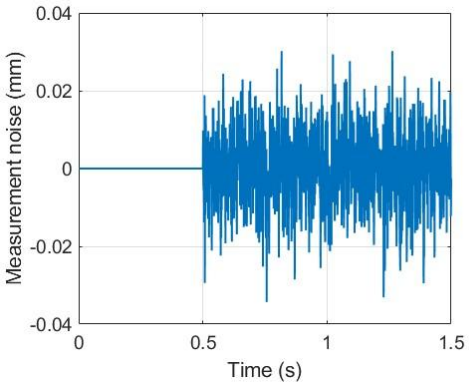

Figure 4.22 Measurement noise in the second set with larger noise

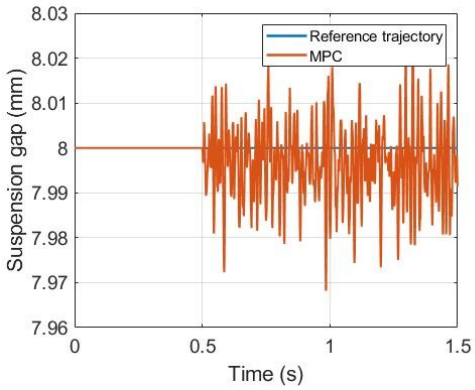

Figure 4.23 Suspension gap for MPC under larger noise

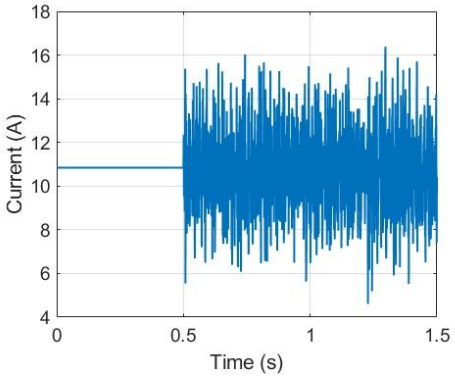

Figure 4.24 Control current for MPC under larger noise

Figure 4.25 to Figure 4.27 present the results under an even higher level of measurement noise, also applied after the 1-second mark. The noise applied to the system ranges from -0.1 mm to +0.1 mm, introducing a significant disturbance compared to previous simulations. Despite this disturbance, MPC manages to stabilize the system, maintaining a suspension gap close to the target. The mean suspension gap is 7.967 mm, with a minimum of 7.752 mm and a maximum of 8.064 mm, demonstrating good control with only minor deviations. The control current reflects the system's efforts to counteract the noise, with a mean current output of 9.48 A, ranging from 0 A to 29.10 A. The wide range of current values indicates that the controller is actively adjusting to maintain stability despite the noise.

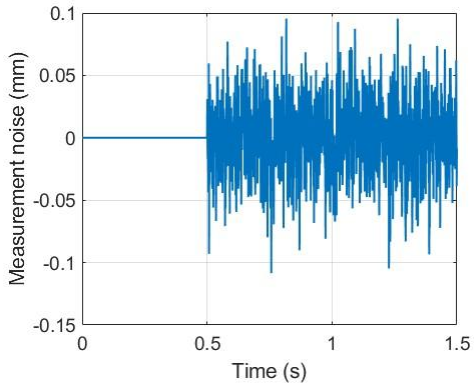

Figure 4.25 Measurement noise in the third set with largest noise

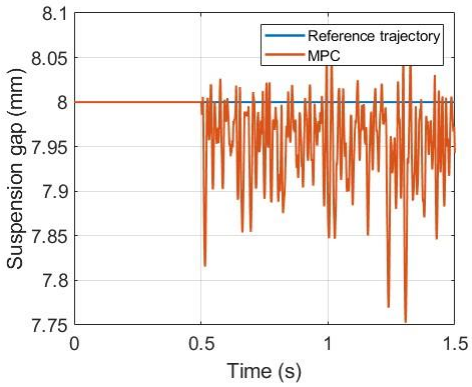

Figure 4.26 Suspension gap for MPC under largest noise

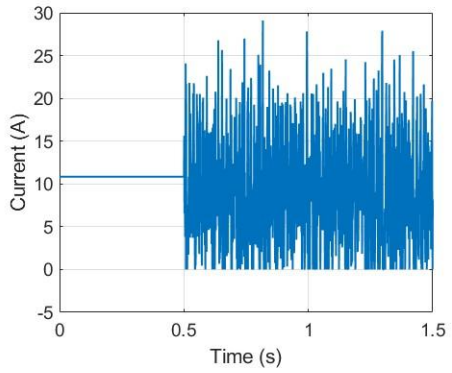

Figure 4.27 Control current for MPC under largest noise

In summary, the results consistently demonstrate that MPC outperforms PID in handling measurement noise. While PID becomes unstable under more significant noise, MPC continues to maintain system stability across all tested noise levels, with smoother current output and better tracking of the suspension gap.

4.4.5. Impact of Prediction Model Inaccuracy

This section investigates the impact of mismatches between the predictive model in the MPC controller and the actual system dynamics on the control performance of a single-point magnetic levitation system, which is consistent with the one conducted in Section 3.2. The predictive model in the MPC controller remains unchanged, while the mass parameter in the dynamic model is varied to simulate changes in the vehicle's mass due to different passenger loads. The objective is to evaluate the robustness of the MPC controller when the actual system mass deviates from the assumed model mass. The simulations are divided into three groups: in the first group, both the predictive model and the actual system have a mass of 750 kg; in the second group, the predictive model assumes a mass of 700 kg, while the actual system has a

mass of 750 kg; and in the third group, the predictive model assumes a mass of 800 kg, while the actual system again has a mass of 750 kg. In all three simulations, the prediction horizon is set to 5, the control horizon is set to 1, and the control step size is 0.001 seconds. Each simulation begins from a landing state where the suspension gap is 18 mm, and then the system rises to achieve a stable suspension at the target gap of 8 mm.

Figure 4.28 provides an overview of the suspension gap over time for three different controlled objects with masses of 700kg, 750kg, and 800kg, while the MPC controller's predictive model assumes a fixed mass of 750kg. Initially, all objects start with a suspension gap of 18 mm, and they quickly descend toward the target gap of 8 mm. The overall response is similar for all three cases, with each object reaching close to the target within the first 0.2 seconds. At this scale, no significant differences are visible between the systems with different masses, as they all converge to the desired gap at approximately the same time.

Figure 4.29 focuses on the period between 0.2 and 0.3 seconds, zooming in on the details of the transient response. Here, the effect of the mass differences becomes more apparent. The 700kg object, which is lighter than the 750kg predictive model, exhibits the largest undershoot, with the suspension gap dropping slightly below the target of 8 mm before oscillating and eventually stabilizing. In contrast, the 800kg object, which is heavier than the predictive model, shows a small overshoot, where the gap briefly exceeds 8 mm before settling. The 750kg object, whose mass matches the predictive model, tracks the reference trajectory most closely, with minimal deviation and oscillation.

These differences in response indicate that when the actual mass of the controlled object

deviates from the mass assumed in the MPC predictive model, the system exhibits varying transient behaviors. The 700kg object experiences more oscillations and a larger undershoot, while the 800kg object shows a faster settling time with a slight overshoot. The 750kg object demonstrates the most stable performance, closely following the reference trajectory without significant overshoot or undershoot.

Figure 4.30 and Figure 4.31 indicate the corresponding current. As seen in both the suspension gap and current plots, the object with a mass of 750kg, which matches the predictive model, exhibits the most stable and optimal performance. The suspension gap tracks the reference closely, with minimal overshot or undershoot, and the current response also stabilizes quickly. After the initial spike of 45 A to initiate the levitation, the current smoothly reduces to approximately 10 A by 0.2 seconds, maintaining this value for the rest of the simulation. This indicates that for the nominal case, the MPC controller accurately predicts the system dynamics, leading to efficient control with minimal corrections.

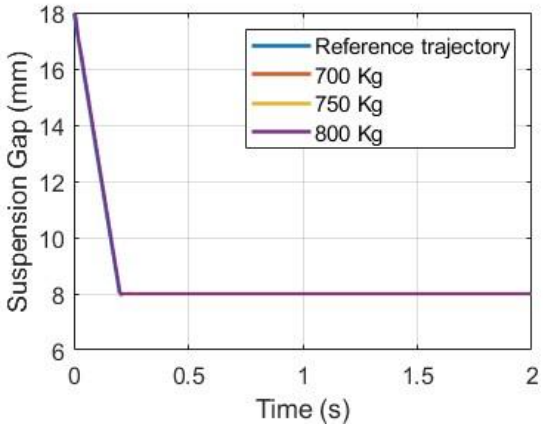

Figure 4.28 Suspension gap over time for different masses

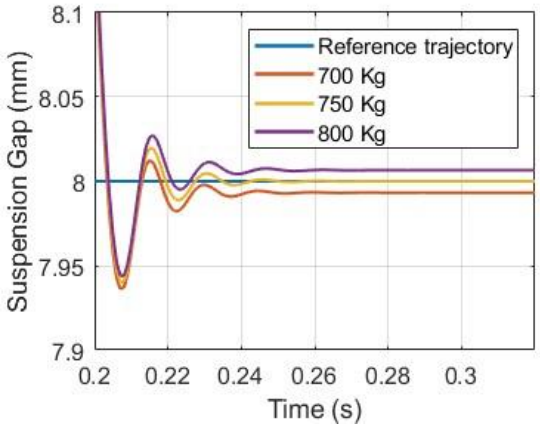

Figure 4.29 Detailed view of suspension gap transients for different masses

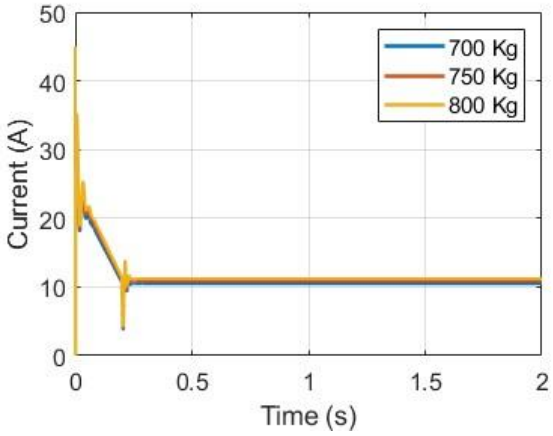

Figure 4.30 Current over time for different masses

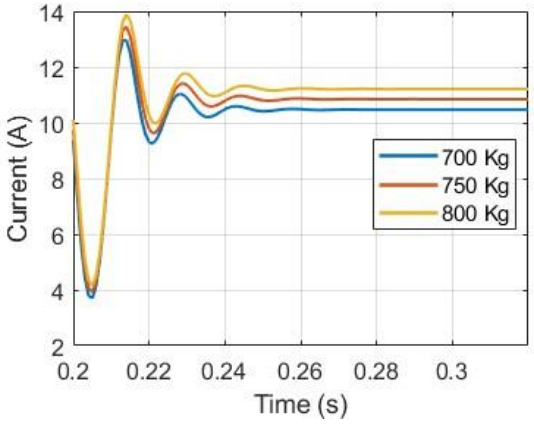

Figure 4.31 Detailed view of current transients for different masses

4.5. Experiments

The experimental setup and methods are designed to validate the theoretical analysis of the magnetic levitation control system. This section focuses on the implementation of the control strategies developed in the earlier sections, utilizing the magnetic levitation platform to demonstrate key principles of nonlinear control and system stabilization. The system, being a classic example of an unstable open-loop process, requires precise closed-loop control to maintain levitation of the steel ball. Through real-time data acquisition and control, the experiment allows for the observation of system behavior under various conditions, highlighting the performance of different control strategies such as PID and MPC. The following sections will provide a detailed description of the experimental apparatus, procedures, and the specific parameters used during testing, followed by an analysis of the experimental results.

4.5.1. Introduction of Experimental Equipment

The experimental equipment, as shown in Figure 4.32 and Figure 4.33, consists of an electromagnet, a steel ball, an LED light source, a photoelectric sensor, a power amplifier, and a control module. The primary objective of this setup is to maintain the stable levitation of the steel ball through closed-loop feedback control.

The electromagnet is placed at the top of the equipment and provides the magnetic force necessary to lift and suspend the steel ball directly below it. The balance between the magnetic force generated by the electromagnet and the gravitational force acting on the steel ball is crucial for maintaining stable levitation. However, this balance is inherently unstable, meaning that any disturbance can cause the ball to either fall or be pulled into the electromagnet. Therefore, the system requires continuous real-time feedback to adjust the current flowing through the electromagnet to keep the ball suspended at a desired height.

Figure 4.33 illustrates the working principle of the system. The steel ball is suspended at a distance (denoted as X) below the electromagnet. The LED light source illuminates the ball, and the photoelectric sensor measures the intensity of the reflected light, which changes as the ball moves. The sensor detects these changes and sends a signal to the control system to adjust the current supplied to the electromagnet via the power amplifier (drive circuit). When the ball moves away from the desired position, the control system increases or decreases the current in the electromagnet to restore the ball to its equilibrium position. This closed-loop feedback system relies on precise sensor measurements and real-time adjustments to ensure stability. The system is also equipped with Analog-to-Digital (AD) and Digital-to-Analog (DA) converters,

allowing the analog sensor data to be processed by the digital control system running on a computer. The power amplifier then translates the control signals into the necessary current adjustments for the electromagnet.

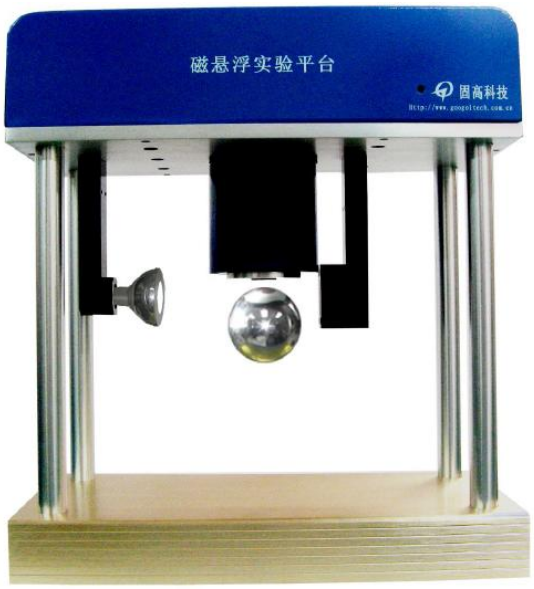

Figure 4.32 Photograph of the magnetic levitation experimental equipment

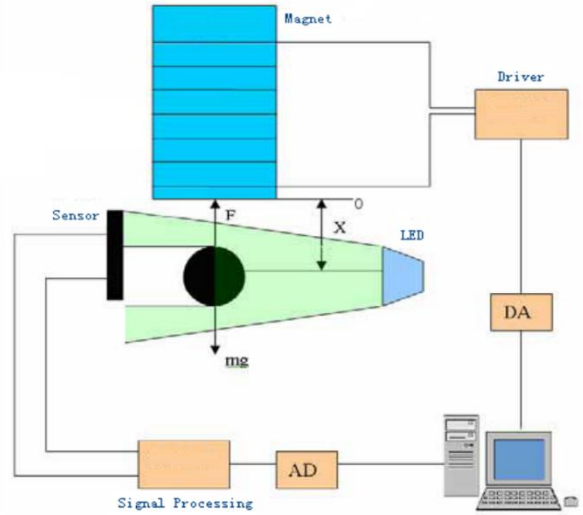

Figure 4.33 Schematic diagram of the magnetic levitation experimental equipment

Table 4.1 lists the parameters of the steel ball levitation system. The input signal of the system is in the form of voltage. The input voltage and operating current are related through Equation (4.54) where u represents the voltage and i represents the current. By substituting these parameters and Equation (4.54) into Equation (3.7), the relationship among the suspension force, voltage, and suspension gap can be derived.

$$u = 9.776i - 5.778 \tag{4.54}$$

Table 4.1 Electromagnet coil specifications

Parameters	Specification
Electromagnet coil turns	2450
Resistance	13.8Ω
Core diameter	22mm
Wire gauge	0.8mm
Mass of the steel ball	83.5g
Diameter of the steel ball	39.2mm

4.5.2. Levitation Process Test

This section uses the steel ball levitation system to evaluate the performance of PID and MPC controllers. The control aim is to levitate the steel ball from 38.5mm to 34mm and be stable at 34mm, which is the distance between the center of the ball and the bottom of the electromagnet. The prediction model in the MPC controller is based on the linearized system, derived using the method described in Section 4.2.1. Additionally, the Kalman filter state observer, introduced in Section 4.3 is implemented in the MPC controller. The control time step is set to 0.002 seconds. The parameters for both the PID and MPC controllers are provided in Table 4.2. and

Table 4.3, respectively.

Table 4.2 Parameters of the PID controller for the steel ball levitation system

P	I	D
10	0.1	50

Table 4.3 Parameters of the MPC controller for the steel ball levitation system

Parameters	Specification
Prediction horizon	5
Control horizon	1
Output constraints	Minimum 0 V; Maximum 10 V
Trajectory reference	34 mm
Input weight	0
Output weight	1
Control time step	0.002s

The prediction model used in the MPC controller is described by Equation (4.13) and Equation (4.14), where $A = \begin{pmatrix} 1 & 0.002 \\ 0.5445 & 1 \end{pmatrix}$, $B = \begin{pmatrix} 0 \\ -0.0017 \end{pmatrix}$, and $C = \begin{pmatrix} 1 \\ 0 \end{pmatrix}$. Both the PID and MPC controllers are implemented in SIMULINK and communicate with the hardware levitation system through a specialized signal interface. The controllers output voltage signals, which are then converted to current applied to the electromagnet by the DA converter.

Figure 4.34 represents the suspension gap during the steel ball levitation. The reference trajectory requires the ball to be levitated from an initial gap of 38.5 mm to 34 mm. The ball is supported by supporting seat at 38.5 mm. The PID controller shows significant oscillations during the rise phase, especially between 0 to 0.8 seconds. It struggles to follow the reference closely, resulting in a slower stabilization around 1 second. Despite eventually stabilizing at 34 mm, the path to this point involves noticeable fluctuations. The MPC controller tracks the reference trajectory more smoothly. The rise phase is better controlled, with fewer oscillations compared to the PID controller. By around 0.9 seconds, the system reaches the target gap of 34

mm with minimal overshoot and stabilizes more effectively than the PID controller.

Figure 4.35 and Figure 4.36 show the corresponding output voltage from the controllers and the current through the coil. The PID controller initially exhibits voltage peaks, reaching approximately 8.5V, while the MPC controller shows a slightly higher initial voltage peak around 9V. However, the MPC controller stabilizes the voltage more smoothly, and by 0.9 seconds, it settles near 4.5V. This smoother voltage response highlights the MPC's ability to optimize control actions, resulting in fewer fluctuations. The current is directly proportional to the applied voltage through the linearized transfer function.

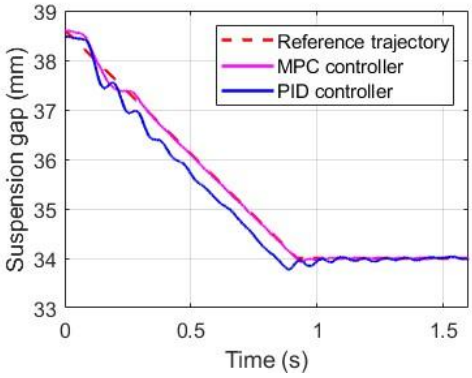

Figure 4.34 Suspension gap during levitation process using PID and MPC controllers

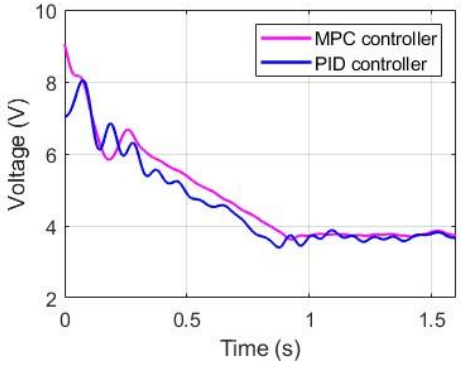

Figure 4.35 Operating voltage during levitation process using PID and MPC controllers

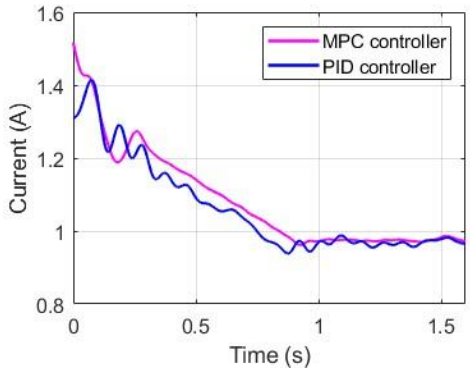

Figure 4.36 Coil current during levitation process using PID and MPC controllers

4.5.3. Trajectory Tracking Test

This experimental section aims to validate the performance of the MPC in trajectory tracking. The experimental setup remains the same as the steel ball levitation system used in previous sections. The parameters for both the PID and MPC controllers are consistent with those presented in Section 4.6.2.

In this experiment, the steel ball is initially stabilized at a suspension gap of 36 mm. After reaching steady state, the ball is required to follow a sinusoidal trajectory defined by Equation 4.59. The sinusoidal trajectory has a variation amplitude of 36±3 mm, and the reference trajectory is expressed as:

$$Trajectory\ reference = 36 + A\sin\left(Freq \times t\right) \tag{4.55}$$

The parameter A is the amplitude of the sinusoidal component of the trajectory reference and $Freq$ determines the frequency of the sinusoidal trajectory, directly affecting how fast the steel ball oscillates around the nominal suspension gap of 36 mm. A higher value of $Freq$ will result in a higher oscillation frequency, meaning the ball will need to follow quicker changes in the

reference trajectory. This will provide an opportunity to assess how effectively the MPC and PID controllers respond to rapid variations in the target position and maintain accurate tracking under different dynamic conditions.

Figure 4.37 shows the suspension gap over time, and Figure 4.38 illustrates the corresponding control voltage applied to the electromagnet for both the PID and MPC controllers when $A = 0.001\ m\ and\ Freq = 2\ rad/s$. The MPC controller follows the reference trajectory with minimal deviation, closely matching the sinusoidal pattern. The tracking is precise, with very small fluctuations from the reference, indicating that the MPC controller is effectively optimizing control actions to ensure the steel ball follows the desired path. The PID controller also tracks the trajectory reasonably well, but it exhibits slightly more lag and greater deviations compared to the MPC controller. Around the peaks and troughs of the sinusoidal trajectory, the PID controller tends to overshoot or undershoot more than the MPC, resulting in less precise tracking.

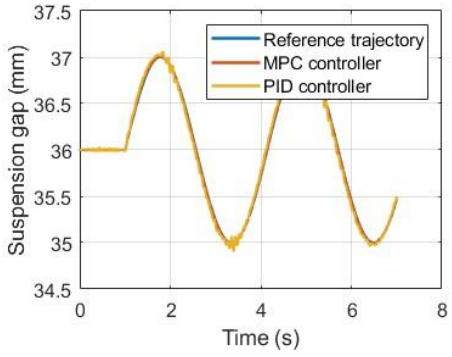

Figure 4.37 Suspension gap response for $A = 0.001\ m\ and\ Freq = 2\ rad/s$ using MPC and PID controllers

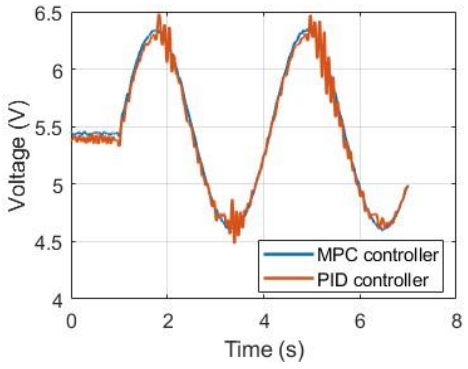

Figure 4.38 Control voltage response for $A = 0.001\ m\ and\ Freq = 2\ rad/s$ using MPC and PID controllers

Compared to the results shown in Figure 4.37 and Figure 4.38, where the sinusoidal trajectory had a smaller amplitude $A = 0.001\ m$, the tracking performance in Figure 4.39 with a larger amplitude $A = 0.001\ m$ demonstrates that both the PID and MPC controllers face more challenging control conditions. However, the MPC controller continues to maintain superior tracking performance with minimal deviation in both cases, showing its robustness even as the trajectory amplitude increases. The PID controller, on the other hand, exhibits more noticeable overshoot and undershoot in Figure 4.37 compared to Figure 4.39, indicating that the larger amplitude introduces greater difficulty in maintaining precise control.

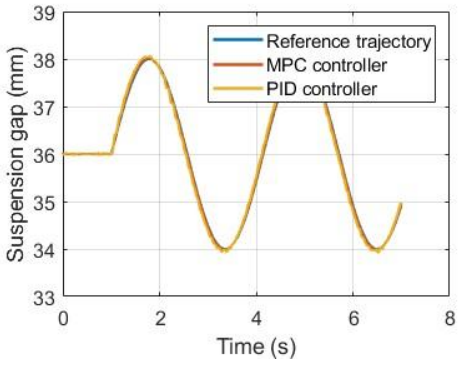

Figure 4.39 Suspension gap response for $A = 0.002\ m\ and\ Freq = 2\ rad/s$ using MPC and PID controllers

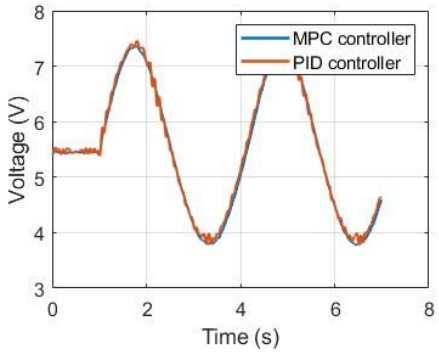

Figure 4.40 Control voltage response for $A = 0.002\ m\ and\ Freq = 2\ rad/s$ using MPC and PID controllers

Figure 4.41 illustrates the suspension gap response for a sinusoidal trajectory with an amplitude $A = 0.003m$, while Figure 4.42 shows the corresponding control voltage for both MPC and PID controllers. The MPC controller tracks the reference trajectory more accurately, with minimal deviations and smoother transitions at the peaks and troughs. The voltage response further supports this, as the MPC controller applies more consistent and smooth voltage

adjustments, oscillating between 5V and 8V, whereas the PID controller shows larger voltage fluctuations, ranging from 4.5V to almost 9V. Compared to previous results with smaller amplitudes, both controllers face greater challenges with the larger amplitude. However, the MPC controller remains more stable and efficient, delivering better performance in terms of both tracking accuracy and control smoothness. The PID controller, on the other hand, becomes more reactive and less effective in handling the larger sinusoidal variations, with more aggressive voltage corrections and larger deviations from the reference trajectory.

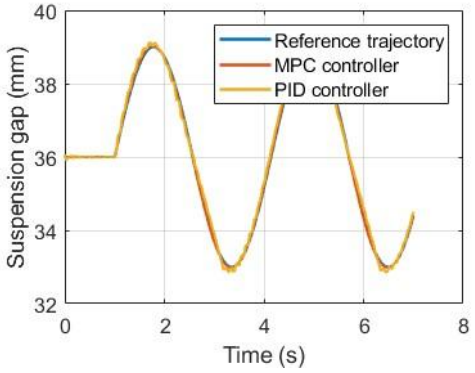

Figure 4.41 Suspension gap response for $A = 0.003\ m\ and\ Freq = 2\ rad/s$ using MPC and PID controllers

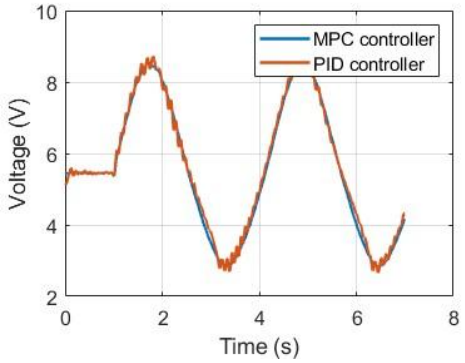

Figure 4.42 Control voltage response for $A = 0.003\ m\ and\ Freq = 2\ rad/s$ using MPC and PID controllers

Figure 4.43 illustrates the suspension gap response for a sinusoidal trajectory with $A = 0.001\ m\ and$ Freq $= 6$ rad/s, while Figure 4.44 shows the corresponding control voltage. The MPC controller maintains close tracking of the reference trajectory with minimal deviation, even at the higher frequency, showing accurate control through the peaks and troughs of the trajectory. In contrast, the PID controller exhibits slightly larger deviations, with more noticeable lags and small overshoots, particularly during transitions. The voltage response

further supports this observation, as the MPC controller applies smoother voltage adjustments, oscillating between 5V and 6.5V, while the PID controller experiences larger fluctuations and aggressive spikes, ranging from 4.5V to nearly 7V. Compared to previous results at lower frequencies, both controllers face increased challenges at the higher frequency of $Freq = 6\,rad/s$, but the MPC controller continues to outperform the PID controller, delivering more precise tracking and smoother control under faster dynamic conditions.

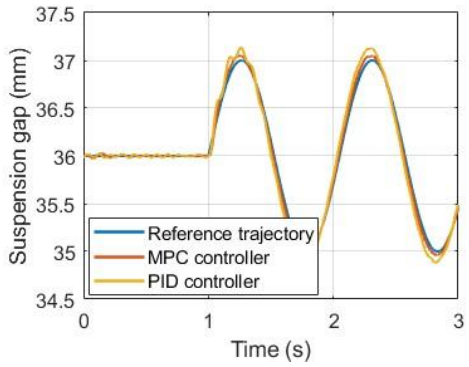

Figure 4.43 Suspension gap response for $A = 0.001\,m\ and\ Freq = 6\,rad/s$ using MPC and PID controllers

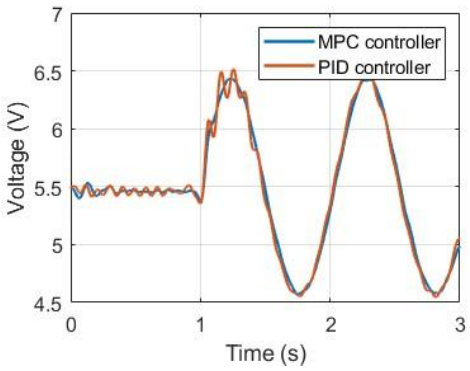

Figure 4.44 Control voltage response for $A = 0.001\,m\ and\ Freq = 6\,rad/s$ using MPC and PID controllers

Figure 4.45 shows the suspension gap response for a sinusoidal trajectory with $A = 0.002\,m\ and\ Freq = 6\,rad/s$, while Figure 4.46 presents the corresponding control voltage. The MPC controller demonstrates precise tracking of the reference trajectory, maintaining tight control with minimal deviations, even at the higher frequency and larger amplitude. The PID controller shows more significant deviations, with noticeable overshoots and undershoots, particularly at the peaks and troughs, indicating difficulties in maintaining precision under these more demanding conditions. The voltage response further highlights the difference, with

the MPC controller applying smooth and consistent voltage adjustments, oscillating between 5V and 7.5V. The PID controller, on the other hand, exhibits more pronounced voltage fluctuations, ranging from 4.5V to nearly 8V, reflecting its more reactive control behavior.

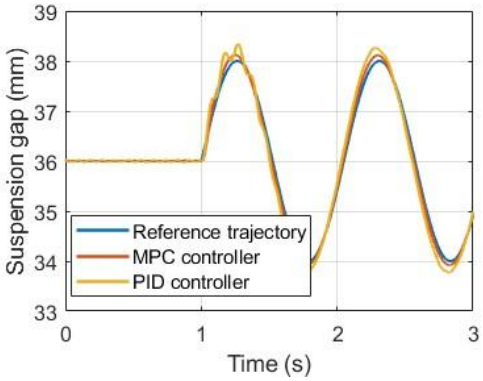

Figure 4.45 Suspension gap response for $A = 0.002\,m\ and\ Freq = 6\,rad/s$ using MPC and PID controllers

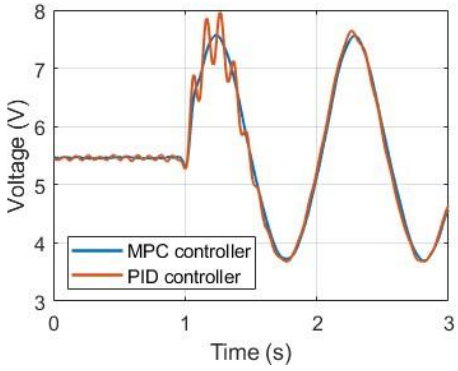

Figure 4.46 Control voltage response for $A = 0.002\,m\ and\ Freq = 6\,rad/s$ using MPC and PID controllers

Figure 4.47 shows the suspension gap response for a sinusoidal trajectory with $A = 0.003\,m\ and\ Freq = 6\,rad/s$, while Figure 4.48 presents the corresponding control voltage. The MPC controller tracks the reference trajectory closely, with minimal deviations even at higher frequency and amplitude, while the PID controller exhibits larger deviations, particularly at the peaks and troughs, where overshoots and undershoots are more pronounced. In terms of voltage control, the MPC controller with output constraints is 0V to 10V maintains a smoother response, oscillating between 5V and 9V, occasionally nearing the 10V system limit but generally staying within operational bounds. In contrast, the PID controller frequently hits the 10V hardware cap, indicating more aggressive control and reduced effectiveness as it relies on maximum output for corrections. The frequent voltage limit constraint hampers the PID

controller's ability to effectively control the suspension gap, leading to larger deviations.

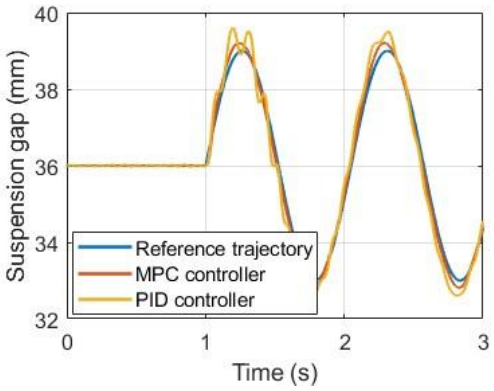

Figure 4.47 Suspension gap response for $A = 0.003\,m\ and\ Freq = 6\,rad/s$ using MPC and PID controllers

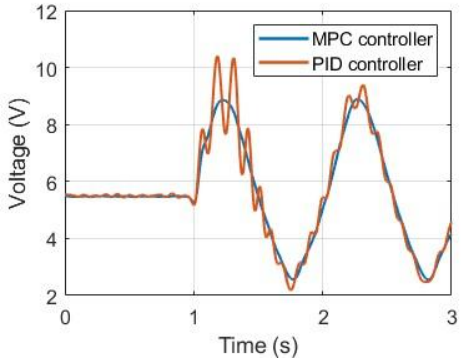

Figure 4.48 Control voltage response for $A = 0.003\,m\ and\ Freq = 6\,rad/s$ using MPC and PID controllers

4.5.4. Impact of Prediction Model Inaccuracy

In the previous section, the MPC controller was implemented with an accurate prediction model, resulting in effective control performance. In this section, the impact of prediction model accuracy on control effectiveness will be examined by comparing the performance when the prediction model is accurate versus when it is inaccurate. The experimental setup remains the steel ball levitation system, with the prediction model using the parameters outlined in Table 4.1 and

Table 4.3. However, to test the effect of model inaccuracy, the mass parameter in the prediction model will differ from the actual mass of the steel ball. This experiment will highlight how mismatches between the prediction model and the real system affect the control results and overall stability.

Figure 4.49 shows the suspension gap response for three different prediction model masses

100g, 83.5g (the actual system mass), and 70g while Figure 4.50 presents the corresponding control voltage. The model with the accurate mass of 83.5g follows the reference trajectory most closely, exhibiting minimal oscillations and a smooth transition from 38.5 mm to 34 mm. The model with an overestimated mass of 100g descends more slowly and experiences more pronounced oscillations before stabilizing, as the system's response is sluggish due to the heavier assumed mass. The model with an underestimated mass of 70g shows the fastest descent but experiences the most severe oscillations and overshoot, indicating that the system overreacts to control inputs because of the lighter mass assumption. In terms of control voltage, the accurate 83.5g model exhibits a smooth voltage response, peaking around 8V and stabilizing near 4V as the system reaches the desired gap. The 100g model displays higher initial voltage peaks and more oscillations as the system struggles to reach stability. The 70g model, similar to its gap response, shows larger voltage fluctuations, reflecting the controller's aggressive corrections in response to the underestimated mass.

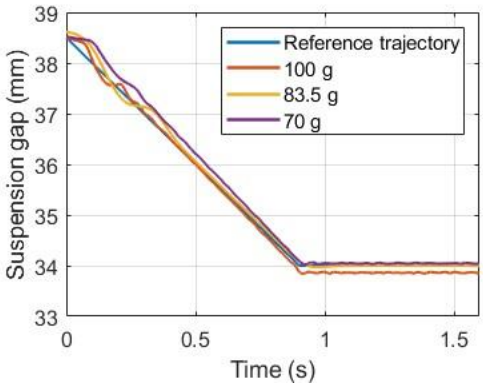

Figure 4.49 Suspension gap response with inaccurate prediction model masses

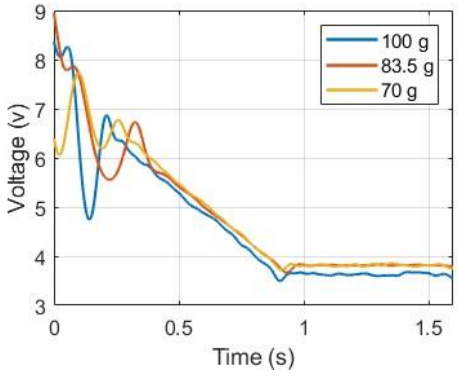

Figure 4.50 Control voltage response with inaccurate prediction model masses

4.6. Conclusions

This chapter thoroughly investigates the application of MPC in a magnetic levitation system. Several aspects of the system were analyzed, including control performance across different prediction horizons, the impact of output constraints, trajectory tracking abilities, sensitivity to measurement noise, and the effects of mismatches between the predictive model and the actual system.

The simulations conducted throughout this chapter highlight the effectiveness of MPC in stabilizing the suspension gap of a magnetic levitation system under various conditions, including different prediction horizons, control output constraints, mass mismatches, and measurement noise.

Analysis of different prediction horizons: The simulation results demonstrate that the MPC controller performs efficiently across different prediction horizons. Shorter horizons, such as 5 and 10, result in larger overshoots and longer stabilization times, while longer horizons, such as 30 and 40, provide smoother, more stable control. The system's response improves as the prediction horizon increases, with minimal overshoot and faster stabilization at a prediction horizon of 40, balancing both accuracy and computational demands. The longer horizons reduce aggressive control actions, leading to more consistent current usage and efficient control of the suspension gap.

Analysis of MPC controller output constraints: Varying the output current constraints from 45 A to 60 A has a minimal impact on the overall levitation performance. While there are slight differences in the current values at the beginning of the levitation process, the suspension gap

stabilizes consistently across all constraint scenarios. This indicates that the MPC controller can adapt effectively to different current limits while maintaining stable suspension gap control, demonstrating its flexibility in handling practical system constraints.

Trajectory tracking simulation: The MPC controller outperforms the PID controller in tracking dynamic target references across different train speeds. At lower speeds, both controllers perform similarly, but as the speed increases, the PID controller struggles to maintain the desired gap, resulting in larger errors and slower recovery times. The MPC controller consistently maintains smaller errors and faster convergence to the target gap, especially at higher speeds, highlighting its superior capability in handling dynamic viaduct displacements during high-speed maglev train operations.

Measurement noise impact simulation: When measurement noise is introduced, the MPC controller proves to be more robust than the PID controller. In low-noise scenarios, MPC maintains stability with minor oscillations, while PID shows larger fluctuations. Under higher noise levels, the PID controller becomes unstable and diverges, while MPC continues to track the target gap with only moderate oscillations. This demonstrates MPC’s robustness in handling sensor noise and its ability to maintain control accuracy even under noisy conditions.

Impact of mass mismatch on MPC control: The MPC controller shows good adaptability when the mass of the controlled object deviates from the predictive model's assumed mass. While the lighter object (700kg) exhibits more oscillations and a larger undershoot, and the heavier object (800kg) shows slight overshoot, the system is able to stabilize in both cases. The nominal case (750kg) matches the predictive model and achieves the most stable control

performance. This emphasizes the importance of accurately modeling the system's mass in the predictive model for optimal control.

The simulations consistently demonstrate that MPC is a robust and highly effective control strategy for magnetic levitation systems. It significantly outperforms traditional PID control, especially in scenarios with dynamic conditions, disturbances, or system uncertainties. However, the results also highlight the importance of having an accurate predictive model. When the predictive model in the MPC controller does not match the actual system dynamics, such as when the mass of the controlled object differs from the assumed model mass, control performance is impacted. For example, a lighter object (700kg) leads to increased oscillations and undershoot, while a heavier object (800kg) results in overshoot. Although MPC can still stabilize the system, the transient performance is less optimal compared to the case where the mass matches the predictive model (750kg). This underlines the critical need for accurate modeling in MPC to achieve the best possible control outcomes.

Despite this, MPC's general advantages remain clear across all tested conditions. It excels at managing complex systems, handling multiple constraints, and adjusting to dynamic changes in real-time. The ability of MPC to predict future system states and optimize control actions makes it highly adaptable and robust, even when faced with disturbances like sensor noise or mass variations. As demonstrated in the trajectory tracking and measurement noise simulations, MPC maintains a higher level of precision and stability compared to PID control, ensuring minimal deviations from the desired performance.

In Section 4.5.2, the MPC and PID controllers were compared in a levitation experiment, where the steel ball was raised from a resting position to a stable height. The MPC controller demonstrated smoother control with fewer oscillations and faster stabilization compared to the PID controller, which exhibited larger overshoots and slower response times. This highlighted the MPC controller's ability to maintain stability effectively during the levitation process.

In Section 4.5.3, the controllers were tested in a trajectory-following experiment where the steel ball tracked a sinusoidal path. The MPC controller outperformed the PID controller, showing more accurate tracking with minimal deviation from the reference trajectory. The PID controller experienced larger oscillations and more reactive voltage fluctuations. The MPC's predictive capabilities allowed it to anticipate changes more effectively, resulting in smoother control performance and better stability overall.

In Section 4.5.4, the limitations of the MPC controller became apparent when the accuracy of the prediction model was altered. The experiment examined the effects of both overestimated and underestimated mass values in the prediction model. When the prediction model's mass deviated from the actual system mass (83.5g), the MPC controller's performance deteriorated. An overestimated mass (100g) resulted in slower response times and increased oscillations, while an underestimated mass (70g) caused faster descent but with greater instability and more severe oscillations. This sensitivity to model inaccuracies highlighted a key limitation of MPC: its reliance on the accuracy of the prediction model. When the model is inaccurate, the control effectiveness is significantly compromised. Even though the MPC controller still outperformed the PID controller in these cases, its performance was far from optimal, showing that the

advantages of MPC can be diminished when model mismatches occur.

In conclusion, while MPC provides clear benefits over traditional control methods like PID, particularly in terms of adaptability, precision, and robustness, it is also highly sensitive to the accuracy of its predictive model. The design and integration of the Kalman filter observer significantly enhanced the system's resilience to measurement noise. However, further improvements are needed to address model inaccuracies, especially in systems like magnetic levitation trains where mass can vary frequently. This insight sets the stage for exploring adaptive or robust MPC techniques that can better handle uncertainties in the system model, thereby enhancing its applicability in real-world magnetic levitation systems and other complex control environments.

The contributions of this chapter include:

1) Problem-specific formulation of linear MPC for EMS maglev suspension control:

A linearized model was derived from the nonlinear electromagnetic suspension dynamics, considering mass, coil parameters, and operating point. The resulting MPC framework was tailored to address system-specific challenges such as soft constraints on current, limited prediction horizon, and actuator saturation.

2) Kalman filter design for noisy measurements in maglev suspension control:

Rather than using ideal or noise-free data, this chapter incorporates band-limited measurement noise, reflecting real sensor conditions. The Kalman filter design is specifically tuned and validated for this EMS setup, enabling reliable state estimation for feedback control.

3) Comprehensive performance evaluation:

The chapter provides simulation results demonstrating MPC's ability to achieve fast convergence, good tracking, and constraint handling. A detailed comparison with PID

controllers under both ideal and noisy conditions was carried out, highlighting MPC's superior robustness and dynamic response.

4) Practical controller configuration and tuning:

The design choices in prediction horizon, weighting matrices, and constraints were not arbitrarily selected but rather optimized through parameter sweeps, offering engineering guidance for future implementation in full-scale systems.

5) Foundation for adaptive MPC development:

This chapter serves as a critical foundation for the AMPC framework proposed in Chapter 5. The observed sensitivity of MPC performance to model mismatch justifies the need for an adaptive approach, thus creating a clear progression in the research logic.

Chapter 5. Adaptive Model Predictive Control for Maglev Suspension System

Building upon the findings from the previous chapter, where the limitations of MPC were highlighted, this chapter introduces AMPC based on the Autoregressive with Exogenous Variables (ARX) model to address the challenges posed by model inaccuracies. While the previous experiments showed the sensitivity of MPC to an accurate prediction model, AMPC offers a solution by dynamically updating the model parameters to reflect changes in the system. This chapter will first detail the ARX-based approach for adaptive MPC, followed by simulations and experimental validation to assess the effectiveness of AMPC in handling model uncertainties and disturbances.

5.1. Introduction to ARX-based AMPC

AMPC is an advanced form of MPC that adapts the prediction model in real time to handle changes in system dynamics [143-147]. Unlike traditional MPC, which relies on a fixed model, AMPC continuously updates the model parameters based on real-time data, making it more robust in environments with varying conditions such as load changes or system uncertainties. One common approach to achieve this is through the ARX model, which uses system input and output data to refine the prediction model [148, 149]. This dynamic adjustment improves control accuracy and ensures better performance in systems where a static model may lead to degraded control.

AMPC shares a similar structure with traditional MPC in terms of workflow, but with a key difference in how the prediction model is handled. Both AMPC and MPC use the following

general process: prediction of future states, optimization of control actions over a finite time horizon, and the application of the first control action to the system. However, the main distinction between the two lies in the real-time model adaptation in AMPC, which is absent in standard MPC. The structure and workflow of AMPC follow a clear and logical process:

(1). **System (with Input/Output)**: The process begins with the system, which is being controlled. The system receives input signals (such as voltage or current) and outputs the corresponding system responses (like position or speed).

(2). **Real-time Data Collection:** The system's input and output data are continuously collected in real-time. This data forms the basis for updating the control model and ensures that the control actions reflect the current state of the system.

(3). **ARX Model Update:** Using the collected data, the prediction model is updated using an ARX model. This step ensures that the prediction model reflects any changes in the system dynamics, such as variations in mass or external disturbances.

(4). **Prediction and Optimization:** With the updated ARX model, the AMPC controller predicts future system states over a defined time horizon. It then solves an optimization problem to find the control actions that will minimize the cost function, such as minimizing errors or reducing energy usage, while respecting system constraints.

(5). **Control Action:** Once the optimal control actions are calculated, the first control action in the sequence is applied to the system. This allows for real-time adjustments to the system's inputs to achieve the desired output.

(6). **Feedback Loop:** The process continues in a feedback loop. The system's response to the

applied control action is measured and fed back into the process, ensuring that the model and control actions continuously adapt to any changes in the system.

5.2. ARX Based Adaptive MPC Controller Design

5.2.1. ARX Model

The ARX model is a widely used linear model in system identification and control systems. The ARX model describes the relationship between the inputs and outputs of a dynamic system using a combination of past system outputs (autoregressive part) and past/current inputs (exogenous input part) [150-154]. It is commonly used for estimating models from input-output data, especially in applications like AMPC. The maglev control system is inherently nonlinear, particularly due to the nonlinear relationship between electromagnetic force and the suspension gap. However, it can be linearized around the operating point to simplify the control design process like described in Section 4.2.1. Once the system is linearized, the ARX model can be used to identify and capture the dynamics of this linearized model.

The general form of an ARX model is given by the equation:

$$y_t + a_1 y_{t-1} + a_2 y_{t-2} + \cdots + a_n y_{t-n} = b_1 u_{t-1} + b_2 u_{t-2} + \cdots + b_m u_{t-m} + e(t) \quad (5.1)$$

This can be rewritten as:

$$y_t = -a_1 y_{t-1} - a_2 y_{t-2} - \cdots - a_n y_{t-n} + b_1 u_{t-1} + b_2 u_{t-2} + \cdots + b_m u_{t-m} + e(t) \quad (5.2)$$

Where $y(t)$ is the system output at time t, $u(t)$ is the system input at time t, a_i and b_i are the model parameters, representing the dynamic relationship between inputs and outputs, and $e(t)$ is the error term accounting for noise and disturbances. n is the number of past outputs considered in the model. This means the ARX model will use the past n outputs to predict the

current output. m is the number of past inputs considered in the model. This means the ARX model will use the past m inputs to predict the current output.

The ARX model can be written in a more compact matrix form for estimation purposes:

$$\mathrm{y}_t = \varphi^T(t)\theta + e(t) \tag{5.3}$$

Where: $\varphi(t)$ is the regression vector containing past outputs and inputs:

$$\boldsymbol{\varphi}(t) = \begin{bmatrix} -\mathrm{y}_{t-1} \\ -\mathrm{y}_{t-2} \\ \vdots \\ -\mathrm{y}_{t-n} \\ u_{t-1} \\ u_{t-2} \\ \vdots \\ u_{t-m} \end{bmatrix} \tag{5.4}$$

θ is the parameter vector containing the unknown coefficients:

$$\boldsymbol{\theta} = \begin{bmatrix} a_1 \\ a_2 \\ \vdots \\ a_n \\ b_1 \\ b_2 \\ \vdots \\ b_m \end{bmatrix} \tag{5.5}$$

This matrix form simplifies the problem of identifying the system's parameters $\boldsymbol{\theta}$.

To estimate the unknown parameter vector $\boldsymbol{\theta}$, Least Squares Estimation method is used. The goal is to minimize the sum of squared errors between the actual output and the model predicted output.

The sum of squared errors (cost function) is:

$$J(\theta) = \sum_{t=1}^{T} (\mathrm{y}_t - \varphi^T(t)\theta)^2 \tag{5.6}$$

To minimize this, the below least squares equation will be solved. The equation gives the optimal estimate $\widehat{\boldsymbol{\theta}}$ for the system parameters based on the collected data:

$$\widehat{\boldsymbol{\theta}} = (\boldsymbol{\Phi}^T\boldsymbol{\Phi})^{-1}\boldsymbol{\Phi}^T\boldsymbol{Y} \tag{5.7}$$

$$\boldsymbol{\Phi} = \begin{bmatrix} \varphi^T(1) \\ \varphi^T(2) \\ \vdots \\ \varphi^T(T) \end{bmatrix} \tag{5.8}$$

$$\boldsymbol{Y} = \begin{bmatrix} \mathrm{y}_1 \\ \mathrm{y}_2 \\ \vdots \\ \mathrm{y}_T \end{bmatrix} \tag{5.9}$$

Where $\widehat{\boldsymbol{\theta}}$ is the estimated parameter vector, $\boldsymbol{\Phi}$ is the matrix of regression vectors, $\boldsymbol{Y}$is the vector of observed values.

Once the parameter vector $\boldsymbol{\theta}$ has been estimated, it can be used to update the ARX model in real-time. This process involves continuously collecting new data and re-estimating the parameters at each time step to reflect the changing system dynamics. The updated model at time step t can be expressed as:

$$\mathrm{y}_t = -\hat{a}_1\mathrm{y}_{t-1} - \hat{a}_2\mathrm{y}_{t-2} - \cdots - \hat{a}_n\mathrm{y}_{t-n} + \hat{b}_1u_{t-1} + \hat{b}_2u_{t-2} + \cdots + \hat{b}_mu_{t-m} \tag{5.10}$$

Where $\hat{a}_i$ and $\hat{b}_i$ are the newly estimated parameters at time t.

Once the ARX model is updated, it is important to validate the model by comparing the predicted output $\hat{y}(t)$ with the actual system output $y(t)$ for data not used in the parameter estimation. This can be done by calculating the prediction error:

$$e(t) = \mathrm{y}_t - \widehat{y_t} \tag{5.11}$$

If the error is small, the ARX model is considered valid. If not, the model structure (order n and m) or the parameter estimation method may need to be revised.

The ARX model can be converted into state-space form:

$$A = \begin{bmatrix} -\hat{a}_1 & -\hat{a}_2 & \dots & -\hat{a}_n \\ 1 & 0 & \dots & 0 \\ 0 & 1 & \dots & 0 \\ \vdots & \vdots & \ddots & 0 \end{bmatrix} \tag{5.12}$$

$$B = \begin{bmatrix} \hat{b}_1 & \hat{b}_2 & \dots & \hat{b}_m \\ 0 & 0 & \dots & 0 \\ \vdots & \vdots & \ddots & \vdots \\ 0 & 0 & \dots & 0 \end{bmatrix}$$

$$C = [1\ 0 \dots 0]$$

The ARX model update process can be summarized as:

(1). Data Collection: Collect input-output data from the system.

(2). Model Structure: Set up the ARX model with chosen orders m and n.

(3). Regression Vector: Form the regression vector $\varphi(t)$ using past inputs and outputs.

(4). Parameter Estimation: Use the least squares method to estimate the parameter vector θ.

(5). Model Update: Continuously update the ARX model with new data, adjusting the parameters θ in real-time.

(6). Validation: Validate the updated model by comparing predicted and actual outputs.

(7). Conversion to State-Space: Convert the ARX model into state-space.

5.2.2. Integration of ARX Model with Adaptive MPC

5.2.2.1.Nominal operating point updating

In traditional MPC, the nominal operating point is where the plant model applies, typically when the system is linearized around this condition to create a linear time-invariant (LTI) approximation[155]. Following the ARX model updating process, it is crucial to incorporate the nominal operating point into the AMPC framework [156, 157]. The nominal operating point, representing the steady-state values for system inputs and outputs, serves as the reference

around which the ARX-based model is linearized. The controller predicts future system states over a horizon based on deviations from the nominal operating point. If the nominal values are not updated to reflect the actual operating conditions, the deviations calculated by the controller will be incorrect, leading to inaccurate predictions and suboptimal control actions.

In AMPC, as the system changes over time, the nominal operating point needs to be updated to reflect the changing plant model. The updated model is expressed in terms of deviations from the nominal conditions, ensuring control accuracy despite varying dynamics or external influences:

$$\Delta x_{t+1} = A(x_t - \bar{x}) + B(u_t - \overline{u_t}) \tag{5.13}$$

$$\Delta \mathrm{y}_t = C(x_t - \bar{x}) + D(u_t - \overline{u_t}) \tag{5.14}$$

Where Δx_{t+1} is the deviation of the next state from its nominal value, A is the state transition matrix, B is the input-to-state matrix C is the state-to-output matrix, D is the input-to-output matrix, x_t and $u(t)$ are the actual system states and inputs time t, $\bar{x}$ and $\overline{u_t}$ represent the nominal (steady state) values and $\Delta \mathrm{y}_t$ is the deviation of the output from its nominal value.

5.2.2.2.Kalman Filter Adaptation in ARX-Based AMPC

In traditional MPC, the Kalman filter is used to estimate the states of the system, handling noise in the measurements by correcting the predicted states based on observed outputs. The model parameters (such as A, B and C) are fixed once the system is linearized around a nominal operating point, which makes the Kalman filter a static estimator in traditional MPC. In this case, the Kalman gain is computed once and remains constant during operation by Equation (4.52). In ARX model based AMPC, the Kalman filter needs to be dynamic. This is because

AMPC must update the system's model parameters, including the state transition matrix A_t and the measurement matrix C_t, in real time as the plant model adapts to the system's evolving dynamics. While A_t does not directly appear in the Kalman gain Equation (4.52), it does influence the state prediction and the covariance matrix prediction step, which subsequently affects the Kalman gain computation. The covariance prediction is influenced by the process model (including A_t) as follows:

$$\boldsymbol{P_t^- = A_t P_{t-1} A_t^T + Q} \tag{5.15}$$

The optimal Kalman gain can then be derived as

$$\boldsymbol{K_t^* = \frac{P_t^- H C_t^T}{C_t P_t^- C_t^T + R_c}} \tag{5.16}$$

The covariance matrix $\boldsymbol{P_t}$ can be represented as

$$\boldsymbol{P_t = (I - K_t C_t) P_t^-} \tag{5.17}$$

5.2.3. Prediction Model and Cost Function in ARX-Based AMPC

The control system under consideration is the suspension unit in Section 3.2. The prediction model employed in the ARX-based AMPC is initially the linearized model from Section 4.2.1. This model was derived by linearizing the system dynamics around a nominal operating point to form a state-space representation suitable for MPC. However, in AMPC, the parameters of the state-space equations—such as the state transition matrix *A* and input matrix *B*—are time-varying. These parameters are continuously updated based on the real-time data from the ARX model, allowing the controller to adapt to changes in the system's dynamics.

In AMPC, the cost function is generally similar to that of traditional MPC, as it still aims to minimize tracking errors and control effort over a prediction horizon. However, the key

difference in AMPC lies in the adaptation of the predictive model, which can lead to dynamic changes in the weighting matrices or model parameters used in the cost function. Both MPC and AMPC use a quadratic cost function to penalize deviations between the predicted output and the reference trajectory as well as large control efforts. The general form of the cost function in both is Equation (4.15).

5.3. Simulation Results of Adaptive MPC

In the simulation study, the basic control object is the single-point suspension system described in Section 3.2, a simplified model of an EMS unit. The control time step is set to 0.001 seconds. Initially, both MPC and AMPC use the same linearized prediction model from Section 4.2.1, where the nonlinear system is linearized around a nominal operating point with a suspension gap of 8 mm. As the simulation progresses, the prediction model in AMPC is continually updated based on real-time data, while traditional MPC retains its initial linearized model. This ensures that AMPC can adapt to any changes in system dynamics, providing a more robust control response under varying conditions.

The specific parameters used for the AMPC controller are outlined in Table 5.1. The prediction horizon for the simulation is 5 steps, while the control horizon is 1 step. The trajectory reference is set to 8 mm, meaning the target suspension gap remains at this nominal point. The output constraints restrict the control input (current) to a range of 0 to 60 A, ensuring that the control actions remain within the physical limits of the EMS unit.

Table 5.1 Parameters of the AMPC controller for the EMS unit

Parameters	Specification
Prediction horizon	5
Control horizon	1
Output constraints	Minimum 0 A; Maximum 60 A
Trajectory reference	8 mm
Input weight	0
Output weight	1
Control time step	0.001s
Nominal point of EMS unit	Suspension gap at 8 mm
Nominal input of EMS unit	10.84 A
Nominal output of EMS unit	8 mm

5.3.1. Comparison of MPC and AMPC Performance Under Conditions of Levitation and Steady-State Suspension

The simulation results for the single-point suspension system indicate that when the system mass is accurately modeled at 750 kg, both MPC and AMPC demonstrate similar performance in terms of suspension gap control. As illustrated in Figure 5.1 and Figure 5.2, both controllers bring the suspension gap from an initial 18 mm down to the target 8 mm efficiently, with comparable response times and minimal deviation. The steady-state behavior of both MPC and AMPC in this nominal case shows negligible error, and the required current stabilizes around 10.84 A for both controllers. This indicates that under ideal model conditions, AMPC's adaptive features do not provide a significant advantage, as the static prediction model in MPC is already well-suited to the system.

When a model mismatch is introduced with an actual system mass of 650 kg, AMPC exhibits superior control precision by reducing steady-state error compared to MPC. Figure 5.3 and Figure 5.4 demonstrate that MPC, with its fixed prediction model, shows a noticeable steady-state error, failing to bring the suspension gap precisely to the 8 mm target. AMPC, however, adapts to the lighter mass, achieving a suspension gap much closer to the desired reference and thereby reducing steady-state error.

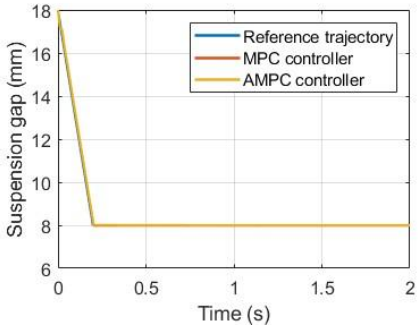

Figure 5.1 Suspension gap response for 750 kg mass with MPC and AMPC

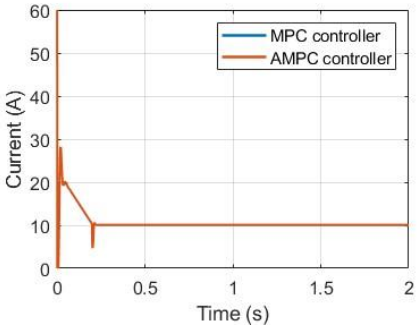

Figure 5.2 Control current for 750 kg mass with MPC and AMPC

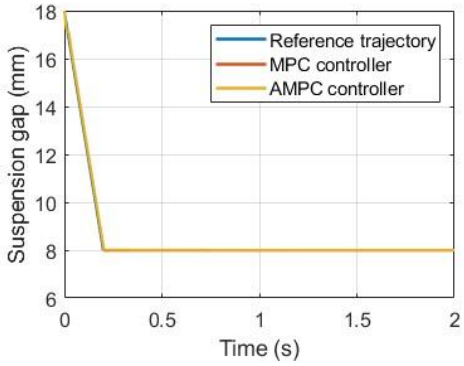

Figure 5.3 Suspension gap response for 650 kg mass with MPC and AMPC prediction

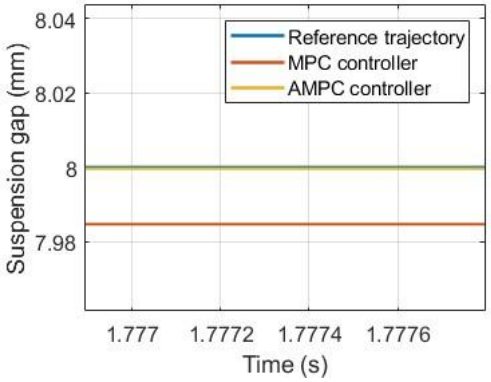

Figure 5.4 Detailed view of steady-state suspension gap for 650 kg mass with MPC

model mismatch and AMPC prediction model mismatch

Figure 5.5 to Figure 5.6 illustrate the results for actual system masses of 850 kg and 1000 kg, respectively. In Figure 5.5 and Figure 5.6, the suspension gap response for a system mass of 850 kg shows both controllers responding to the reference trajectory with comparable initial behavior. However, a clear distinction in steady-state performance is observed. AMPC is able to closely track the reference suspension gap of 8 mm with minimal steady-state error, demonstrating its adaptive capabilities in mitigating the impact of the model mismatch. MPC, on the other hand, exhibits a slight offset above the target gap, indicating its limited ability to adjust under model mismatch conditions.

When the actual mass of the system increases to 1000 kg, the model mismatch becomes more pronounced. Figure 5.7 and Figure 5.8 illustrate the suspension gap response under these conditions. The results reveal that AMPC continues to provide a response that closely follows the reference trajectory. MPC, however, exhibits a more significant steady-state error, struggling to accurately track the target gap due to the larger discrepancy between the prediction model and the actual system.

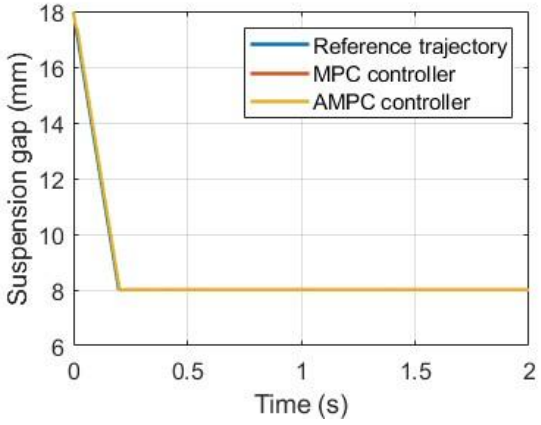

Figure 5.5 Suspension gap response for 850 kg mass with MPC and AMPC prediction model mismatch

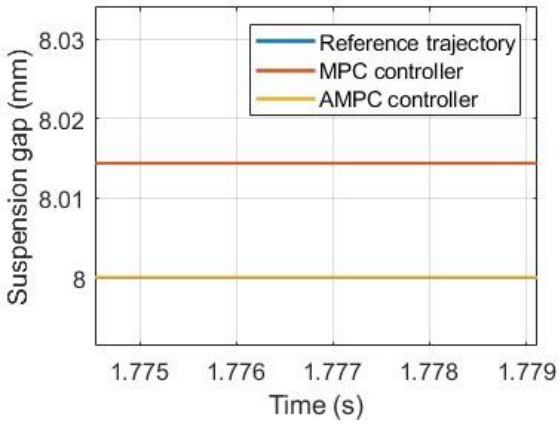

Figure 5.6 Detailed view of steady-state suspension gap for 850 kg mass with MPC and AMPC prediction model mismatch

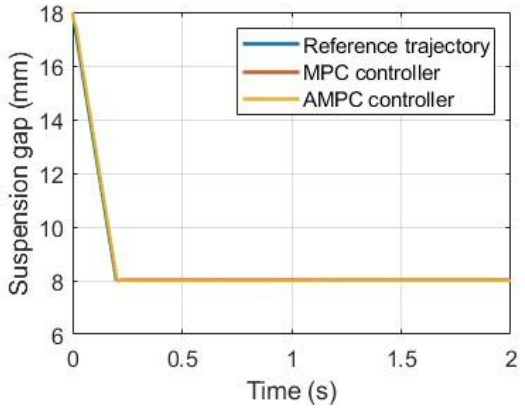

Figure 5.7 Suspension gap response for 1000 kg mass with MPC and AMPC prediction model mismatch

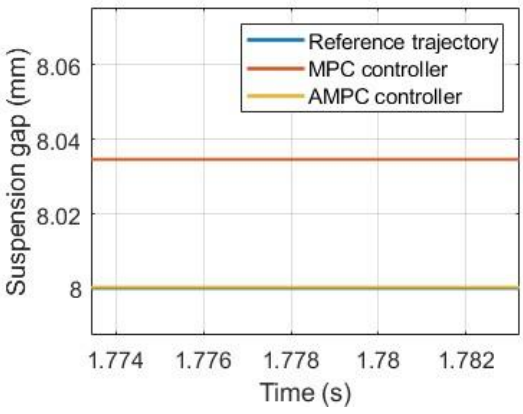

Figure 5.8 Detailed view of steady-state suspension gap for 1000 kg mass with MPC and AMPC prediction model mismatch

5.3.2. Trajectory Tracking

Similar to the analysis in Section 4.4.3, this simulation examines the trajectory tracking capabilities of the AMPC and MPC controllers for the magnetic levitation suspension unit. To

maintain a stable suspension gap of 8 mm under these dynamic conditions, both controllers are tasked with following a sinusoidal trajectory that models the vertical movement of a 25-meter viaduct span. The target trajectory is defined by the function: $y = 1.7\sin(\text{frequency} \cdot t) + 8$. Four specific frequencies were selected, corresponding to speeds of 40 km/h, 80 km/h, 120 km/h, and 160 km/h as the train crosses a single 25-meter viaduct span. These frequencies—1.4 rad/s, 2.79 rad/s, 4.19 rad/s, and 5.59 rad/s—serve to test the controllers' performance across a range of operational conditions. The actual controlled system has a mass of 1000 kg, whereas the initial prediction model for both MPC and AMPC assumes a nominal mass of 750 kg. This mismatch allows for the evaluation of each controller's capacity to handle discrepancies between the model and actual conditions, particularly in terms of stability and accuracy.

Building on the simulated conditions, Figure 5.9 and Figure 5.10 compare the tracking performance of MPC and AMPC controllers for a 1000 kg system across different speeds. In Figure 5.10, which shows the time series of the suspension gap, both controllers initially follow the sinusoidal reference trajectory closely at lower speeds (40 km/h and 80 km/h). However, as speed increases to 120 km/h and 160 km/h, MPC begins to show more noticeable lag and overshoot, particularly at the peaks and troughs of the trajectory. This deterioration in tracking accuracy can be attributed to MPC's reliance on a static prediction model, which becomes less representative of the actual system as dynamic demands increase.

In contrast, AMPC, with its adaptive prediction model, maintains tighter alignment with the reference trajectory, effectively minimizing deviations. Figure 5.10 highlights this difference

through the error between the actual and reference suspension gaps. At lower speeds, both controllers exhibit small tracking errors, with AMPC achieving slightly better precision. As speed increases, MPC's error magnitude grows significantly, reaching up to 0.05 mm at 160 km/h. The increased error in MPC reflects the limitations of its unchanging model in adapting to high-speed changes in system dynamics.

AMPC's lower error profile, particularly at higher speeds, is a result of its ability to continuously update the prediction model to reflect the system's current state more accurately. By incorporating real-time updates, AMPC's model remains more representative of the actual dynamics, leading to more precise control actions and reduced overall error. This adaptability is essential for maintaining precise and responsive control, especially in applications like high-speed maglev systems where model accuracy directly impacts system stability and performance.

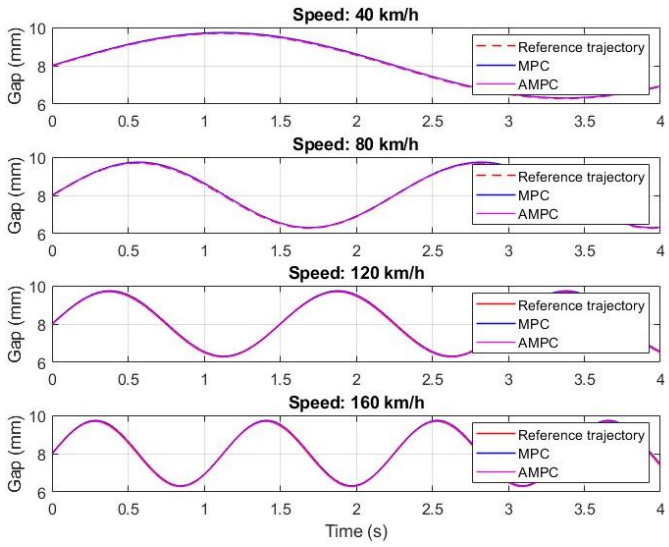

Figure 5.9 Comparison of suspension gap tracking between MPC and AMPC controller at different train speeds

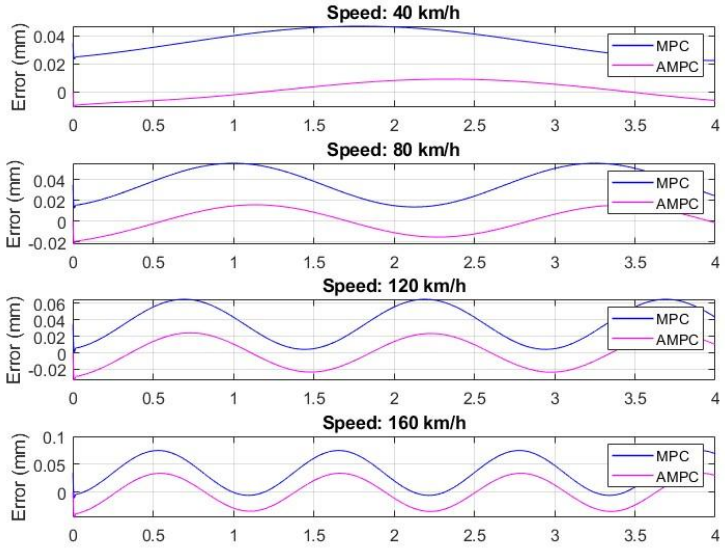

Figure 5.10 MPC and AMPC error time series from simulation at different speeds

5.3.3. Impact of Measurement Noise

In this section, measurement noise is introduced to assess the performance of the MPC and AMPC controllers under conditions that closely resemble real-world scenarios. This simulation follows the methodology in Section 4.4.4, where Gaussian noise is applied to the suspension gap output to emulate sensor inaccuracies. The noise is generated in real-time using Simulink's Band-Limited White Noise block, designed to introduce zero-mean noise with specific variance and bandwidth parameters. This setup realistically reflects the effects of sensor imperfections on the control system, allowing for an analysis of how well MPC and AMPC handle noisy measurements.

Figure 5.11 displays the noise profile, which fluctuates around zero with a maximum amplitude of approximately ±0.1 mm. This noise mimics the random fluctuations typically found in practical sensor readings. Figure 5.12 shows the suspension gap maintained by the MPC and

AMPC controllers in the presence of this noise, with both controllers attempting to stabilize the gap at the target of 8 mm.

The results in Figure 5.12 indicate that both MPC and AMPC controllers perform similarly in managing the suspension gap amidst measurement noise. Both controllers exhibit comparable levels of deviation from the target gap, with fluctuations around ±0.15 mm. This outcome suggests that, under these noise conditions, the adaptive nature of AMPC does not yield a significant advantage over the traditional MPC.

In Figure 5.13, the AMPC and MPC controllers are tested for their ability to track a sinusoidal trajectory under the influence of measurement noise, with a target speed corresponding to 160 km/h. The measurement noise has an amplitude of ±0.1 mm, as previously described. The results show that both controllers perform similarly, effectively following the reference trajectory despite the presence of noise. The suspension gap remains close to the desired trajectory for both controllers, with only minor variations observed due to the noise. Both MPC and AMPC demonstrate resilience in maintaining stable tracking and do not exhibit significant differences in their responses.

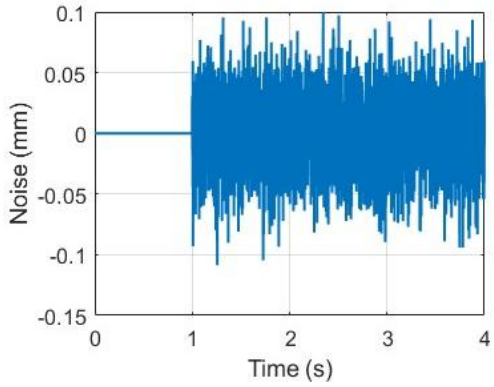

Figure 5.11 Measurement noise

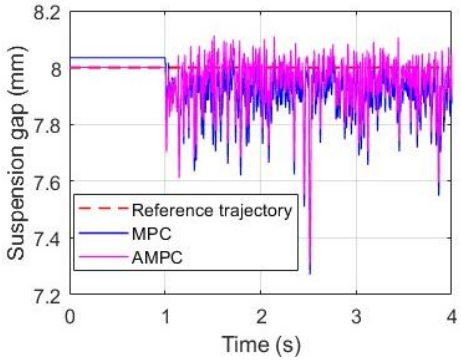

Figure 5.12 Steady-state suspension performance under measurement noise

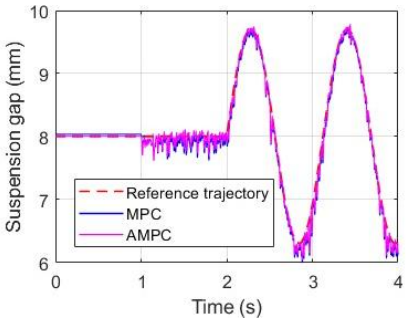

Figure 5.13 Tracking performance with measurement noise

5.4. Experiments

This chapter presents the experimental validation of the MPC and AMPC control strategies, using the magnetic levitation apparatus described in Section 4.5. Building upon the simulation studies, these experiments aim to assess the real-world effectiveness of the controllers within the magnetic levitation system, which includes an electromagnet, steel ball, photoelectric position sensor, power amplifier, and control modules configured for precise suspension control.

The experimental setup is designed around two primary tasks that replicate key aspects of the simulations. The first task, lift-off, examines the controllers' ability to stabilize the steel ball from an initial rest position to the desired suspension gap, providing insight into each controller's effectiveness in achieving stable levitation. The second task, trajectory tracking, evaluates the controllers' performance in dynamic conditions, where the suspension gap must follow a sinusoidal reference path.

5.4.1. Levitation Process Test

This section examines the performance of the MPC and AMPC controllers in the levitation process using the magnetic suspension equipment described in Section 4.5. The control objective is to achieve stable levitation of a steel ball with a mass of 83.5 g and a diameter of 39.2 mm. To assess the controllers' robustness to model inaccuracies, the initial prediction model in both MPC and AMPC is intentionally set with an incorrect mass—specifically, values of 70 g and 100 g—rather than the actual 83.5 g. This controlled model mismatch allows for a comparative analysis of each controller's capacity to handle deviations from the actual system parameters. In this test, the controllers must bring the steel ball from an initial rest position to a target suspension gap and stabilize it, despite the prediction model's mass deviation. By comparing the stabilization time, control effort, and error magnitudes, this experiment provides insight into how MPC and AMPC adjust to the incorrect model and their effectiveness in achieving steady-state control under these conditions.

Table 5.2 presents the key parameters for both MPC and AMPC controllers, which share identical configurations across all listed parameters.

Table 5.2 Parameters of the MPC and AMPC controllers for the steel ball suspension system

Parameters	MPC	AMPC
Prediction horizon	5	5
Control horizon	1	1
Output constraints	Minimum 0 V Maximum 10 V	Minimum 0 V Maximum 10 V
Trajectory reference	8 mm	8 mm
Input weight	0	0
Output weight	1	1
Control time step	0.002s	0.002s
Nominal point of steel ball	Suspension gap at 34 mm	Suspension gap at 34 mm

Figure 5.14 to Figure 5.16 illustrate the levitation performance of both MPC and AMPC controllers with initial model mass values of 70g and 100g, while the actual steel ball mass is 83.5g. Figure 5.14 shows the suspension gap, defined as the distance between the ball's center and the lower edge of the electromagnet. Figure 5.15 presents the output voltage of the controllers, and Figure 5.16 depicts the error between the actual suspension gap and the target value. In Figure 5.14, the AMPC controllers (initialized with model masses of both 70g and 100g) successfully bring the steel ball to the target levitation gap of 34mm within 1 second, achieving this with minimal overshoot. The MPC controllers, in comparison, also reach the desired levitation gap but exhibit slightly larger deviations initially. Specifically, the MPC controller with the 100g model mass overshoots by approximately 0.3mm, whereas the 70g model mass setup overshoots by about 0.25mm. Figure 5.15 shows the controller output voltages. Initially, both MPC and AMPC controllers display high voltage peaks to achieve rapid

positioning. The MPC controllers reach peak voltages of around 9V, whereas the AMPC controllers exhibit slightly lower peaks, around 8.5V. Over time, a key difference emerges in the final stabilized voltages: AMPC controllers settle near a stable voltage of around 3.8V, while MPC controllers, especially with the 100g model, stabilize at a slightly higher voltage around 3.9V. This difference in final voltage is due to AMPC's ability to continuously adapt to the actual mass of the system, thus optimizing the control effort required for steady suspension. In contrast, the MPC controllers are less efficient, resulting in a slightly higher steady-state voltage due to the initial model inaccuracy. Figure 5.16, the error plot further illustrates the advantage of AMPC. The AMPC controllers maintain near-zero steady-state error, while the MPC controllers exhibit small but persistent errors. The MPC controller with the 100g model mass shows a positive error of about 0.2mm, and the 70g model displays a minor negative error of approximately -0.1mm. This indicates that AMPC's adaptive capabilities allow it to maintain closer alignment with the reference trajectory, minimizing errors resulting from model discrepancies.

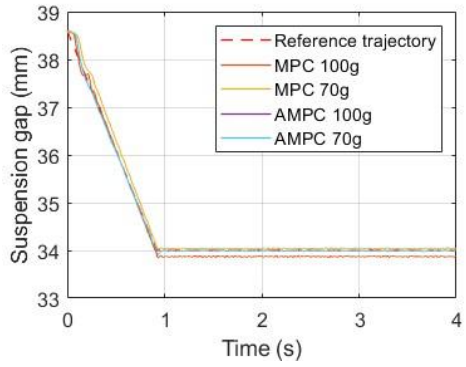

Figure 5.14 Suspension gap during levitation process for inaccurate prediction model

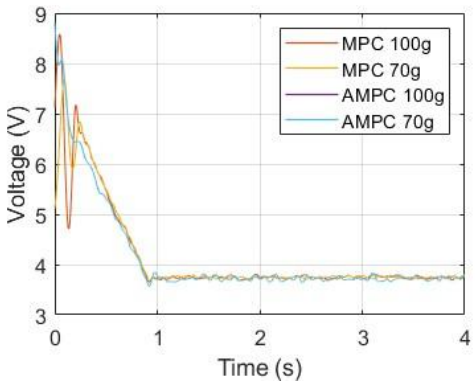

Figure 5.15 Control voltage during levitation process for inaccurate prediction model

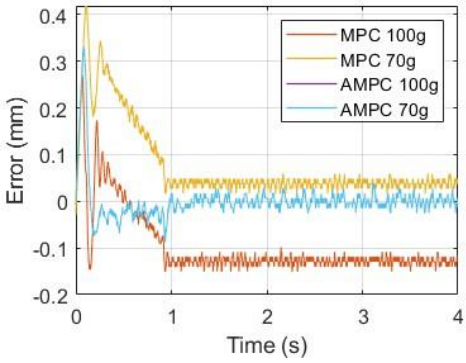

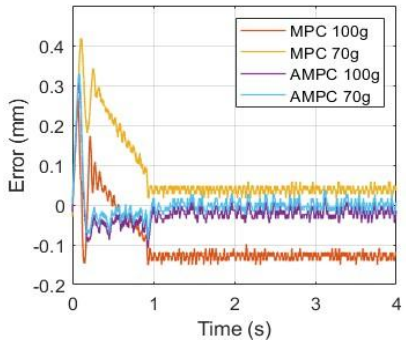

Figure 5.16 Suspension gap error during levitation process for inaccurate prediction model

5.4.2. Trajectory Tracking Test

In this section, the performance of MPC and AMPC controllers is evaluated in tracking dynamic target trajectories under varying conditions. Similar to the setup in Section 5.4.1, the steel ball is initially stabilized at a specific suspension point before beginning the trajectory

tracking. The trajectory reference is defined as

$Trajectory\ reference = 34 + Asin\ (Freq \times t)$ with amplitudes A of 1 mm and 2 mm, and frequencies $Freq$ of 6 rad/s and 12 rad/s, respectively. The initial prediction model used by both controllers in this test remains consistent with Section 5.4.1 and is similarly inaccurate, with the prediction model mass not matching the actual system mass. This introduces an additional layer of challenge for the controllers, as they must track the target trajectory while compensating for the discrepancy in the prediction model. The parameters for prediction horizon, control horizon, output constraints, and weighting factors are maintained as per the previous levitation test to ensure a direct comparison of the MPC and AMPC's tracking capabilities.

Figures 5.18 through 5.23 illustrate the trajectory tracking performance of MPC and AMPC controllers under two sets of conditions: varying reference trajectory amplitudes and different prediction model masses (70g and 100g). The target trajectories for the suspension gap are sinusoidal paths with frequencies of 6 rad/s (Figures 5.18 to 5.20) and 12 rad/s (Figures 5.21 to 5.23), and amplitude variations of 1 mm. At the 6 rad/s frequency, as shown in Figure 5.17, the AMPC controller closely aligns the suspension gap with the reference trajectory, maintaining deviations within ±0.05 mm. In contrast, the MPC-controlled suspension, particularly with the 100g prediction model, exhibits larger deviations, peaking at approximately ±0.1 mm. At the higher frequency of 12 rad/s (Figure 5.20), AMPC continues to provide tight control, with deviations around ±0.1 mm, while the MPC performance further declines, with the 100g model showing deviations that reach ±0.2 mm.

The control voltage outputs in Figure 5.18 and Figure 5.21 further underscore AMPC's efficiency. For the 6 rad/s frequency, AMPC stabilizes within a voltage range of 3.5 V to 4.5 V, whereas MPC with the 100g model peaks near 4.8 V, indicating a greater control effort. At 12 rad/s, AMPC maintains voltage levels between 3.2 V and 4.5 V, while MPC demonstrates larger fluctuations, especially with the 100g model, reaching up to 5 V.

Tracking error analysis in Figure 5.19 and Figure 5.22 reinforces AMPC's advantage in accuracy. At 6 rad/s, AMPC limits the error to about ±0.05 mm, while MPC errors, particularly with the 100g model, rise to around ±0.15 mm. At 12 rad/s, AMPC keeps errors within ±0.1 mm, whereas MPC errors increase, with the 100g model showing peaks near ±0.2 mm.

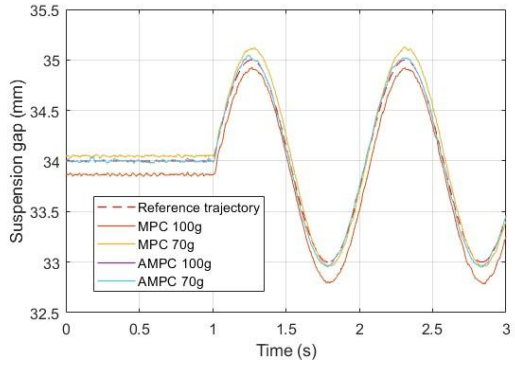

Figure 5.17 Suspension gap during trajectory tracking at 6 rad/s with inaccurate prediction model

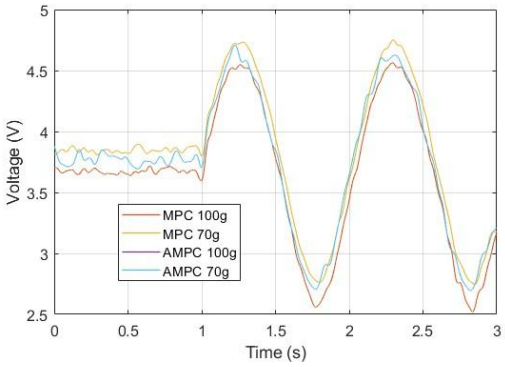

Figure 5.18 Control voltage during trajectory tracking at 6 rad/s with inaccurate prediction model

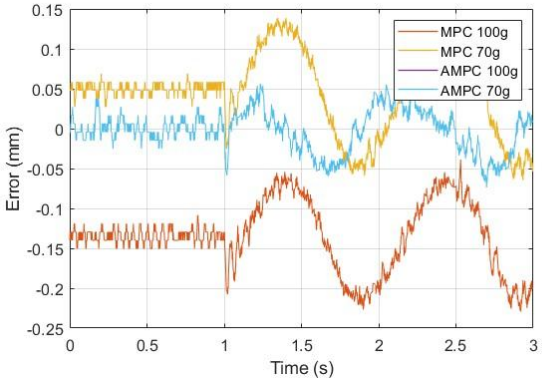

Figure 5.19 Tracking error during trajectory tracking at 6 rad/s with inaccurate prediction model

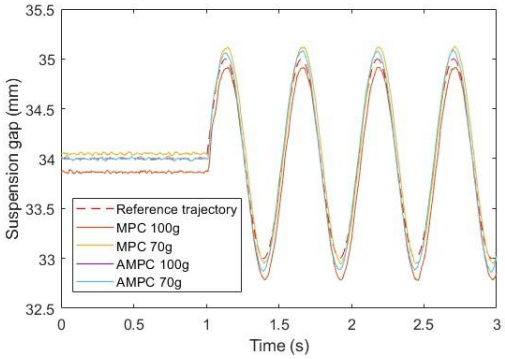

Figure 5.20 Suspension gap during trajectory tracking at 12 rad/s with inaccurate prediction model

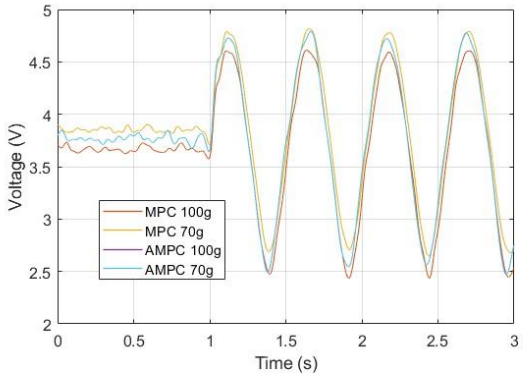

Figure 5.21 Control voltage during trajectory tracking at 12 rad/s with inaccurate prediction model

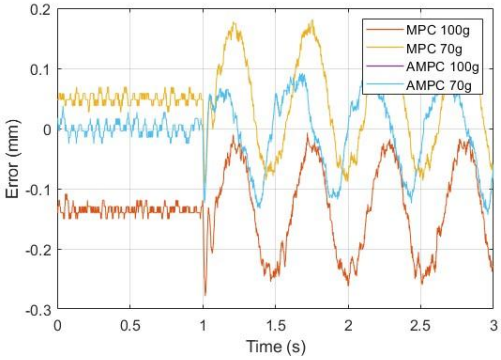

Figure 5.22 Tracking error during trajectory tracking at 12 rad/s with inaccurate prediction model

5.4.3. Discussion

This experimental study highlights the practical benefits of AMPC over traditional MPC in a magnetic suspension system under various operational scenarios. Both levitation and trajectory tracking tasks demonstrate AMPC's robustness and adaptability in handling model

discrepancies, particularly when the prediction model mass does not match the actual system mass.

In the levitation process, AMPC consistently achieved more accurate suspension gap control with minimal steady-state error and lower control effort, as reflected in stabilized voltage outputs. The MPC controller, however, exhibited slightly higher voltage demands and residual errors when the prediction model mass deviated from the actual mass, underscoring the limitations of a static prediction model.

In the trajectory tracking tests, AMPC maintained a closer alignment with the sinusoidal reference trajectories across both frequencies (6 rad/s and 12 rad/s) and amplitude conditions, while MPC exhibited larger tracking errors and required greater control effort. The adaptability of AMPC's prediction model allowed it to continuously adjust to the system's dynamic changes, resulting in superior tracking accuracy.

Overall, AMPC's ability to dynamically update the prediction model significantly enhanced its control accuracy and stability under varied conditions, reinforcing its suitability for applications requiring high precision and resilience to model uncertainties. This study supports the integration of adaptive control strategies in real-world magnetic levitation systems, where varying parameters, such as load changes, demand continuous model adjustments for optimal performance.

5.5. Conclusions

This chapter extensively explores the implementation and effectiveness of AMPC in a magnetic suspension system, demonstrating how adaptive control strategies can overcome limitations

inherent in traditional MPC. By dynamically updating the prediction model to reflect real-time system variations, AMPC proves to be robust in managing discrepancies in the prediction model, particularly when the actual system parameters, such as mass, deviate from the assumed values.

The initial levitation process simulations indicate that both MPC and AMPC can achieve stable suspension when the system mass is accurately represented in the model. However, under model mismatch conditions—where the actual system mass varies from the prediction model—AMPC consistently provides more accurate control, achieving closer adherence to the desired suspension gap with reduced steady-state error compared to MPC. This improvement is largely attributed to AMPC's capacity to update the prediction model parameters in real time, thereby minimizing control errors resulting from model inaccuracies.

Trajectory tracking tests further highlight AMPC's adaptability, especially when the suspension system is required to follow sinusoidal reference paths simulating real-world viaduct displacements. At lower frequencies, both controllers perform well, but as frequency increases, MPC's tracking accuracy deteriorates, leading to significant deviations from the target trajectory. AMPC, however, maintains higher accuracy by dynamically adapting to the system's changing dynamics, effectively minimizing tracking errors and reducing the control effort needed. This adaptability makes AMPC particularly advantageous in high-speed applications where maintaining precise tracking of the target trajectory is critical.

The addition of measurement noise emulates realistic sensor conditions, revealing that AMPC and MPC display similar performance in the presence of noise. Both controllers demonstrate

effective tracking despite the noise, suggesting that while AMPC excels in handling model variations, both approaches manage sensor noise similarly within the given experimental conditions.

Overall, this study validates AMPC's superiority in adapting to real-time system changes, maintaining control accuracy, and enhancing stability under varied conditions, positioning it as a valuable approach for applications demanding high precision and resilience to dynamic system uncertainties. The chapter supports the adoption of adaptive control in practical maglev suspension systems, addressing the challenges of real-time adjustments and the need for robust performance amid fluctuating conditions, such as changes in load or external disturbances.

the key innovation in this chapter lies in the application and integration of these techniques to address specific challenges inherent to real-world maglev systems. The primary contributions of this chapter can be summarized as follows:

1) Application to EMS maglev suspension system with real-time model adaptation:

The chapter presents a practical application of ARX-based AMPC to a magnetic levitation suspension system, which involves strong nonlinearities and time-varying dynamics. This implementation demonstrates how AMPC can compensate for model mismatches (e.g., system mass variations) in real time, addressing a critical issue for the deployment of MPC-based methods in real-world maglev systems.

2) Comparative simulation and experimental study across multiple scenarios:

To highlight the benefits of AMPC, extensive simulations and experimental validations were conducted under three challenging conditions: (i) model mismatch, (ii) dynamic trajectory

tracking, and (iii) measurement noise. These conditions closely mimic realistic operational environments for maglev systems. The comparative results between MPC and AMPC show that AMPC can consistently reduce steady-state errors and improve trajectory tracking under varying conditions, validating its robustness and effectiveness.

3) Demonstration of continuous model update using ARX:

The proposed AMPC design employs a recursive ARX model update combined with Kalman filter adaptation. While AMPC theory is known, this work demonstrates how to integrate real-time model identification with MPC to enhance adaptability. It also highlights practical implementation strategies such as updating the nominal operating point and dynamically adjusting the Kalman gain.

4) Performance impact in precision control contexts:

As shown in both simulations and experiments, AMPC achieves lower control error even under small deviations (e.g., 0.02 mm), which is crucial for maglev suspension systems where even minor errors can impact ride quality and safety. The value of AMPC here is not just in average performance, but in reducing sensitivity to unmodeled dynamics.

Chapter 6. Two-Point Suspension Controller Design Based on ARX-AMPC

In this chapter, the focus shifts from single-point to two-point suspension control, leveraging the ARX-AMPC framework developed and tested in previous simulations and experiments. While the initial simulations and experiments in prior chapters concentrated on a single-point suspension system—essentially the smallest suspension unit of a maglev train—this setup served as an introductory test bed for suspension control algorithms. However, real-world maglev train systems are inherently more complex, as they require multi-point coupled suspension control to achieve stable levitation and ride quality across the entire vehicle structure.

The transition from single-point to two-point suspension introduces new challenges in control strategy, including the handling of coupling effects between suspension points. These effects require the controller to adapt dynamically not only to each suspension point but also to the interaction between them, which is vital for the stability and performance of the full maglev train system. This chapter aims to explore these multi-point control dynamics, utilizing the ARX-AMPC approach to manage the coupling and improve suspension stability in the two-point setup.

6.1. Dynamic Model of the Two-Point Suspension System

6.1.1. System Overview

The two-point suspension system, illustrated in Figure 6.1, represents a simplified model for analyzing the levitation control of a maglev train segment. This system consists of a rigid

suspension frame equipped with four electromagnets, organized into two pairs. Each pair of electromagnets is connected to a separate controller, with Electromagnet No.1 and Electromagnet No.2 managed by Controller 1, and Electromagnet No.3 and Electromagnet No.4 managed by Controller 2. The two electromagnets within each pair are wired in series, so they share the same current input, which allows for balanced force generation on each side of the frame.

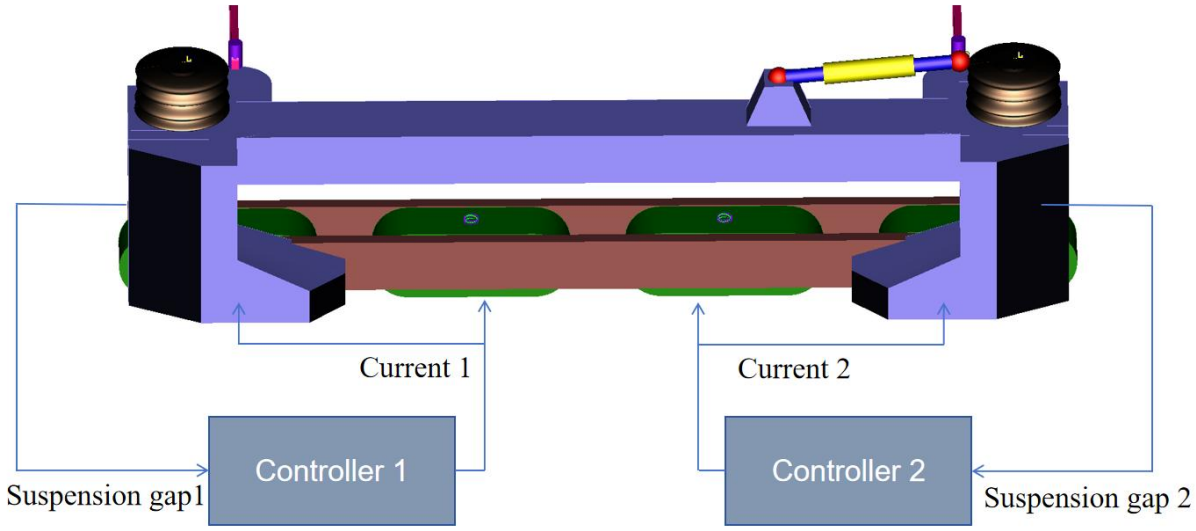

Figure 6.1 Schematic diagram of the two-point suspension system structure

In this configuration, the controller regulates two independent current channels, one for each pair of electromagnets, enabling Multi-Input Multi-Output (MIMO) control. The MIMO capability of the controller simplifies the system design by eliminating the need for separate controllers for each pair of electromagnets. When an electric current flows through the electromagnets, they produce magnetic forces that attract the track positioned above, thereby lifting and stabilizing the frame in the vertical direction. The spacing and orientation of the electromagnets are crucial for maintaining stability and preventing unwanted tilting during

operation. This two-point configuration, which simplifies the dynamics while still capturing the core aspects of multi-point levitation, serves as a valuable model for testing advanced control algorithms.

The controller must regulate the combined electromagnetic forces generated by the two pairs of electromagnets to maintain a stable suspension gap between the frame and the track. This vertical gap is crucial to ensure continuous levitation without physical contact with the track.

The transition from single-point to two-point suspension introduces several nontrivial challenges and new dynamics that justify a dedicated investigation:

1) Strong inter-point coupling:

In the two-point maglev configuration, the levitation forces at the front and rear points are dynamically coupled through the rigid body motion of the vehicle segment. A disturbance or control action at one point can directly affect the other, introducing interaction dynamics that are absent in single-point systems. This coupling necessitates more careful controller design and coordination.

2) Increased dimensionality and complexity:

The system expands from a SISO to a 4-state MIMO system involving both translational and rotational motion. The control input now needs to regulate not only the levitation gaps at both points but also the pitch angle, which requires satisfying multiple objectives simultaneously under constrained input conditions.

3) Tighter stability and coordination requirements:

Unlike single-point control where local stability suffices, the two-point system must maintain

coordinated suspension behavior to avoid oscillations or instability in body pitch. As shown in simulation and experimental results, improper coordination may lead to increased overshoot or oscillation at one end, even if the other point is well-controlled.

4) Validation in a realistic setting:

This chapter contributes by implementing and evaluating MPC, AMPC, and PID controllers in a physically representative two-point maglev suspension platform, providing comparative insights into how model adaptation benefits not just tracking performance but also inter-point stability and coordination.

6.1.2. Assumptions of Dynamic Model

In developing the dynamic model for the two-point suspension system, several simplifications are made to streamline the analysis and focus on the primary control objectives. These assumptions, outlined below, help reduce the complexity of the system and allow for more straightforward mathematical modeling.

Simplifying Assumptions:

1. **Rigid Body Assumption**: The suspension frame is assumed to be a rigid body, meaning it does not deform under electromagnetic forces. This simplifies the analysis by allowing us to treat the frame as a single, solid object with fixed geometric properties.
2. **Fixed Electromagnetic Force Application Points**: The points where the electromagnetic forces act is assumed to be fixed. This means the forces generated by each electromagnet are applied consistently at the same points on the suspension frame, ensuring predictable force distribution.

3. **Negligible Air Resistance**: Air resistance is ignored in this model. Given that the system operates in a relatively controlled environment, the impact of air drag is considered minimal and is therefore not included in the dynamic equations.

Coordinate System Definition

To describe the motion and orientation of the suspension frame, a coordinate system is established as shown in Figure 6.2. In this system:

- **Vertical Axis (z-axis)**: The z-axis represents the vertical direction, along which the suspension gap (distance between the frame and the track) is controlled. The z-coordinate of the frame's center of mass denotes its vertical position relative to the track.
- **Rotation about Center (θ)**: The frame's orientation is described by an angle θ, representing the rotation about the center of the frame. This angle is critical for maintaining the stability of the system, as deviations from zero indicate tilting. Positive and negative values of θ correspond to clockwise and counterclockwise rotations, respectively, relative to the horizontal plane.

By defining this coordinate system, we can express the system's dynamics in terms of vertical displacement and rotational angle, allowing for a clear and concise formulation of the control objectives in the upcoming sections.

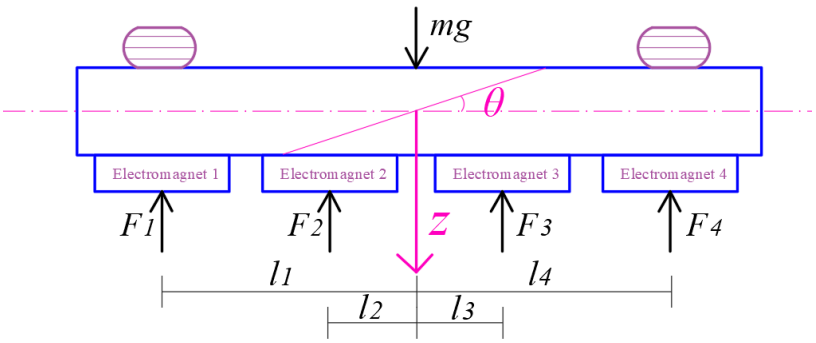

Figure 6.2 Coordinate system definition for vertical position and rotation angle

6.1.3. Force Analysis of the Suspension Frame

In the two-point suspension system, each electromagnet generates an upward electromagnetic force that acts to lift and stabilize the suspension frame relative to the track. The primary forces in this system include the individual electromagnetic forces from each electromagnet and the gravitational force acting on the frame.

Electromagnetic Forces

As shown in Figure 6.2, each of the four electromagnets produces an upward electromagnetic force labeled F_1, F_2, F_3 and F_4. These forces are arranged as follows:

- F_1 and F_2: These forces are produced by Electromagnet No.1 and Electromagnet No.2 on the left side of the suspension frame. Although both electromagnets are supplied by the same current, the resulting forces F_1 and F_2 may differ due to variations in the gap distance between each electromagnet and the track. Thus, $F_1 \neq F_2$ despite the same current input.
- F_3 and F_4: Similarly, these forces are generated by Electromagnet No.3 and Electromagnet No.4 on the right side of the suspension frame. Although these electromagnets share the same current, variations in the gap distance may result in $F_3 \neq F_4$.

These variations in force due to differing gap distances add complexity to the control task, as they influence both the vertical position and angular stability of the frame. The controller must account for these differences to maintain a balanced suspension.

Gravitational Force

The gravitational force, denoted by mg, acts vertically downward at the center of mass of the suspension frame. This force remains constant and represents the primary load that the electromagnetic forces must counterbalance to achieve levitation. Since mg acts at the center of mass, any imbalance in electromagnetic forces between the left and right sides will create a rotational moment about this center.

The combination of the electromagnetic forces F_1, F_2, F_3 and F_4, along with the gravitational force mg,, defines the dynamic behavior of the suspension frame. The balance and control of these forces are essential to achieving stable suspension, with minimal tilt or deviation from the target position. Adjusting the input currents allows the controller to manipulate these forces to stabilize both the height and angle of the frame relative to the track.

6.1.4. Derivation of Dynamic Equations

The dynamics of the two-point suspension system can be described by analyzing the forces and moments acting on the suspension frame, with each electromagnet positioned at a unique distance from the center of mass.

Translational Dynamics

The total upward force F_{total} acting on the suspension frame along the z-axis is the sum of the individual electromagnetic forces generated by each electromagnet:

$$F_{\text{total}} = F_1 + F_2 + F_3 + F_4 \tag{6.1}$$

The net vertical force, which includes the gravitational force mg, determines the vertical acceleration $\ddot{z}$ of the suspension frame's center of mass. Applying Newton's second law along the z-axis yields:

$$m\ddot{z} = F_{\text{total}} - mg \tag{6.2}$$

Where m is the mass of the suspension frame, g represents gravitational acceleration, z denotes the vertical displacement of the center of mass.

Rotational Dynamics

For rotational dynamics, each electromagnet's force contributes a moment about the center of mass depending on its specific distance L_i from this point. Letting L_1 and L_2 represent the lever arms for F_1 and F_2 (acting on one side of the frame), and L_3 and L_4 for F_3 and F_4 (acting on the other side), the net moment M around the center of mass can be expressed as:

$$M = L_3F_3 + L_4F_4 - (L_1F_1 + L_2F_2) \tag{6.3}$$

Applying Newton's second law for rotational motion:

$$J\ddot{\theta} = M = L_3F_3 + L_4F_4 - (L_1F_1 + L_2F_2) \tag{6.4}$$

Where J is the moment of inertia of the suspension frame about its center of mass, θ represents the angular displacement (tilt) of the frame, $\ddot{\theta}$ denotes the angular acceleration.

With the dynamic model for the two-point suspension system the focus now shifts to designing appropriate controllers to regulate the suspension system's behavior and achieve the desired stability.

6.2. Controller Design for Two-Point Suspension System

In this section, PID, MPC and AMPC controllers are designed for the two-point suspension system established in Section 6.1.

6.2.1. PID Controller Design for Two-Point Suspension System

The PID controller applied in this design is inherently a Single-Input Single-Output (SISO) controller. Unlike MPC and AMPC controllers, which can manage multiple inputs and outputs simultaneously, the PID controller can only handle one control variable in response to a single measurement signal. Therefore, in the two-point suspension system, two separate PID controllers would be required to manage each electromagnet pair independently. Each controller regulates the current for one side of the suspension system based on feedback from a single measurement, aiming to maintain stability at the designated suspension gap.

The SISO nature of PID control supports the decision to directly apply the single-point suspension parameters to the two-point system because each suspension point can be independently controlled using a separate PID loop. In the single-point system, the PID parameters were tuned to maintain a stable suspension gap by adjusting the current based on local feedback. Since the core control requirement for each suspension point remains the same—keeping the suspension gap stable—these parameters are expected to provide effective local control for each point in the two-point system without additional tuning. Thus, rather than recalibrating the PID controller for the two-point system, the parameters established for single-point suspension are adopted directly.

Table 6.1 Parameters of PID controller for two-point suspension system

P	I	D
12000	10000	1000

6.2.2. MPC Controller Design for Two-Point Suspension System

The MPC approach provides an advanced control strategy for the two-point suspension system, capable of handling the multi-input, multi-output (MIMO) nature of this system. Unlike the PID controller, which operates in a SISO framework, MPC allows simultaneous control over both suspension points, accounting for interactions and coupling effects in real time. This makes MPC particularly suited to managing the complex dynamics of the two-point suspension system, where both vertical position and tilt angle stability must be maintained.

6.2.2.1.Prediction Model and Control Objectives

The MPC controller is designed based on the dynamic equations derived in Section 6.1.4. It relies on a linearized prediction model that captures the system's vertical and rotational dynamics. This model is essential for the MPC controller to predict future behavior accurately and make optimal control decisions. The two-point suspension system is inherently nonlinear; however, to simplify control design, the system is linearized around a nominal operating point, where the suspension gap and tilt angle are close to their target values. The linearization process involves taking the nonlinear equations of motion derived in Section 6.1.4 and expanding them around a nominal operating point using a Taylor series expansion. For the two-point suspension system, the goal is to linearize the equations around a nominal suspension gap $z = z_{\text{target}}$ and a tilt angle $\theta = 0$.

The electromagnetic force of the four electromagnets can be described:

$$F_i = k_i \frac{I_i^2}{z_i^2} \tag{6.5}$$

Where k_i is the proportionality constant related to the electromagnet properties, I_i is the current through the $i-th$ electromagnet, z_i is the distance between the $i-th$ electromagnet and the rail.

To linearize the equations in Section 6.1.4, expanding the electromagnetic force F_i as a Taylor series around the nominal point and keeping only the first-order terms yields:

$$F_i \approx F_{i,\,\text{nom}} + \left.\frac{\partial F_i}{\partial z}\right|_{z=z_{\text{target}}} \delta z + \left.\frac{\partial F_i}{\partial I}\right|_{I=I_{i,\,\text{nom}}} \delta I_i \tag{6.6}$$

Where $F_{i,\,\text{nom}} = k_i \frac{I_{i,\text{nom}}^2}{z_{\text{target}}^2}$ is the force at the nominal point, $\frac{\partial F_i}{\partial z} = -2k_i \frac{I_{i,\,\text{nom}}^2}{z_{\text{target}}^2}$ is the partial derivative of force with respect to z and $\frac{\partial F_i}{\partial I} = 2k_i \frac{I_{i\,\text{nom}}}{z_{\text{target}}^2}$ is the partial derivative of force with respect to I.

Define the state vector $\mathbf{x} = [\delta z, \delta \dot{z}, \delta\theta, \delta\dot{\theta}]^T$ and the input vector $\mathbf{u} = [\delta I_1, \delta I_2]^T$. Substituting the linearized forces into the equations of motion gives the following approximate linearized system:

$$m\delta\ddot{z} = \left(-2k_1 \frac{I_{1,\,\text{nom}}^2}{z_{\text{target}}^3}\right)\delta z + 2k_1 \frac{I_{1,\,\text{nom}}}{z_{\text{target}}^2}\delta I_1 + \left(-2k_3 \frac{I_{2,\,\text{nom}}^2}{z_{\text{target}}^3}\right)\delta z + 2k_3 \frac{I_{2,\,\text{nom}}}{z_{\text{target}}^2}\delta I_2 \tag{6.7}$$

$$J\delta\ddot{\theta} = L_3\left(-2k_3 \frac{I_{2,\,\text{nom}}^2}{z_{\text{target}}^3}\delta z + 2k_3 \frac{I_{2,\,\text{nom}}}{z_{\text{target}}^2}\delta I_2\right) - L_1\left(-2k_1 \frac{I_{1,\,\text{nom}}^2}{z_{\text{target}}^3}\delta z + 2k_1 \frac{I_{1,\,\text{nom}}}{z_{\text{target}}^2}\delta I_1\right) \tag{6.8}$$

Reorganizing these equations into a standard state-space form yields:

$$\dot{\mathbf{z}} = \boldsymbol{A}\mathbf{z} + \boldsymbol{B}\mathbf{u} \tag{6.9}$$

$$\mathbf{y} = \boldsymbol{C}\mathbf{z} + \boldsymbol{D}\mathbf{u} \tag{6.10}$$

The matrix $\boldsymbol{A}$ represents the effects of state variables on the system dynamics:

$$A = \begin{bmatrix} 0 & 1 & 0 & 0 \\ a_{21} & 0 & a_{23} & 0 \\ 0 & 0 & 0 & 1 \\ a_{41} & 0 & a_{43} & 0 \end{bmatrix} \tag{6.11}$$

where $a_{21} = -2\left(\frac{k_1 I_{\cdots}^2}{m z_{\text{target}}^3} + \frac{k_3 I_{2\text{ nam}}^2}{m z_{\text{target}}^3}\right)$, $a_{23} = -2\left(\frac{k_2 I_{2,\text{nom}}^2}{m z_{\text{target}}^3} + \frac{k_4 I_{I_{\text{taom}}}^2}{m z_{\text{target}}^{\text{ang}}}\right)$, $a_{41} = -\frac{L_1 k_1 I_{1,\text{ nom}}^2}{J z_{\text{target}}^3} + \frac{L_3 k_3 I_{2,\text{ nom}}^2}{J z_{\text{target}}^3}$ and $a_{43} = \frac{L_2 k_2 I_{1,\text{nom}}^2}{J z_{\text{target}}^3} - \frac{L_4 k_4 I_{2,\text{ nom}}^2}{J z_{\text{target}}^3}$.

The matrix BB captures the influence of input currents on system dynamics:

$$B = \begin{bmatrix} 0 & 0 \\ b_{21} & b_{22} \\ 0 & 0 \\ b_{41} & b_{42} \end{bmatrix} \tag{6.12}$$

where $b_{21} = \frac{2k_1 I_{1,\text{nom}}}{m z_{\text{target}}^2}$, $b_{22} = \frac{2k_2 I_{2\text{ nom}}}{m z_{\text{target}}^2}$, $b_{41} = \frac{2L_1 k_1 I_{1,\text{ nom}}}{J z_{\text{target}}^2}$ and $b_{42} = \frac{2L_3 k_3 I_{2,\text{ nom}}}{J z_{\text{target}}^2}$.

These values ensure that the linearized model captures the effects of changes in z, θ and input currents on the system dynamics. This state-space model enables the MPC controller to predict future states and optimize control inputs accordingly for the two-point suspension system.

As discussed in Section 4.3, the Kalman filter provides optimal state estimates by filtering out measurement noise and using a predictive correction approach. In the two-point suspension system, the Kalman filter is similarly applied to improve state estimation accuracy, crucial for the MPC's prediction model. In the single-point suspension system, the Kalman filter estimated the vertical position and velocity of a single suspension gap based on sensor measurements affected by noise. The state vector in the single-point system was simpler, typically including only the gap z and its velocity $\dot{z}$. For the two-point suspension system, however, the state vector is expanded to include:

1. The vertical position z and velocity $\dot{z}$ of the suspension gap.
2. The tilt angle θ and angular velocity $\dot{\theta}$ of the suspension frame.

Thus, the state vector becomes:

$$\mathbf{z} = [z, \dot{z}, \theta, \dot{\theta}]^T \tag{6.13}$$

The Kalman filter is adapted to handle this expanded state vector, predicting and correcting both the suspension gap and tilt angle simultaneously. This involves recalculating the state transition matrix $\boldsymbol{A}$, input matrix $\boldsymbol{B}$, and measurement matrix $\boldsymbol{C}$ to accommodate the additional rotational dynamics in the two-point system. The Kalman gain, prediction step, and correction step are consistent with the single-point system, as detailed in Section 4.3.3. However, they are adapted for the two-point suspension system by substituting the expanded state vector and updated system matrices.

6.2.2.2.Cost Function and Constraints

The cost function J used in the MPC controller is a quadratic function that aggregates penalties for state deviations (errors) and control inputs over a prediction horizon N_p:

$$J = \frac{1}{2}\sum_{k=1}^{N_p} \left(e_{(t+k|t)}^T Q e_{(t+k|t)} + u_{(t+k|t)}^T R u_{(t+k|t)}\right) \tag{6.14}$$

Where:

- $e_{(t+k|t)}$ is the error vector at future step $t+k$ relative to the current time t, defined as the difference between the predicted system state and the reference (target) state. Specifically, $e_{(t+k|t)} = \mathbf{z}_{\text{ref}} - \mathbf{z}_{(t+k|t)}$, where $\mathbf{z}$ represents the suspension gap and θ (tilt angle),
- $u_{(t+k|t)}$ represents the control input vector, which includes the current inputs I_1 and I_2 applied to the two electromagnet pairs,

- Q is the state weighting matrix, which determines the importance of tracking accuracy in the suspension gap and tilt angle,
- R is the input weighting matrix, which penalizes excessive control input to limit energy usage and wear on the electromagnets.

The control input currents I_1 and I_2 applied to the electromagnets are constrained to lie within safe operating limits:

$$I_{min} \leq I_i \leq I_{max} \text{ for } i = 1,2 \tag{6.15}$$

where I_{min} and I_{max} are the minimum and maximum allowable currents for each electromagnet.

The suspension gap $\boldsymbol{z}$ and tilt angle θ are also constrained to maintain stability and avoid mechanical limits:

$$z_{min} \leq z \leq z_{max} \tag{6.16}$$

$$\theta_{min} \leq \theta \leq \theta_{max} \tag{6.17}$$

These constraints are integrated into the MPC optimization problem, ensuring that the computed control actions keep the system within its operational boundaries. Together, the cost function and constraints ensure that the MPC controller minimizes deviations while respecting the system's physical limits, resulting in a stable and efficient suspension control solution. This design enables the controller to handle the MIMO nature of the two-point system effectively, enhancing both suspension stability and tilt management.

6.2.3. ARX-MPC Controller Design for Two-Point Suspension System

The ARX-MPC controller for the two-point suspension system builds on the single-point ARX-

MPC design outlined in Section 5.2. In adapting the ARX-MPC for two-point control, the approach leverages the same fundamental ARX model structure but expands it to accommodate the MIMO dynamics of the two-point system, including both the vertical suspension gap z and the tilt angle θ, along with their respective velocities. The system is modeled as a MIMO system, requiring two control inputs—currents to the electromagnets on either side of the suspension frame. In the two-point system, Equation (5.2) extends to include additional terms to capture the interactions between suspension gap and tilt angle, using an expanded regression vector that includes both inputs and outputs for each suspension point. The regression vector is expanded accordingly to reflect these interactions:

$$\mathbf{y}(t) = -\boldsymbol{A}_{\mathrm{ARX}}\mathbf{y}(t-1) + \boldsymbol{B}_{\mathrm{ARX}}\boldsymbol{u}(t-1) + \boldsymbol{E}(t) \tag{6.18}$$

where:

- $\mathbf{y}(t) = [z, \dot{z}, \theta, \dot{\theta}]^T$, representing the vertical gap, gap velocity, tilt angle, and angular velocity,
- $\boldsymbol{A}_{\mathrm{ARX}}$ and $\boldsymbol{B}_{\mathrm{ARX}}$ are parameter matrices that capture the effects of past outputs and inputs, respectively,
- $\mathbf{u}(t) = [I_1, I_2]^T$, representing the control inputs (currents to the electromagnets).
- $\boldsymbol{E}(t)$ represents disturbance or noise.

The ARX model parameters $\boldsymbol{A}_{\mathrm{ARX}}$ and $\boldsymbol{B}_{\mathrm{ARX}}$ are updated in real-time, providing the ARX-MPC controller with a dynamic prediction model that adapts as the system dynamics evolve. The prediction model in ARX-MPC uses the updated ARX parameters to project the future states over a specified prediction horizon N_p. At each time step, the updated ARX model

generates a new prediction model based on recent input-output data, which provides a real-time representation of the system's behavior. The prediction of future states is achieved by iteratively applying the ARX model over the prediction horizon:

$$\hat{\mathbf{y}}(t+k \mid t) = A_{\mathrm{ARX}}\hat{\mathbf{y}}(t+k-1 \mid t) + B_{\mathrm{ARX}}\boldsymbol{u}(t+k-1 \mid t) \tag{6.19}$$

for $k = 1,2,\dots,N_p$, where $\hat{\mathbf{y}}(t+k \mid t)$ represents the predicted output at future step $t+k$, based on information available at time t.

The same Kalman filter framework used in Section 4.3.3 and Section 6.2.2.1 is applied here. The Kalman gain calculation, prediction step, and correction step remain consistent but now use the updated state vector and system matrices.

The cost function in the ARX-MPC controller for the two-point suspension system is structured similarly to that in the single-point system, as it aims to minimize tracking errors and control efforts over a prediction horizon. This quadratic cost function considers both the vertical suspension gap and the tilt angle, penalizing deviations from desired values for each.

The cost function is:

$$J = \frac{1}{2}\sum_{k=1}^{N_p} \left(\hat{e}(t+k \mid t)^T \boldsymbol{Q}\hat{e}(t+k \mid t) + \mathbf{u}(t+k \mid t)^T \boldsymbol{R}\mathbf{u}(t+k \mid t)\right) \tag{6.20}$$

where:

- $\hat{e}(t+k \mid t) = \mathbf{y}_{\mathrm{ref}}(t+k) - \hat{\mathbf{y}}(t+k \mid t)$ is the error between the reference trajectory $\mathbf{y}_{\mathrm{ref}}$ (target gap and tilt angle) and the predicted output,
- $\boldsymbol{Q}$ is the weighting matrix that penalizes deviations in both the gap and tilt angle,
- $\boldsymbol{R}$ penalizes the control effort applied to each electromagnet.

The constraints are the same as those outlined in Section 6.2.2.2.

6.3. Simulation Results of Two-Point Suspension Control

Building on the dynamic modeling of the two-point suspension system in Section 6.1 and the controller designs presented in Section 6.2, this section conducts simulation studies to evaluate the performance of the PID, MPC, and ARX-MPC controllers. These simulations aim to test the controllers' ability to handle the coupled dynamics of the two-point system and achieve the desired control objectives.

The initial scenarios involve the bogie levitating from a dropped state at an initial suspension gap of 18 mm to a target gap of 8 mm at two different velocities, 5 mm/s and 50 mm/s. These tests assess the controllers' ability to manage the levitation process under standard conditions. Subsequently, the system parameters are adjusted to introduce more challenging conditions, including an increase in the bogie weight from 750 kg to 1000 kg and an initial tilt angle of 0.001 rad. The suspension gaps at both ends of the bogie and the control currents for the electromagnets are recorded to analyze the controllers' effectiveness in maintaining stability and tracking the reference trajectory under these varying conditions.

6.3.1. Levitation Process Simulation

This section presents a simulation study of the levitation process for the two-point suspension system described in Section 6.1. The control objective is to lift the maglev bogie from a resting state (landing position) to the desired suspension gaps at both ends while maintaining stability and minimizing oscillations.

The system, modeled in SIMULINK, is a MIMO system. The control inputs are the two

currents supplied to the electromagnets on either side of the suspension frame, and the outputs are the real-time suspension gaps at the two ends of the frame. The dynamic properties of the system, including the mass of the suspension frame, the electromagnet characteristics, and other relevant parameters, are provided in Table 6.2.

Table 6.2 System parameters of the two-point suspension model

m	750 kg
J	$330 \cdot kg \cdot m^2$
$l_1 = l_4$	1.15 m
$l_2 = l_3$	0.372 m
$\frac{\mu_0 n^2 A}{4}$	0.0015

Figure 6.3 to Figure 6.8 illustrate the levitation process of the two-point maglev bogie system under PID, MPC, and AMPC controllers. The control objective is to lift the bogie from an initial suspension gap of 18 mm to the target gap of 8 mm at a constant rate of 5 mm/s. The figures include the suspension gap trajectories and the corresponding control currents for each controller.

For the PID controller, the suspension gap trajectories (Figure 6.3) exhibit noticeable overshoots of approximately 0.35 mm and 0.3 mm for suspension gaps 1 and 2, respectively, after reaching the target position. These overshoots are followed by oscillations that gradually diminish over time, with stabilization occurring around 2.5 seconds. This extended settling time indicates that the PID controller struggles to provide prompt stabilization for the two-point system. Furthermore, the corresponding control currents (Figure 6.4) highlight a significant limitation of the PID controller. Both current channels exceed the system's physical

constraint of 60 A, with peaks reaching approximately 65 A and 62 A during the initial phase. These values are well beyond the safe operational range of the system, posing risks to hardware safety and energy efficiency. Additionally, the currents exhibit fluctuations during the stabilization phase, suggesting inefficiencies in control force application.

In contrast, the MPC controller (Figure 6.5 and Figure 6.6) delivers significantly improved performance. The suspension gap trajectories reach the target position without any overshoots or oscillations, stabilizing smoothly at the 8 mm gap. The stabilization time is reduced to approximately 2.1 seconds for both suspension gaps, indicating a more efficient control process. The corresponding control currents remain well within the system's physical constraints, peaking at 20 A during the transition phase and stabilizing at approximately 10.8 A for both channels. This adherence to current limits ensures safe and energy-efficient operation while maintaining precise control of the suspension gap.

The AMPC controller (Figure 6.7 and Figure 6.8) further enhances performance, building upon the strengths of the MPC controller. Similar to the MPC, the suspension gap trajectories are smooth, with no overshoots or oscillations. However, the AMPC achieves slightly faster stabilization times of approximately 2.0 seconds for both suspension gaps, demonstrating its ability to adapt dynamically to the system's behavior. The corresponding control currents closely mirror those of the MPC controller, with a peak of 20 A during the transition and steady-state values of approximately 10.8 A. This indicates that the AMPC controller effectively maintains system stability and energy efficiency while offering a faster response.

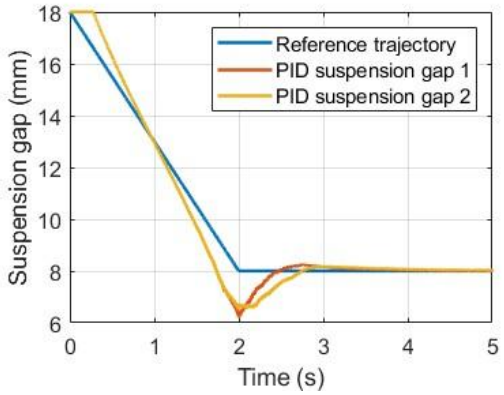

Figure 6.3 Suspension gaps during the slow levitation process of the two-point suspension system controlled by PID

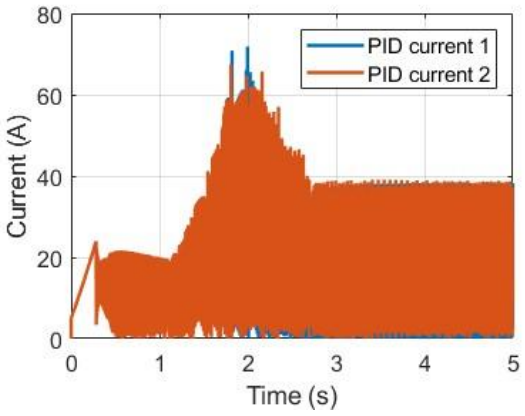

Figure 6.4 Control currents during the slow levitation process of the two-point suspension system controlled by PID

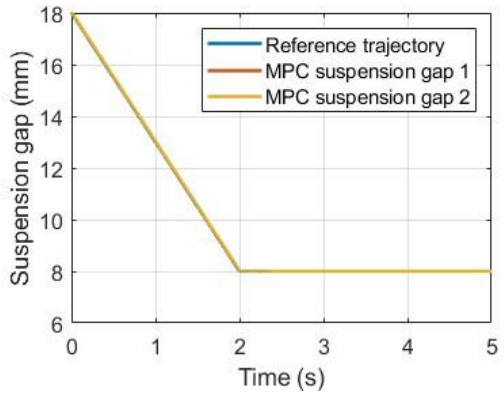

Figure 6.5 Suspension gaps during the slow levitation process of the two-point suspension system controlled by MPC

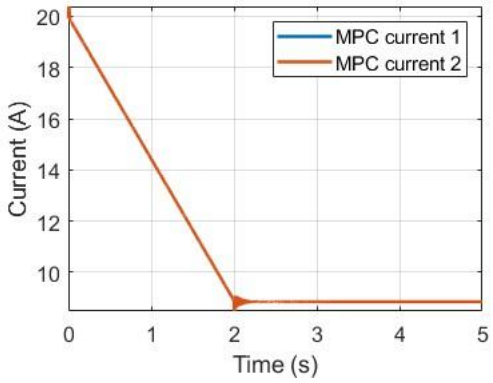

Figure 6.6 Control currents during the slow levitation process of the two-point suspension system controlled by MPC

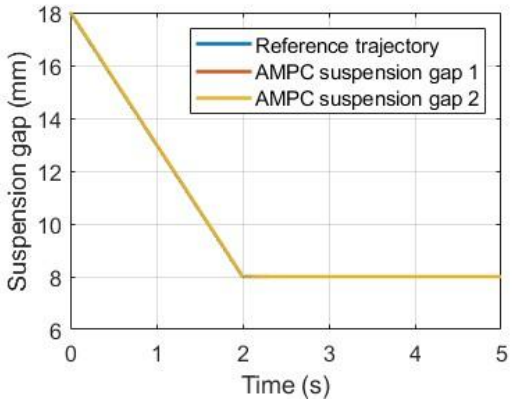

Figure 6.7 Suspension gaps during the slow levitation process of the two-point suspension system controlled by AMPC

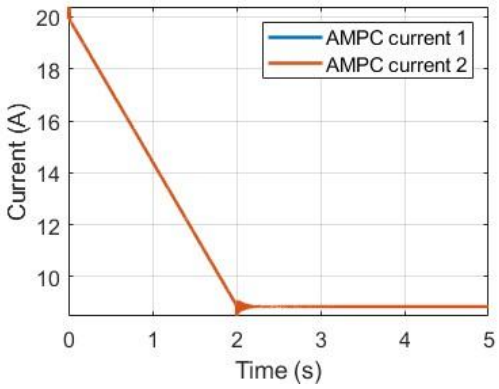

Figure 6.8 Control currents during the slow levitation process of the two-point suspension system controlled by AMPC

The faster levitation process at a speed of 50 mm/s provides further insights into the performance differences among the controllers, particularly under more challenging dynamic conditions. Figure 6.9 to Figure 6.14 illustrate the suspension gap and control current data for the PID, MPC, and AMPC controllers.

The PID controller, as shown in Figure 6.9, fails to stabilize the suspension gaps. The system demonstrates significant oscillations for both suspension gaps, with Gap 2 diverging entirely around the 2-second mark. This instability is further corroborated by Figure 6.10, where the control currents exhibit rapid spikes exceeding 200 A. These spikes not only exceed the physical constraints of the electromagnets but also signify the inability of the PID controller to handle the faster levitation process. The divergence highlights the limitations of PID in managing higher-speed dynamics due to its single-input, single-output design and fixed parameters.

Based on Figure 6.11 and Figure 6.13, the MPC and AMPC controllers successfully stabilize the suspension gaps at the target value of 8 mm within approximately 0.2 seconds after the start of the levitation process. This quick response indicates the effectiveness of both controllers in handling the faster levitation speed of 50 mm/s.

In Figure 6.12 and Figure 6.14, the control currents show an initial peak as the levitation process begins, with values reaching approximately 25 A. Both controllers then rapidly adjust the currents, converging to a steady-state value of around 10 A. This behavior demonstrates their ability to handle the increased dynamic demand without overshooting the physical constraints of the system.

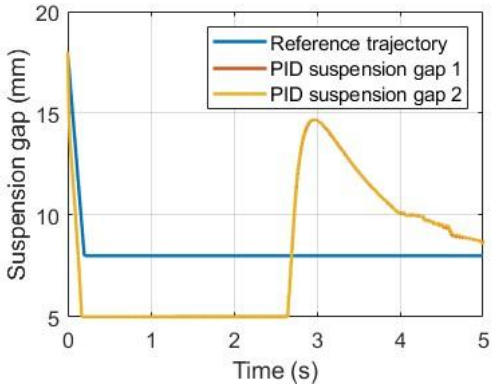

Figure 6.9 Suspension gaps during the fast levitation process of the two-point suspension system controlled by PID

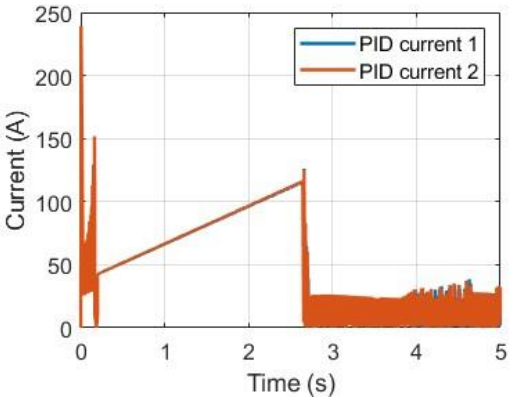

Figure 6.10 Control currents during the fast levitation process of the two-point suspension system controlled by PID

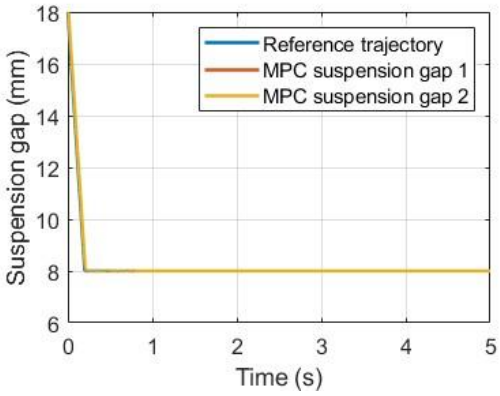

Figure 6.11 Suspension gaps during the fast levitation process of the two-point suspension system controlled by MPC

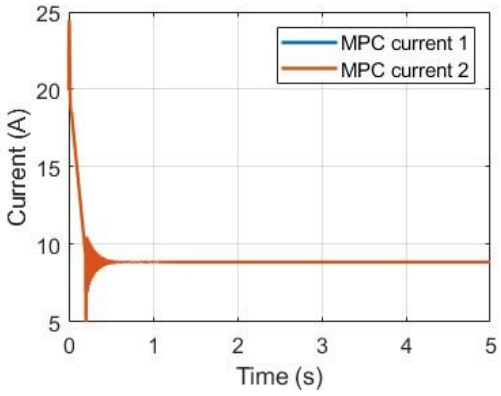

Figure 6.12 Control currents during the fast levitation process of the two-point suspension system controlled by MPC

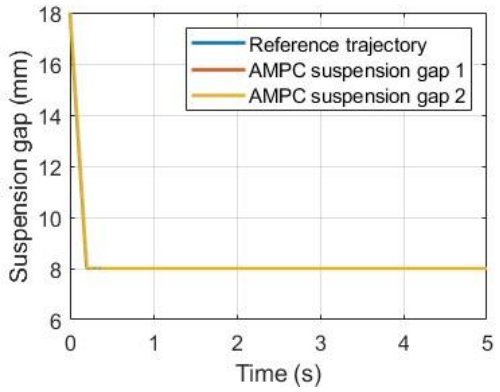

Figure 6.13 Suspension gaps during the fast levitation process of the two-point suspension system controlled by AMPC

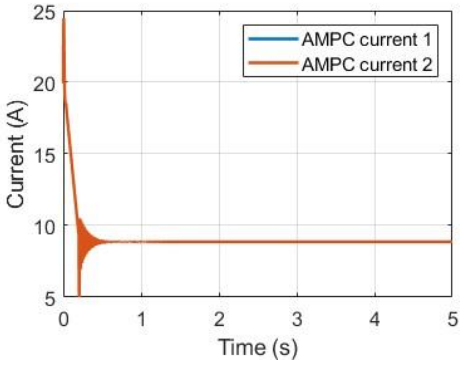

Figure 6.14 Control currents during the fast levitation process of the two-point suspension system controlled by AMPC

During the levitation process, as shown in Figure 6.15 through Figure 6.20, the system weight was increased to 1000 kg with an initial tilt angle of 0.001 rad, and the suspension velocity was set to 50 mm/s. Figure 6.15 depicts the suspension gaps controlled by the PID controller. The The PID controller exhibits complete divergence during the levitation process. The two

suspension gaps deviate significantly from the reference trajectory, failing to stabilize at the desired 8 mm gap. Moreover, the control currents generated by the PID controller exceed 200 A, far surpassing the physical constraint of 60 A. Such excessive current not only indicates the controller's lack of robustness but also poses a risk to the physical integrity of the system, making PID unsuitable for this scenario.

The MPC controller achieves stabilization of the suspension gaps, as shown in Figure 6.17. The gaps align with the target 8 mm within approximately 0.25 seconds. However, a steady-state error of approximately 0.1 mm is observed, as the suspension gaps do not perfectly match the reference trajectory. This steady-state error stems from the mismatch between the prediction model (assuming a system mass of 750 kg) and the actual system weight of 1000 kg. The corresponding control currents, depicted in Figure 6.18, remain well-regulated, with peak values of 51 A and 50 A, remaining within the operational constraints.

Figure 6.19 illustrates the suspension gaps controlled by the AMPC controller. The AMPC effectively stabilizes both gaps at the desired 8 mm with negligible steady-state error. Moreover, the AMPC controller achieves stabilization slightly faster than the MPC controller, with the system reaching stability in approximately 0.2 seconds. This improvement is attributed to the adaptive nature of the AMPC, which continuously updates the prediction model to mitigate the effects of model mismatch. The control currents generated by the AMPC controller, as shown in Figure 6.20, are well within the system's safe limits, peaking at 51 A and 50 A, similar to those of the MPC controller.

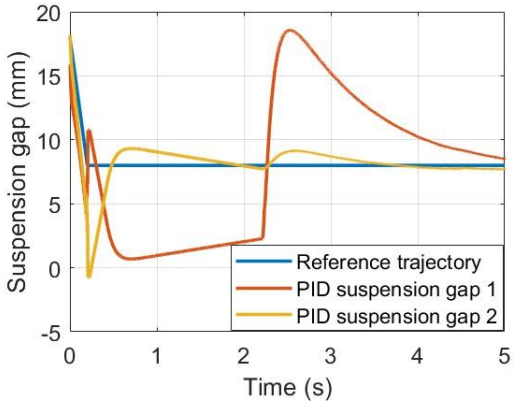

Figure 6.15 Suspension gaps during levitation under PID control in a two-point maglev bogie system with increased weight and initial tilt

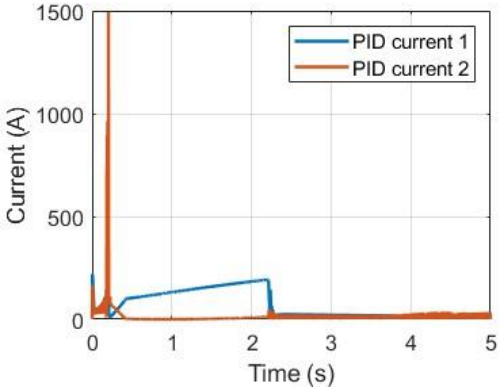

Figure 6.16 Control currents under PID control in a two-point maglev bogie system with increased weight and initial tilt

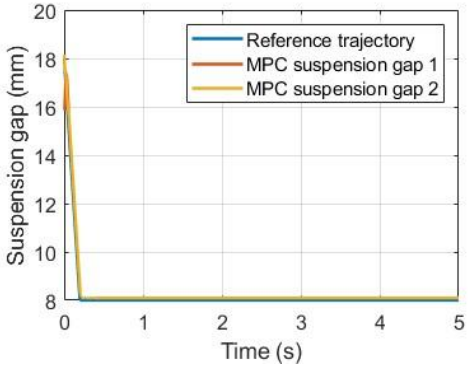

Figure 6.17 Suspension gaps during levitation under MPC control in a two-point maglev bogie system with increased weight and initial tilt

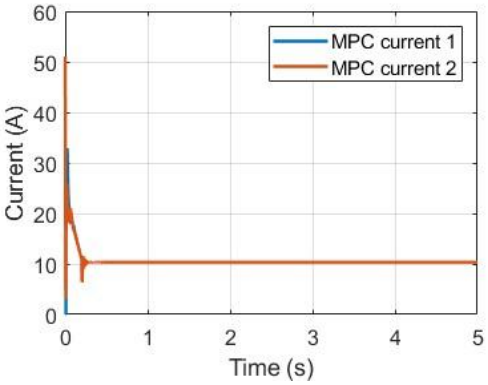

Figure 6.18 Control currents under MPC control in a two-point maglev bogie system with increased weight and initial tilt

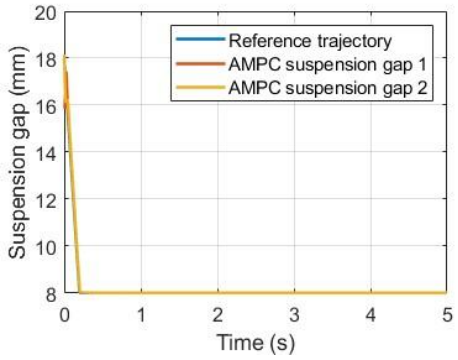

Figure 6.19 Suspension gaps during levitation under AMPC control in a two-point maglev bogie system with increased weight and initial tilt

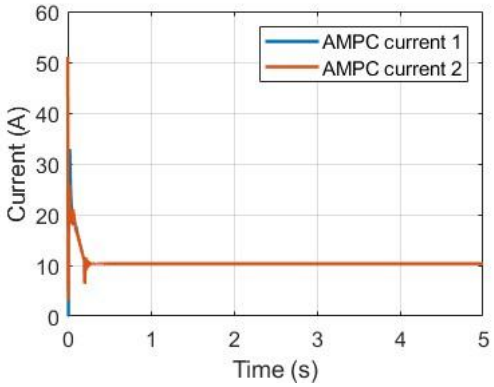

Figure 6.20 Control currents under AMPC control in a two-point maglev bogie system with increased weight and initial tilt

6.3.2. Discussion

The simulation studies in this chapter provide an in-depth evaluation of PID, MPC, and AMPC controllers under diverse operating conditions for a two-point maglev bogie system. The scenarios include varying levitation speeds, increased system weight, and initial tilt angles, offering a comprehensive analysis of each control strategy's strengths and limitations.

The PID controller failed to stabilize the system in more demanding conditions, with the suspension gaps diverging and control currents exceeding 200 A, far surpassing the physical limit of 60 A. This highlights its inability to manage the coupled dynamics of the two-point suspension system effectively. The MPC controller successfully stabilized the system in standard conditions, such as a levitation speed of 5 mm/s and a system weight of 750 kg, where the suspension gaps reached the target of 8 mm within 0.25 seconds. However, when the system weight increased to 1000 kg and a tilt angle of 0.001 rad was introduced, the MPC controller

exhibited steady-state errors of approximately 0.1 mm due to the mismatch between the prediction model (750 kg) and the actual system parameters. Despite these errors, the control currents remained within acceptable limits, peaking at 25 A.

The AMPC controller demonstrated superior adaptability by dynamically updating its prediction model to mitigate parameter mismatches. Under challenging conditions, such as an increased system weight and initial tilt, AMPC stabilized the suspension gaps at the target of 8 mm within 0.2 seconds, with no steady-state errors. The control currents generated by AMPC were well-regulated, peaking at 26 A, and consistently remained within system constraints. Even at a faster levitation speed of 50 mm/s, AMPC maintained its precision and stability, effectively addressing the system's dynamic changes.

The results underline the limitations of PID control in handling complex dynamics and illustrate the strengths of MPC and AMPC in achieving robust stabilization. AMPC, with its adaptive prediction model, proves particularly effective in minimizing errors and ensuring system stability under varying and challenging conditions, making it a robust choice for two-point suspension systems.

6.4. Experiments

The experimental study presented in this section builds upon the simulation studies conducted in Section 6.3, transitioning from numerical analysis to real-world validation. While the simulation models provided insight into the dynamics and control performance of the two-point suspension system, this experimental investigation employs a full-scale 1:1 maglev bogie structure system to verify the practical feasibility of the designed controllers.

6.4.1. Introduction of The Experiment Instruments

The experimental setup is depicted in Figure 6.21, which illustrates the physical structure and key components of the 1:1 scale maglev bogie suspension system. The figure highlights the central bogie frame supported by two air springs and equipped with four evenly distributed electromagnets. The electromagnets are divided into two groups: the front group and the rear group, with each pair connected in series, ensuring synchronized current for the magnets in the same group.

In Figure 6.21, the electrical cabinet provides the necessary DC 330V and DC 110V power supply to the system, ensuring stable and sufficient energy for the operation of the electromagnets. The operating console is shown as the interface for real-time system control, allowing commands to be sent to the controller while monitoring critical parameters during the experiment. The control box is responsible for directing current to the electromagnets based on the control signals calculated by the control algorithm. The air springs, visible beneath the suspension frame, are connected to an air source system, which adjusts their pressure to simulate different loading conditions, such as varying passenger loads. These elements are integrated to provide a comprehensive experimental platform for testing and validating the control algorithms under realistic conditions.

The operational workflow includes initializing the system through the electrical cabinet and the control box, which energizes the electromagnets to set the baseline suspension gaps. Real-time data from the gap sensors at both ends of the bogie frame is processed by the controller, and corresponding control actions are applied to the electromagnets. During the experiments,

the air springs apply dynamic loads to the suspension frame, enabling the evaluation of the control algorithms' performance and robustness. The data acquisition system records the suspension gaps, electromagnet currents, and air spring pressures, providing detailed insights into system dynamics and control effectiveness.

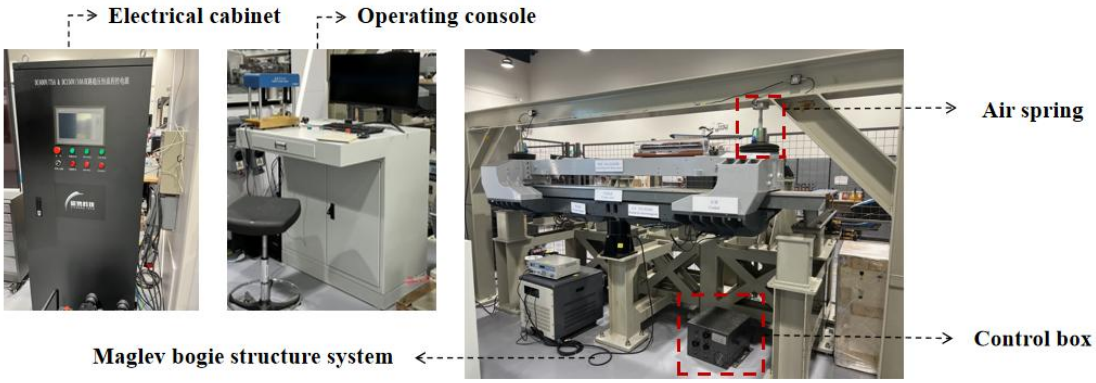

Figure 6.21 The experimental setup of the full-scale 1:1 maglev bogie suspension system

6.4.2. Levitation Experiment for Two-Point Suspension System

This experiment aims to evaluate the performance of PID, MPC, and AMPC controllers in the levitation process of a two-point suspension system. Starting from a suspension gap of 17 mm, the system was tasked with achieving a stable levitation gap of 8 mm. The two-point suspension system, with its inherent coupling dynamics, presents significant control challenges due to interactions between the suspension points and the rotational stability requirements. The experiment utilized the full-scale maglev bogie described in Section 6.4.1, with the controllers designed in Section 6.2. The control parameters remained consistent with those used in the simulation studies in Section 6.3. Figure 6.22 to Figure 6.27 depict the suspension gaps and corresponding control currents during the levitation process under each control strategy,

providing insight into their ability to manage the transition to stable levitation.

The PID controller, as seen in Figure 6.22 and Figure 6.23, struggled with the coupling dynamics of the two-point system. The suspension gaps exhibited significant oscillations, with an overshoot of approximately 3 mm occurring around 1.2 seconds. Stabilization to the target gap required roughly 3 seconds. Moreover, the suspension gaps at the two points were not synchronized, revealing the PID controller's inherent limitations in handling MIMO systems. The control currents showed substantial fluctuations, with peak values exceeding 20 A. This inefficiency reflects the challenges of the PID controller in dealing with interaction forces and rotational dynamics, making it unsuitable for precise control in this application.

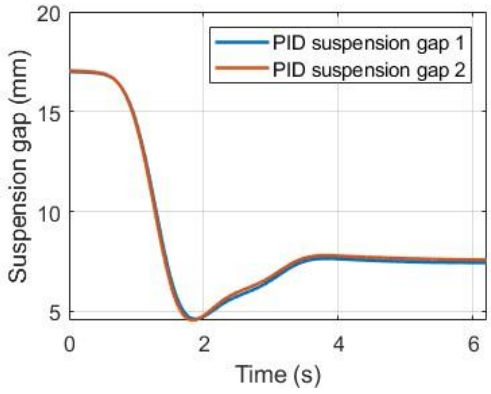

Figure 6.22 Suspension gaps during levitation under PID control for the two-point suspension system

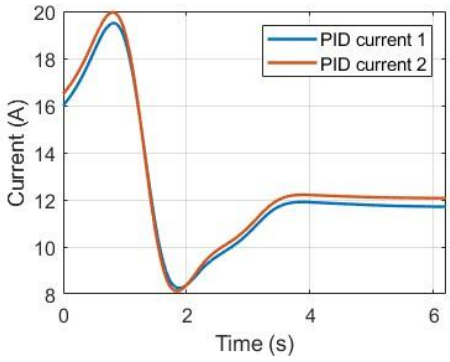

Figure 6.23 Control currents during levitation under PID control for the two-point suspension system

The MPC controller demonstrates smoother transitions compared to the PID controller, as shown in Figure 6.24. The suspension gaps overshoot slightly but avoid the large oscillations observed with PID. However, due to the discrepancy between the prediction model and the actual system, the MPC controller introduces a considerable steady-state error, with the final

suspension gaps deviating notably from the target of 8 mm. This steady-state error is non-negligible and undermines the accuracy of the MPC controller in achieving precise levitation. Figure 6.25 shows that the control currents for the MPC controller stabilize at around 12 A, with initial peaks reaching approximately 22 A. While the MPC controller handles the transient phase better than PID, the static error remains a significant limitation.

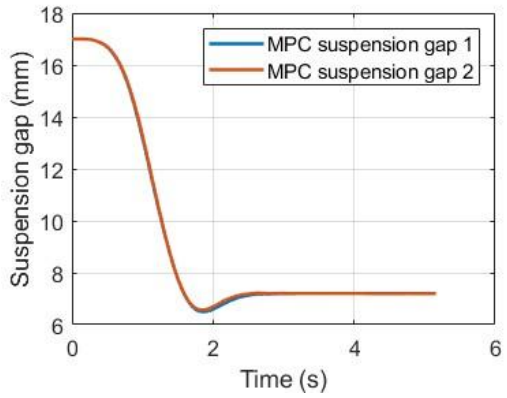

Figure 6.24 Suspension gaps during levitation under MPC control for the two-point suspension system

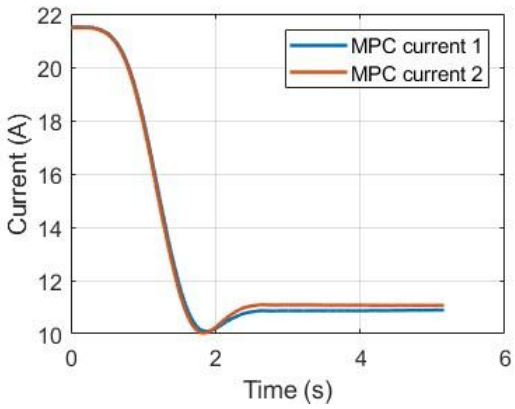

Figure 6.25 Control currents during levitation under MPC control for the two-point suspension system

The AMPC controller outperforms both PID and MPC, as demonstrated in Figure 6.26 and Figure 6.27. The suspension gaps transition smoothly from 17 mm to 8 mm with minimal overshoot and, importantly, no visible steady-state error. This superior performance stems from the AMPC controller's ability to dynamically update its prediction model using real-time system data. By adapting the model to reflect the actual dynamics, the AMPC controller compensates for the inaccuracies that led to the MPC controller's steady-state error. The control currents for AMPC peak similarly to MPC but stabilize more quickly and with better symmetry

between the two electromagnet groups.

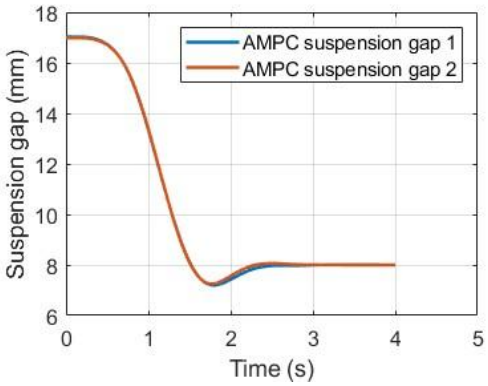

Figure 6.26 Suspension gaps during levitation under AMPC control for the two-point suspension system

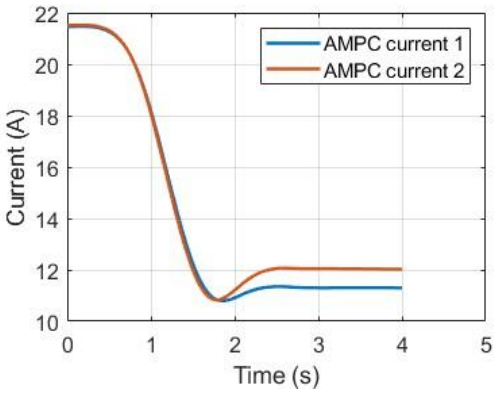

Figure 6.27 Control currents during levitation under AMPC control for the two-point suspension system

The results of this experiment highlight the significant advantages of the AMPC controller in managing both transient and steady-state performance in a realistic two-point suspension system. The PID controller struggles to adapt to the coupled dynamics and parameter variations, leading to large oscillations and high current demand. The MPC controller, though more effective in transient performance, suffers from substantial steady-state error due to its reliance on a static prediction model. In contrast, the AMPC controller leverages its adaptive capabilities to achieve precise levitation control while effectively mitigating the effects of system asymmetries and model inaccuracies.

6.4.3. Loading Experiment for Two-Point Suspension System

The loading experiment, as detailed in this section, evaluates the performance and robustness of the three controllers when the maglev bogie is subjected to incremental loading conditions. Following the levitation process described in Section 6.4.2, the maglev bogie was stabilized at

an 8 mm suspension gap under the control of the respective controllers. Subsequently, incremental loads were applied to each end of the suspension frame using the air springs, simulating varying passenger or cargo conditions. This experimental procedure allows for a comprehensive assessment of the controllers' ability to maintain stability under dynamic loading scenarios.

The loading process begins with an initial stable suspension state. At this point, a load of 20 kg is applied simultaneously to both ends of the suspension frame. The system is allowed to stabilize before the next increment is introduced. This process continues incrementally, with loads increasing to 50 kg, 80 kg, 110 kg, 140 kg, 170 kg, and finally 200 kg at each end. Between each loading step, the system is monitored to ensure stability before proceeding. The air springs were used to apply these loads with precise control, and real-time measurements of the suspension gaps and control currents were recorded throughout the experiment. The experimental data includes the suspension gaps at both ends of the bogie frame and the corresponding control currents for each controller. This data highlights the controllers' performance under increasing loads, focusing on their ability to maintain the desired suspension gap of 8 mm.

The experimental results for the PID, MPC, and AMPC controllers under the loading test, as illustrated in Figure 6.28 to Figure 6.33, provide critical insights into their performance under varying load conditions. Figure 6.28 and Figure 6.29 present the performance of the PID controller. It successfully maintained the target suspension gap under loads up to 80 kg. However, as the load increased to 110 kg, the PID controller failed to stabilize the suspension

gap, with deviations growing uncontrollably. During the stable phases, the current peaked at approximately 25 A, but instability prevented the controller from managing higher loads effectively. This behavior indicates the limitations of the PID controller in adapting to rapidly changing load conditions due to its fixed parameters.

The MPC controller's results, shown in Figure 6.30 and Figure 6.31, reveal that it failed to achieve the target 8 mm suspension gap even in its initial steady state. The suspension gap deviated by approximately 0.7 mm due to the mismatch between the prediction model and the actual system dynamics. During the loading phase, the system maintained stability up to 50 kg, but instability occurred when the load reached 80 kg, with the suspension gap deviating uncontrollably. The inability to stabilize larger loads highlights the effect of the static prediction model, which does not adapt to changes in system parameters such as increased mass.

Figure 6.32 and Figure 6.33 highlight the performance of the AMPC controller. Unlike the PID and MPC controllers, the AMPC controller achieved the target 8 mm suspension gap in the initial unloaded condition. The controller successfully stabilized the system as the load increased incrementally, maintaining stability up to 170 kg with minimal deviations in the suspension gap, which remained within ±0.2 mm during stable periods. However, upon 200 kg, the system lost stability, with the suspension gaps deviating significantly and the current output rising sharply before failure. The AMPC controller's adaptive prediction model enabled it to accommodate the dynamic changes in load effectively, outperforming both the PID and MPC controllers up to 170 kg.

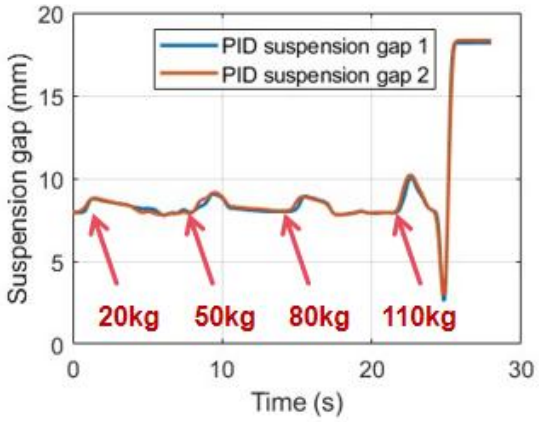

Figure 6.28 Suspension gap under PID control during loading experiment

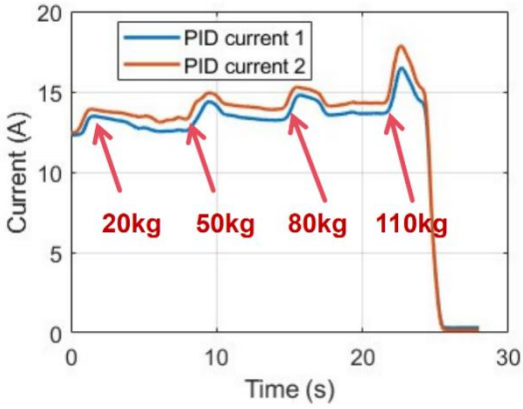

Figure 6.29 Control current under PID control during loading experiment

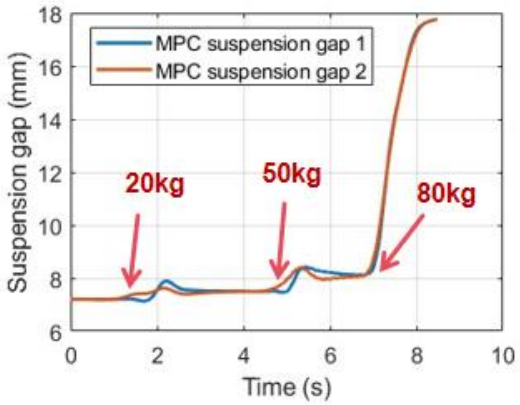

Figure 6.30 Suspension gap under MPC control during loading experiment

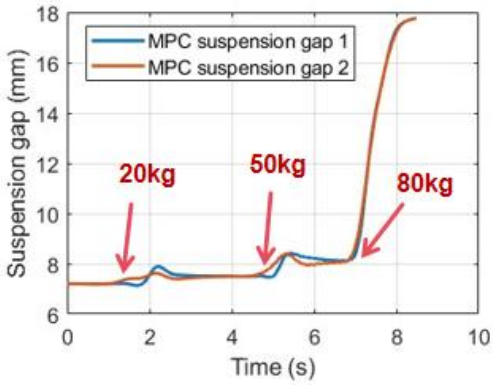

Figure 6.31 Control current under MPC control during loading experiment

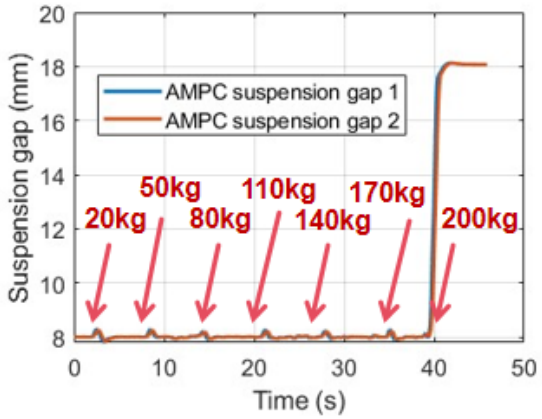

Figure 6.32 Suspension gap under AMPC control during loading experiment

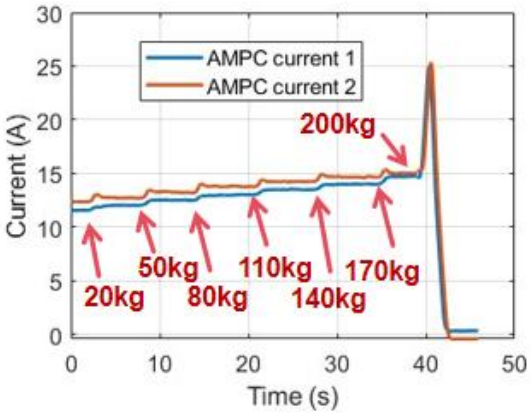

Figure 6.33 Control current under AMPC control during loading experiment

6.4.4. Discussion

In conclusion, the PID controller lost stability beyond 120 kg, and the MPC controller failed at 50 kg, demonstrating significant limitations in handling dynamic loading. The AMPC controller, while maintaining stability up to 170 kg, failed when the load surpassed this value. These results underscore the superior adaptability and robustness of the AMPC controller compared to the other two controllers, particularly in scenarios with substantial and varying loads.

6.5. Conclusions

This chapter explored the dynamics, control strategies, and performance evaluation of a two-point maglev suspension system through simulations and experiments. Starting with the development of a detailed dynamic model, the chapter introduced the two-point suspension system, incorporating rotational stability and interactions between the two suspension points. The system dynamics were expressed using state-space equations, and the control objectives were outlined to ensure stable levitation and robust response to disturbances.

Three controllers—PID, MPC, and AMPC—were designed and analyzed for the two-point system. The PID controller, leveraging parameters from the single-point system, demonstrated basic control capabilities but lacked adaptability to dynamic changes. The MPC controller provided enhanced performance by optimizing control inputs over a prediction horizon; however, its fixed prediction model introduced steady-state errors under mismatched conditions. The AMPC controller, utilizing an adaptive prediction model based on the ARX framework, outperformed the other controllers, effectively managing uncertainties and maintaining stability under varying conditions.

The simulation studies concentrated on the levitation process, where the system transitioned from a lowered state to the target suspension gap of 8 mm. The performance of the three controllers was evaluated under varying initial conditions and system parameters. The results demonstrated that the AMPC controller exhibited superior performance, maintaining minimal steady-state errors and achieving faster convergence compared to the MPC and PID controllers. The MPC controller, while improving upon PID, showed steady-state errors due to the mismatch between its prediction model and the actual system dynamics. The PID controller struggled with stability under dynamic conditions, particularly with higher initial deviations.

Experiments were conducted to validate the simulation findings using a full-scale 1:1 maglev bogie system. The levitation experiments reinforced the simulation results, highlighting the AMPC controller's adaptability and robustness. In contrast, the MPC and PID controllers showed limitations in handling model mismatches and system uncertainties. The loading experiments further emphasized these differences, with the AMPC controller successfully

maintaining stability under loads up to 200 kg, far exceeding the capabilities of the MPC and PID controllers.

In summary, this chapter demonstrated the feasibility and effectiveness of AMPC in controlling a two-point maglev suspension system, particularly in scenarios involving dynamic loads and model uncertainties. While the AMPC controller consistently outperformed the other strategies, the results also highlighted the importance of further refining adaptive techniques to handle extreme operating conditions and enhance system robustness.

Chapter 7. Dynamic Performance Analysis of the Maglev Train with AMPC Controller

7.1. Introduction

Building upon the findings of the previous chapter, which demonstrated the feasibility and superior performance of AMPC in a two-point maglev suspension system, this chapter further expands the study by incorporating a three-dimensional dynamic interaction model of the maglev train. This model integrates the interactions between the train, track, and bridge system, providing a comprehensive analysis of the maglev system's behavior under practical operating conditions.

The focus of this chapter lies in evaluating the dynamic performance of the maglev train under varying track irregularities and operating speeds. Track irregularities—categorized as smooth, moderate, and severe—are applied symmetrically to both rails to simulate real-world disturbances. These disturbances introduce challenges for the suspension system in maintaining stable levitation, particularly at higher speeds and under dynamic loading conditions. The three-dimensional model captures not only the vertical dynamics of the suspension gaps and suspension forces but also the vibrational response of the vehicle body, expressed as acceleration.

Given the observed similarity in dynamic responses among the suspension bogies, the analysis focuses on the third suspension bogie as a representative case. The study investigates the system's behavior under severe track irregularities at four distinct speeds—60 km/h, 100 km/h, 140 km/h, and 180 km/h—to assess the robustness and adaptability of the AMPC controller.

Comparisons with smooth and moderate irregularities further emphasize the progressive impact of increasing track disturbances on the suspension system.

The introduction of the three-dimensional dynamic model enables a holistic evaluation of the maglev system's performance, considering the complex interplay between the suspension system, track irregularities, and bridge dynamics. By analyzing the suspension gaps, electromagnet currents, suspension forces, and the vehicle's vibrational acceleration, this chapter highlights the AMPC controller's ability to manage external disturbances and maintain stability across a wide range of operating conditions. The results provide critical insights into the system's robustness and passenger comfort, offering valuable guidance for the optimization of maglev train control strategies in real-world applications.

7.2. Maglev Trian-track-bridge Dynamic Model

7.2.1. Multi Body Dynamic Model of the Maglev Train

The maglev train model described is based on the experimental train developed by Tongji University, as depicted in Figure 7.1. Figure 7.2 elucidates the structural nuances of one maglev bogie, which comprises a single carriage supported by five maglev bogies. Each bogie is equipped with four air springs that facilitate the connection to the carriage, serving to mitigate some of the vibrations transmitted from the bogie to the carriage. Additionally, each bogie is decoupled into left and right sections, with each section housing four electromagnets. These electromagnets are responsible for generating the levitation force that sustains the train in suspension. The left part and right part of one maglev bogie are connected by anti-rolling beams.

Figure 7.1 Tongji University maglev train

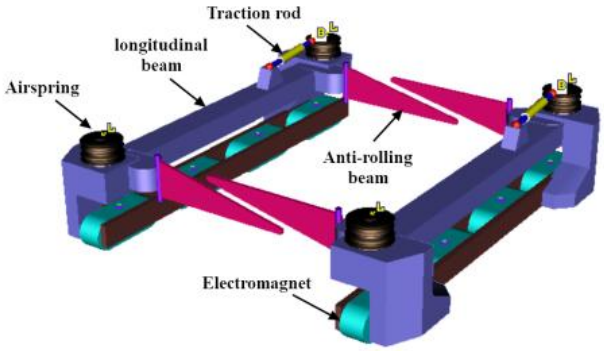

Figure 7.2 Structural diagram of maglev bogie

The carriage and each decoupled half of the maglev bogie are endowed with six degrees of freedom: vertical levitation, lateral sway, longitudinal motion (forth and back), yaw, pitch, and roll. This comprehensive range of motion ensures the train's adaptability to various track conditions and dynamic requirements. Figure 7.4 illustrates the interaction forces between the bogies and the carriage, with the vertical force denoted as $FxxZ$ and the lateral force as $FxxY$. Additionally, the figure represents the maglev force of every magnet with the symbol $FBxZx$ and the interaction force between the connected anti-rolling beams as $FRxZx$. All the forces

are simplified to concentrated force. These forces govern the stability and maneuverability of the maglev train system.

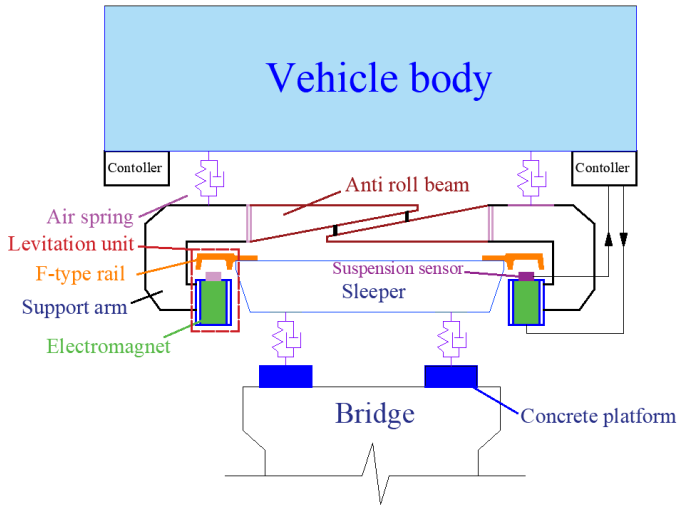

Figure 7.3 Simplified maglev train-track-bridge system

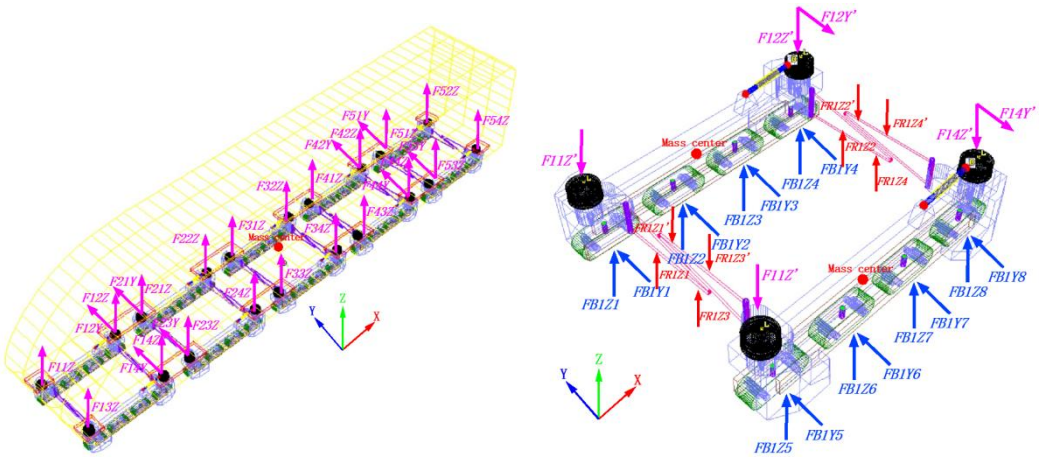

(a) Force of carriage (b) Force of bogie

Figure 7.4 Interaction force between bogies and carriage

Based on the force dynamics within the train system, it is feasible to establish force equilibrium equations for both the carriage and the bogies. These equations take into account the various

forces acting upon each component of the system, ensuring a comprehensive understanding of the interaction between the carriage, bogies, and the generated levitation forces.

(1). Lateral force equilibrium equation of carriage

$$M_c \ddot{y}_c + \sum_{i=1}^{5} \sum_{j=1}^{4} F_{ijy} = 0 \tag{7.1}$$

where M_c is the mass of the carriage, $\ddot{y}_c$ is the lateral acceleration of the carriage, F_{ijy} is the lateral force from the ith bogie and jth air spring applied to the carriage.

(2). Vertical force equilibrium equation of carriage

$$M_c \ddot{z}_c + \sum_{i=1}^{5} \sum_{j=1}^{4} F_{ijz} = 0 \tag{7.2}$$

where $\ddot{z}_c$ is vertical acceleration of the carriage, F_{ijz} is vertical force from the ith bogie and jth airspring applied to the carriage.

(3). Rolling force equilibrium equation of carriage

$$J_{cx} \ddot{\alpha}_{cx} + \left(\sum_{i=1}^{5} \sum_{j=3}^{4} F_{ijz} - \sum_{i=1}^{5} \sum_{j=1}^{2} F_{ijz} \right) l_{cy} - \sum_{i=1}^{5} \sum_{j=1}^{4} F_{ijy} \, h_{cz} = 0 \tag{7.3}$$

where J_{cx} is rotational inertia of the carriage around X-axis, $\ddot{\alpha}_{cx}$ is angular acceleration of the carriage around X-axis, l_{cy} is the distance between the mass center of carriage and the position of F_{ijz} along Y-axis, h_{cz} is the distance between the center of carriage mass and the position of

F_{ijy} along Z-axis.

(4). Yawing force equilibrium equation of carriage

$$J_{cx}\ddot{\alpha}_{cx} + \left(\sum_{i=1}^{5}\sum_{j=3}^{4} F_{ijz} - \sum_{i=1}^{5}\sum_{j=1}^{2} F_{ijz}\right) l_{cy} - \sum_{i=1}^{5}\sum_{j=1}^{4} F_{ijy}\, h_{cz} = 0 \tag{7.4}$$

where J_{cz} is rotational inertia of the carriage around Z-axis, $\ddot{\alpha}_{cz}$ is angular acceleration of the carriage around Z-axis.

(5). Pitching force equilibrium equation of carriage

$$J_{cy}\ddot{\alpha}_{cy} + \left(\sum_{i=4}^{5}\sum_{j=1}^{4} F_{ijz}\, l_{cijx} + F_{32z} l_{c32x} + F_{34z} l_{c34x} - F_{31z} l_{c31x} - F_{33z} l_{c33x} - \sum_{i=1}^{5}\sum_{j=1}^{4} F_{ijz} l_{cijx}\right) = 0 \tag{7.5}$$

where J_{cy} is rotational inertia of the carriage around Y-axis. $\ddot{\alpha}_{cy}$ is angular acceleration of the carriage around Y-axis. l_{cijx} is the distance between the mass center of carriage and the position of F_{ijy} along X-axis.

(6). Lateral force equilibrium equation of maglev bogie

$$M_b \ddot{y}_b - \sum_{i=1}^{4} F_{b1yi} + F'_{12y} = 0 \tag{7.6}$$

where M_b is the mass of the unilateral bogie. $\ddot{y}_b$ is the lateral acceleration of the unilateral bogie along Y-axis. $F'_{12\mathrm{y}}$ is the force applied to bogie from air spring along Y-axis. F_{b1yi} is the guiding force of the ith electromagnet along Y-axis.

(7). Vertical force equilibrium equation of maglev bogie

$$M_b\ddot{z}_b - \sum_{i=1}^{4} F_{b1zi} + \sum_{i=1}^{2} F'_{1iz} - \sum_{i=1}^{4} F_{r1zi} = 0 \tag{7.7}$$

where $\ddot{z}_b$ is the vertical acceleration of the unilateral bogie along Z-axis, F_{b1zi} is the guiding force of the ith electromagnet along Z-axis, F'_{1iz} is the force applied to bogie from air spring along Z-axis, F_{r1zi} is the force from the anti-roll bar along Z-axis.

(8). Rolling force equilibrium equation of maglev bogie

$$\begin{aligned} J_{bx}\ddot{\alpha}_{bx} - \sum_{i=1}^{2} F_{r1zi}l_{lri} + \sum_{i=3}^{4} F_{r1zi}l_{lri} - F_{r1z1}l_{lxr1} + F_{r1z2}l_{lxr2} - F_{r1z3}l_{lxr3} + F_{r1z4}l_{lxr4} \\ + F'_{11z}l_{lra} - F'_{12z}l_{lra} = 0 \end{aligned} \tag{7.8}$$

where J_{bx} is rotational inertia of the unilateral bogie around X-axis, $\ddot{\alpha}_{bx}$ is angular acceleration of the unilateral bogie around X-axis, F_{r1zi} is the force from the anti-roll bar along Z-axis, l_{lri} is the distance between the mass center of the unilateral bogie and the ith connection point of the anti-roll bar along Y-axis, F_{b1yi} is the guiding force of the ith electromagnet along Y-axis, h_{bd} is the distance between the mass center of the unilateral bogie and F_{b1yi} along Z-axis, F_{b1zi} is the levitation force of the ith electromagnet along Z-axis, l_{by1} is the distance between the mass center of the unilateral bogie and F_{b1zi} along Y-axis, $F'_{12\mathrm{y}}$ is the force applied to bogie

from air spring along Y-axis, h_{bd} is the distance between the center of the unilateral bogie mass and F'_{1y1} along Z-axis, F'_{1iz} is the force applied to bogie from the ith air spring along Z-axis, l_{ay} is the distance between the mass center of the unilateral bogie and airspring along Y-axis.

(9). Pitching force equilibrium equation of maglev bogie

$$J_{by}\ddot{\alpha}_{by} - \sum_{i=1}^{2} F_{b1zi}l_{lxi} + \sum_{i=3}^{4} F_{b1zi}l_{lxi} - F_{r1z1}l_{lxr1} + F_{r1z2}l_{lxr2} - F_{r1z3}l_{lxr3} + F_{r1z4}l_{lxr4} + F'_{11z}l_{lxa} - F'_{12z}l_{lxa} = 0 \tag{7.9}$$

where J_{by} is rotational inertia of the unilateral bogie around Y-axis, $\ddot{\alpha}_{by}$ is angular acceleration of the unilateral bogie around Y-axis, l_{lxi} is the distance along the X-axis between the mass center of the unilateral bogie and the ith lateral force, l_{lxri} is the distance along the X-axis between the mass center of the unilateral bogie and the ith connection of anti-roll bar.

(10).Yawing force equilibrium equation of maglev bogie

$$J_{bz}\ddot{\alpha}_{bz} + \sum_{i=1}^{2} F_{b1yi}\, l_{lxi} - \sum_{i=3}^{4} F_{b1yi}\, l_{lxi} + F'_{12y}l_{lxa} = 0 \tag{7.10}$$

where J_{bz} is rotational inertia of the unilateral bogie around Z-axis. $\ddot{\alpha}_{bz}$ is angular acceleration of the unilateral bogie around Z-axis.

(11).Vertical force equilibrium equation of air spring

$$\left(z_c - z_{b1}\right)k_z + \left(\alpha_{cx}l_{cy} - \alpha_{bx}l_{ay}\right)k_z + \left(\alpha_{cy}l_{cx1} - \alpha_{by}l_{ax}\right)k_z + \left(\dot{z}_c - \dot{z}_{b1}\right)c_z + \left(\dot{\alpha}_{cx}l_{cy} - \dot{\alpha}_{bx}l_{ay}\right)c_z + \left(\dot{\alpha}_{cy}l_{cx1} - \dot{\alpha}_{by}l_{ax}\right)c_z - F_{11z} = 0 \tag{7.11}$$

where z_c is the displacement of carriage along Z-axis, z_{b1} is the displacement of the unilateral bogie, k_z is the stiffness coefficient of the air spring, c_z is the damping coefficient of the air spring.

Drawing from the force analysis and dynamic equilibrium equations, it is possible to construct a simulation model of the maglev train system within Universal Mechanisms (UM), a software designed for multi-body dynamics modeling. By employing the programming language specific to UM, these equations can be translated into a format that the software can interpret and execute. This approach allows for the simulation of the maglev train's behavior under various conditions, offering valuable insights into its dynamics, stability, and overall performance. Table 7.1 enumerates all the parameters required for the equilibrium equations.

Table 7.1 Parameters of 3D maglev system

Symbol	Value
M_c	$12.77 \times 10^{-3}\ kg$
M_b	$750\ kg$
J_{cx}	$2.21 \times 10^{3}\ kg \cdot m^2$
J_{cy}	$3.85 \times 10^{5}\ kg \cdot m^2$
J_{cz}	$3.88 \times 10^{5}\ kg \cdot m^2$
J_{bx}	$460\ kg \cdot m^2$
J_{by}	$1150\ kg \cdot m^2$
J_{bz}	$1200\ kg \cdot m^2$
k_z	$10000\ kN/m$
c_z	$50\ kNs/m$
l_{cy}	$1.01\ m$
h_{cz}	$0.7\ m$

7.2.2. Finite Element Dynamic Model of Guideway System

Benefiting from its low contact noise, the maglev train can operate within urban areas without disturbing the surrounding residents. Consequently, there is no necessity to construct underground tracks, allowing for the selection of viaducts as guideways. This choice not only proves to be more cost-effective but also simplifies the construction process and minimizes the impact on the urban environment. In this section, a finite element model of the standard viaduct guideway system will be developed to serve as the foundational basis for analyzing the dynamic interaction characteristics of the maglev train-track-bridge system. This model aims to comprehensively understand the structural and dynamic responses of the system under

various operational conditions. For example, it aims to obtain the acceleration, displacement and model shapes of the bridges and tracks, thereby facilitating a detailed analysis of the interactions between the maglev train and its supporting infrastructure. The construction of the finite element model adheres to the specifications delineated in Figure 7.5 and Figure 7.6.

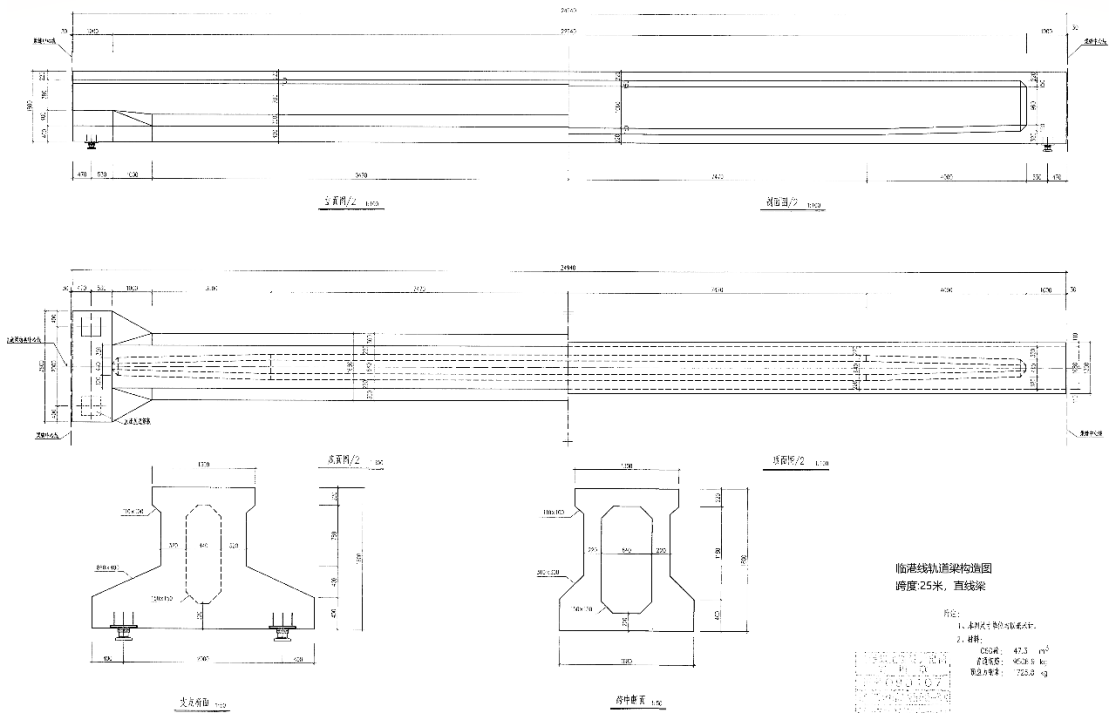

Figure 7.5 Design drawings of bridges

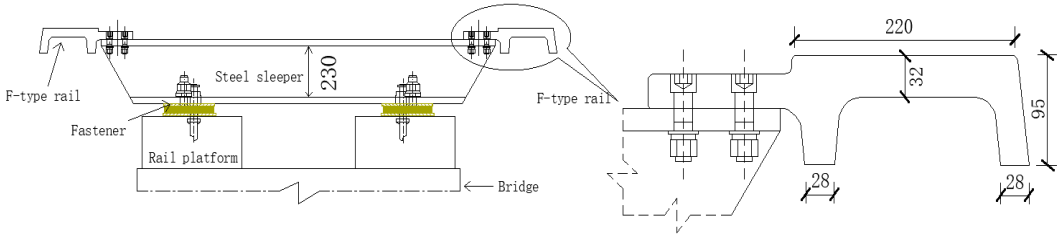

Figure 7.6 Design drawings of sleepers and tracks

The track-bridge system is conducted by ANSYS using solid185 unit. The construction

materials for the bridge are specified as concrete C60, in accordance with the Chinese standard, with the omission of rebars for simplification. The materials utilized for the F-type rails and sleepers are steel Q345, also adhering to the Chinese standard. The design of the simple supported bridge has a span length of 25 meters, with the F-type rail segmented into three parts: two 10-meter sections flanking a central 5-meter section, as illustrated in Figure 7.7. The assembly methodology employs fixed joints to simulate the connection between the F-type rail and the sleepers. The connection between the sleepers and the bearing platform is represented through the use of spring damping units. This approach not only simplifies the model but also ensures that essential dynamic interactions are effectively captured.

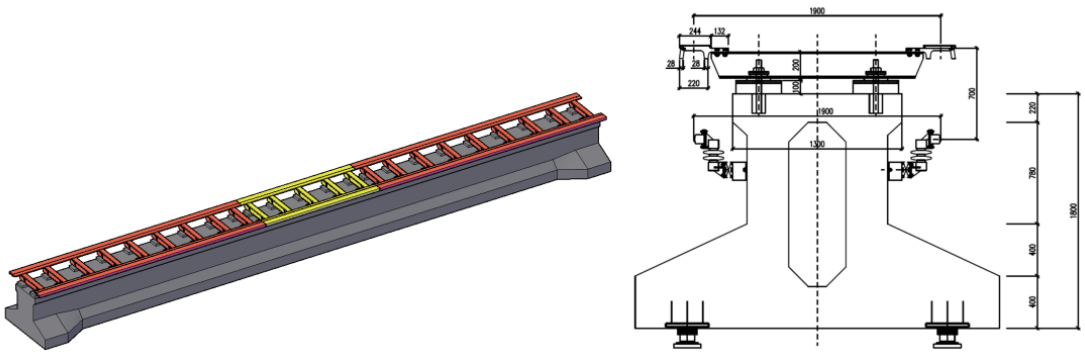

Figure 7.7 Diagrammatic drawings of track-bridge system

Upon the development of the finite element guideway system within ANSYS, the modal shapes of both the bridge and track skeletons can be obtained. Utilizing the Craig-Bampton mode synthesis method [158], the simulation model of the guideway system is integrated with the dynamic simulation model of the train body. This integration facilitates the conduct of interaction dynamic analysis, enabling the following comprehensive examination of the

system's behavior under various operational scenarios.

7.2.3. Controller Design

The AMPC designed for the two-point suspension system in Chapter Chapter 6 is utilized to control the full maglev train system. The two-point AMPC has demonstrated its effectiveness in handling MIMO dynamics, managing disturbances, and maintaining robust performance in the two-point suspension system. These characteristics are directly relevant to the full maglev train system, where multiple suspension gaps and tilt angles need to be controlled simultaneously. Although the full train system introduces additional complexities due to the interactions among multiple bogies, the underlying principles of suspension control remain consistent.

Instead of using a detailed prediction model for the entire train, the two-point prediction model is applied to each bogie. This approach reduces computational complexity while maintaining sufficient accuracy for effective control. In the full train system, each bogie operates as an independent unit within the overall train structure. By applying the two-point suspension model to each bogie, the control strategy balances simplicity and performance.

The AMPC uses the same cost function and constraints as in Chapter Chapter 6. The cost function minimizes the deviations of suspension gaps and tilt angles from their references while penalizing excessive control efforts. Constraints ensure that input currents remain within the physical limits of the electromagnets and that suspension gaps are maintained within safe ranges.

7.2.4. Model Verification Using Field Test Data

To guarantee the accuracy of the simulation model, a field test was conducted. A straight section of the bridges and tracks were chosen as the monitoring objects. The span of the bridge is 25m and the bridge has simple supports at its two ends. Two accelerometers and one draw-wire displacement sensor were installed on the bottom of the bridge at its middle span, as shown in Figure 7.8. One of the accelerometers was to monitor the vertical vibration and the other is to monitor the lateral vibration of the bridge. The draw-wire displacement sensor was to monitor the vertical displacement of the bridge.

Figure 7.8 Monitoring points of the bridge

Figure 7.9 to Figure 7.11 demonstrate the comparison between simulation and field measurement data, offering insight into the accuracy of the simulation model for the maglev train-track-bridge system. The maglev vehicle traversed the measurement point at a speed of 30 km/h. The displacement time history of the bridge at its midspan is shown in Figure 7.9. Both the simulation data and the monitoring data reveal a maximum displacement of approximately -1.8 mm. This agreement indicates that the simulation accurately replicates the static and dynamic displacement behavior of the bridge under maglev train loading, effectively capturing the bridge's midspan deflection profile. Figure 7.10 illustrates the frequency

spectrum of the bridge's vibration derived from monitoring and simulation data. Both data sets exhibit a dominant vibration frequency near 7.8 Hz in the monitoring results and 7.6 Hz in the simulation results. The difference of 0.2 Hz corresponds to a 2.6% error. This close match in the dominant frequency demonstrates the simulation model's ability to reproduce the bridge's primary dynamic characteristics, including its natural frequency and resonance behavior.

The vibration time history of the bridge's midspan is presented in Figure 7.11. The acceleration profile shows a strong correlation between the monitoring and simulation data. The peak acceleration observed in the monitoring data is 0.058 m/s², compared to 0.056 m/s² in the simulation, reflecting an error of approximately 3.4%. The alignment in vibration patterns and decay rates underscores the model's capability to replicate the transient dynamics induced by the maglev vehicle.

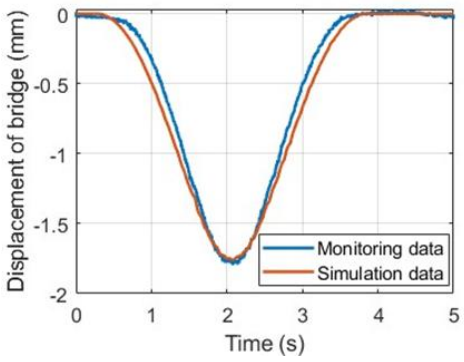

Figure 7.9 Midspan displacement of the bridge

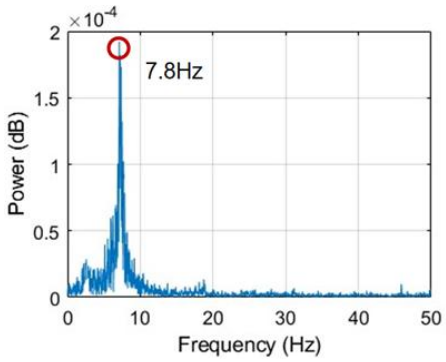

Figure 7.10 Frequency spectrum of bridge Vibration

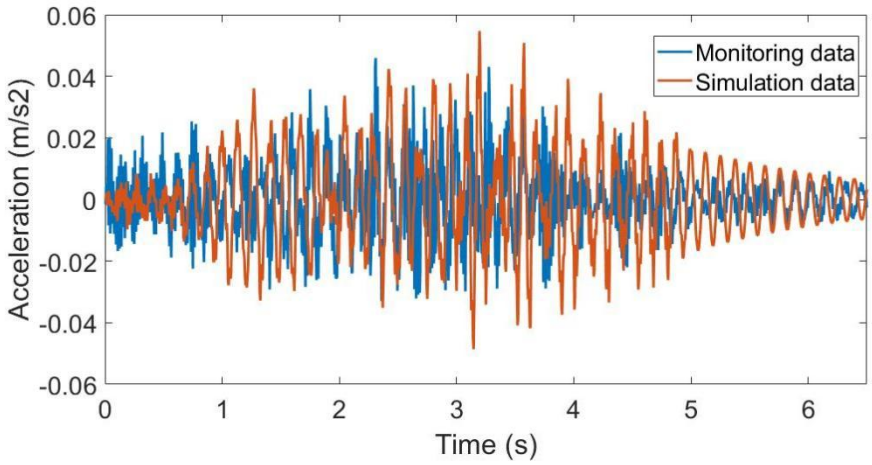

Figure 7.11 Vibration time history of bridge

7.3. Simulation Results and Analysis

7.3.1. Track Irregularities

The verification of the bridge model in Section 7.2.4 demonstrated its accuracy in replicating the dynamic response of the bridge under maglev train loading, as validated through a comparison of simulation results and field test data. Building on this foundation of confidence in the simulation model, this section incorporates track irregularities to evaluate their influence on the dynamic interaction between the maglev train, track, and bridge. This analysis provides critical insights into the robustness of the suspension system and the controller's ability to handle real-world operating conditions.

In real-world applications, maglev trains operate on guideways that are rarely perfectly smooth. Track irregularities, including deviations in vertical alignment and surface imperfections, are inevitable due to construction tolerances, material wear, and environmental effects such as thermal expansion or ground settlement. These irregularities can significantly influence the

dynamic interaction between the maglev train, the track, and the bridge, potentially affecting the suspension stability and passenger comfort. To accurately assess the performance of the maglev suspension system and its controllers, it is essential to incorporate track irregularities into the simulation model. By introducing irregularities, the simulation provides a more realistic representation of operating conditions, enabling a detailed evaluation of how the train's suspension system responds to disturbances.

In this study, track irregularities are generated using power spectral density (PSD) functions, allowing for the systematic examination of the maglev train's dynamic performance under different roughness levels. This enables an in-depth analysis of the controller's ability to maintain suspension stability and mitigate the effects of guideway imperfections. The PSD function used for generating track roughness is expressed as:

$$S(\Omega) = A_s \cdot \frac{1}{\Omega^2}, \Omega = \frac{2\pi}{\lambda} \tag{7.12}$$

where $S(\Omega)$ is power spectral density as a function of the wave number, Ω is wave number inversely related to the wavelength λ and A_s is roughness amplitude defining the magnitude of track roughness.

Multiple track roughness profiles were generated to evaluate the maglev train's performance under varying track conditions. The track irregularity spectrum was constructed by superimposing two key wavelengths: a short wavelength of 1.2 m, determined by the sleeper spacing, and a long wavelength of 25 m, corresponding to the bridge span. This combination ensures the inclusion of both local and structural-scale irregularities, providing a comprehensive representation of real-world track conditions. Three levels of track roughness

were considered, characterized by their roughness parameters (A_s) derived from the standard PSD function:

① **Smooth irregularity:** $A_s = 1.5 \times 10^{-7}$m. This represents a very smooth guideway with minimal irregularities, serving as the baseline for assessing the train's suspension system performance under ideal conditions.

② **Moderate irregularity:** $A_s = 5 \times 10^{-7}$m. This profile simulates a typical guideway with moderate deviations, reflecting the conditions of an average operational track.

③ **Severe irregularity:** $A_s = 1 \times 10^{-6}$m. This introduces significant track irregularities, testing the robustness and adaptability of the maglev suspension system under challenging conditions.

Figure 7.12 illustrates the track roughness profiles generated based on the described PSD function and parameters for a 500-meter segment. Three levels of track irregularities are presented, representing smooth, moderate, and severe irregularity conditions. The vertical axis indicates the amplitude of track irregularities in millimeters, while the horizontal axis shows the track length in meters.

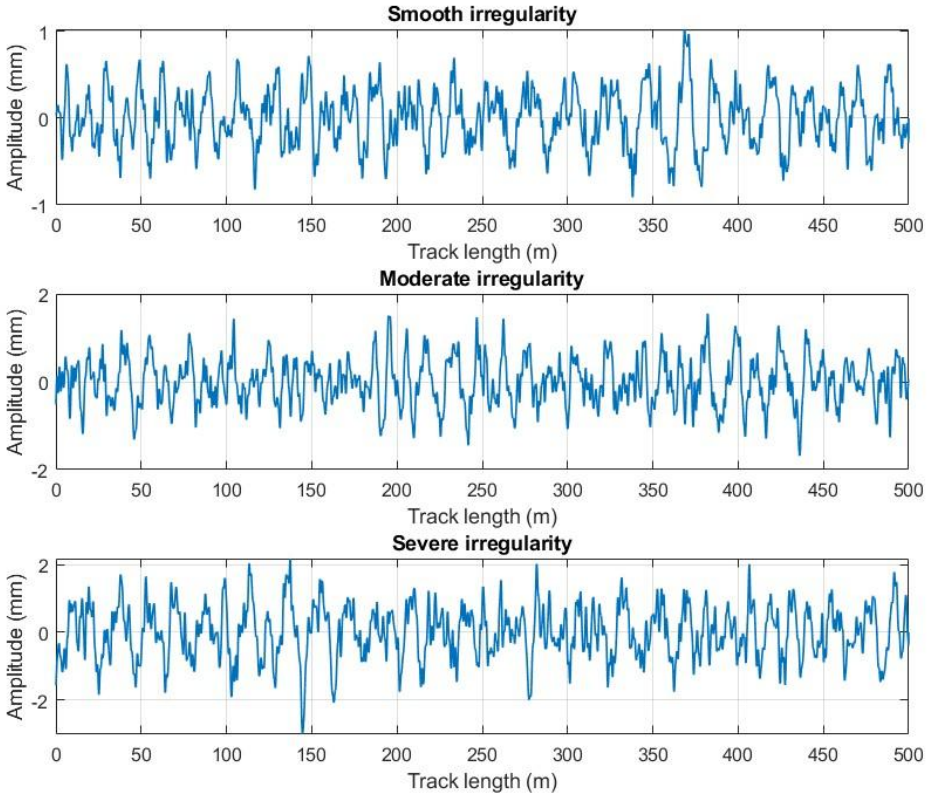

Figure 7.12 Track irregularity profiles for smooth, moderate, and severe conditions

7.3.2. Suspension Performance Under Speed 20 km/h

The track irregularities established in Section 7.3.1, including smooth, moderate, and severe roughness spectra, are applied symmetrically to both the left and right tracks. In this section, the performance of the maglev train under varying track irregularities is evaluated as the vehicle travels at various speeds over two-span bridges. The study focuses on the suspension gaps and electromagnet currents for the five bogies along the vehicle length and the vibration of carriage. Each bogie consists of eight electromagnets, with four electromagnets on each side of the bogie. The front two electromagnets on each side are connected in series, sharing the same current, and the rear two electromagnets on each side are similarly connected. The AMPC

designed in Chapter 6 is employed in this study.

7.3.2.1.Suspension Performance Under Smooth Track Irregularities

Figure 7.13 and Figure 7.14 illustrate the results for the first suspension bogie. The suspension gaps at the four endpoints on each side fluctuate dynamically within the range of 7.6 mm to 8.4 mm, showing that the AMPC controller maintains control accuracy despite disturbances. The responses between the left and right sides show slight differences due to localized variations in track irregularities. The corresponding current responses, depicted in Figure 7.14, oscillate between 5.0 A and 6.5 A, with noticeable adjustments as the controller compensates for real-time disturbances. The smoothness of current variation indicates that the AMPC controller effectively balances the left and right electromagnet forces to stabilize the bogie.

For the second suspension bogie, Figure 7.15 and Figure 7.16 reveal a slight increase in suspension gap deviations, with values ranging between 7.5 mm and 8.5 mm. The irregularities become more pronounced compared to the first bogie, reflecting the cumulative propagation of disturbances as the train progresses along the track. The corresponding current responses exhibit oscillations between 5.2 A and 6.8 A, with slightly higher peaks compared to the first bogie, particularly on the rear electromagnets. This indicates the controller's increased efforts to compensate for amplified disturbances.

Figure 7.17 and Figure 7.18 show the performance of the third suspension bogie. Here, the suspension gap deviations increase further, ranging between 7.5 mm and 8.6 mm. The amplitude of oscillations is more pronounced compared to the earlier bogies, suggesting that track disturbances are accumulating and propagating along the train. The corresponding

currents oscillate between 5.3 A and 6.9 A, with noticeable imbalances between the front and rear electromagnets on both sides. This highlights the controller's effort to counteract increasing disturbances.

The fourth suspension bogie results, presented in Figure 7.19 and Figure 7.20, demonstrate a further amplification of irregularities, with suspension gap deviations ranging between 7.4 mm and 8.7 mm. The corresponding currents show oscillations between 5.3 A and 7.0 A, with the amplitude of current variations reflecting the greater dynamic challenges posed by track irregularities. Differences between the left and right sides become more evident, as the disturbances act asymmetrically on the bogie.

For the fifth suspension bogie, Figure 7.21 and Figure 7.22 display the most significant suspension gap deviations, ranging from 7.3 mm to 8.8 mm. These results indicate the cumulative effect of track irregularities as disturbances propagate along the train. The current responses exhibit oscillations between 5.4 A and 7.2 A, with larger amplitudes compared to earlier bogies. Despite these challenges, the AMPC controller effectively manages to stabilize the bogie, albeit with increased control efforts.

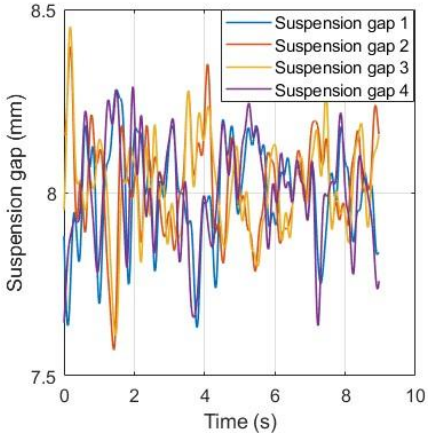

Figure 7.13 Suspension gaps of bogie 1 under smooth track irregularities

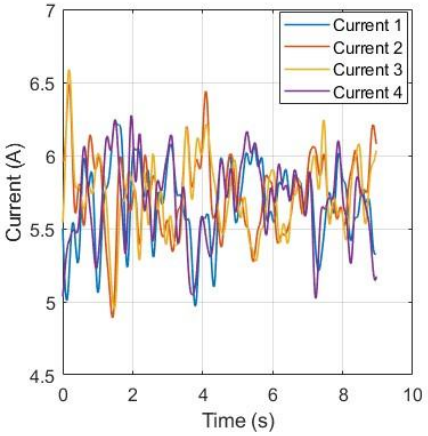

Figure 7.14 Electromagnet currents of bogie 1 under smooth track irregularities

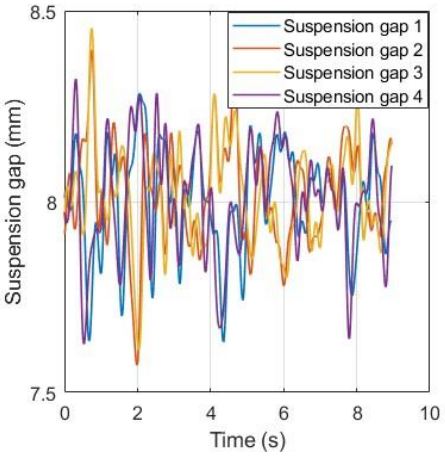

Figure 7.15 Suspension gaps of bogie 2 under smooth track irregularities

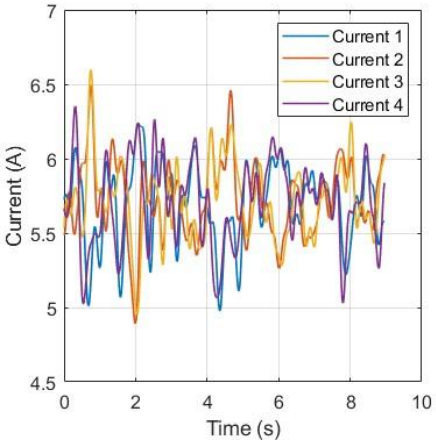

Figure 7.16 Electromagnet currents of bogie 2 under smooth track irregularities

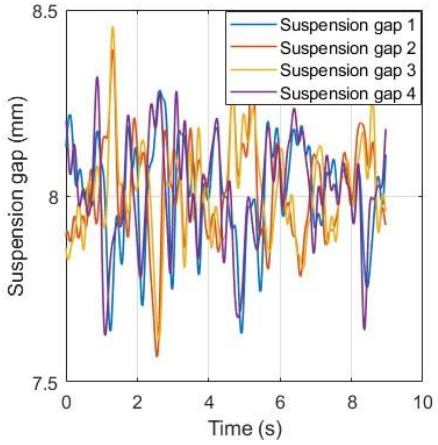

Figure 7.17 Suspension gaps of bogie 3 under smooth track irregularities

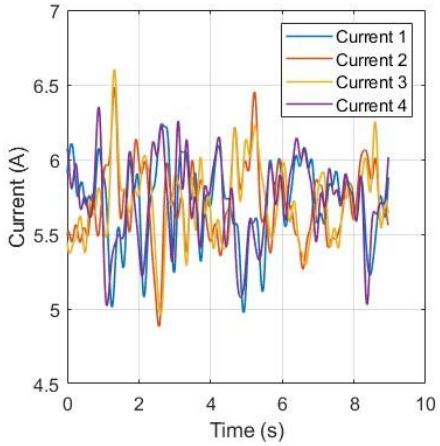

Figure 7.18 Electromagnet currents of bogie 3 under smooth track irregularities

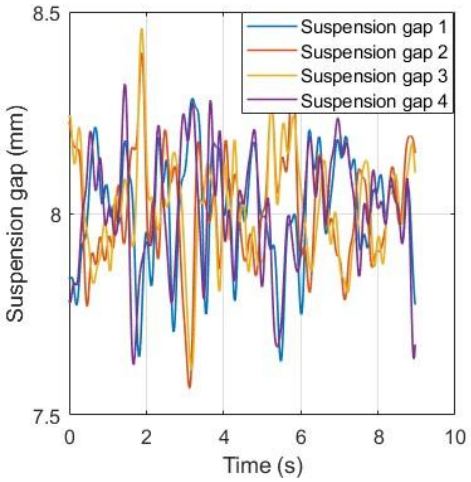

Figure 7.19 Suspension gaps of bogie 4 under smooth track irregularities

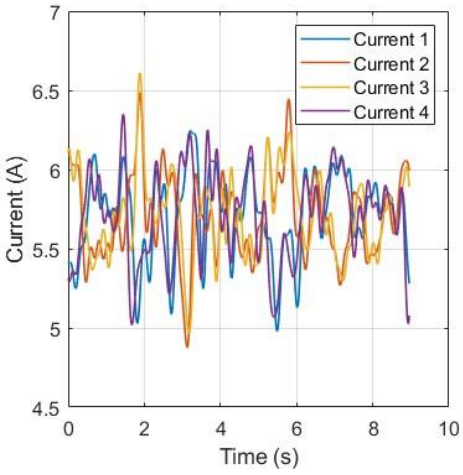

Figure 7.20 Electromagnet currents of bogie 4 under smooth track irregularities

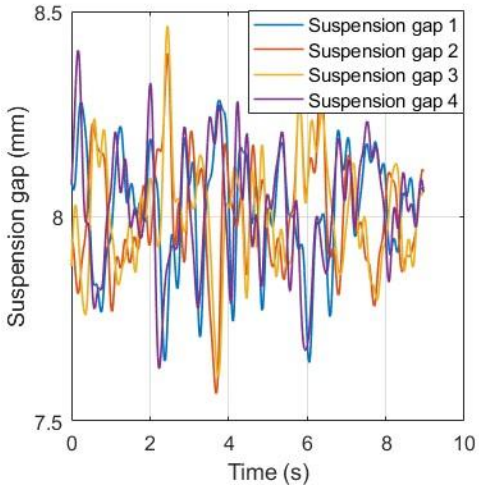

Figure 7.21 Suspension gaps of bogie 5 under smooth track irregularities

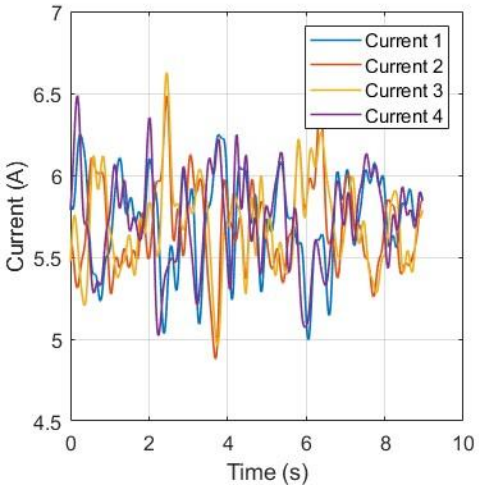

Figure 7.22 Electromagnet currents of bogie 5 under smooth track irregularities

The suspension forces for the five bogies, shown in Figure 7.23 to Figure 7.32, exhibit consistent dynamic behavior under smooth track irregularities as the maglev train travels at 20 km/h. Across all bogies, the suspension forces for the left and right sides fluctuate within a range of approximately 5.0 kN to 7.5 kN, with the mean values stabilizing around 6.2 kN. The variations in suspension forces display similar patterns for each bogie, characterized by small fluctuations around the mean values, with no significant discrepancies between the left and right sides. The front and rear bogies exhibit slightly larger peaks in some instances, likely due to more prominent dynamic interactions near the train's extremities.

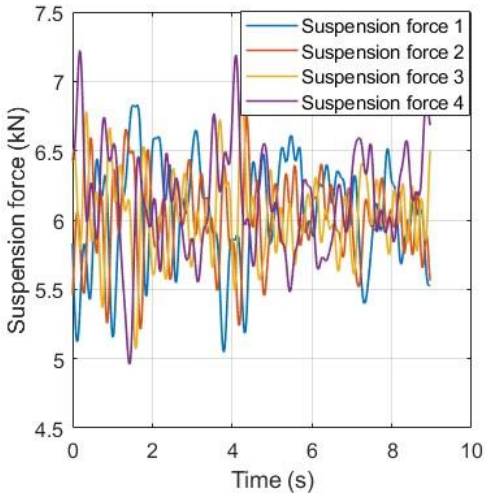

Figure 7.23 Suspension force of left-side electromagnets on bogie 1 under smooth track irregularities

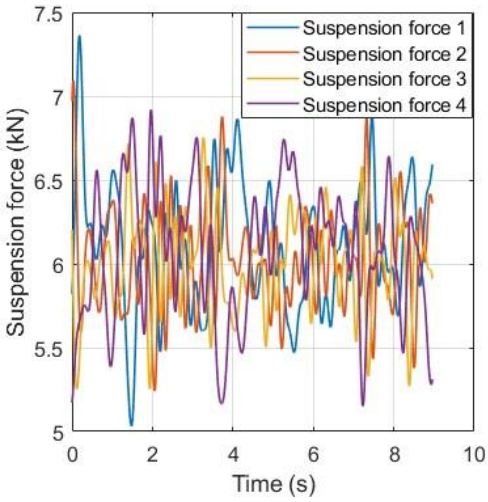

Figure 7.24 Suspension force of right-side electromagnets on bogie 1 under smooth track irregularities

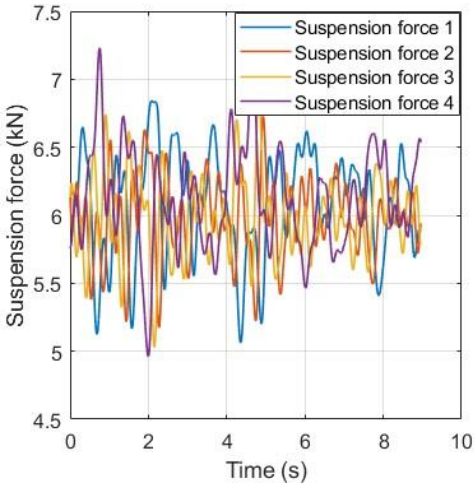

Figure 7.25 Suspension force of left-side electromagnets on bogie 2 under smooth track irregularities

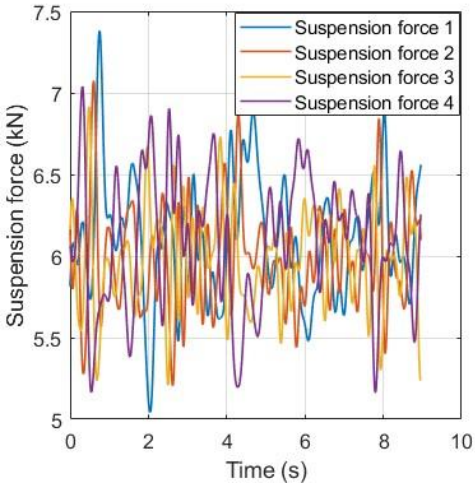

Figure 7.26 Suspension force of right-side electromagnets on bogie 2 under smooth track irregularities

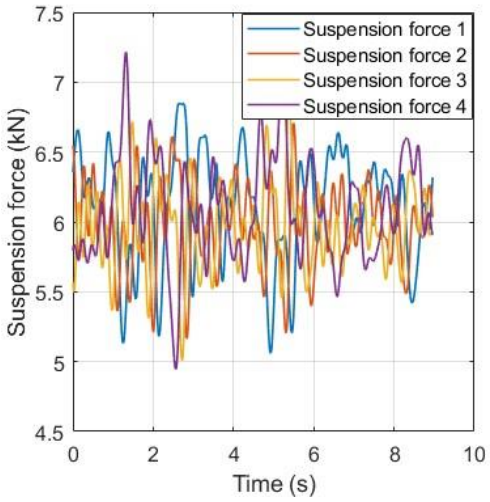

Figure 7.27 Suspension force of left-side electromagnets on bogie 3 under smooth track irregularities

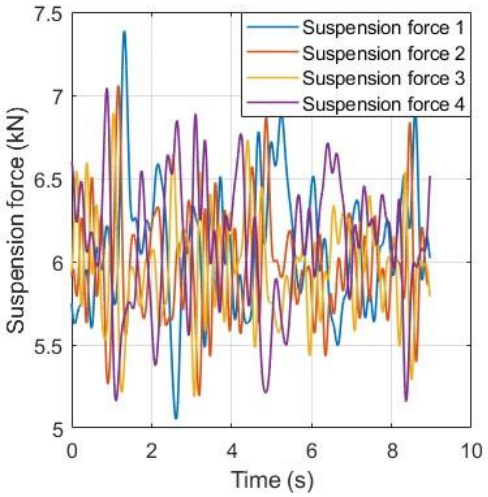

Figure 7.28 Suspension force of right-side electromagnets on bogie 3 under smooth track irregularities

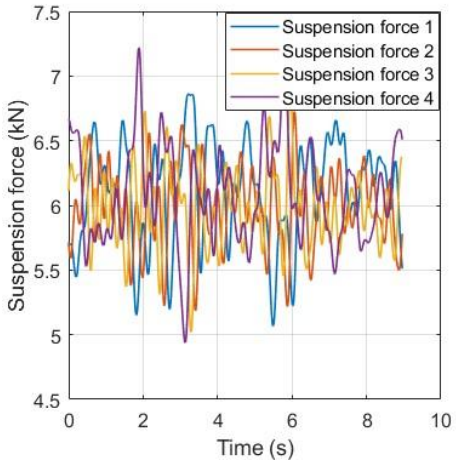

Figure 7.29 Suspension force of left-side electromagnets on bogie 4 under smooth track irregularities

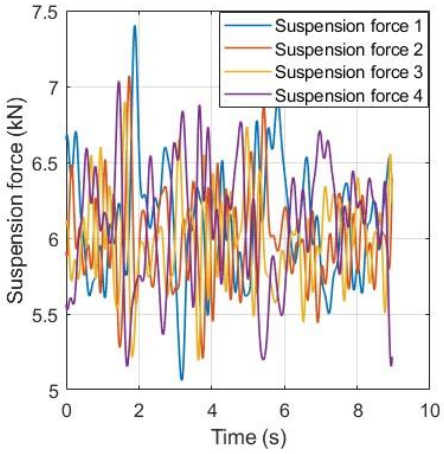

Figure 7.30 Suspension force of right-side electromagnets on bogie 4 under smooth track irregularities

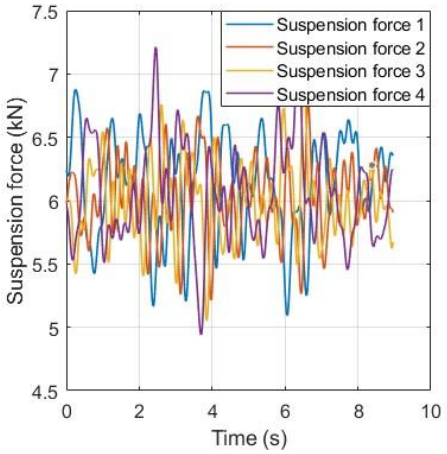

Figure 7.31 Suspension force of left-side electromagnets on bogie 5 under smooth track irregularities

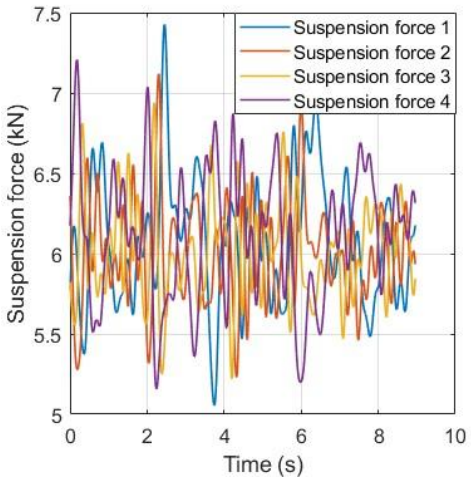

Figure 7.32 Suspension force of right-side electromagnets on bogie 5 under smooth track irregularities

The vibration acceleration at the midsection of the carriage is presented in Figure 7.33. The acceleration fluctuates within a range of approximately -4× 10^{-3} m/s² to 4 × 10^{-3} m/s². These oscillations exhibit a regular pattern, indicating the influence of the track irregularities transferred through the suspension system.

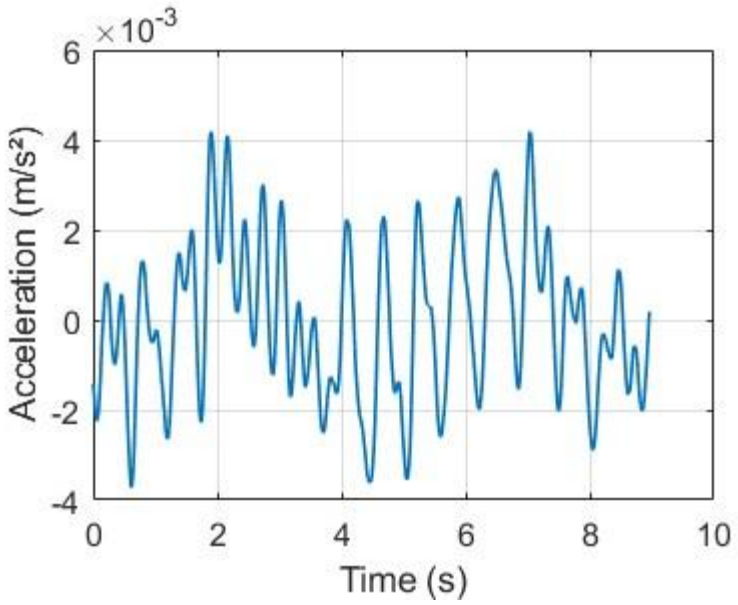

Figure 7.33 Carriage midsection vibration acceleration under smooth track irregularities

7.3.2.2.Suspension Performance Under Moderate Track Irregularities

The results presented in Figure 7.34 to Figure 7.43 correspond to the suspension gaps and electromagnet currents for the five bogies as the train operates under moderate track irregularities at a speed of 20 km/h.

The suspension gaps for each bogie exhibit fluctuations within a range of approximately 7.4 mm to 8.8 mm, showing a slightly greater variation compared to the smooth track irregularities. This increase in fluctuation reflects the influence of moderate irregularities on the suspension control system, which is required to adapt to additional disturbances.

The electromagnet currents also show a corresponding increase in variability, with current values fluctuating between approximately 4.5 A and 7.5 A across all bogies. Similar to the suspension gaps, the current oscillations indicate the system's active effort to maintain stable suspension gaps in response to moderate disturbances. The magnitude of these variations

remains controlled, highlighting the capability of the AMPC to stabilize the system despite the presence of moderate irregularities.

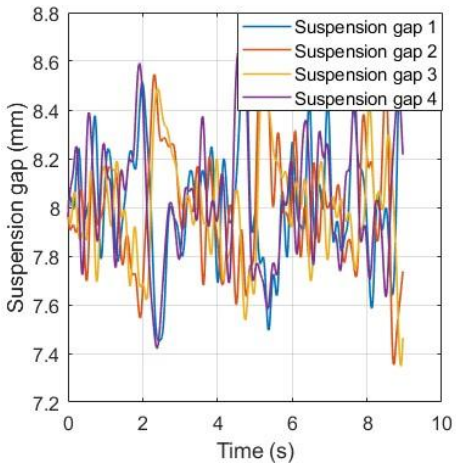

Figure 7.34 Suspension gaps of bogie 1 under moderate track irregularities

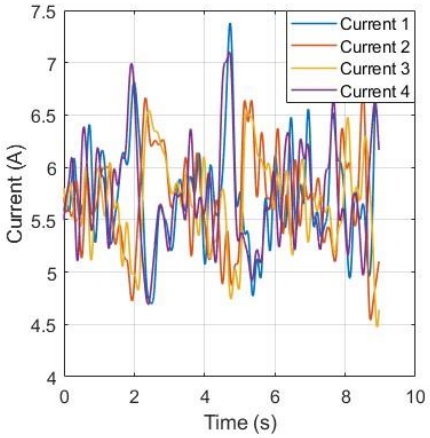

Figure 7.35 Electromagnet currents of bogie 1 under moderate track irregularities

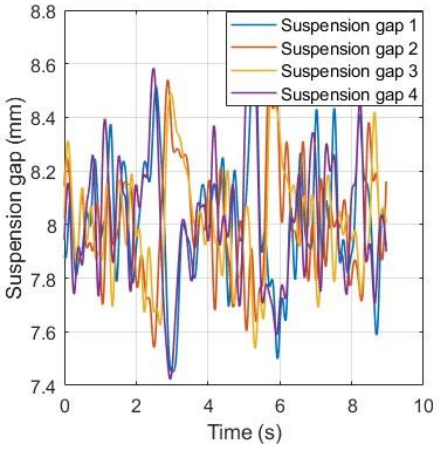

Figure 7.36 Suspension gaps of bogie 2 under moderate track irregularities

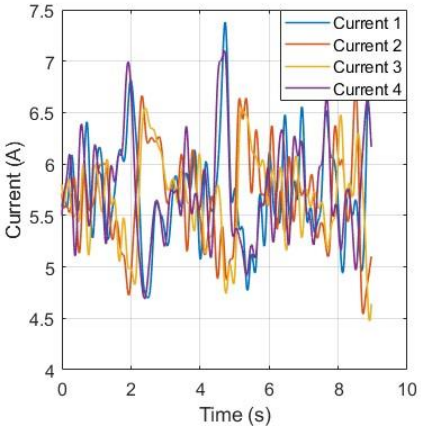

Figure 7.37 Electromagnet currents of bogie 2 under moderate track irregularities

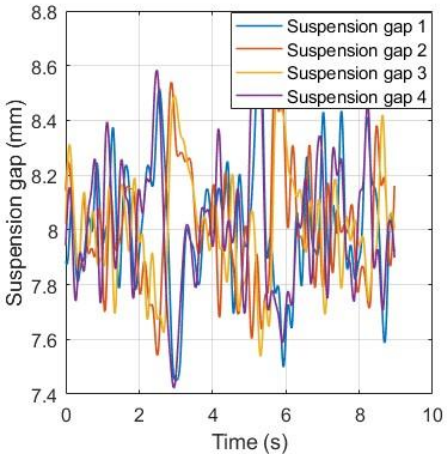

Figure 7.38 Suspension gaps of bogie 3 under moderate track irregularities

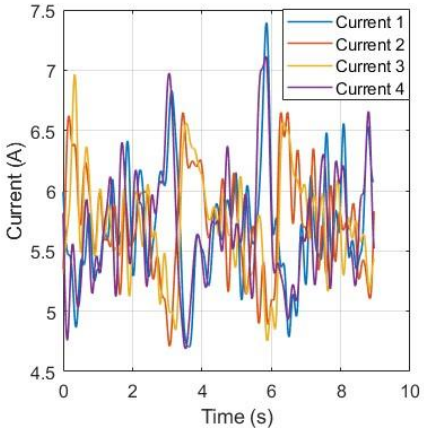

Figure 7.39 Electromagnet currents of bogie 3 under moderate track irregularities

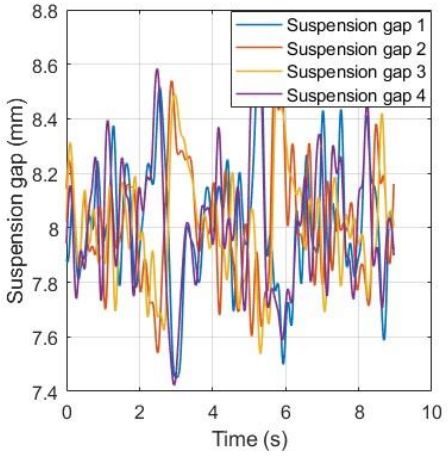

Figure 7.40 Suspension gaps of bogie 4 under moderate track irregularities

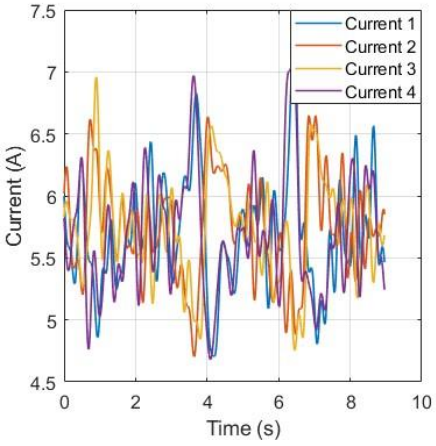

Figure 7.41 Electromagnet currents of bogie 4 under moderate track irregularities

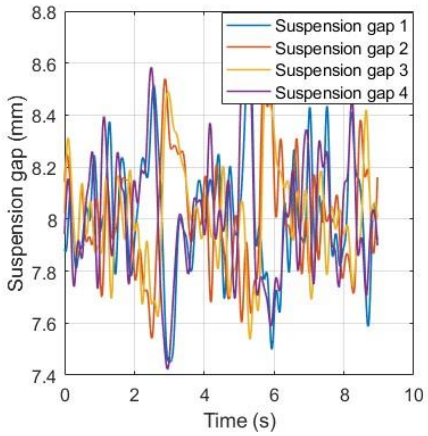

Figure 7.42 Suspension gaps of bogie 5 under moderate track irregularities

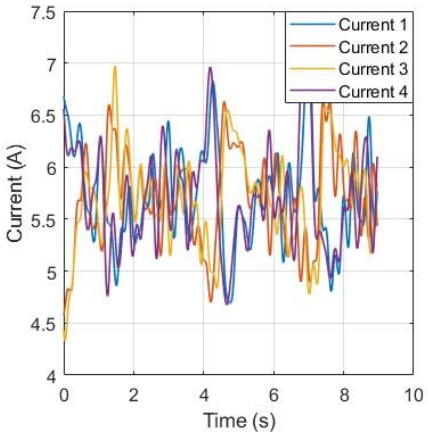

Figure 7.43 Electromagnet currents of bogie 5 under moderate track irregularities

Under moderate track irregularities, the suspension forces for all five bogies exhibit a stable yet dynamic response, fluctuating within the range of 4.5 kN to 8.5 kN, as shown in Figure 7.44 to Figure 7.53. Compared to the smooth irregularity results, where the suspension forces were confined to a smaller range of 5.0 kN to 7.5 kN, the moderate irregularities introduce larger oscillations. These increased fluctuations reflect the system's active adaptation to disturbances induced by the track irregularities, which causes more pronounced peaks and troughs in the suspension forces.

The forces on the left and right sides of each bogie generally maintain a high degree of symmetry, demonstrating the AMPC controller's ability to regulate and balance the system effectively. For instance, the force curves of the left and right sides align closely, indicating consistent control performance across both sides despite the increased disturbance. However, localized irregularities occasionally lead to small discrepancies between the left and right forces, particularly during moments of sharper changes in the track profile. Such discrepancies

are quickly compensated for, as observed in the forces returning to their average range.

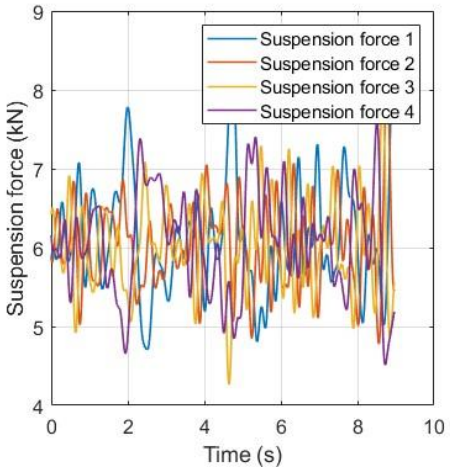

Figure 7.44 Suspension force of left-side electromagnets on bogie 1 under moderate track irregularities

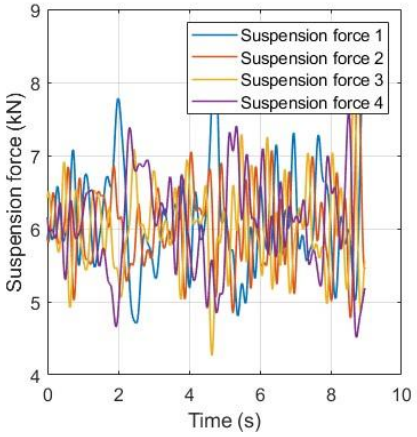

Figure 7.45 Suspension force of right-side electromagnets on bogie 1 under moderate track irregularities

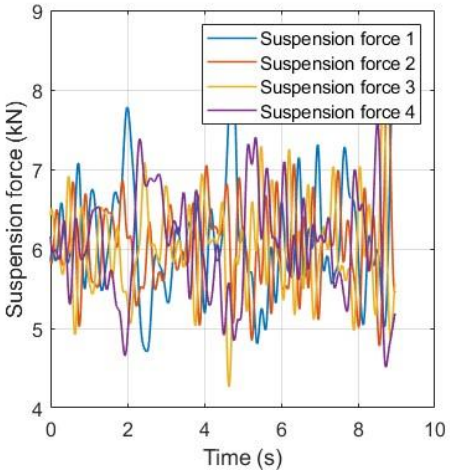

Figure 7.46 Suspension force of left-side electromagnets on bogie 2 under moderate track irregularities

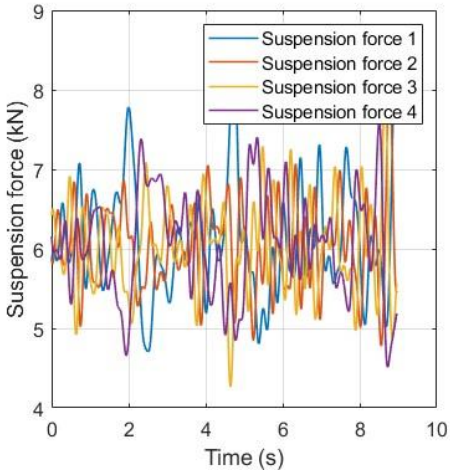

Figure 7.47 Suspension force of right-side electromagnets on bogie 2 under moderate track irregularities

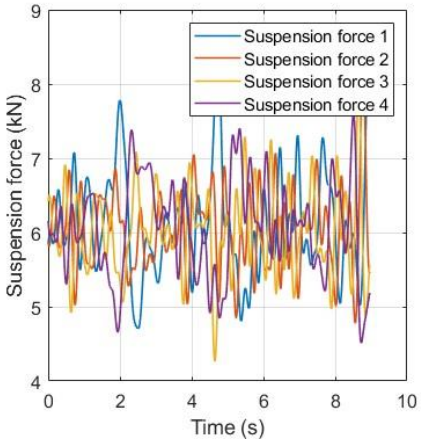

Figure 7.48 Suspension force of left-side electromagnets on bogie 3 under moderate track irregularities

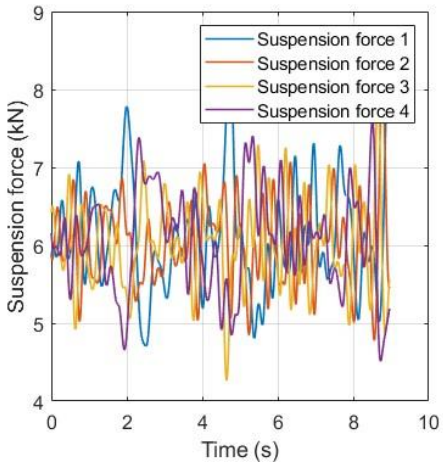

Figure 7.49 Suspension force of right-side electromagnets on bogie 3 under moderate track irregularities

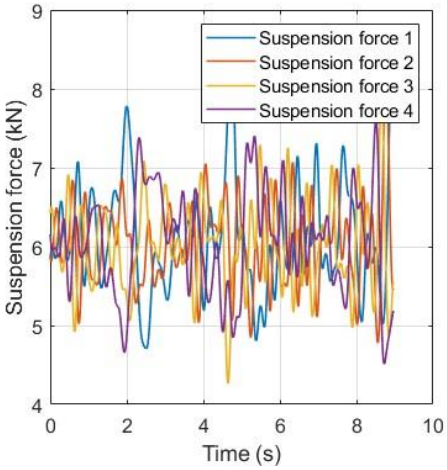

Figure 7.50 Suspension force of left-side electromagnets on bogie 4 under moderate track irregularities

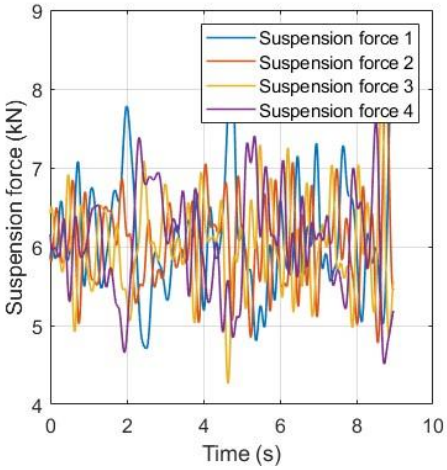

Figure 7.51 Suspension force of right-side electromagnets on bogie 4 under moderate track irregularities

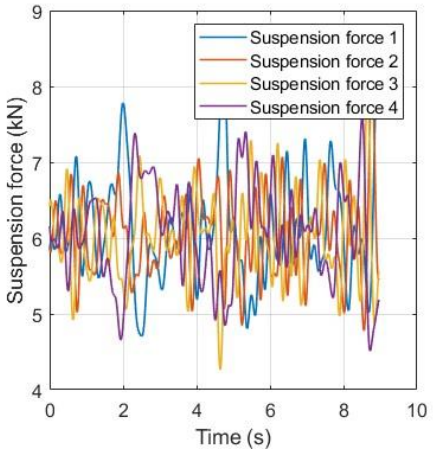

Figure 7.52 Suspension force of left-side electromagnets on bogie 5 under moderate track irregularities

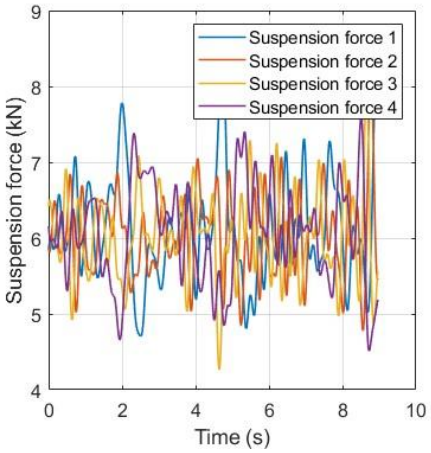

Figure 7.53 Suspension force of right-side electromagnets on bogie 5 under moderate track irregularities

Figure 7.54 shows the vibration acceleration of the carriage center when the train travels at 20 km/h over a moderately irregular track. The acceleration fluctuates within the range of approximately -5.0 × 10^{-3} m/s² to 9.0 × 10^{-3} m/s². Compared to the smooth irregularity case, the amplitude of vibration accelerations increases significantly, reflecting the greater influence of track disturbances on the system dynamics.

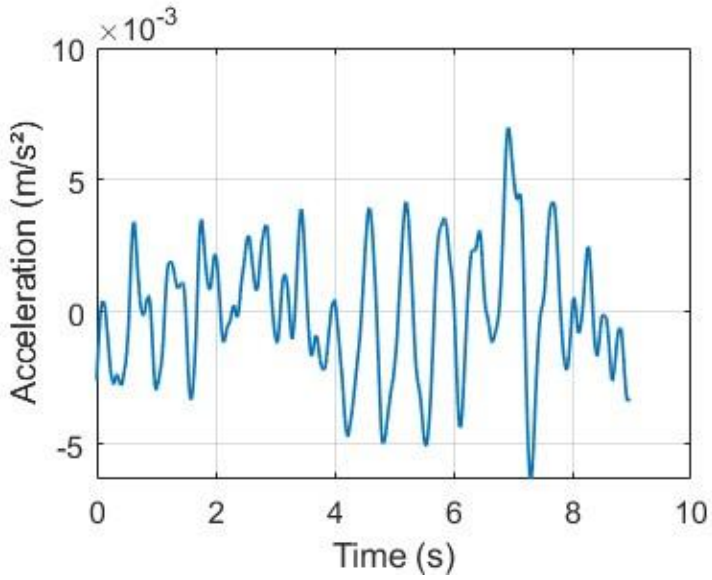

Figure 7.54 Carriage midsection vibration acceleration under moderate track irregularities

7.3.2.3.Suspension Performance Under Severe Track Irregularities

Under the severe track irregularity condition, the suspension system of the maglev train experiences substantial deviations, as shown in Figure 7.55 to Figure 7.64.

The suspension gaps for all bogies display larger oscillations compared to the smooth and moderate irregularity cases. The range of suspension gaps fluctuates between 6.9 mm and 9.1 mm, which is more significant than in the previous conditions. This indicates that severe irregularities amplify the disturbance effects, challenging the stability of the suspension system. Despite these disturbances, the gaps remain within acceptable limits, demonstrating the robustness of the AMPC controller.

The corresponding electromagnet currents exhibit significant variations as the control system adjusts to stabilize the suspension gaps. The current fluctuates between 3.6 A and 8 A, indicating a broader range compared to the smooth and moderate irregularity cases. This larger

current range highlights the increased control effort required to counteract the more severe disturbances caused by the irregular track.

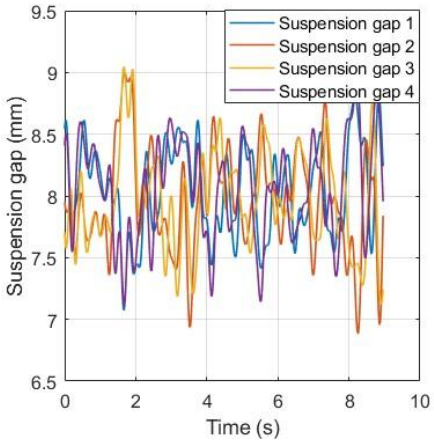

Figure 7.55 Suspension gaps of bogie 1 under severe track irregularities

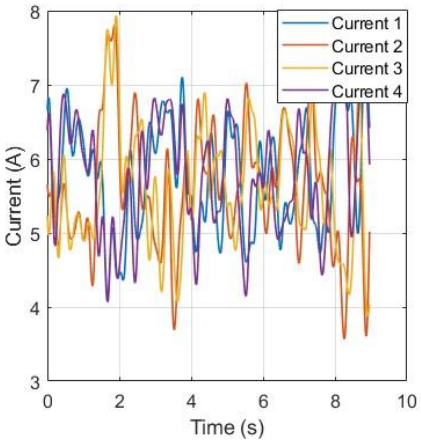

Figure 7.56 Electromagnet currents of bogie 1 under severe track irregularities

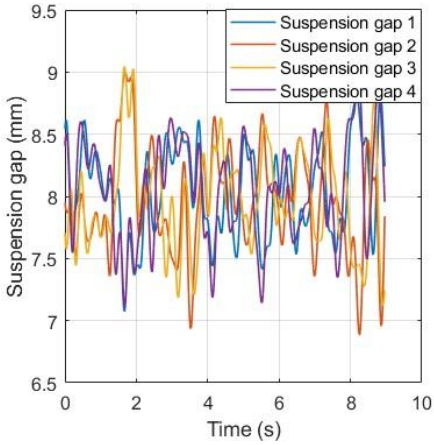

Figure 7.57 Suspension gaps of bogie 2 under severe track irregularities

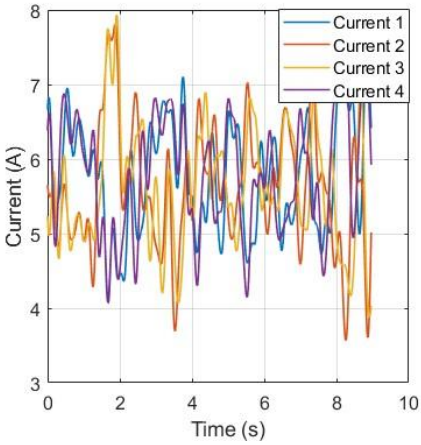

Figure 7.58 Electromagnet currents of bogie 2 under severe track irregularities

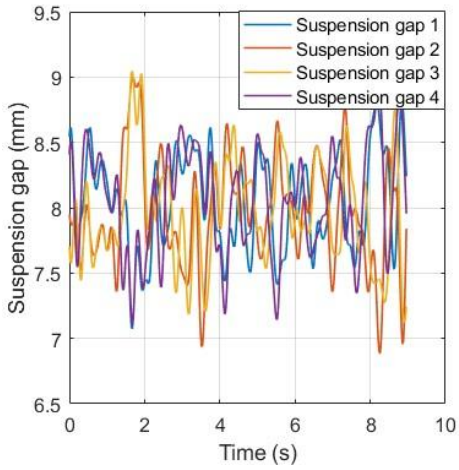

Figure 7.59 Suspension gaps of bogie 3 under severe track irregularities

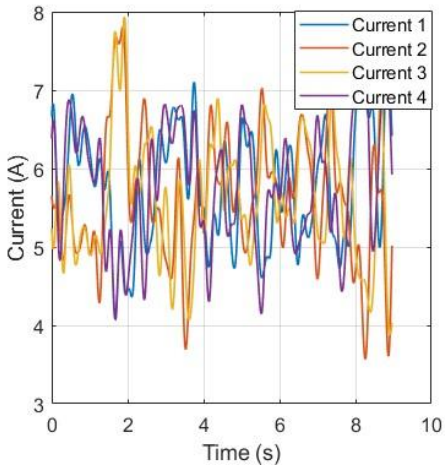

Figure 7.60 Electromagnet currents of bogie 3 under severe track irregularities

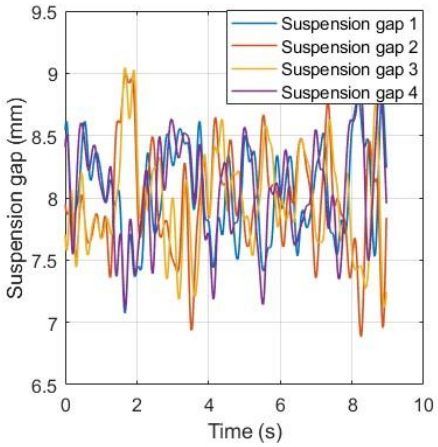

Figure 7.61 Suspension gaps of bogie 4 under severe track irregularities

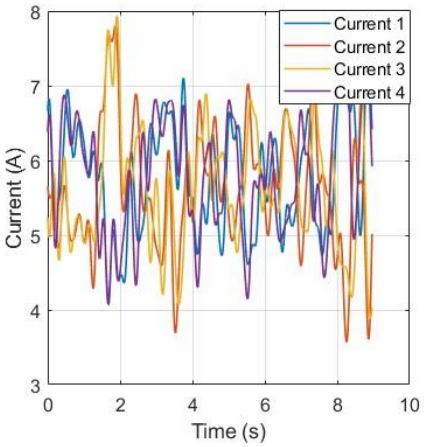

Figure 7.62 Electromagnet currents of bogie 4 under severe track irregularities

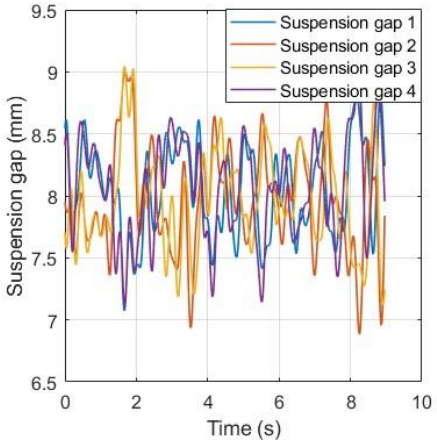

Figure 7.63 Suspension gaps of bogie 5 under severe track irregularities

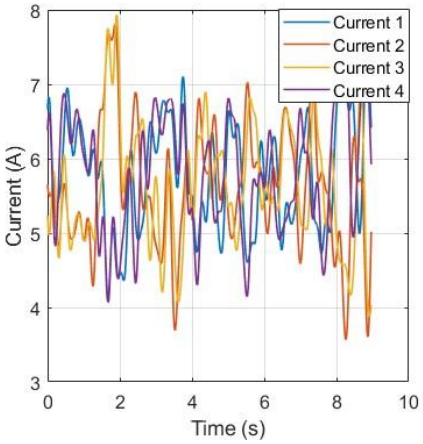

Figure 7.64 Electromagnet currents of bogie 5 under severe track irregularities

the suspension force data for the five bogies, presented in Figure 7.65 to Figure 7.74, exhibit consistent trends across all bogies. The forces fluctuate within the range of 3.1 kN to 9.8 kN, reflecting the dynamic impact caused by the severe irregularities. Across the five bogies, the suspension forces of the four electromagnets on each side demonstrate similar oscillatory behavior, with occasional sharp peaks and troughs. While the fluctuations are far more pronounced under severe irregularities compared to smooth and moderate conditions, the suspension forces remain within acceptable operational limits, showing the effectiveness of the control strategy in mitigating the effects of track disturbances. However, the larger and more frequent variations indicate the additional effort required to stabilize the system as the track conditions deteriorate.

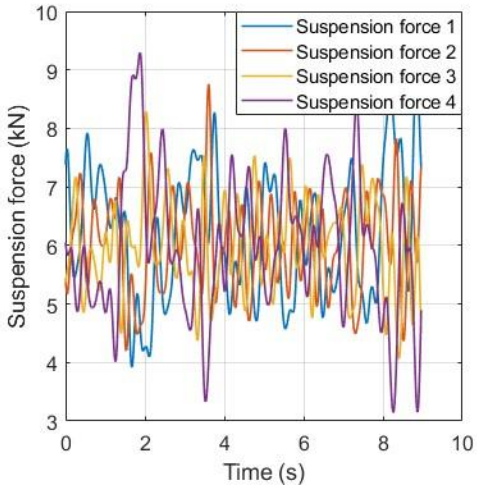

Figure 7.65 Suspension force of left-side electromagnets on bogie 1 under severe track irregularities

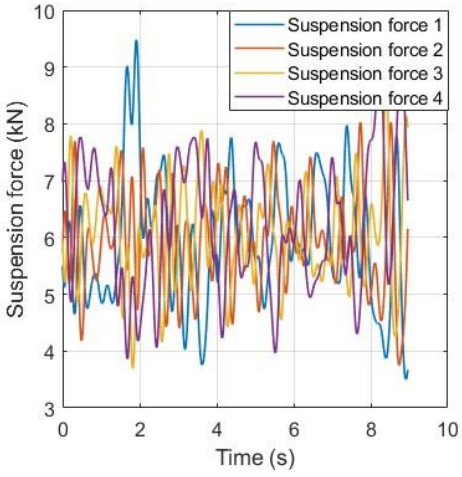

Figure 7.66 Suspension force of right-side electromagnets on bogie 1 under severe track irregularities

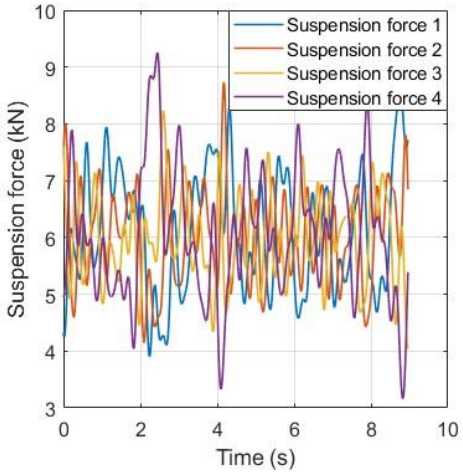

Figure 7.67 Suspension force of left-side electromagnets on bogie 2 under severe track irregularities

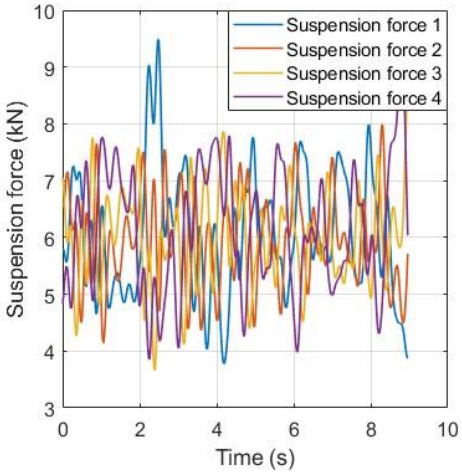

Figure 7.68 Suspension force of right-side electromagnets on bogie 2 under severe track irregularities

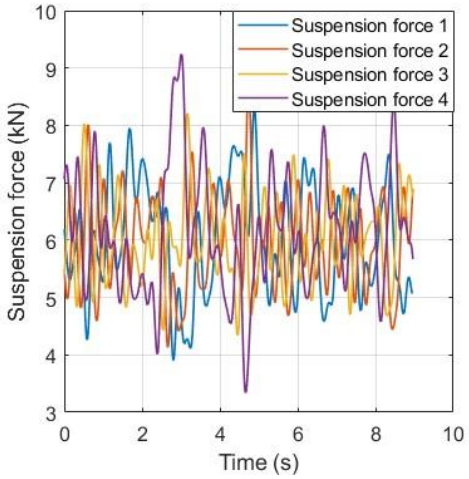

Figure 7.69 Suspension force of left-side electromagnets on bogie 3 under severe track irregularities

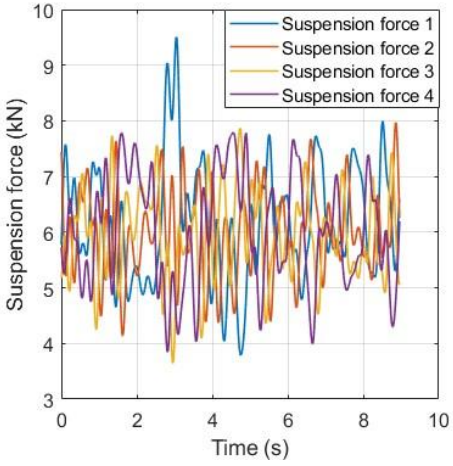

Figure 7.70 Suspension force of right-side electromagnets on bogie 3 under severe track irregularities

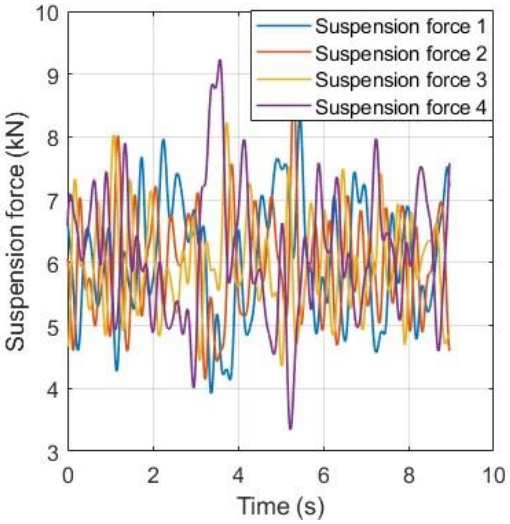

Figure 7.71 Suspension force of left-side electromagnets on bogie 4 under severe track irregularities

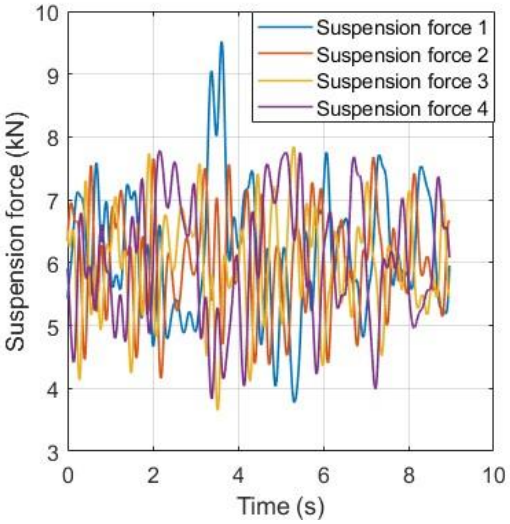

Figure 7.72 Suspension force of right-side electromagnets on bogie 4 under severe track irregularities

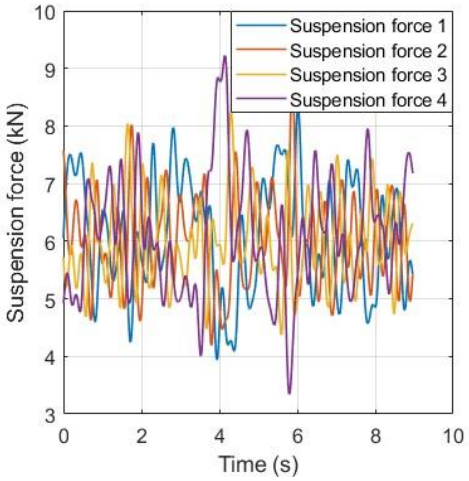

Figure 7.73 Suspension force of left-side electromagnets on bogie 5 under severe track irregularities

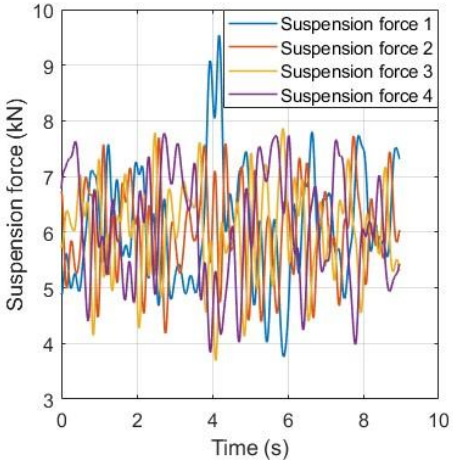

Figure 7.74 Suspension force of right-side electromagnets on bogie 5 under severe track irregularities

The vibration acceleration of the carriage under severe track irregularities shows significant fluctuations, with amplitudes ranging from -0.01 m/s² to 0.01 m/s². Compared with the results from smooth and moderate irregularities, the carriage vibration becomes noticeably more intense, both in magnitude and frequency.

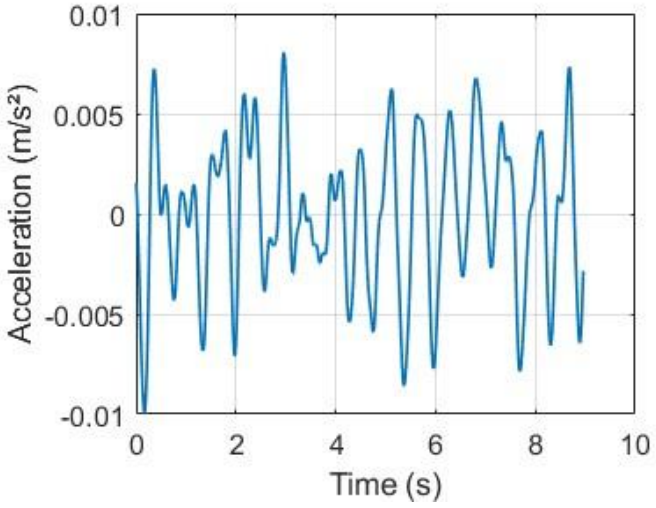

Figure 7.75 Carriage midsection vibration acceleration under severe track irregularities

7.3.2.4.Ride Quality Evaluation

This section introduces widely adopted ride quality evaluation method: the Sperling Ride Quality Index. The Sperling ride quality index was proposed by German scholar Sperling and his colleagues as a metric for evaluating the running quality of railway vehicles. Based on extensive experimental investigations on the physiological effects of vibration on the human body, the index was established to assess both the intrinsic operational quality of the vehicle and the subjective ride comfort experienced by passengers.

The operational quality of a vehicle is primarily determined by the vehicle's structural and dynamic characteristics, while ride comfort depends on the vehicle–passenger interaction with the vibration environment. This sensitivity is reflected through frequency-dependent correction coefficients applied to the vibration signal. The Sperling index has been widely adopted internationally, including by the International Union of Railways (UIC)

The ride quality index for passenger and freight cars in China is defined as:

$$W_i = 7.08^{10}\sqrt{\frac{A_i^3}{f_i}F(f_i)} \tag{7.13}$$

Where A is the vibration acceleration amplitude (in m/s²), f is the vibration frequency (in Hz), $F(f_i)$ is the frequency correction factor, which varies according to vibration direction and frequency band, as shown in Table 7.2.

Table 7.2 Frequency correction coefficient K_f

Frequency Band	**Vertical Vibration**	**Lateral Vibration**
$0.5-5.9\text{Hz}$	$F(f_i)=0.325f$	$0.5-5.4\text{Hz}: F(f_i)=0.8f$
$5.9-20\text{Hz}$	$F(f_i)=\frac{400}{f^2}$	$5.4-26\text{Hz}: F(f_i)=\frac{650}{f^2}$
$>20\text{Hz}/>26\text{Hz}$	$F(f_i)=1$	$F(f_i)=1$

Once the ride quality index is calculated, the ride comfort grade can be determined according to Table 4.2.

Table 7.3 Ride quality grades for passenger

Grade	**Evaluation**	**Index Range (Passenger)**
I	Excellent	<2.5
II	Good	2.5-2.75
III	Acceptable	2.75-3.0

In practice, train vibration is a stochastic process, with vibration frequency and amplitude varying over time. Therefore, it is often necessary to consider multiple frequency components in a given direction. In such cases, the vibration signal is divided into multiple frequency bands, each with its own partial Sperling index, and a composite index is calculated over the entire frequency range to evaluate the overall ride quality.

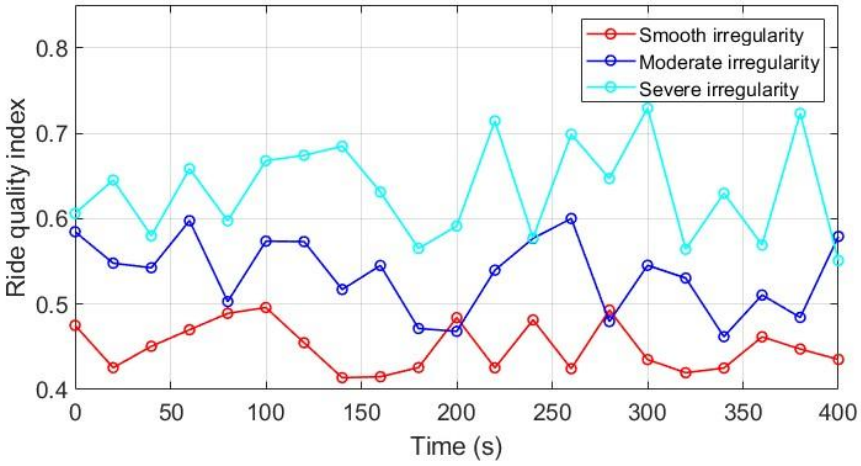

Figure 7.76 Ride quality index under different track irregularities

Figure 7.76 presents the variation of the Sperling ride quality index under three levels of vertical track irregularities: smooth, moderate, and severe. The index is calculated using vertical acceleration data collected from the center of the passenger cabin. Each data point represents an evaluation conducted every 20 seconds, yielding a time-resolved depiction of ride comfort over a 400-second simulation duration. Across all levels of track irregularity, the ride quality index remains well below the Grade I threshold of 2.5 defined in the Chinese Sperling standard, indicating that the vertical ride comfort consistently meets the “excellent” classification. Specifically, under smooth irregularity, the index fluctuates between 0.42 and 0.5; under moderate irregularity, it rises to the range of 0.5–0.6; and under severe irregularity, it reaches 0.6–0.75. Despite the increase in index values with worsening track conditions, the system maintains excellent ride quality throughout, demonstrating the effectiveness of the suspension control strategy. In particular, these results reflect the strong performance of the

AMPC algorithm applied in this study. The AMPC controller effectively compensates for dynamic disturbances and system nonlinearities, thereby suppressing excessive vibration even under severe irregularities.

7.3.3. Suspension Performance Under Speeds from 60 km/h to 180 km/h

Based on the findings from the previous section, the suspension gaps, currents, and suspension forces of different bogies exhibit similar trends under the same operating conditions. Therefore, in this section, the third bogie is selected as the representative case for further investigation. The focus is on evaluating the system's performance at different train speeds under severe track irregularity conditions.

The suspension gap fluctuates notably as the train speed increases. At 60 km/h, the suspension gap demonstrates relatively smaller variations, primarily ranging between 6.9 mm and 9.1 mm. As the speed increases to 100 km/h, the suspension gap range expands slightly to approximately 6.5 mm to 9.3 mm, indicating the control system's response to the increased dynamic effects. At 140 km/h, the gap shows more pronounced fluctuations, with values extending between 6.5 mm and 9.4 mm. At the highest speed of 180 km/h, the suspension gap variability increases further, reaching a range of 5.9 mm to 10 mm, highlighting the difficulty in maintaining precise suspension under higher speeds and severe irregularities.

The corresponding electromagnet current follows a similar trend of increased fluctuations with higher speeds. At 60 km/h, the current oscillates within a stable range of 3.8 A to 7.9 A, reflecting the system's smooth control. At 100 km/h, the current variation increases slightly, with values ranging from 3 A to 8 A. As the speed rises to 140 km/h, the current fluctuates more

significantly between 3 A and 8.5 A, showcasing the increased workload of the control system. Finally, at 180 km/h, the current exhibits the largest range of 2.4 A to 9.8 A, corresponding to the greater effort required to stabilize the suspension under severe irregularities and high dynamic forces.

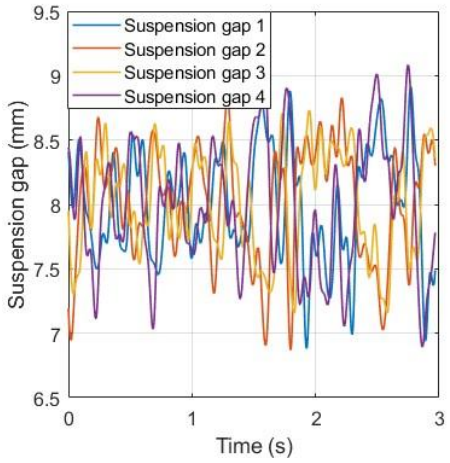

Figure 7.77 Suspension gaps of bogie 3 under severe track irregularities at 60 km/h

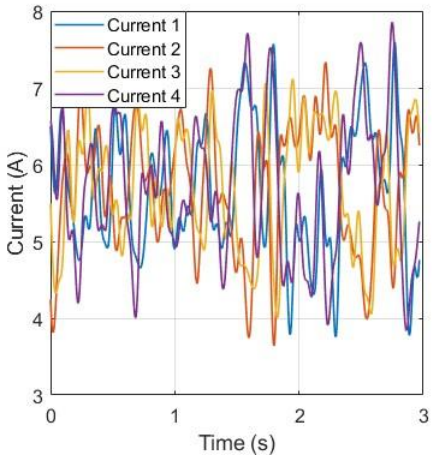

Figure 7.78 Electromagnet currents of bogie 3 under severe track irregularities at 60 km/h

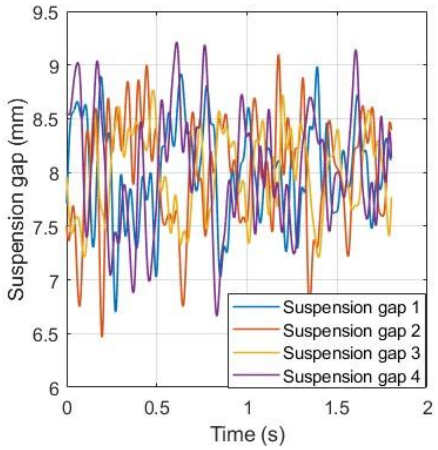

Figure 7.79 Suspension gaps of bogie 3

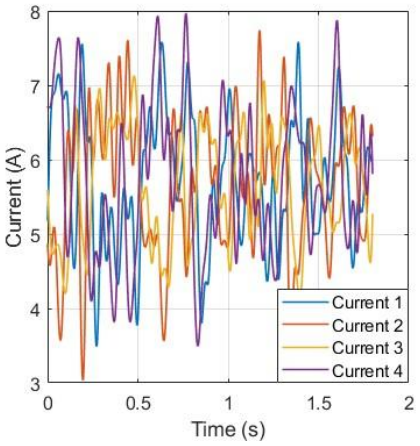

Figure 7.80 Electromagnet currents of

under severe track irregularities at 100 km/h

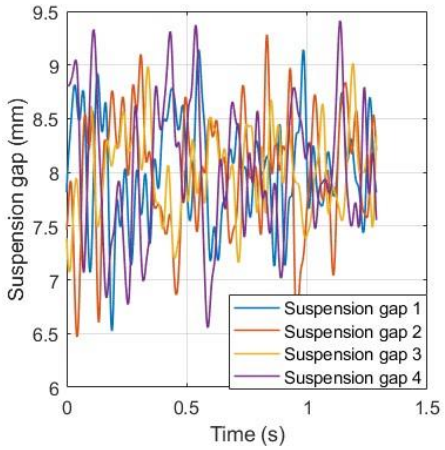

Figure 7.81 Suspension gaps of bogie 3 under severe track irregularities at 100 km/h

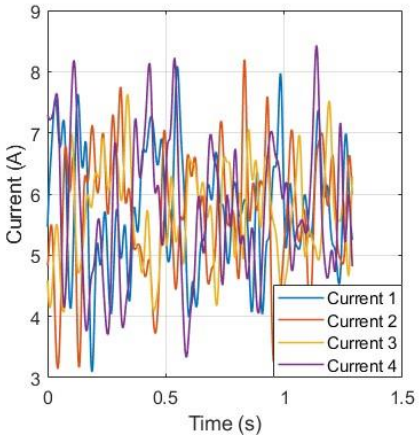

Figure 7.82 Electromagnet currents of bogie 3 under severe track irregularities at 100 km/h

under severe track irregularities at 140 km/h

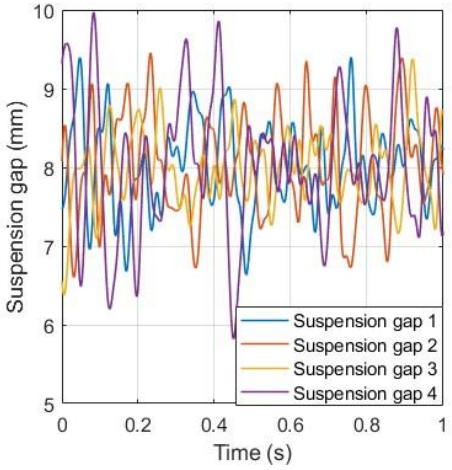

Figure 7.83 Suspension gaps of bogie 3 under severe track irregularities at 140 km/h

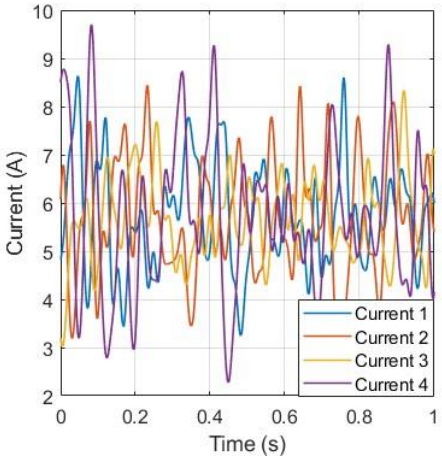

Figure 7.84 Electromagnet currents of bogie 3 under severe track irregularities at 140 km/h

under severe track irregularities at 180 km/h

Figure 7.85 Suspension gaps of bogie 3 under severe track irregularities at 180 km/h

Figure 7.86 Electromagnet currents of bogie 3 under severe track irregularities at 180 km/h

The vehicle body acceleration data under severe track irregularities at different speeds (60 km/h,

100 km/h, 140 km/h, and 180 km/h) reveal a significant increase in both amplitude and frequency content as the train speed increases. At 60 km/h, the carriage acceleration shows relatively small oscillations, primarily within the range of -0.06 m/s² to 0.06 m/s², indicating a smoother vibration response. As the speed increases to 100 km/h, the vibration amplitude rises to approximately -0.1 m/s² to 0.1 m/s², with more frequent oscillations, reflecting greater disturbance caused by the interaction with the track irregularities. At 140 km/h, the acceleration further increases to -0.18 m/s² to 0.18 m/s², and the frequency of oscillations becomes more prominent, showing that the higher speed amplifies the vehicle's dynamic response to the track irregularities. Finally, at 180 km/h, the amplitude reaches its peak, ranging between -0.3 m/s² and 0.3 m/s², with a clear increase in vibration intensity and frequency content, suggesting that severe irregularities at higher speeds lead to more pronounced dynamic interactions.

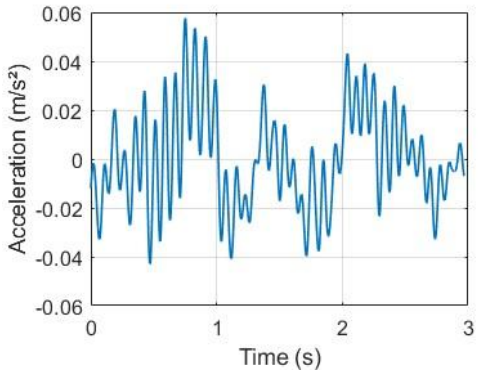

Figure 7.85 Carriage midsection vibration acceleration under severe track irregularities at speed 60 km/h

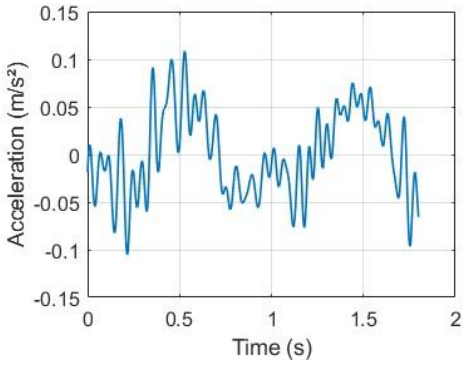

Figure 7.86 Carriage midsection vibration acceleration under severe track irregularities at speed 100 km/h

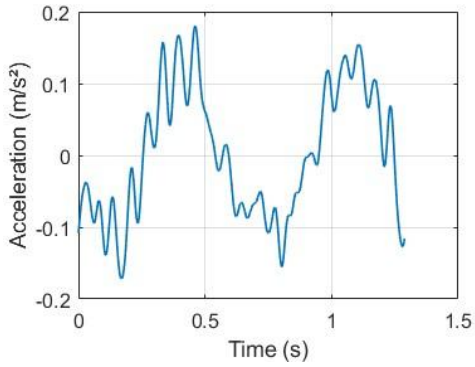

Figure 7.87 Carriage midsection vibration acceleration under severe track irregularities at speed 140 km/h

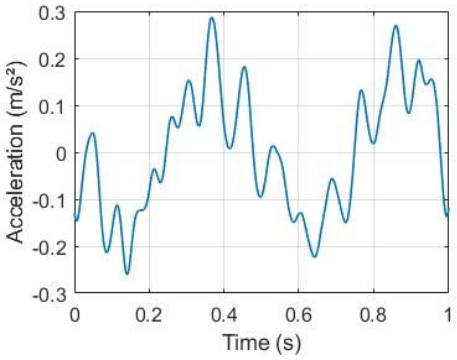

Figure 7.88 Carriage midsection vibration acceleration under severe track irregularities at speed 180 km/h

7.4. Conclusions

This chapter presents a comprehensive analysis of the dynamic interaction of a maglev train using a three-dimensional model that integrates the train, track, and bridge dynamics. The focus was on evaluating the maglev suspension system's performance under varying levels of track irregularities (smooth, moderate, and severe) and operating speeds (60 km/h, 100 km/h, 140 km/h, and 180 km/h), with particular attention given to the third suspension bogie as a representative case.

The results demonstrated that track irregularities significantly impact the suspension system's performance, particularly at higher operating speeds. For smooth irregularities, the system maintained relatively stable suspension gaps, suspension forces, and current, with minor oscillations observed. The suspension gaps remained close to the target value of 8 mm, while the currents showed limited fluctuations within the range of 3.6 A to 8 A. The carriage vibrational response, reflected by the acceleration, also exhibited minimal variation, ensuring

passenger comfort.

Under moderate irregularities, the dynamic responses exhibited larger oscillations compared to the smooth case. The suspension gaps fluctuated between 7.1 mm and 8.9 mm, while the electromagnet currents increased in magnitude and variation, ranging from 4 A to 8.5 A. Suspension forces oscillated more prominently, reaching values between 5 kN and 8.5 kN. Correspondingly, the carriage's vibrational acceleration increased slightly, reflecting the suspension system's response to the moderate disturbances.

For severe irregularities, the system experienced the most significant disturbances. The suspension gaps exhibited increased fluctuation amplitudes, ranging from 6.9 mm to 9.1 mm, while the electromagnet currents varied more drastically, reaching 3.6 A to 8 A. Suspension forces oscillated more prominently, with peaks close to 9 kN, reflecting the suspension system's effort to maintain levitation under high external disturbances. The carriage acceleration also demonstrated substantial increases, with the amplitude growing significantly as operating speeds increased, particularly at 140 km/h and 180 km/h.

A key observation was the progressive effect of increasing operating speeds on the suspension system's performance. At higher speeds, the oscillations in suspension gaps, electromagnet currents, and suspension forces became more pronounced. Specifically, at 180 km/h, the system struggled to maintain stability under severe irregularities, with the suspension gaps deviating further from the target value. The carriage's vibrational acceleration also increased proportionally with speed, reaching peaks of 0.3 m/s^2. This highlights the critical importance of designing robust control strategies to mitigate the impact of track disturbances at high-speed

operation.

By incorporating a three-dimensional dynamic interaction model, this chapter provided a holistic understanding of the maglev system's behavior under real-world conditions, considering the interactions between the train, track, and bridge dynamics. The findings highlight the AMPC controller's superior ability to manage dynamic disturbances, maintain suspension stability, and minimize system oscillations. Compared to conventional control strategies, AMPC demonstrated robustness in handling model uncertainties and external disturbances, even under severe irregularities and high speeds.

In conclusion, while the AMPC controller effectively managed the suspension system's performance across varying track conditions and speeds, the results underscore the challenges posed by severe track irregularities and high-speed operation. The findings provide valuable insights for further refining control algorithms to enhance system robustness, improve passenger comfort, and ensure operational stability in practical maglev applications. Future work will focus on optimizing the AMPC framework for extreme dynamic conditions and extending the analysis to more complex multi-bogie systems.

Chapter 8. Conclusions and Recommendations

8.1. Major Conclusions

This thesis has made some contributions to the modeling, control, and performance optimization of maglev suspension systems, particularly in the context of electromagnetic suspension (EMS) systems. The research successfully addressed the primary objectives outlined in the introduction, as detailed below:

(1). Development of a Numerical Dynamic Model and Controller Design

The thesis successfully developed a comprehensive numerical dynamic model for the EMS system. PID and MPC strategies were implemented and analyzed. While PID control demonstrated reasonable performance under low-frequency conditions, it was found to be inadequate in handling high-frequency noise and varying system dynamics. This objective was met by demonstrating the superiority of MPC in terms of trajectory tracking, stability, and noise robustness.

(2). Investigation of Advanced Control Methods: MPC and AMPC

The investigation into MPC for maglev suspension systems was carried out thoroughly, with the integration of Kalman filters to enhance state estimation in noisy environments. MPC showed significant improvements over traditional PID, especially in managing dynamic changes and constraints. The introduction of AMPC with ARX-based adaptive models further enhanced the system's robustness, demonstrating its capability to handle model mismatches and improve tracking accuracy in real-time. This objective was met through extensive simulation and experimental validation of both MPC and AMPC, confirming their

effectiveness in real-world scenarios.

(3). Evaluation of Control Strategies under Track Irregularities and High-Speed Operations

The dynamic performance analysis of maglev systems under varying track conditions and high-speed operations was another key objective. By modeling the interactions between the train, track, and bridge, the research demonstrated how track irregularities and speed affect the suspension system's performance. AMPC outperformed MPC and PID in maintaining stable suspension gaps and minimizing vibrations under severe track disturbances and at high speeds. This objective was successfully met, providing a clear demonstration of AMPC's superiority in complex operational environments.

(4). Experimental Validation and Real-World Applicability

Through the design of experiments focused on levitation and trajectory tracking, this thesis validated the simulation results and provided concrete evidence of the proposed control methods' real-world applicability. The integration of measurement noise in the experiments demonstrated the robustness of MPC and AMPC in handling imperfect sensor data, which is critical for practical deployment. This objective was fulfilled by performing experiments that corroborated the simulation findings and emphasized the feasibility of these advanced control methods in real-world systems.

8.2. Recommendations and Future Works

While the research in this thesis has successfully addressed the stated objectives, several opportunities for further development and optimization exist. Future work in the area of maglev

suspension control could focus on the following:

(1). Exploration of Advanced Adaptive Control Algorithms Based on MPC Framework

Future research could explore the integration of advanced adaptive control algorithms within the MPC framework. For instance, Reinforcement Learning (RL) and other machine learning techniques could be utilized to serve as the core algorithms for model updating. These approaches offer the potential for more dynamic adaptation to environmental changes and system uncertainties, further improving the system's robustness and efficiency. Specifically, RL could optimize control parameters in real-time, offering a promising solution to handle complex, uncertain systems such as maglev transportation.

(2). Energy-Efficient Control Strategies

As maglev transportation becomes more widespread, optimizing energy efficiency will become increasingly important. Future research could focus on developing control strategies that minimize energy consumption while maintaining the required performance and stability. This could involve refining AMPC or investigating hybrid control strategies to reduce energy usage in practical applications.

(3). Integration of Control Circuit Simulation with Dynamic Models

One of the next steps could be the establishment of a more detailed control circuit simulation model, integrating it with the existing dynamic models. This integration would enable more accurate simulations of the entire system, considering not only the mechanical dynamics but also the control circuitry’s impact on system performance. This would be crucial for refining control strategies and ensuring their reliability in practical applications.

(4). Long-Term Field Testing and System Validation

While this research has validated the control strategies through simulations and short-term experiments, long-term field testing under various environmental conditions will be essential to fully understand the system's behavior in real-world scenarios. Further experimental studies could examine the long-term effects of different control strategies on system performance, energy consumption, and maintenance needs.

Chapter 9. Reference

1. Legg, S., *World Population Prospects 2024: Summary of Results.* Interaction (Melbourne), 2024. **52**(3).
2. Shah, K. J., Pan, S. Y., Lee, I., Kim, H., You, Z., Zheng, J. M., and Chiang, P. C., *Green transportation for sustainability: Review of current barriers, strategies, and innovative technologies.* Journal of Cleaner Production, 2021. **326**: p. 129392.
3. Zhao, X., Ke, Y., Zuo, J., Xiong, W., and Wu, P., *Evaluation of sustainable transport research in 2000–2019.* Journal of cleaner production, 2020. **256**: p. 120404.
4. Lee, H.W., Kim, K.C. and Lee, J., *Review of maglev train technologies.* IEEE transactions on magnetics, 2006. **42**(7): p. 1917-1925.
5. Lai, Q., Liu, J., Haghani, A., Meng, L., and Wang, Y., *Energy-efficient speed profile optimization for medium-speed maglev trains.* Transportation Research Part E: Logistics and Transportation Review, 2020. **141**: p. 102007.
6. Powell, J. and Danby, G., *Maglev: The New Mode of Transport for the 21st Century.* 21St Century Science and Technology, 2003. **16**(2): p. 43-57.
7. Liu, R. and Deng, Y., *Comparing operating characteristics of high-speed rail and maglev systems: case study of Beijing-Shanghai corridor.* Transportation research record, 2004. **1863**(1): p. 19-27.
8. Tandan, G.K., Sen, P.K., Sahu, G., Sharma, R. and Bohidar, S., *A review on development and analysis of maglev train.* International Journal of Research in Advent Technology, 2015. **3**(12): p. 14-17.
9. Lin, G.B. and Sheng, X.W., *Application and further development of Maglev transportation in China.* Инновационные транспортные системы и технологии, 2018. **4**(3): p. 36-43.
10. Palmer, C., *Engineered to go fast, maglev trains inch forward.* Engineering S, 2021.
11. Tanaka, K., *Impacts of the opening of the maglev railway on daily accessibility in Japan: A comparative analysis with that of the Shinkansen.* Journal of Transport Geography, 2023. **106**: p. 103512.
12. Kim, M., Jeong, J.H., Lim, J., Kim, C.H. and Won, M., *Design and control of levitation and guidance systems for a semi-high-speed maglev train.* Journal of Electrical Engineering & Technology, 2017. **12**(1): p. 117-125.
13. Ahmed, R., Jun, Y.L., Azhar, M.F. and Junejo, N.U.R., *Comprehensive study and review on maglev train system.* Applied Mechanics and Materials, 2014. **615**: p. 347-351.
14. Geerlings, H., *The rise and fall of new technologies: Maglev as technological substitution?* Transportation planning and technology, 1998. **21**(4): p. 263-286.
15. Kim, M., Jeong, J.H., Lim, J., Kim, C.H. and Won, M., *Design and control of levitation and guidance systems for a semi-high-speed maglev train.* Journal of Electrical Engineering and Technology, 2017. **12**(1): p. 117-125.
16. Chamraz, Š., M. Huba, and K. Žáková, *Stabilization of the magnetic levitation system.* Applied Sciences, 2021. **11**(21): p. 10369.

17. Lin, C.M., Lin, M.H. and Chen, C.W., *SoPC-based adaptive PID control system design for magnetic levitation system.* IEEE Systems journal, 2011. **5**(2): p. 278-287.
18. Rawlings, J.B., Mayne, D.Q. and Diehl, M., *Model predictive control: theory, computation, and design*. Vol. 2. 2017: Nob Hill Publishing Madison, WI.
19. Bächle, T., Hentzelt, S. and Graichen, K., *Nonlinear model predictive control of a magnetic levitation system.* Control Engineering Practice, 2013. **21**(9): p. 1250-1258.
20. Holkar, K.S. and Waghmare, L.M., *An overview of model predictive control.* International Journal of control and automation, 2010. **3**(4): p. 47-63.
21. Kouvaritakis, B. and Cannon, M., *Model predictive control.* Switzerland: Springer International Publishing, 2016. **38**: p. 13-56.
22. Liu, Z., Long, Z. and Li, X., *Maglev trains*. 2015: Springer.
23. Goodall, R., *Dynamics and control requirements for EMS Maglev suspensions.* 2004.
24. Zhou, D., Hansen, C.H., Li, J. and Chang, W., *Review of coupled vibration problems in EMS maglev vehicles.* International Journal of Acoustics and Vibration, 2010. **15**(1): p. 10.
25. Long, Z., He, G. and Xue, S., *Study of EDS & EMS hybrid suspension system with permanent-magnet Halbach array.* IEEE Transactions on magnetics, 2011. **47**(12): p. 4717-4724.
26. Han, Q., *Analysis and modeling of the EDS maglev system based on the Halbach permanent magnet array*. 2004, University of Central Florida.
27. Wang, H.P., Li, J. and Zhang, K., *Vibration analysis of the maglev guideway with the moving load.* Journal of Sound and Vibration, 2007. **305**(4-5): p. 621-640.
28. Zheng, X.J., Wu, J.J. and Zhou, Y.H., *Numerical analyses on dynamic control of five-degree-of-freedom maglev vehicle moving on flexible guideways.* Journal of sound and Vibration, 2000. **235**(1): p. 43-61.
29. Zhao, C.F. and Zhai, W.M., *Maglev vehicle/guideway vertical random response and ride quality.* Vehicle system dynamics, 2002. **38**(3): p. 185-210.
30. Yang, Y.B. and Yau, J.D., *An iterative interacting method for dynamic analysis of the maglev train–guideway/foundation–soil system.* Engineering Structures, 2011. **33**(3): p. 1013-1024.
31. Zhang, L. and Huang, J., *Dynamic interaction analysis of the high-speed maglev vehicle/guideway system based on a field measurement and model updating method.* Engineering Structures, 2019. **180**: p. 1-17.
32. Wen, J., Liu, Y. and Zhu, D., *The multiple degrees of freedom magnet-track relationship in Maglev train*. in *5th International Conference on Information Engineering for Mechanics and Materials*. 2015. Atlantis Press.
33. Wang, Z.L., Xu, Y.L., Li, G.Q., Yang, Y.B., Chen, S.W. and Zhang, X.L., *Modelling and validation of coupled high-speed maglev train-and-viaduct systems considering support flexibility.* Vehicle System Dynamics, 2019. **57**(2): p. 161-191.
34. Liu, W. and W. Guo, *Random vibration analysis of coupled three-dimensional maglev vehicle-bridge System.* Advances in Civil Engineering, 2019. **2019**: p. 1-14.
35. Wang, H., Deng, Z., Ma, S., Sun, R., Li, H. and Li, J., *Dynamic simulation of the HTS*

maglev vehicle-bridge coupled system based on levitation force experiment. IEEE Transactions on Applied Superconductivity, 2019. **29**(5): p. 1-6.

36. Li, M., Luo, S., Ma, W., Lei, C., Li, T., Hu, Q., Zhang, X. and Han, Y., *Experimental study on dynamic performance of medium and low speed maglev train-track-bridge system.* International Journal of Rail Transportation, 2021. **9**(3): p. 232-255.
37. Feng, Y., Zhao, C., Zhai, W., Tong, L., Liang, X. and Shu, Y., *Dynamic performance of medium speed maglev train running over girders: field test and numerical simulation.* International Journal of Structural Stability and Dynamics, 2023. **23**(01): p. 2350006.
38. Liu, W. and Guo, W., *Vibration analysis of EMS-Type maglev vehicles traveling over a long-span bridge with double lines.* Ksce journal of civil engineering, 2020. **24**(5): p. 1531-1544.
39. Wang, D., Li, X., Liang, L. and Qiu, X., *Dynamic interaction analysis of bridges induced by a low-to-medium–speed maglev train.* Journal of Vibration and Control, 2020. **26**(21-22): p. 2013-2025.
40. Wang, J., Jin, X. and Cao, Y., *Modeling and simulation of maglev train-guideway-tunnel-soil system for vibration.* International Journal of the Physical Sciences, 2011. **6**: p. 4388-4404.
41. Li, M., Gao, D., Li, T., Luo, S., Ma, W., Chen, X. and Tong, L., *Dynamic interaction of medium–low-speed maglev train running on the turnout made of steel structures.* Vehicle System Dynamics, 2023. **61**(4): p. 1129-1150.
42. Wang, L., Deng, Z., Wang, H., Li, H., Li, K. and Ma, S., *Dynamic responses of HTS maglev system under track random irregularity.* IEEE Transactions on Applied Superconductivity, 2020. **30**(4): p. 1-7.
43. Rojas-Moreno, A. and Cuevas-Condor, C., *PD and PID control of a maglev system an experimental comparative study*. in *2017 IEEE XXIV International Conference on Electronics, Electrical Engineering and Computing (INTERCON)*. 2017. IEEE.
44. Yaseen, M.H., *A comparative study of stabilizing control of a planer electromagnetic levitation using PID and LQR controllers.* Results in physics, 2017. **7**: p. 4379-4387.
45. Ghosh, A., Krishnan, T.R., Tejaswy, P., Mandal, A., Pradhan, J.K. and Ranasingh, S., *Design and implementation of a 2-DOF PID compensation for magnetic levitation systems.* ISA transactions, 2014. **53**(4): p. 1216-1222.
46. Swain, S.K., Sain, D., Mishra, S.K. and Ghosh, S., *Real time implementation of fractional order PID controllers for a magnetic levitation plant.* AEU-International Journal of Electronics and Communications, 2017. **78**: p. 141-156.
47. Kong, E., Song, J.S., Kang, B.B. and Na, S., *Dynamic response and robust control of coupled maglev vehicle and guideway system.* Journal of Sound and Vibration, 2011. **330**(25): p. 6237-6253.
48. Yang, J., Zolotas, A., Chen, W.H., Michail, K. and Li, S., *Robust control of nonlinear MAGLEV suspension system with mismatched uncertainties via DOBC approach.* ISA transactions, 2011. **50**(3): p. 389-396.
49. Xu, J., Chen, Y.H. and Guo, H., *Robust levitation control for maglev systems with guaranteed bounded airgap.* ISA transactions, 2015. **59**: p. 205-214.

50. Goel, A. and Swarup, A., *A novel high-order sliding mode control of magnetic levitation system*. in *2016 IEEE 59th International Midwest Symposium on Circuits and Systems (MWSCAS)*. 2016. IEEE.
51. Sun, Y.G., Xie, S., Xu, J.Q. and Lin, G.B., *A robust levitation control of maglev vehicles subject to time delay and disturbances: Design and hardware experimentation.* Applied Sciences, 2020. **10**(3): p. 1179.
52. Wai, R.J. and Lee, J.D., *Development of levitation control for linear maglev rail system via backstepping design technique*. in *2006 IEEE Conference on Robotics, Automation and Mechatronics*. 2006. IEEE.
53. Malik, A.S., Ahmad, I., Rahman, A.U. and Islam, Y., *Integral backstepping and synergetic control of magnetic levitation system.* IEEE Access, 2019. **7**: p. 173230-173239.
54. He, G., Li, J. and Cui, P., *Nonlinear control scheme for the levitation module of maglev train.* Journal of Dynamic Systems, Measurement, and Control, 2016. **138**(7): p. 074503.
55. Tzeng, Y.K. and Wang, T.C., *Dynamic analysis of the maglev system using controlled-pm electromagnets and robust zero-power-control strategy.* IEEE Transactions on Magnetics, 1995. **31**(6): p. 4211-4213.
56. Park, J.S., Kim, J.S. and Lee, J.K., *Robust control of maglev vehicles with multimagnets using separate control techniques.* KSME international journal, 2001. **15**: p. 1240-1247.
57. Liu, H., Zhang, X. and Chang, W., *PID control to maglev train system*. in *2009 International Conference on Industrial and Information Systems*. 2009. IEEE.
58. Ni, F., Mu, S., Kang, J. and Xu, J., *Robust controller design for maglev suspension systems based on improved suspension force model.* IEEE Transactions on Transportation Electrification, 2021. **7**(3): p. 1765-1779.
59. Raj, R., Swain, S.K. and Mishra, S.K., *Optimal control for magnetic levitation system using HJB equation based LQR*. in *2018 2nd International Conference on Power, Energy and Environment: Towards Smart Technology (ICEPE)*. 2018. IEEE.
60. Abbas, A.A., Ammar, H.H. and Elsamanty, M.M., *Controller Design and Optimization of Magnetic Levitation System (MAGLEV) using Particle Swarm optimization technique and Linear Quadratic Regulator (LQR)*. in *2020 2nd Novel Intelligent and Leading Emerging Sciences Conference (NILES)*. 2020. IEEE.
61. Dey, S., Dey, J. and Banerjee, S., *Optimization algorithm based PID controller design for a magnetic levitation system*. in *2020 IEEE Calcutta Conference (CALCON)*. 2020. IEEE.
62. Gandhi, R.V. and Adhyaru, D.M., *Feedback linearization based optimal controller design for electromagnetic levitation system*. in *2016 International Conference on Control, Instrumentation, Communication and Computational Technologies (ICCICCT)*. 2016. IEEE.
63. Tran, A.T., Suzuki, S. and Sakamoto, N., *Nonlinear optimal control design considering a class of system constraints with validation on a magnetic levitation system.* IEEE Control Systems Letters, 2017. **1**(2): p. 418-423.

64. Ataşlar-Ayyıldız, B., Karahan, O. and Yılmaz, S., *Control and robust stabilization at unstable equilibrium by fractional controller for magnetic levitation systems.* Fractal and Fractional, 2021. **5**(3): p. 101.
65. Sain, D., Swain, S.K. and Mishra, S.K., *Real time implementation of optimized I-PD controller for the magnetic levitation system using Jaya algorithm.* IFAC-PapersOnLine, 2018. **51**(1): p. 106-111.
66. Wai, R.J., Lee, J.D. and Chuang, K.L., *Real-time PID control strategy for maglev transportation system via particle swarm optimization.* IEEE Transactions on Industrial Electronics, 2010. **58**(2): p. 629-646.
67. Pati, A. and Negi, R., *Suboptimal control of magnetic levitation (Maglev) system*. in *Proceedings of 3rd International Conference on Reliability, Infocom Technologies and Optimization*. 2014. IEEE.
68. Zhang, Z., Zhou, Y. and Tao, X., *Model predictive control of a magnetic levitation system using two-level state feedback.* Measurement and control, 2020. **53**(5-6): p. 962-970.
69. Dalwadi, N., D. Deb, and S. Muyeen, *A reference model assisted adaptive control structure for maglev transportation system.* Electronics, 2021. **10**(3): p. 332.
70. Zhou, D., Yu, P., Wang, L. and Li, J., *An adaptive vibration control method to suppress the vibration of the maglev train caused by track irregularities.* Journal of Sound and Vibration, 2017. **408**: p. 331-350.
71. Yaseen, H.M.S., Siffat, S.A., Ahmad, I. and Malik, A.S., *Nonlinear adaptive control of magnetic levitation system using terminal sliding mode and integral backstepping sliding mode controllers.* ISA transactions, 2022. **126**: p. 121-133.
72. Huang, C.M., Yen, J.Y. and Chen, M.S., *Adaptive nonlinear control of repulsive maglev suspension systems.* Control Engineering Practice, 2000. **8**(12): p. 1357-1367.
73. Bidikli, B. and Bayrak, A., *A self-tuning robust full-state feedback control design for the magnetic levitation system.* Control Engineering Practice, 2018. **78**: p. 175-185.
74. Xu, J., Du, Y., Chen, Y.H. and Guo, H., *Adaptive robust constrained state control for non-linear maglev vehicle with guaranteed bounded airgap.* IET Control Theory & Applications, 2018. **12**(11): p. 1573-1583.
75. Zhang, Z. and Li, X., *Real-time adaptive control of a magnetic levitation system with a large range of load disturbance.* Sensors, 2018. **18**(5): p. 1512.
76. Milani, R.H., Zarabadipour, H. and Shahnazi, R., *An adaptive robust controller for time delay maglev transportation systems.* Communications in Nonlinear Science and Numerical Simulation, 2012. **17**(12): p. 4792-4801.
77. Chen, C., Xu, J., Ji, W., Chao, R. and Sun, Y., *Adaptive levitation control for characteristic model of low speed maglev vehicle.* Proceedings of the Institution of Mechanical Engineers, Part C: Journal of Mechanical Engineering Science, 2020. **234**(7): p. 1456-1467.
78. Ren, Q., Zhang, J., Zhou, H. and Mo, F., *Robust Adaptive Levitation Control for Medium and Low-Speed Maglev with Magnetic Saturation and Eddy Current Effect.* Journal of Vibration Engineering & Technologies, 2023: p. 1-15.

79. Shafiq, M. and Akhtar, S., *Inverse model based adaptive control of magnetic levitation system*. in *2004 5th Asian Control Conference (IEEE Cat. No. 04EX904)*. 2004. IEEE.
80. Humaidi, A.J., Badr, H.M. and Hameed, A.H., *PSO-based active disturbance rejection control for position control of magnetic levitation system*. in *2018 5th International Conference on Control, Decision and Information Technologies (CoDIT)*. 2018. IEEE.
81. Ahmad, A.K., Saad, Z., Osman, M.K., Isa, I.S., Sadimin, S. and Abdullah, S.S., *Control of magnetic levitation system using fuzzy logic control*. in *2010 Second International Conference on Computational Intelligence, Modelling and Simulation*. 2010. IEEE.
82. Zhang, J., Wang, X. and Shao, X., *Design and real-time implementation of Takagi–Sugeno fuzzy controller for magnetic levitation ball system.* IEEE Access, 2020. **8**: p. 38221-38228.
83. Sun, Y., Li, W., Xu, J., Qiang, H. and Chen, C., *Nonlinear dynamic modeling and fuzzy sliding-mode controlling of electromagnetic levitation system of low-speed maglev train.* Journal of Vibroengineering, 2017. **19**(1): p. 328-342.
84. Wai, R.J. and Lee, J.D., *Adaptive fuzzy-neural-network control for maglev transportation system.* IEEE Transactions on Neural Networks, 2008. **19**(1): p. 54-70.
85. Wai, R.J., Chen, M.W. and Yao, J.X., *Observer-based adaptive fuzzy-neural-network control for hybrid maglev transportation system.* Neurocomputing, 2016. **175**: p. 10-24.
86. Sun, Y., Wang, L., Xu, J. and Lin, G., *An intelligent coupling 3-grade fuzzy comprehensive evaluation approach with AHP for selection of levitation controller of maglev trains.* IEEE Access, 2020. **8**: p. 99509-99518.
87. Lairi, M. and Bloch, G., *A neural network with minimal structure for maglev system modeling and control*. in *Proceedings of the 1999 IEEE International Symposium on Intelligent Control Intelligent Systems and Semiotics (Cat. No. 99CH37014)*. 1999. IEEE.
88. Yau, J., *Vibration control of maglev vehicles traveling over a flexible guideway.* Journal of sound and vibration, 2009. **321**(1-2): p. 184-200.
89. Qin, Y., Peng, H., Ruan, W., Wu, J. and Gao, J., *A modeling and control approach to magnetic levitation system based on state-dependent ARX model.* Journal of Process Control, 2014. **24**(1): p. 93-112.
90. Zhang, C.L., Wu, X.Z. and Xu, J., *Particle swarm sliding mode-fuzzy PID control based on maglev system.* IEEE Access, 2021. **9**: p. 96337-96344.
91. Ataşlar-Ayyıldız, B. and Karahan, O., *Design of a MAGLEV system with PID based fuzzy control using CS algorithm.* Cybernetics and Information Technologies, 2020. **20**(5): p. 5-19.
92. Shiakolas, P.S., Van Schenck, S.R., Piyabongkarn, D. and Frangeskou, I., *Magnetic levitation hardware-in-the-loop and MATLAB-based experiments for reinforcement of neural network control concepts.* IEEE Transactions on Education, 2004. **47**(1): p. 33-41.
93. Xu, S., Xu, Z., Jin, N. and Shi, L., *Levitation control scheme for the hybrid Maglev system based on neuron-PID control*. in *2005 International Conference on Electrical Machines and Systems*. 2005. IEEE.

94. Sun, Y., Xu, J., Qiang, H., Wang, W. and Lin, G., *Hopf bifurcation analysis of maglev vehicle–guideway interaction vibration system and stability control based on fuzzy adaptive theory.* Computers in Industry, 2019. **108**: p. 197-209.
95. Sun, Y., Wang, S., Lu, Y., Xu, J. and Xie, S., *Control of time delay in magnetic levitation systems.* IEEE Magnetics Letters, 2021. **13**: p. 1-5.
96. Chen, C., Xu, J., Rong, L., Ji, W., Lin, G. and Sun, Y., *Neural-network-state-observation-based adaptive inversion control method of maglev train.* IEEE Transactions on Vehicular Technology, 2022. **71**(4): p. 3660-3669.
97. Hu, W., Zhou, Y., Zhang, Z. and Fujita, H., *Model predictive control for hybrid levitation systems of maglev trains with state constraints.* IEEE Transactions on Vehicular Technology, 2021. **70**(10): p. 9972-9985.
98. Darby, M.L. and Nikolaou, M., *MPC: Current practice and challenges.* Control Engineering Practice, 2012. **20**(4): p. 328-342.
99. Qin, S.J. and Badgwell, T.A., *An overview of industrial model predictive control technology*. in *AIche symposium series*. 1997. New York, NY: American Institute of Chemical Engineers, 1971-c2002.
100. Schwenzer, M., Ay, M., Bergs, T. and Abel, D., *Review on model predictive control: An engineering perspective.* The International Journal of Advanced Manufacturing Technology, 2021. **117**(5): p. 1327-1349.
101. Camacho, E.F., Bordons, C., Camacho, E.F. and Bordons, C., *Constrained model predictive control*. 2007: Springer.
102. Rawlings, J.B. and Mayne, D.Q., *Model predictive control: theory and design, Nob Hill Pub.* Madison, Wisconsin, 2009. **825**.
103. Biegler, L.T., *Nonlinear programming: concepts, algorithms, and applications to chemical processes*. 2010: SIAM.
104. Brunton, S.L., Proctor, J.L. and Kutz, J.N., *Discovering governing equations from data by sparse identification of nonlinear dynamical systems.* Proceedings of the national academy of sciences, 2016. **113**(15): p. 3932-3937.
105. Ljung, L., *Perspectives on system identification.* Annual Reviews in Control, 2010. **34**(1): p. 1-12.
106. Williams, C.K. and Rasmussen, C.E., *Gaussian processes for machine learning*. Vol. 2. 2006: MIT press Cambridge, MA.
107. Hutter, F., Kotthoff, L. and Vanschoren, J., *Automated machine learning: methods, systems, challenges*. 2019: Springer Nature.
108. Stellato, B., Banjac, G., Goulart, P., Bemporad, A. and Boyd, S., *OSQP: An operator splitting solver for quadratic programs.* Mathematical Programming Computation, 2020. **12**(4): p. 637-672.
109. Wright, S.J., *Primal-dual interior-point methods*. 1997: SIAM.
110. Gill, P.E., Murray, W. and Saunders, M.A., *SNOPT: An SQP algorithm for large-scale constrained optimization.* SIAM review, 2005. **47**(1): p. 99-131.
111. Boyd, S., Parikh, N., Chu, E., Peleato, B. and Eckstein, J., *Distributed optimization and statistical learning via the alternating direction method of multipliers.* Foundations and

Trends® in Machine learning, 2011. **3**(1): p. 1-122.
112. Bemporad, A. and Morari, M., *Control of systems integrating logic, dynamics, and constraints.* Automatica, 1999. **35**(3): p. 407-427.
113. Bertsimas, D. and Tsitsiklis, J.N., *Introduction to linear optimization*. Vol. 6. 1997: Athena scientific Belmont, MA.
114. Patrinos, P. and Bemporad, A., *An accelerated dual gradient-projection algorithm for embedded linear model predictive control.* IEEE Transactions on Automatic Control, 2013. **59**(1): p. 18-33.
115. Diehl, M., Ferreau, H.J. and Haverbeke, N., *Efficient numerical methods for nonlinear MPC and moving horizon estimation.* Nonlinear model predictive control: towards new challenging applications, 2009: p. 391-417.
116. Athans, M. and Falb, P.L., *Optimal control: an introduction to the theory and its applications*. 2007: Courier Corporation.
117. Maciejowski, J., *Predictive control.* Constraints, 2001.
118. Zhu, B., Zheng, Z. and Xia, X., *Constrained adaptive model-predictive control for a class of discrete-time linear systems with parametric uncertainties.* IEEE Transactions on Automatic Control, 2019. **65**(5): p. 2223-2229.
119. Richards, A.G., *Robust constrained model predictive control*. 2005, Massachusetts Institute of Technology.
120. Streif, S., Kögel, M., Bäthge, T. and Findeisen, R., *Robust nonlinear model predictive control with constraint satisfaction: A relaxation-based approach.* IFAC Proceedings Volumes, 2014. **47**(3): p. 11073-11079.
121. Qin, S.J. and Badgwell, T.A., *A survey of industrial model predictive control technology.* Control engineering practice, 2003. **11**(7): p. 733-764.
122. Parisio, A., Rikos, E. and Glielmo, L., *A model predictive control approach to microgrid operation optimization.* IEEE Transactions on Control Systems Technology, 2014. **22**(5): p. 1813-1827.
123. Zhang, H., Seal, S., Wu, D., Bouffard, F. and Boulet, B., *Building energy management with reinforcement learning and model predictive control: A survey.* IEEE Access, 2022. **10**: p. 27853-27862.
124. Kapania, N.R. and Gerdes, J.C., *Path tracking of highly dynamic autonomous vehicle trajectories via iterative learning control*. in *2015 American control conference (ACC)*. 2015. IEEE.
125. He, H., Han, M., Liu, W., Cao, J., Shi, M. and Zhou, N., *MPC-based longitudinal control strategy considering energy consumption for a dual-motor electric vehicle.* Energy, 2022. **253**: p. 124004.
126. Nascimento, T.P., Dórea, C.E. and Gonçalves, L.M.G., *Nonholonomic mobile robots' trajectory tracking model predictive control: a survey.* Robotica, 2018. **36**(5): p. 676-696.
127. Teatro, T.A., Eklund, J.M. and Milman, R., *Nonlinear model predictive control for omnidirectional robot motion planning and tracking with avoidance of moving obstacles.* Canadian Journal of Electrical and Computer Engineering, 2014. **37**(3): p.

151-156.
128. Sun, Y., He, Z., Xu, J., Li, F. and Zhang, D., *Cooperative model predictive levitation control for two-points electromagnetic levitation system of high-speed maglev vehicle.* IEEE Transactions on Intelligent Vehicles, 2023.
129. Liu, Y., Fan, K. and Ouyang, Q., *Intelligent traction control method based on model predictive fuzzy PID control and online optimization for permanent magnetic maglev trains.* IEEE Access, 2021. **9**: p. 29032-29046.
130. Brzezina, W. and Langerholc, J., *Lift and side forces on rectangular pole pieces in two dimensions.* Journal of Applied Physics, 1974. **45**(4): p. 1869-1872.
131. Chen, X., Ma, W., Luo, S. and Zou, R., *Study on lateral stability of levitation modules for low- and medium-speed maglev trains.* Archive of Applied Mechanics, 2019. **90**(2): p. 437-447.
132. Köhler, J., Müller, M.A. and Allgöwer, F., *Analysis and design of model predictive control frameworks for dynamic operation—An overview.* Annual Reviews in Control, 2024. **57**: p. 100929.
133. Ding, B. and Yang, Y., *Model predictive control*. 2024: John Wiley & Sons.
134. Garcia, C.E., Prett, D.M. and Morari, M., *Model predictive control: Theory and practice—A survey.* Automatica, 1989. **25**(3): p. 335-348.
135. Khodarahmi, M. and Maihami, V., *A review on Kalman filter models.* Archives of Computational Methods in Engineering, 2023. **30**(1): p. 727-747.
136. Zenere, A. and Zorzi, M., *Model predictive control meets robust Kalman filtering.* IFAC-PapersOnLine, 2017. **50**(1): p. 3774-3779.
137. Garriga, J.L. and Soroush, M., *Model predictive control tuning methods: A review.* Industrial & Engineering Chemistry Research, 2010. **49**(8): p. 3505-3515.
138. Welch, G., *An Introduction to the Kalman Filter.* 1995.
139. Simon, D., *Kalman filtering.* Embedded systems programming, 2001. **14**(6): p. 72-79.
140. Bishop, G. and Welch, G., *An introduction to the kalman filter.* Proc of SIGGRAPH, Course, 2001. **8**(27599-23175): p. 41.
141. Sudhahar, S., Ganesh Babu, C. and Sharmila, D., *Kalman Filter-Based MPC Control Design and Performance Assessment of MIMO System*. in *Data Engineering and Communication Technology: Proceedings of ICDECT 2020*. 2021. Springer.
142. Franklin, G.F., *Feedback Control of Dynamic Systems*. 1994, Addison-Wesley.
143. Adetola, V., DeHaan, D. and Guay, M., *Adaptive model predictive control for constrained nonlinear systems.* Systems & Control Letters, 2009. **58**(5): p. 320-326.
144. Pereida, K. and Schoellig, A.P., *Adaptive model predictive control for high-accuracy trajectory tracking in changing conditions*. in *2018 IEEE/RSJ International Conference on Intelligent Robots and Systems (IROS)*. 2018. IEEE.
145. Zhang, S., Dai, L., and Xia, Y., *Adaptive MPC for constrained systems with parameter uncertainty and additive disturbance.* IET Control Theory & Applications, 2019. **13**(15): p. 2500-2506.
146. Sasfi, A., Zeilinger, M.N. and Köhler, J., *Robust adaptive MPC using control contraction metrics.* Automatica, 2023. **155**: p. 111169.

147. Nouwens, S.A.N., Paulides, M.M. and Heemels, M., *Constraint-adaptive MPC for linear systems: A system-theoretic framework for speeding up MPC through online constraint removal.* Automatica, 2023. **157**: p. 111243.
148. Liu, X., Qiu, L., Fang, Y., Wang, K., Li, Y. and Rodríguez, J., *Fuzzy Approximation ARX Model-based Intelligent Two-Horizon Robust FCS-MPC for Power Converter.* IEEE Transactions on Transportation Electrification, 2023.
149. Tian, B. and Peng, H., *RBF-ARX model-based MPC approach to inverted pendulum: An event-triggered mechanism.* Chaos, Solitons & Fractals, 2023. **176**: p. 114081.
150. Bermudez, M., Arahal, M.R., Duran, M.J. and Gonzalez-Prieto, I., *Model predictive control of six-phase electric drives including ARX disturbance estimator.* IEEE Transactions on Industrial Electronics, 2020. **68**(1): p. 81-91.
151. Perez, A. and Yang, Y., *Offset-free ARX-based adaptive model predictive control applied to a nonlinear process.* ISA transactions, 2022. **123**: p. 251-262.
152. Kang, T., Peng, H., Xu, W., Sun, Y. and Peng, X., *Deep Learning-Based State-Dependent ARX Modeling and Predictive Control of Nonlinear Systems.* IEEE Access, 2023. **11**: p. 32579-32594.
153. Zhang, H., Chen, J., Hua, C., Ding, Z., Lu, P. and Yang, C., *Proportional-Integral Control and ARX-based Model Predictive Control for Extractive Dividing Wall Column.* Chemical Engineering and Processing-Process Intensification, 2024. **196**: p. 109643.
154. Perez, A. and Yang, Y., *Adaptive model predictive control based on the steady state constrained ARX model*. in *2018 IEEE Green Energy and Smart Systems Conference (IGESSC)*. 2018. IEEE.
155. Harbi, I., Rodriguez, J., Liegmann, E., Makhamreh, H., Heldwein, M.L., Novak, M., Rossi, M., Abdelrahem, M., Trabelsi, M., Ahmed, M. and Karamanakos, P., *Model-predictive control of multilevel inverters: challenges, recent advances, and trends.* IEEE Transactions on Power Electronics, 2023. **38**(9): p. 10845-10868.
156. Zhou, F., Peng, H., Qin, Y., Zeng, X., Xie, W. and Wu, J., *RBF-ARX model-based MPC strategies with application to a water tank system.* Journal of Process Control, 2015. **34**: p. 97-116.
157. Zhou, F., Peng, H., Qin, Y., Zeng, X., Tian, X. and Xu, W., *A RBF-ARX model-based robust MPC for tracking control without steady state knowledge.* Journal of Process Control, 2017. **51**: p. 42-54.
158. Rixen, D.J., *A dual Craig–Bampton method for dynamic substructuring.* Journal of Computational and applied mathematics, 2004. **168**(1-2): p. 383-391.